# מכון ויצמן למדע

# Weizmann Institute of Science

Thesis for the degree
**Doctor of Philosophy**

**חבור לשם קבלת התואר**
**דוקטור לפילוסופיה**


by:
**Guy Y. Garty**

supervisor
Prof. A. Breskin

**מאת**
**גיא י. גרטי**
**מנחה**
**פרופ. ע. ברסקין**


# פתוח שיטה ננודוסימטרית המבוססת על ספירת יונים וחקר יישומיה ברדיוביולוגיה

# Development of ion-counting nanodosimetry and evaluation of its relevance to radiation biology

January 2004

**טבת תשס"ד**

Submitted to the Scientific Council of the
Weizmann Institute of Science
Rehovot, Israel

**מוגש למועצה המדעית של**
**מכון ויצמן למדע**
**רחובות, ישראל**

## *Table of contents*

## *Acknowledgements*

It is my pleasure to thank my advisor, Prof. A. Breskin, for introducing me to the field of radiation detection physics and for supporting my foray into the realms of biology. His continued encouragement and support throughout this work is indeed appreciated.

Many thanks to Dr. S. Shchemelinin, with whom I have worked closely for the last five years. I have found our long discussions both fruitful and enlightening. Thanks also to Dr. R. Chechik who extended her interest and support, through many fruitful discussions. Thanks to Gili Assaf, who did some of the experiments described here as a part of her masters thesis.

To Dr. Corinne Leloup, who performed most of the biological experiments described below. I don't know how I would have managed without her continued support.

I would also like to extend thanks to M. Klin, Y. Asher, the workers of the physics machine shop and the electronics group for their extensive and continuous technical support and to Dr. Armin Schon of El-Mul technologies ltd. for the generous donation of the MCP and phosphor plates used in this study.

To the staff of the WIS accelerator labs and in particular to Yigal Shachar. His support was truly above and beyond the call of duty.

To my collaborators abroad (Dr. R. Schulte, Dr. V. Bashkirov, Dr. J. Milligan and Dr. B. Grosswendt) and at WIS (Prof. Z. Livneh and Dr. T. Paz-Elitzur) for their continuous support of this project.

I would like to thank the many generations of students who passed through the radiation detector physics lab while I was there (Amir, Thierry, Efrat, Dirk and Gili as well as many summer students, rotation students and postdocs) for their assistance in coping with the practical sides of experimental physics as well as for making my stay in the group a pleasurable one.

This work was partially supported by the National Medical Technology Testbed Inc. (NMTB) under the U.S. Department of the Army Medical Research Acquisition Activity, Cooperative Agreement Number DAMD17-97—2-7016 and by the MINERVA Foundation. The views, opinions and/or findings contained in this report are those of the authors and should not be construed as a position, policy, decision or endorsement of the US Federal Government and NMTB.

## *List of abbreviations*

| | | |
|---|---|---|
| $A_1$-$A_4$ | - | Apertures 1-4 below the ion extraction aperture |
| AS | - | Anti-Scattering |
| bp | - | base pair |
| BER | - | Base Excision Repair |
| CCD | - | Charge Coupled Device (camera) |
| CFD | - | Constant Fraction Discriminator |
| CL | - | Clustered Lesions |
| CMOS | - | Complementary Metal Oxide Semiconductor |
| CPU | - | Cluster Pile-Up |
| CVD | - | Chemical Vapor Deposition diamond |
| DAQ | - | Data AcQuisition system |
| DC | - | Direct Current (used here to mean constant voltage) |
| DME | - | Dimethyl Ether |
| DNA | - | Deoxy-riboNucleic Acid |
| DSB | - | Double Strand Break |
| EDTA | - | EthyleneDiamineTetraAcetic acid |
| eq. | - | Equation |
| FP | - | Fragmented (form of the plasmid) |
| FWHM | - | Full Width at Half Maximum |
| IC | - | Ion Counter |
| INFN-LNL | - | Instituto Nazionale di Fisica Nucleare – Laboratori Nazionali di Legnaro (Padova, Italy) |
| IV | - | Interaction Volume |
| LB | - | Luria-Bertani bacterial growth medium |
| LP | - | Linear (form of the plasmid) |
| LET | - | Linear Energy Transfer (=dE/dx) |
| LGS | - | Linear Gate Stretcher |
| LLUMC | - | Loma-Linda University Medical Center (Loma-Linda, CA) |
| MC | - | Montè – Carlo |
| MCP | - | Micro-Channel Plate |
| MSAC | - | Multi-Step Avalanche Chamber |
| MWPC | - | Mult-Wire Proportional Counter |
| ND | - | NanoDosimeter |
| NER | - | Nucleotide Excision Repair |
| OC | - | Open Circular (form of the plasmid) |
| $OD_{600}$ | - | Optical density at a wavelength of 600nm |
| OPAC | - | OPtical Avalanche Chamber |
| pH | - | Acidity |
| PIN | - | Positive-Intrinsic-Negative (diode) |
| PMT | - | PhotoMultiplier Tube |
| PPIC | - | Paralel Plate Ionization Chamber |
| ppm | - | parts per million |
| PTB | - | Physikalisch-Technische Bundesanstalt (Braunschweig, Germany) |
| RBE | - | Relative Biological effectiveness |
| RMS | - | Root of the Mean of the Squares |
| SEC | - | Single Electron Counter |
| SEL | - | Single Event Latchup |
| SEU | - | Single Event Upset |
| SC | - | SuperCoiled (form of the plasmid) |
| SV | - | Sensitive Volume |
| SSB | - | Single Strand Break |

| | | |
|---|---|---|
| TAC | - | Time to Amplitude Converter |
| TBE | - | Gel running buffer (Tris-Boric acid-EDTA) |
| TE | - | Tris-EDTA buffer |
| TEG | - | Tissue Equivalent Gas |
| TEPC | - | Tissue Equivalent Proportional Counter |
| WIS | - | Weizmann Institute of Science (Rehovot, Israel) |

## List of units

In general MKS units were used with the standard prefixes (p, n, μ, m, c, k, M). The only deviations are:

| | | |
|---|---|---|
| 1eV | = | $1.6\ 10^{-19}$ J |
| 1 Gy | = | 1 J/kg = 0.1 krad |
| 1 Da | = | Mass of a single H atom ≅ $1.7\ 10^{-27}$ kg |
| 1 Torr | = | 1 mm of Hg = 133 Pa |
| 1 g/cm$^3$ | - | rather then 1000 kg/m$^3$ |
| cm$^2$/g | - | Reduced length (length/density) |
| 1 MB/sec | = | 1 MegaByte/sec |
| Coulomb | - | Was spelled out to avoid confusion |
| Hz | - | Was generally used as an average frequency of a stochastic pulse sequence and does not imply periodic behavior. |
| 1 mM | = | 1 milliMolar = $10^{-3}$ Mole/liter = $6.022\ 10^{17}$ molecules/cm$^3$ |
| 1 L | = | $10^3$ cm$^3$ |
| Min | - | Minute |
| kRPM | = | $10^3$ Cycles per minute |

## List of symbols

| | |
|---|---|
| $A$ | Effective mass number of target |
| $a_o$ | Bohr radius = $0.529\ 10^{-8}$ cm |
| $b$ | Correlation length of lesions on the DNA in the model of [111] |
| $B_i$ | Binding energy of state $i$ |
| $b_{nl}$ | Parameter for calculation of K shell ionization cross section |
| $c$ | Velocity of light |
| $c_1 \ldots c_6$ | Dimensionless fitting parameters |
| $c_{nl}$ | Parameter for calculation of K shell ionization cross section |
| $C$ | Electron shell correction to Bethe-Bloch equation |
| $D$ | Diameter |
| $d$ | Distance |
| $\tilde{D}$ | Dose |
| $dE$ | Deposited energy |
| $D_i$ | Ion diffusion coefficient |
| $d_k$ | Parameter for calculation of K shell ionization cross section |
| $dx$ | Length of track segment |
| $d\sigma/d\Omega$ | Differential cross section with respect to solid angle |
| $d\sigma/d\varepsilon$ | Differential cross section with respect to outgoing electron kinetic energy |
| $E$ | Electric field |
| $E_m$ | The maximal allowable energy transfer between a projectile and a free electron |
| $f(n_{ion})$ | (Absolute) ion cluster-size distribution |
| $f(t, x)$ | Probability of an ion formed at $x$ to arrive to the IC after time $t$. |
| $f_1(x, y)$ | Probability of a projectile traversing the SV at $(x, y)$ and along $z$ to induce one ion which is successfully extracted from the SV. |

$FP$, $FP^M$ model simulated and measured fraction of FP plasmid
$G_{DSB}$ Yield of double strand breaks
$G_{tot}$ Yield of clustered lesions
$I$ Target ionization potential
$i_{PPIC}$ Ionization chamber current
$i, j$ Generic index
$k$ Ratio of ionization mean free paths, for unit density media
$K$ Kinetic energy
$\tilde{K}$ $0.154\ MeV\ g^{-1}\ cm^2$ – Lumped constant for the Bethe-Bloch equation
$k_b$ Boltzmann constant = $1.38\ 10^{-23}\ J/°K$
$k_b\ T_{eff}$ Average kinetic energy of ions in electric field
$K_i$ Ion mobility
$\tilde{L}$ Mean chord length
$L, l$ Length
$LP$, $LP^M$ model simulated and measured fraction of LP plasmid
$m_\nu$ Mass of particle ν
$n$ Generic index
$N$ Molecular density
$N_A$ $=6.022\ 10^{23}$ – the Avogadro number
$N_c$ Number of colonies
$n_e$ Electron cluster size
$n_{ion}$ Ion cluster size
$\tilde{n}_\nu$ Electron occupancy number in state ν
$OC$,$OC^M$ model simulated and measured fraction of OC plasmid
$P$ Pressure
$\ddot{P}$ The binomial distribution
$\dddot{P}$ The trinomial distribution
$p$ Probability
$\tilde{p}(i)$ Probability that given $i$ strand breaks at least two will be on opposite strands.
$p_{SB}$ Probability for a single ion to be converted to a single strand break
$p_{tot}$ Probability for a single ion to be converted to a single lesion
$Ry$ Rydberg constant=13.61 eV
$S$ Mass stopping power
$SC$, $SC^M$ model simulated and measured fraction of SC plasmid
$T$ Temperature
$t$ Time
$U$ Ratio of kinetic energy to ionization potential
$v$ Ion drift velocity
$V$ Volume
$V_{SV}$ Volume of the sensitive volume
$W_i$ The mean energy per ion pair (integral – i.e. in an infinitely thick target)
$w_i$ The mean energy per ion pair (differential – i.e. in an infinitely thin target)
$x$ Cartesian coordinate #1 (along the SV major axis)
$X_D$ Intermediate variable in the model of [111]
$y$ Cartesian coordinate #2
$Y_D$ Intermediate variable in the model of [111]
$z$ Cartesian coordinate #3 (along the projectile track)
$Z$ Effective atomic number of target
$z_{eff}$ Effective charge state of projectile
$z_p$ Projectile charge

$\alpha$ Conversion factor from the absolute to the conditional cluster size

distribution

| | |
|---|---|
| $\beta$ | Projectile velocity |
| $\delta(\rho)$ | Density correction to Bethe-Bloch equation |
| $\Delta t$ | Time interval |
| $\Delta y$ | RMS of ion transverse diffusion |
| $\varepsilon$ | Outgoing electron kinetic energy |
| $\varepsilon(x, y, z)$ | Ion extraction efficiency map |
| $\varepsilon_0$ | Permittivity of vacuum |
| $\eta$ | Screening parameter |
| $\vartheta, \theta$ | Polar angle |
| $\Lambda$ | Scale |
| $\lambda$ | Mean free path for ionization |
| $\mu$ | Yield of SSBs per Gy per Da |
| $\mu'$ | Yield of isolated lesions per Gy per Da |
| $\mu_0$ | Yield of SSBs per Da before irradiation |
| $\mu'_0$ | Yield of isolated lesions per Da before irradiation |
| $\nu$ | Generic index |
| $\rho$ | Target density |
| $\sigma_c^K$ | Cross section for K-shell ionization |
| $\sigma^{el}$ | Elastic cross section |
| $\sigma^{exc}$ | Excitation cross section |
| $\sigma^{ion}$ | Ionization cross section |
| $\sigma_{SB}(n_{SB})$ | Cross section for generating $n_{SB}$ strand breaks |
| $\sigma_{tot}(n_{tot})$ | Cross section for generating $n_{tot}$ lesions |
| $\sigma(n_{ion})$ | Cross section for generating $n_{ion}$ ions |
| $\phi$ | Yield of DSBs per Gy per Da |
| $\phi'$ | Yield of clustered lesions per Gy per Da |
| $\phi_0$ | Yield of DSBs per Da before irradiation |
| $\phi'_0$ | Yield of clustered lesions per Da before irradiation |
| $\varphi(n_{ion})$ | (Conditional) ion cluster-size distribution |
| $\Phi$ | Parameter for calculation of K shell ionization cross section |
| $\Phi_{1Gy}$ | Proton flux required for 1 Gy |
| $\Psi$ | Parameter for calculation of K shell ionization cross section |

# Abstract

The goal of our research is the development of novel concepts and tools for the precise evaluation of the ionization track structure, induced by charged particles traversing a sparse gaseous medium. The *nanodosimeter* is based on counting single radiation-induced ions formed within small volumes of low density gas simulating condensed matter of million times smaller dimensions; it enables, for the **first time**, an experimental evaluation of ionization patterns in condensed matter on nanometer dimensions, based on precise measurements in an expanded gas model. These measurements are relevant for the understanding of radiation damage to tissue, at DNA dimensions.

Within this work we have designed, constructed and tested two nanodosimeters. The nanodosimeters were mounted at accelerator beams (both at the Weizmann institute of Science and at the Loma Linda University-Medical Center in California) and used for measuring the ionization clusters induced by radiation fields spanning 4 orders of magnitude in average ionization density (LET values of 0.4 keV/μm to 700 keV/μm). Up to an LET value of 26 keV/μm, we have reliably measured cluster size distributions in conditions equivalent to the irradiation of DNA *in vitro*. The measured ion cluster size distributions were validated by extensive simulations of primary and secondary interactions in the gas, ion transport and counting.

To complement these measurements, the final effect of radiation on DNA was also quantified by irradiating plasmid DNA. We have measured the formation of single and double strand breaks, as well as clustered lesions containing a combination of strand breaks and base damages, in irradiated DNA.

While both types of measurements yield important data to their respective fields, it is only through a correlation of both measurements, that it is possible to model the phenomena of radiation-induced mutagenesis and cell death, which are induced by large ionization clusters. In this project, we present a basic model, which predicts the measured yields of clustered DNA lesions, based on cluster size distributions within a gas model, measured under equivalent conditions. To the best of our knowledge, this is the **first time** that such a comparison between the physical energy deposition and the biological endpoints, becomes possible.

# Chapter 1 :

# Introduction

## *1.1 Motivation*

Shortly after the discovery of radiation in 1896, it was found to cause adverse effects in living tissue [1]. The most sensitive target for these effects is naturally the DNA – the "blueprint of life". Lesions in DNA interfere with its replication and transcription and if left unrepaired can cause mutation, malfunction, and cell death. These deleterious effects are usually prevented by DNA repair mechanisms, which identify the lesion, remove it and restore the original DNA sequence. In the case of ionizing radiation however, the enzymatic repair mechanisms cannot cope with the *clustered nature* of the lesions, resulting in modification of the organism's genetic code. The complexity of DNA damage, relating directly to its reparability, can be traced back to the complexity of the ionization track structure. *In order to describe the types of damage to be expected in cellular DNA, it is necessary to identify not only the radicals involved and their reactions, but also, since they will react close to their position of formation,* ***their initial spacing relative to each other*** [2]. Indeed figure 1.1a demonstrates the high correlation of ionization events caused by α-particles in a Wilson cloud chamber; the energy deposits formed by a single particle are localized along a thin line. A further magnification of this line shows that the ionizations are clustered on a micron and sub-micron scale. Particularly important are correlated energy depositions on a **few-nanometer** scale, corresponding to short DNA segments of up to 20 base-pairs (bp).

The goal of this research is the development of novel tools for the precise study of the ionization track structure, induced by charged particles traversing a sparse gaseous medium, simulating short segments of DNA. Such measurements can then be correlated, using a biophysical model, to **direct measurements** of DNA lesion-clusters in irradiated DNA.

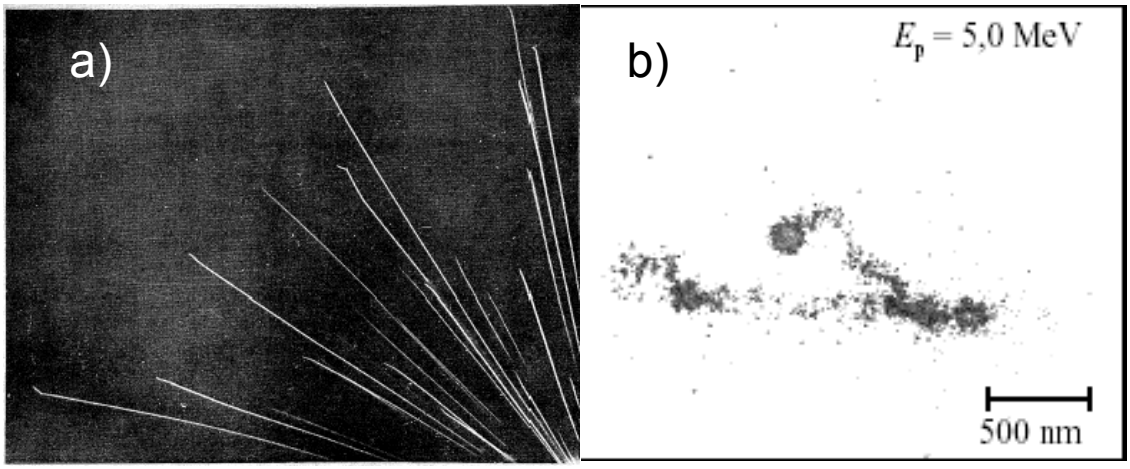


**Figure 1.1: a) A cloud chamber image of α-particles induced by Radium.** This is the first time that the highly localized energy deposition of ionizing radiation was observed. Photo reproduced from CRT Wilson [3].  b) A short segment of a 5 MeV Proton track, measured with the OPAC detector (see §2.3.1 below). Note the clustering of the ionizations within the track segment and the δ-electron track.

The nanodosimeter (ND) developed within this project, is based on **counting single radiation-induced ions** in a gas volume simulating condensed matter. It enables, **for the first time**, the modeling of the interaction of radiation with condensed mater on a **nanometer**

**scale**; this is relevant for the understanding of radiation damage to tissue, at the DNA scale and possibly to nanoelectronic devices.

Compared to other microdosimetric techniques (see §2.2-2.3), the ion counting nanodosimeter presents a much smaller sensitive volume (comparable to a short segment of DNA) and higher sensitivity to single ionization events within this volume. It is free of the most common type of secondary effects – due to radiation interaction with the detector walls. Due to the free choice of operating gas, it is also much more versatile than other devices.

The ion counting nanodosimeter provides a significant step forward in the field of radiation physics. It provides new, previously inaccessible, information on the nanometer-scale fluctuations in the track structure of ionizing radiation. The nanodosimetric measurements can be correlated with precise measurements of the effects of radiation on DNA. This correlation, through a biophysical model, enables for the first time the prediction of radiation effects in nanometer-sized biological systems.

In the field of radiation monitoring and protection, a nanodosimeter accompanied by such a model may be used for quantifying the "lethality" of known and unknown radiation environments (e.g. in space). In the field of radiation medicine it can be used for quantifying the "lethality" of a therapeutic ion beam both to the tumor and the surrounding tissue, enabling better optimization of radiation therapy protocols.

## *1.2 Overview of the project*

Within this work, an ion counting nanodosimeter (ND) was designed (based on a prototype by Dr. Shchemelinin) and two ND systems were constructed at the WIS machine shop and characterized by Mr. Garty and Dr. Shchemelinin. The front end electronics as well as the data acquisition system were designed by Dr. Bashkirov of LLUMC, while the offline analysis software was written by Mr. Garty.

The NDs were mounted at three accelerators (at the Pelletron and Van de Graaff accelerators at the Weizmann institute of science (WIS) as well as at the proton synchrotron at the Loma Linda university-medical center - LLUMC) and ionization clustering measurements were performed over a wide range of radiation fields, spanning 4 orders of magnitude in specific ionization (LET values between 0.4 and 600 keV/μm). In parallel, we have performed radiobiological measurements of the effects of the same radiation fields on DNA, irradiated *in vitro*. The results of both types of experiments enabled the development of a biophysical model predicting the yield of clustered lesions formed in DNA, based on the ionization clustering measurements using the ND.

Throughout this work, extensive use has been made of dedicated Montè-Carlo (MC) simulations to assess the ND performance. We have written and employed extensive MC simulation codes; they permitted simulating the expected ionization patterns, on the basis of primary and secondary interactions, ion transport and counting in the nanodosimeter and the properties of its data acquisition (DAQ) system. In particular, we have employed the track structure code developed by Dr. Grosswendt (of PTB) which was modified by him, in close cooperation with Mr. Garty, Mrs Assaf and Dr. Shchemelinin, to better model the ND. All track structure simulations shown here were performed by Mrs. Assaf as part of her M.Sc. dissertation. This code is described in detail in Appendix A. We also used the ion drift code developed by Dr. Shchemelinin within this work, for evaluation of the ND's sensitive volume dimensions. The other MC codes used in this work were all written by Mr. Garty.

After a brief theoretical background (§2), the ND construction and characterization are described in detail (§3-§4), including the results of accelerator-based nanodosimetric experiments, utilizing pencil beams of protons and carbon nuclei, carried out at the WIS Pelletron accelerator. These measurements were vital for the characterization of the nanodosimeter, under well defined conditions and as a preparation for the, biologically

relevant, broad-beam experiments described in §5. The latter are the more important ones, as they model the conditions in which the DNA is irradiated. Although, the results of broad-beam irradiations of the ND are the only ones which we have used in the biophysical model, we would not have been able to reliably measure them without a thorough study of the narrow beam irradiations.

The methodology and results of radiobiological experiments designed to measure the formation of lesion clusters in DNA irradiated *in-vitro* are described in §6. These measurements were based on those proposed by Dr. Milligan of UCSD. The low LET measurements at LLUMC were conducted by Dr Milligan and Dr. Bashkirov. The high LET measurements at WIS were performed and analyzed by Dr. Leloup, Mr. Garty, Mrs. Assaf and Mrs. Cristovão (a visitor in our group). The irradiation setup used at WIS was designed by Mr. Garty based on the one Built by Dr. Bashkirov at LLUMC.

In these measurements we have used purified plasmid DNA as a radiation target. The DNA was irradiated by charged particles and γ–rays, spanning an LET range of two orders of magnitude (0.2 to 26 keV/μm). We have chosen to use plasmid DNA as our target system as it allows us to control the presence of enzymatic repair mechanisms. By eliminating repair, we can quantify the initial radiation effects in irradiated DNA; these can be compared to the nanodosimetric measurements. By allowing only certain damages to be repaired, we can probe for specific classes of lesions, such as lesion clusters.

These experiments demonstrated a clear dependence between the lesion yields and ionization density. On the macroscopic scale (LET) we have seen a complex dependence of the clustered-lesion yields on LET, due to radical recombination effects leading to a decrease in damage yields with rising LET. On the nanometer scale, on the other hand, we have seen an increase in the yield of clustered-lesions with ionization density (for radiation fields having the same or almost the same LET).

Based on the nanodosimetric measurements Mr. Garty, in cooperation with Dr. Schulte (of LLUMC) developed a basic biophysical model, for predicting the results of the radiobiological measurements. Such a model (described in §7) permits “calibrating” the newly developed ND in terms of biologically-relevant damage yields. The model details were based on the biological system we have studied. Although the model predicts the general trends observed in the radiobiological measurements, we have seen that it is too simplistic to predict their results accurately. A more complex biophysical model, based also on microdosimetric data and on (known) radical diffusion and reaction mechanisms, is required for more accurate prediction of radiation damage effects in DNA.

# Chapter 2 :

# Theoretical background

This work deals with the application of the study of radiation interactions with a gaseous medium to the problem of the interaction of radiation with condensed matter, in particular DNA. We start with a brief introduction to the theory of the interaction of charged particles with matter. A full theoretical [4] and application-related [5] analysis is given elsewhere. We will then describe the implications of this theory on DNA and (briefly) on microelectronic devices.

Separate sub-sections will describe the current use of gaseous detectors for modeling biological systems (microdosimetry) (§2.2) and the theory of the operation of our nanodosimeter (§2.3.2).

## *2.1 Interaction of radiation with matter*

A fast (but not ultra-relativistic), charged particle, traversing matter, interacts primarily via the electromagnetic interaction, causing excitations and ionizations along its path. The particle's energy loss can be calculated within the framework of relativistic quantum mechanics, giving the Bethe-Bloch equation [4, 5]:

$$\frac{dE}{dx} = -\tilde{K}\frac{Z}{A}\frac{\rho}{\beta^2}\left\{\ln\frac{2mc^2\beta^2 E_M}{I^2(1-\beta^2)} - 2\beta^2 - \frac{2C}{Z} - \delta(\rho)\right\} \qquad (2.1)$$

where the additional terms within the curly brackets (C/Z and δ(ρ)) take into account electron shell or density-related effects [6], additional relativistic effects may also be added [4, 7]. Here $\tilde{K} = \frac{2\pi N_A e^4}{m_e c^2} = 0.154\ MeV\ g^{-1}\ cm^2$; $Z$, $A$, $\rho$ and $I$ are the medium parameters (atomic number, atomic mass, density and average ionization potential, respectively). The parameter $z_p$ is the projectile's charge state, $\beta$ is its velocity; $m_e$ is the electron mass, $c$ the velocity of light and $N_A$ the Avogadro number.

Note that the only medium-related parameters in this formula are the electron density, $Z\rho/A$, and the average ionization potential, $I$. In effect the projectile is traversing a (nearly) **free-electron gas**.

The parameter $E_M$ is the maximal allowable energy transfer between the projectile and the electron emitted in an ionization event. It is found from relativistic two-body kinematics (e.g. §1.5 of [8]) as

$$E_M = \frac{2m_e c^2\beta^2}{1-\beta^2} \qquad (2.2)$$

The probability of generating an electron of energy $E$ (within a track segment of length $l$) is given roughly by the first term in (2.1) [5]:

$$p(E)dE = \tilde{K}\frac{z_p^{\ 2}}{\beta^2}\frac{Z}{A}\frac{\rho l}{E^2} \qquad (2.3)$$

with a cutoff at $E=E_M$ (a more accurate expression as well as discussion are given in [9]). Typical electron range distributions, generated by our MC code (see Appendix A) are given in figure 2.1.

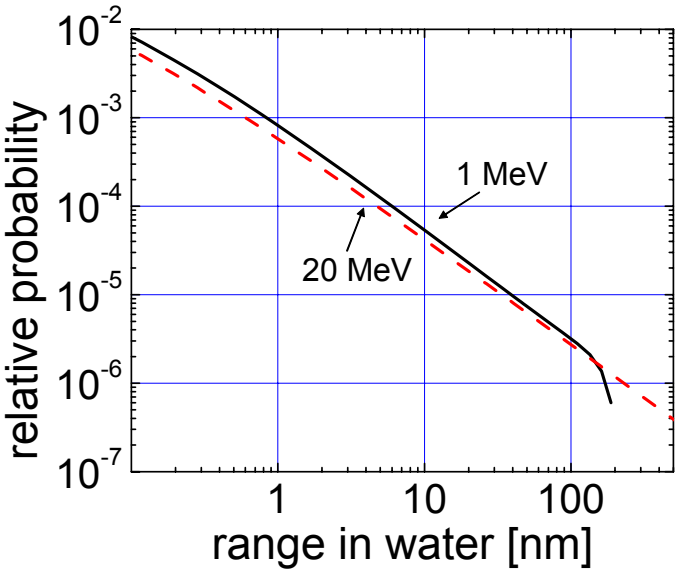


**Figure 2.1: Simulated proton-induced δ-electron range distributions**. The relative probability for a δ-electron of given range to be generated by a 1 MeV proton (solid line) or by a 20 MeV proton (dashed line) in water. The electron energy distributions were calculated as described in Appendix A. They were converted to electron ranges using the formula given in §2.5 of [5].

As can be seen, while most ionization electrons, generated by the projectile will have energy below the ionization threshold of the medium (typically 10 eV), there is a finite probability of generating higher energy electrons. Such electrons, termed δ-electrons, will create further ionizations in the medium and transport energy *away from the main track*.

The track structure of a charged particle can be envisioned as being composed of a central region, consisting of a very thin straight line, containing the primary ionizations, surrounded by a far reaching halo of δ-electron mediated ionizations.

A simulated image of a short segment of a proton track, with its δ-electrons, is given in figure 2.2. In 2.2a, the segment is condensed along its axis ($z$) to demonstrate its extent lateral to $z$. When viewed on the scale of a cell nucleus (typically 3μm diameter - figure 2.2b) the track appears uniform (see also figure 1.1a), a closer look (figure 2.2c) reveals the inherent clustering in the track structure. The consequence of this is that when studying radiation effects on the cell as a whole (microdosimetry), the radiation can be envisioned as a field of "uniform rays". When looking at the DNA scale, on the other hand, this approximation breaks down and we see a stochastic distribution of ionization clusters. **It no longer makes sense to characterize the radiation quality in terms of average ionization density along the track.**

### 2.1.1 Radiation damage to DNA

Radiation damage to DNA occurs via two pathways. About 35% of the damage (depending on the cellular chemistry [2] and slightly on LET [10]), is induced by direct ionization of the DNA. This is termed **"direct damage"**. The remaining 65% are due to the radiolysis of water molecules and formation of reactive species (termed **"indirect damage"**).

In the case of indirect damage, following the initial energy deposition (on a sub-picosecond time scale), the projectile's track consists of free electrons and $H_2O^+$ ions, which will dissociate into a $H^+$ ion and a $OH^\bullet$ radical. The free electron will be captured by an $H^+$ ion

to produce an $H^{\bullet}$ radical, or by a water molecule to form an $H_2O^-$ ion, which will dissociate to a $H^{\bullet}$ radical and a $OH^-$ ion [6].

At a time of about 10 psec, after the passage of the projectile, the track will consist of $H^{\bullet}$ and $OH^{\bullet}$ radicals and (relatively inert) solvated electrons $e^-_{aq}$ [11] (the $H^+$ and $OH^-$ ions can be ignored as they occur naturally in water at a concentration of ~1/μm$^3$; any excess of such ions will disappear by recombination). Roots and Okada [12] have shown that the radical-induced component of the DNA damage can be attributed primarily to the $OH^{\bullet}$ radical.

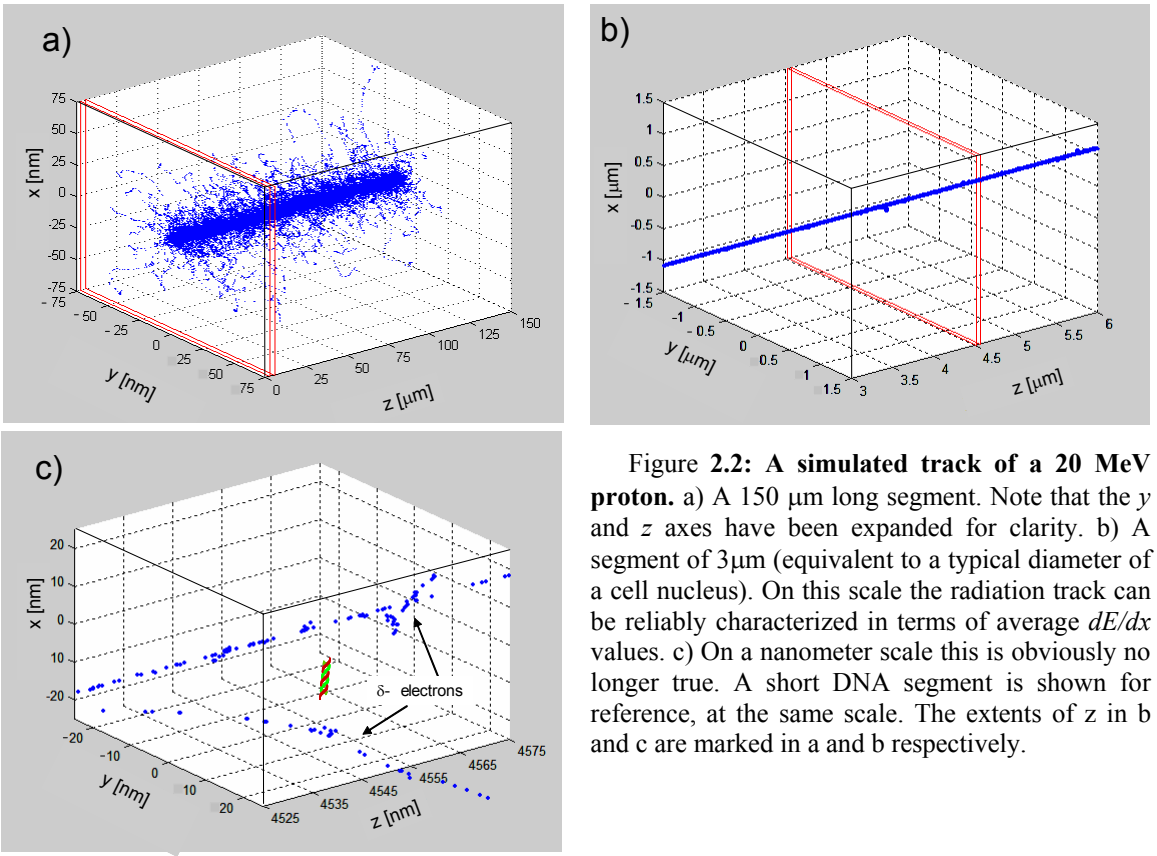


Figure **2.2: A simulated track of a 20 MeV proton.** a) A 150 μm long segment. Note that the *y* and *z* axes have been expanded for clarity. b) A segment of 3μm (equivalent to a typical diameter of a cell nucleus). On this scale the radiation track can be reliably characterized in terms of average *dE/dx* values. c) On a nanometer scale this is obviously no longer true. A short DNA segment is shown for reference, at the same scale. The extents of z in b and c are marked in a and b respectively.

At longer time scales (up to nanoseconds), the radicals diffuse away from the track (if they have not recombined with each other) and react with any molecules which may be present. In the case of tissue this may be proteins, DNA or various radical scavenger molecules (present in the cellular environment to prevent radicals induced by metabolism to damage the DNA). They are already too sparse to recombine with each other. The characteristic diffusion length, before being scavenged, in a cellular environment is a few nm [2], but depends strongly on the (local) cellular chemistry. Only a small fraction of radicals which are not scavenged, and which can diffuse to the DNA molecule will indeed cause damage.

The typical types of damages (caused equally well by direct ionization or by reactive species) are shown in figure 2.3:

**Single strand break (SSB)**: A radical reacts with the sugar-phosphate backbone of the DNA, severing it. This type of damage is rather easy to repair, as the opposite DNA strand remains intact. A *ligase* enzyme simply reconnects the severed link.

**Single base damage (BD):** A radical attacks one of the bases of the DNA, altering it chemically. In repair proficient cells, there exist specific *base excision enzymes*, which can recognize specific types of such lesions and remove the damaged base, forming a "temporary

empty space". The missing base is then inserted by a *DNA polymerase* and the DNA is again intact.

**Double strand break (DSB)**: In some cases two correlated lesions (induced by the same track) may attack the same short segment of DNA. In such a case a DSB may be formed if both radicals induce SSBs on opposite strands of the DNA (within a short distance of each other). This is denoted a **"frank DSB"**. Alternatively, one or both radicals may induce a base damage. During the repair process, the base damage is converted to a strand break. The two SSBs then become an **"induced DSB"**. The repair of such clustered damages is more complicated and generally error prone [13].

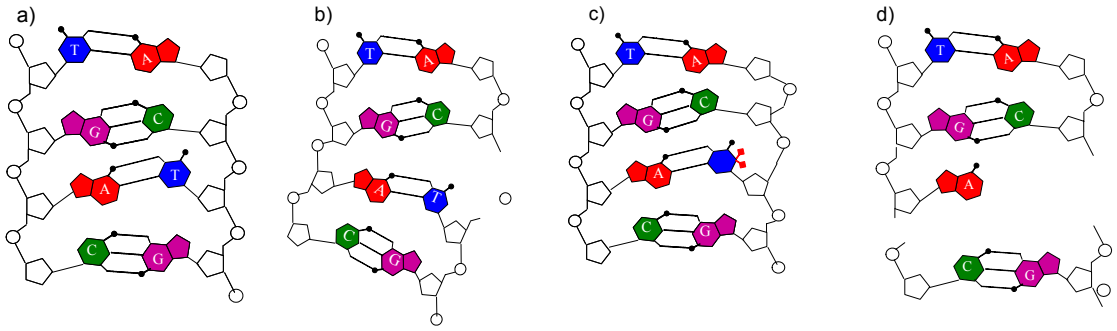


**Figure 2.3: Artist view of damage to DNA**: a) a short (intact) DNA segment. b) A short DNA segment with a single strand break (SSB). c) A short DNA segment with a base lesion (Thymine➔Thymine glycol) – Note the slight distortion of the sugar-phosphate backbone. d) a double strand break formed by the repair of the lesion in c and a direct SSB between A and C in the left hand strand.

#### 2.1.1.1 Relevance of clustered lesions

Of course, more complex damage may occur as a result of more lesions formed within the same short DNA segment. Indeed, the main characteristic of radiation-induced damage is its inherent clustering. Due to the short range (lifetime) of the radicals, most damages are formed within a few to a few tens of nm away from the track. Therefore, while ~3 $10^6$ non-correlated SSBs (caused by a chemical agent for example) are required on average to kill a cell, the typical lethal dose for ionizing radiation is ~1000 SSBs/cell [14].

As noted above, a great deal of DNA damage is also created as a side product of normal cell metabolism [15], the cell must therefore contain elaborate mechanisms to repair damaged DNA (or in some cases to kill the cell [16]). Such mechanisms (described in great detail in [17]) usually consist of enzymatic "proofreading" of the DNA double helix, identifying mismatched pairs (or distorted molecules). Single damaged bases may be excised and replaced using the base excision repair (BER) pathway. Larger damages consisting of several lesions on the same strand are typically repaired using nucleotide excision repair (NER) whereas a short segment of DNA (typically about 7 bases) is excised and replaced by "fresh bases", relying on the information present in the complimentary DNA strand. These mechanisms are rather efficient at repairing isolated damages however they cannot cope with lesion clusters. Small damage clusters (a few close damages) are usually repaired using a **low-fidelity** DNA polymerase (such as *polη* in humans [13], having 95% accuracy, compared to the ppm accuracy of the regular polymerase [17]). This low fidelity polymerase can insert (by force) short DNA segments opposite a damaged DNA strand, regardless of the degree of matching with the second strand; naturally this will lead to some corruption of the data stored within the DNA.

Larger damage clusters are typically repaired using a recombination mechanism, whereas a DNA segment from elsewhere in the genome is copied onto the damaged region. The latter

mechanism may induce large genetic alterations due to the exchange of DNA from one region of the genome to another, effecting gene expression and, in some cases, cell survival [18]. These two repair mechanisms (recombination and low-fidelity NER) are (probably) responsible for evolution.

### 2.1.2 Interaction of radiation with microelectronic devices

Micron and sub micron electronic devices are also susceptible to radiation damage. In fact such devices are often present in high radiation environments, far above the exposures typically encountered by any biological system. Particularly important are the intense radiation fields present in high-energy physics experiments (e.g. [19]), and in space [20]. For example, the central tracking system in the ATLAS detector is expected to receive a dose of $10^6$ -$10^7$ Gy in the first year of operation (the typical dose required to kill a cancerous tumor using proton therapy is about 1 Gy).

Similar to biological matter, following the passage of an ionizing projectile, its track will consist of many *Frenkel defect pairs* [21] (analogous to free radicals) consisting of a displaced atom and the vacancy left by it. Both entities are extremely mobile and tend to aggregate at and react with lattice impurities. These damage clusters are electronically active, namely they act as dopants, being a source (or a trap) for carriers, resulting in accumulated crystalline damage and leading to a degradation of the material properties (carrier mobilities, resistivities etc.) and thus device performance.

Similar to DNA, exposed to radiation, a corruption of stored information can also occur in semiconductor devices. Such devices store information as charge on a capacitor, and it is easy to see how an ionizing particle traversing this device, depositing charges in it, may induce data corruption ("Single Event Upset"-SEU), or cause the device to stop functioning ("Single Event Latchup" - SEL) [22, 23]:

An SEU occurs when a single projectile deposits charge into a sensitive node of a bi-stable storage element, assuming this charge exceeds the critical charge required to change the logic state. This type of event is non-destructive and may be corrected by "rewriting" the changed bit. This type of correction requires the circuit to be designed in such a way that single bit-flips can be easily and rapidly identified and corrected.

An SEL is a more serious and destructive occurrence. In certain cases (particularly in bulk CMOS structures), there exist (parasitic) lateral bipolar transistors. If current is injected into such a structure these transistors become conducting and remain conducting through positive feedback. Such an occurrence may result in high currents passing through the component. Occasionally, it is possible to correct an SEL by powering down the device. In other cases an SEL may lead to irreversible damage to the crystal lattice, effectively destroying the device.

Contrary to biological systems, microelectronic and nanoelectronic devices have no *inherent* error correction and rely on appropriate fault-tolerant design and online correction algorithms to continue functioning in a high intensity radiation environment.

A more detailed analysis, relating to radiation effects in specific electronic devices appears in [21].

## 2.2 Current dosimetric techniques

The field of dosimetry is concerned with the quantification of the amount of energy (per unit mass) deposited in a given medium by ionizing radiation. More generally "dosimetry" can also refer to the assessment of any other aspect of the interaction of radiation with matter. In this work we are concerned with the dosimetry applied to the interaction of radiation with biological matter and the quantification of the biological effects of ionizing radiation. As opposed to the thriving field of "Microdosimetry", dealing with the modeling of radiation interactions with cellular targets, "Nanodosimetry", described in detail in this work, deals

with the study of radiation interactions with nanometer scale targets such as short DNA segments.

Dosimetry in general and microdosimetry in particular rely on the entire arsenal of nuclear physics techniques, from gas based detectors, through liquid bubble chamber-like techniques to advanced solid-state devices. Several samples are described below.

### 2.2.1 Solid-state dosimetry

Quantitative dosimetric techniques typically record the change in physical properties of a material - formation of color centers in radiochromic film [24], breaking or formation of polymer bonds in track-etch detectors [25] or thermoluminescence (§1.5.6.3. of [21]).

Thermoluminescent detectors (TLDs) for example consist of a crystal (e.g. LiF, $CaF_2$ or $Al_2O_3$) activated by a small addition of rare-earth or transition metals. During radiation exposure, traps are filled by the electron and holes formed in the radiation track. Light is emitted when the crystal is heated and the electrons and holes recombine. Such devices are extremely useful for quantification of the absorbed dose in radiation protection and monitoring. They are sensitive to a large dynamic range of doses ($10^{-5}$-$10^{2}$ Gy) and may be reused after heating.

These devices typically have very low spatial resolution (few microns for films and track etch detectors, few mm for TLDs) but high sensitivity, making them useful for radiation protection and are therefore good for radiation monitoring in a known radiation environment. They usually do not allow for a real time measurements or for track structure studies

### 2.2.2 Solid-state based microdosimetric techniques

Naturally, such resolutions, as well as the complicated readout of such detectors are not very useful for microdosimetry. Microdosimetric detectors are required to work at high rates and to give a real-time quantification of the radiation field (as opposed for 24 hour development time required by some radiochromic films for example). Solid-state based microdosimetric detectors rely primarily on silicon or CVD diamond techniques and rarely on germanium or GaAs technology [26], as the high Z of the latter two (>30) prevents their use as a reasonable model for the interaction of radiation with carbon/nitrogen/oxygen-based tissue (Z=6-8).

Semiconductor detectors are naturally micron sized, giving a good measure of the energy deposition spectrum in a micron sized target; they are also much more sensitive to small energy deposits, due to the small band-gap, resulting in a 10 times smaller ionization potential compared to gas detectors, described below.

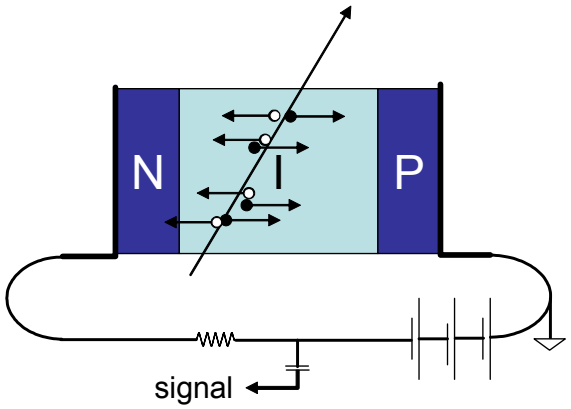


**Figure 2.4 : PIN diode radiation detector.** Holes migrate to the left, electrons to the right, forming a current pulse.

Silicone-based dosimeters typically consist of a properly biased PIN (Positive-Intrinsic-Negative) diode. Radiation-induced electron-hole pairs are formed primarily in the intrinsic region of the diode (due to its much larger volume, compared to the doped regions) the drifting charge result in a current pulse which can be easily detected using standard electronics.

CVD based detectors [27-29] consist of a thin diamond film sandwiched between metal electrodes forming an ionization chamber. The principle of operation is similar to that of a PIN diode. Diamond films are particularly useful for radiation studies due to their radiation hardness and similar Z to that of tissue [28].

However these devices are still too big for nanodosimetry. Solid-state devices can only be made with micron sized sensitive volumes, limited by the size of the required electrical connections. Even micron-scale devices may not be practical as they tend to be prone to radiation damage, resulting in a deterioration of the detector response with time. This is naturally more serious for the smaller, more sensitive devices [29].

An extensive review of semiconductor-based dosimeters appears in [26, 29].

### 2.2.3 Using gas to model condensed matter

As noted above, In order to characterize the severity of damage, expected in irradiated DNA, it is necessary to identify the **nanometric track structure**. Currently track structure parameters in condensed matter cannot be directly measured at the required resolution; they can only be simulated [10, 30] or measured using gas models such as the tissue equivalent proportional chamber (TEPC) [31] which is the workhorse of radiation dosimetry.

In the TEPC, the experimental determination of the distributions of deposited energy in microscopic volumes of condensed matter (e.g. tissue) is done by replacing these small volumes with much larger cavities filled with tissue-equivalent gas (TEG is a gas which has the same elemental composition as "various kinds" of tissue) [32, 33]. These gas models typically have densities of $10^{-3}$ - $10^{-6}$ g/cm$^3$; they are valid if [34]:

(i) the interaction mechanisms of ionizing radiation in the counter gas are similar to those in cell material or, at least, in liquid water,

(ii) the interaction cross sections and the number or kind of the most important energy loss channels are independent of gas density, and

(iii) the particle tracks are not noticeably disturbed by any component of the measuring device.

The first of these three requirements is the most critical one since it is hardly conceivable that gaseous systems, well suited for proportional counter experiments, show the same mechanisms of radiation interaction as sub-cellular material. In this respect, one should keep in mind that even the radiation interaction in water vapor is quite different from that in liquid water, as extensively discussed in [35]. This argument is generally true as far as excitation processes are concerned, but it is generally not true from the point of view of ionization cluster size formation. This is because the energy distribution of secondary electrons, set in motion by impact ionization, does not strongly depend on the type of target molecule (see [34] as well as eq. 2.3 above). The use of gas-filled counters for the above purpose is reasonable since the measurements could be traced back to primary interaction processes by Montè-Carlo simulations. After this traceability has been established, the measurements can be compared with the corresponding data for liquid water or sub-cellular structures if available, and analyzed accordingly.

The second requirement rests upon the empirical observation [36] that the transfer of radiation energy from charged particles depends on the atomic composition of a given material, regardless of the actual chemical combination of the components. Grosswendt [34]

has developed a method for scaling of the gas model dimensions to condensed matter. Essentially, the length scale in condensed matter, $\Lambda_{H_2O}$, is given by

$$(\Lambda\rho)_{H_2O} = (\Lambda\rho)_{C_3H_8} * \frac{(\lambda\rho)_{H_2O}}{(\lambda\rho)_{C_3H_8}} \quad \Rightarrow \quad \Lambda_{H_2O} = \Lambda_{C_3H_8} * \frac{\lambda_{H_2O}}{\lambda_{C_3H_8}} \qquad (2.4)$$

where $\Lambda_{C_3H_8}$ is the scale in gas, $\rho_x$ is the density and $\lambda_x$ is the mean free path for ionization. The values of the mean free path for ionization (scaled by the density, i.e.$\lambda\rho$) for liquid water and propane are shown in figure 2.5a (taken from [34]). As can be seen in 2.5b) the ratio of the two is almost a constant $(\lambda\rho)_{H_2O}/(\lambda\rho)_{C_3H_8} = 1.30 \pm 0.05$, leading to a gas scaling factor of $\Lambda_{H_2O}/\Lambda_{C_3H_8} = 2.8 \quad 10^{-6} = 2.8 nm/mm$ for 0.9 Torr of propane at 20°C (the operating conditions in our nanodosimeter). This allows us to perform a direct simulation of the ionization clusters induced in water by using a propane volume larger by the ratio of mean free paths.

The third requirement is simply a technological issue. The detector must be built with either no material within the beam path or with materials that have the same scattering cross sections as the gas [37]. We have decided to adopt the former solution.

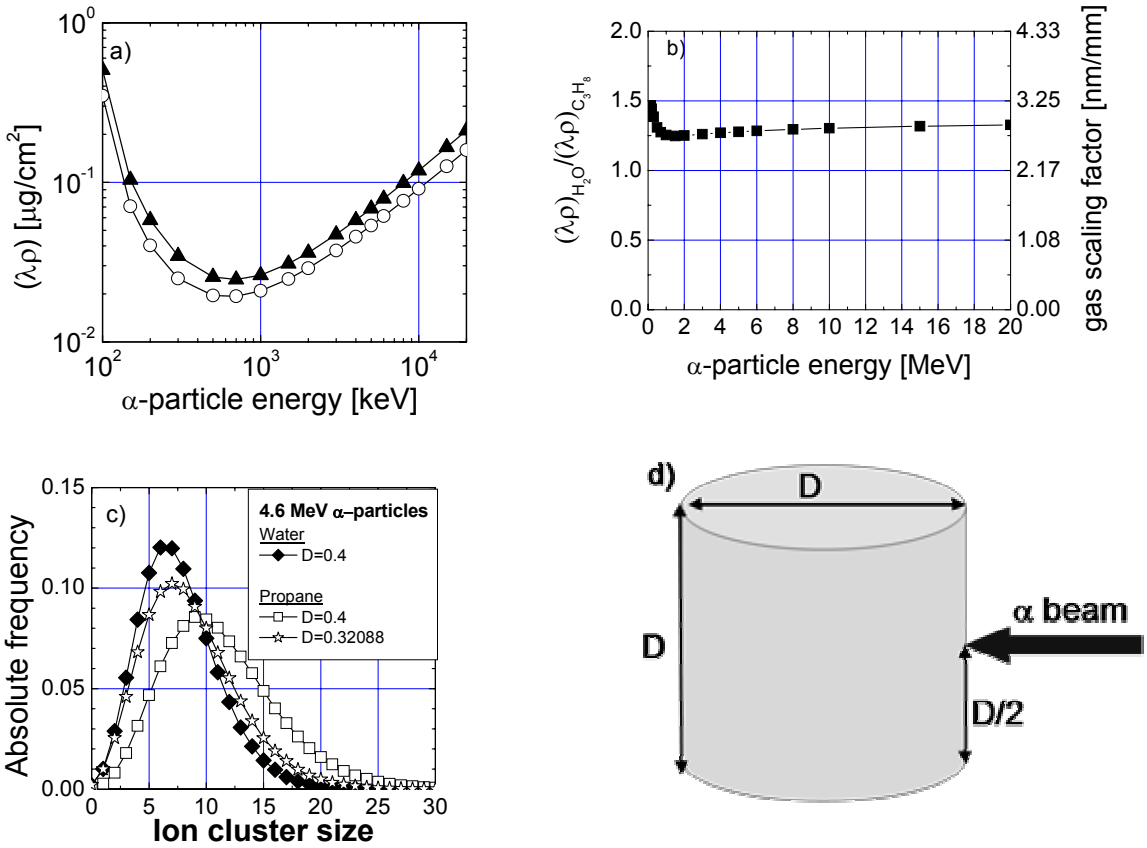


Figure **2.5:a) Mean free path lengths for ionization** (scaled by the density - $\lambda\rho$) of α-particles in liquid water (○) and propane (▲) as a function of the particle energy. b) The gas scaling factor $\Lambda_{H_2O}/\Lambda_{C_3H_8} = \lambda_{H_2O}/\lambda_{C_3H_8}$ as a function of energy. c) Ionization cluster-size distributions in the geometry shown in d) (4.6 MeV α-particles penetrating a cylindrical sensitive volume with diameter=height=*D*). Data are shown for a volume of liquid water (closed symbols) or propane (open symbols) traversed in the plane perpendicular to the cylinders' main axis at half its height. For water $D\rho$=0.4 μg/cm$^2$. For propane, the mass per area is scaled either trivially, by the density ratio, (□ - $D\rho$= 0.4 μg/cm$^2$) or using eq. 2.4: (○- $D\rho$= 0.32 μg/cm$^2$). Figures reproduced from [34].

The choice of gas filing and pressure depends on the condensed-matter system to be simulated. When simulating nanoelectronic devices, gases such as silane ($SiH_4$) and arsine ($AsH_3$) may be used. Although these gases are not very practical as a proportional counter filling gas, they could in principle be used in an ion counting device such as the ND. When simulating tissue, in a proportional counter, the common choice is a hydrocarbon based "Tissue Equivalent Gas" consisting of propane or methane, nitrogen and $CO_2$, at ratios chosen to represent the stochiometry of various types of tissue [32, 33]. It has been shown [38, 39] for example, that when simulating targets on the nanometer level, a gas composed of propane, $CO_2$ and $N_2$ is indeed equivalent to liquid water. For technical reasons we have decided to use pure propane rather than a gas mixture. In [34] this equivalence was also expanded to both pure propane and pure $N_2$.

Figure 2.5c demonstrates this equivalence by giving the simulated cluster size distributions in volumes of propane and liquid water. The volume dimensions were set by the scaling procedure described above. From this figure we see that the gas scaling results in a distortion of the cluster size distribution by 12% (as quantified by the ratio of the first moment of the distribution simulated in water and that simulated in the correctly scaled gas volume – $D$=0.32 $\mu g/cm^2$).

It should be stressed that, by using a gas model of condensed matter, we completely **ignore** the molecular structure and chemical properties of condensed matter, vital to the understanding of damage mechanisms. Beyond that, it is known [40, 41], that the transport of **slow** (<30 eV) electrons in condensed matter and in a gas are vastly different. In a solid, the electron is perturbed by the electric field of neighboring atoms and as a result of this, will deposit its energy in a different manner than in a gas. Nevertheless, the track structure is expected to scale linearly with the density and the study of the features of radiation interaction with gas at nanometric scales is an invaluable tool for the study of radiation action mechanisms also in the condensed phase. The subsequent interpretation, in terms of transport of the slow electrons, the formation of radicals and the understanding of the damages to cells are indeed not trivial; our approach to this problem is detailed in §7.

### 2.2.4 Gas based microdosimetry

The first track structure studies, performed by Wilson at the beginning of the 20$^{th}$ century (eg. [3]) were conducted with a cloud chamber. In this device a saturated gas is exposed to radiation and then subjected to a sharp decrease in pressure. Water droplets then form with the radiation-induced ionizations serving as nucleation sites. By photographing the small water droplets it is possible to visualize the track structure. A good example of this technique is the so called "Harwell chamber" [42, 43] developed in the early 1980s, and used for extensive studies of track structure induced by alpha particles and x-rays in a low-pressure mixture of water vapor, ethanol, hydrogen, nitrogen and oxygen. The Harwell chamber operated at a pressure of about 11 Torr and enabled the study of track structures with 10 nm resolution.

However, most current microdosimetric devices are based on the well known tissue equivalent proportional chamber (TEPC) first suggested by Rossi [31] almost 50 years ago. They consist of a gaseous detection volume, typically containing tissue equivalent gas mixtures [32, 33], at atmospheric pressure, and surrounded by walls of conducting tissue-equivalent plastic [44]. The ionization electrons created within the gas volume are collected using electric fields and multiplied in the high electric field in the vicinity of a thin wire.

While many elaborate designs have been proposed for these chambers, which are in routine use for radiation monitoring all over the earth, in flights [45] and even in space [46], they are limited in their applicability:

In most TEPC designs there is at least some overlap between the ionization volume and the charge amplification volume. This may result in a geometrically non-uniform response (different gain for electrons deposited in different regions). This nonuniformity can be somewhat overcome by confining the charge multiplication region, using additional electrodes (for example [47, 48]), but these distort the measured radiation field [49].

A more severe limitation is that of target size and sensitivity. Conventional TEPC designs are only able to reliably model radiation effects on targets larger than about 1 μm. Smaller simulated targets may be achieved by reducing the TEPC dimensions [50] or decreasing the gas pressure [48], however these devices must be operated at extremely high gains (as only a few electrons are deposited in the gas volume), which only aggravates the previous problems. Furthermore, at such high gains, the gas multiplication statistics [51] dominate the detector resolution and it is impossible to determine the exact number of primary ionizations.

For understanding radiation damage to DNA we want to measure both single ionization events and large ionization clusters. In a TEPC, this cannot be done. The number of ionizations cannot be found on an event-by event basis and only a somewhat suspect ionization cluster size distribution can be obtained by deconvoluting the TEPC pulse height spectrum, assuming that its single electron response is very well known.

High sensitivity TEPCs also require the use of "special" gases which are able to support the high gains required for single-electron detection. These gasses are not necessarily the same ones required for tissue equivalence, although propane-based tissue equivalent [33] gas is known to support sufficient gain for single-electron detection [52]. As a result of this it becomes impractical to use the TEPC for dosimetric measurements on nanometric scales.

Cesari et al. [48], for example report a TEPC of 100 nm tissue-equivalent SV, using low-pressure (3 Torr) TE gas and 50nm using 1.5 Torr DME. Smaller sensitive volumes could not be reached (with single electron sensitivity) due to voltage breakdown. Due to the need to deconvolute the pulse-height spectrum to obtain cluster size distributions, large probabilities are measured of cluster sizes of a fraction of an electron.

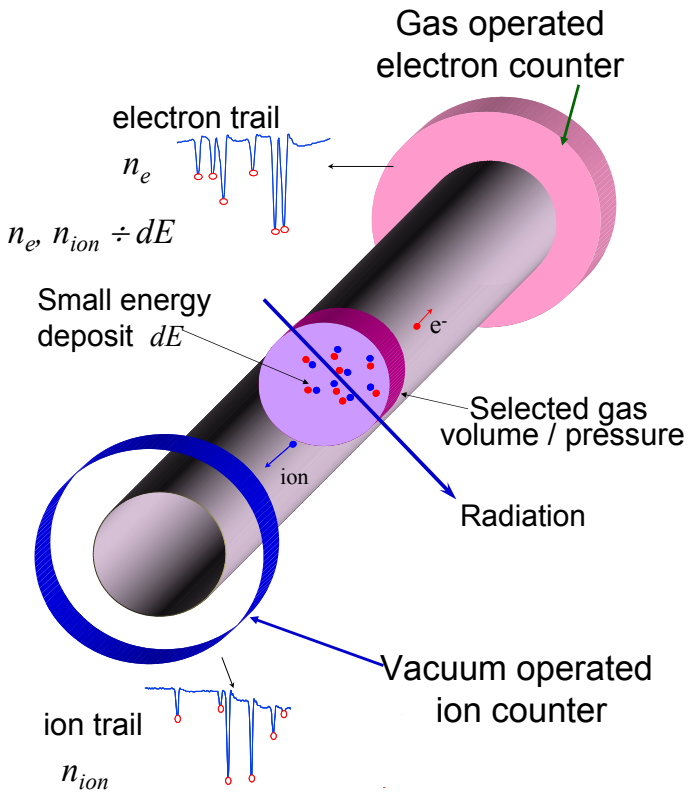


**Figure 2.6: A schematic diagram of the charge counting method**. An energetic charged particle traverses the low-pressure gas ionization volume, depositing many electrons and ions. In the case of electron counting (top right), the electrons from the sensitive volume are extracted into a long drift column, and drift under a weak electric field. They separate by diffusion and are individually multiplied and counted in a gas-based electron multiplier. In the case of ion counting (bottom left), the ions are extracted from the sensitive volume into vacuum, here they are accelerated onto an ion detector where they are detected and counted.

## 2.3 Charge counting nanodosimetry

The charge-counting technique is a powerful new tool, proposed by our group [53], for precise measurements of small energy deposits in gases. It has found use in the study of basic phenomena of ionization statistics in gaseous media [54-56], in the detection and spectroscopy of ultrasoft x-rays [57, 58] and in high-resolution dosimetric measurements at the 1-100 nm level (see for example [59-63]).

The charge counting technique, shown schematically in figure 2.6, is based on the conversion, in a low-pressure gas, of ionizing radiation into a cluster of charges (ions or electrons). The deposited charges are extracted by an electric field $E_1$, from the interaction region into a detection region where they are *individually* multiplied and recorded (as described in §2.3.1 and §2.3.2 below), obtaining a *cluster-size distribution*. This distribution can be presented in two (nearly) equivalent ways:

- The **absolute cluster-size distribution** gives the *absolute* probability to generate an ionization cluster of given size, including clusters of size "zero". This distribution is obtained by dividing the yields of the different clusters by the *number of projectiles*. Measurement of this type of distribution requires an efficient trigger and therefore some foreknowledge of the type of radiation field being studied.

- The **conditional cluster-size distribution** gives the *relative* probability to generate an ionization cluster of given size, not including clusters of size "zero". This distribution is obtained by dividing the yields of the different clusters by the yield of all clusters with *at least one detected charge*. This type of measurement does not require a trigger at all (the charge counting begins with the first detected charge and proceeds for a given length of time). The conditional cluster-size distribution can be easily obtained from the absolute one by dividing all cluster probabilities by $1-f_{(0)}$, where $f_{(0)}$ is the probability per projectile of forming a zero-charge cluster.

In our work we have measured **absolute cluster size distributions** as they contain more information than the conditional ones. They also allow a more thorough characterization of the nanodosimeter as the irradiation conditions are better controlled. In the studies described in §5, where we irradiated the ND with a radiation field much larger than its sensitive volume, we have employed the *conditional distribution* to ensure that we are not affected by "zero"-clusters formed by projectiles passing too far from the SV and not depositing any energy in it. The conditional cluster-size distribution was calculated from the absolute one, as described above.

The conditional cluster-size distribution can be interpreted as the cluster size distribution per deposited dose (or energy), thus it is equivalent to the pulse-height distribution of a TEPC (where zero-height pulses cannot be measured). Contrary to a TEPC, the gain fluctuations are not important using this technique, as long as all charges are detected.

While it is generally accepted that the TEPC pulse height spectrum is equivalent to the spectrum of deposited energy, at the limit of low energy deposits (up to 100 eV or so), this equivalence breaks down, due to the stochastic nature of the ionization process. In this regime it is the number of ionizations (corresponding to the number of damages) which is important rather than the quantity of deposited energy (which cannot be measured anyway).

Several variants of the charge counting technique have been developed (three of them in collaboration with our group):

### 2.3.1 Detection of electrons

Perhaps the most natural approach is to detect the individual ionization-induced electrons. Figure 2.7 shows a scheme of the Single Electron counter (SEC) [55], applied to nanodosimetry at INFN-LNL [62-66]. In the SEC, the single radiation-induced electrons,

formed within a wall-less sensitive volume, defined solely by electric fields, are extracted through a small aperture into a long drift column where they drift in a low electric field, diffusing away from each other. Due to the large diffusion, the electrons reach the end of the drift column at well separated times. These electrons are then individually multiplied, detected and counted by a gas-avalanche based electron multiplier [67], placed at the end of the drift column (see for example figure 2.7d).

The main limitation of this technique is the (relatively) large sensitive volume accessible (~20 nm diameter as a lower limit – much better than conventional TEPCs but still not small enough) as well as the low electron extraction efficiency from it (10-20%). Nevertheless, some important work has been done using this technique. De Nardo et al [65] have used a SEC for investigations of an alpha particle track structure at 20 nm resolution. Their results indicate an invariance of the ionization density induced by δ-electrons as a function of distance from the track axis. Figure 2.7c, for example shows the conditional average cluster size (i.e. the number of electrons formed in the SV, averaged over all events where at least one electron was detected) as a function of the distance of the track from the SV center. The left-hand side of the curve is dominated by the direct ionization of the gas in the sensitive volume, by the track core. Naturally, the cluster size decreases as the beam is displaced and an increasingly shorter track segment is within the SV. When the track is completely outside the SV, we see a plateau. This is due to the fact that ionization is now only due to the far reaching δ-electrons. Although less and less δ-electrons reach the SV, their ionization density remains essentially unaltered. We have seen similar results in our simulations.

An alternative concept to the SEC is that of the optical digital ionization chamber [68, 69] and the optical projection avalanche chamber (OPAC) [70-72] developed respectively at Oak-Ridge and at PTB, Germany. Here the whole ionization track segment is imaged, using scintillating gases. Both devices are similar in concept to the cloud chamber used by Wilson in the beginning of the 20th century and its descendant the Harwell chamber [42]

In the Oak-Ridge design, briefly after the charged particle traversal, a high electric field pulse (30 kV; 1 μsec) accelerates the electrons. The fast electrons collide with the gas molecules resulting in scintillation. The resulting light provides a "photograph" of the track structure with a few tens of nm resolution.

In the OPAC, the radiation-induced ions are drifted towards the gas multiplication region. Contrary to the SEC, here the drift length is rather short, limiting diffusion. In the multiplication region, the electrons are multiplied in a multi-step avalanche chamber [73] and each individual electron-avalanche generates scintillation light, which is collected to form an image of the track (with about 40 nm resolution).

**Figure 2.7 (opposite page): a) A scheme of the Single Electron counter** (SEC) at INFN LNL[63-66]. Electrons formed in the sensitive volume (SV) are separated in a 20 cm long drift column and detected in a multi-stage avalanche counter (MSAC). b) The irradiation geometry studied using the SEC consists of an α-particle beam, from a radioactive source, passing at a distance *d* from the sensitive volume. c) The measured average electron-cluster size, as a function of *d*. Open and filled circles correspond to right regular cylindrical volumes of diameter and height equivalent to *D*=21 and *D*=24 nm (see figure 2.5d) and an electron detection efficiency of 25% and 30% respectively. Thick lines are simulation results. See text for interpretation. d) An example of an electron trail, containing 22 electrons induced by a fluorine-K soft x-ray. In this case the trigger was induced by the first electron in the trail. a)-c) reproduced from [66].  d) reproduced from [67]

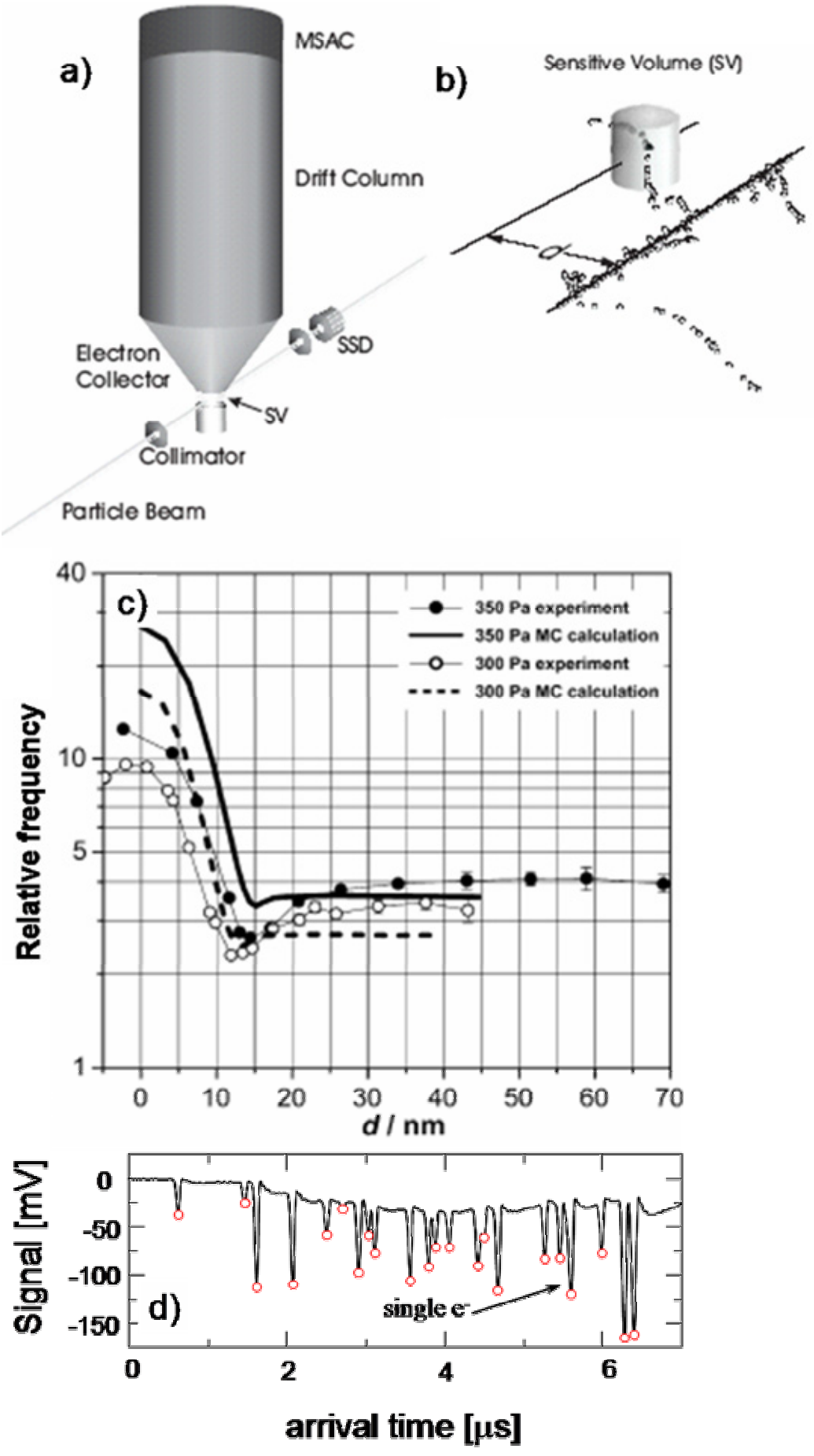
a)
MSAC
Drift Column
SSD
Electron Collector
SV
Collimator
Particle Beam
b)
Sensitive Volume (SV)
c)
350 Pa experiment
350 Pa MC calculation
300 Pa experiment
300 Pa MC calculation
Relative frequency
d / nm
d)
single e⁻
Signal [mV]
arrival time [µs]

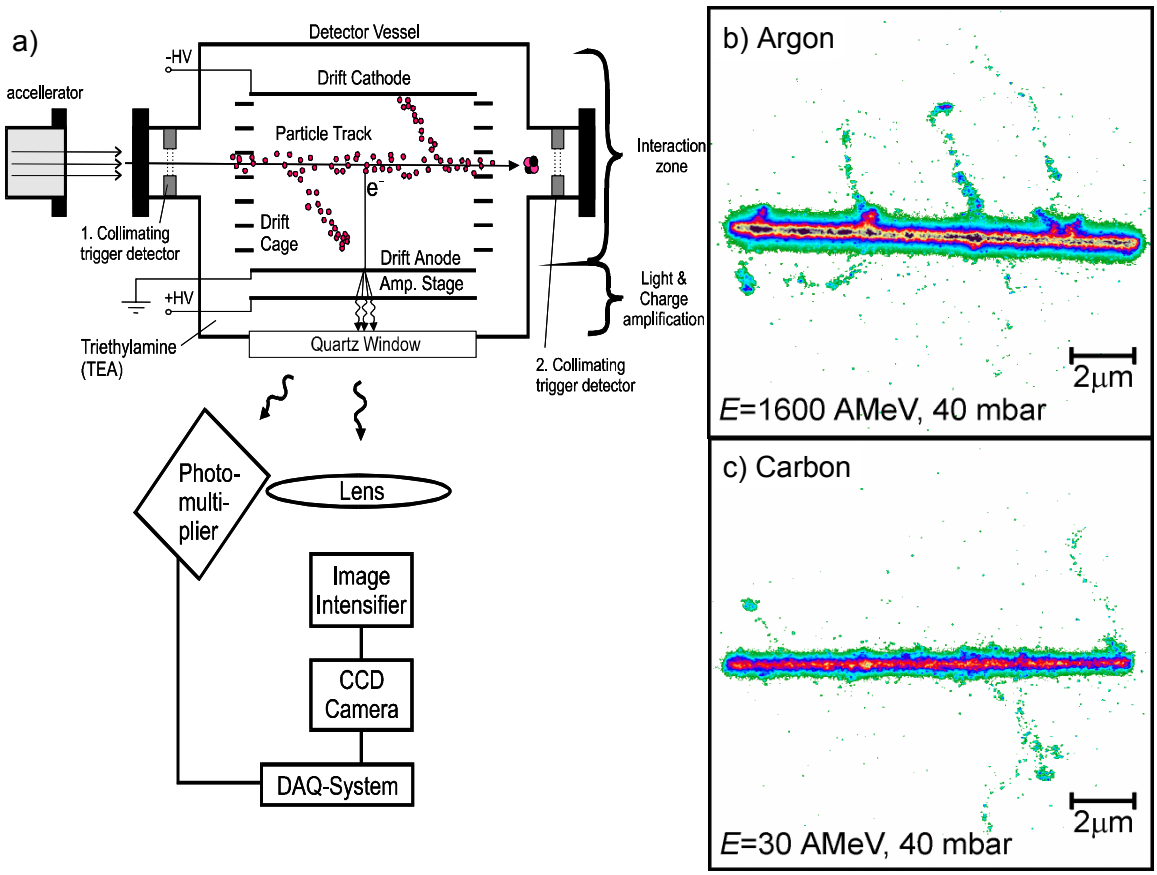


**Figure 2.8: a) a scheme of the PTB OPAC detector.** Electrons formed along a projectile track in TEA are drifted in a low electric field towards a high electric field region. In the high electric field the electron avalanches emit UV light which is recorded by an intensified CCD and a PMT obtaining 3D information (2 space dimensions and one time). b) An image of an Argon nucleus track (57.6 GeV – 70 keV/µm). c) Image of a carbon nucleus track (336 MeV – 70 keV/µm). Taken from [72] © Nuclear Technology Publishing.

The main advantage of these imaging techniques is the fact that a long track segment (a few µm, see figure 2.8) is imaged, while in the SEC we only obtain the number of ionizations within a small volume. Furthermore, due to the efficient coupling of the sensitive volume to the detection volume, much higher single electron detection efficiencies are available. In the OPAC, additional data of the electron drift time is also used to obtain a three dimensional image of the track [70]. These advantages come at the price of somewhat reduced spatial resolution, due to the electron diffusion, either before the high voltage pulse (in the oak-Ridge design), or en route to the multiplication region. In the SEC this diffusion is used to separate the electrons, and contributes to the electron detection efficiency. Contrary to the SEC, these two designs enable the viewing of the track structure on a much larger scale (a few microns, corresponding to a cell nucleus for example). On the other hand single ionizations cannot be resolved so that only an average picture can be obtained. This makes detectors such as the OPAC extremely useful for large scale studies of radiation tracks. They enable, for example a quick and simple method for the quantification of the range distribution of δ-electrons. In an ongoing work [72] the OPAC is used for a systematic comparison of high LET heavy-ion tracks having the same LET but different charge $z_p$. So far, 70 keV/µm Argon nuclei were found to have longer range δ-electrons (and therefore less dense track structure) than carbon nuclei of the same LET (compare figure 2.8 b and c).

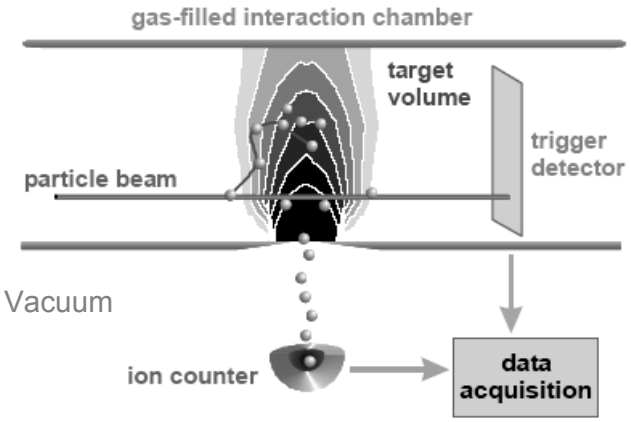


**Figure 2.9: Conceptual scheme of the ion counting ND. See text for details.**

### 2.3.2 Detection of ions

The (too) large sensitive volume attainable when counting electrons is significantly reduced when counting the positive ions induced by the radiation. The typical diffusion for electrons (in 1 Torr propane) is 3 mm (RMS) for 1 cm drift [74]. Ions, on the other hand, have much lower initial kinetic energy, due to their large mass; they undergo significantly reduced diffusion, typically 0.5 mm (RMS) in 1 Torr of propane over 1 cm drift [75]. As a result, it is possible to create sensitive volumes with roughly 1 nm resolution.

A fundamental difference between ion counting and electron counting is the fact that radiation-induced electrons have a wide range of kinetic energies and cannot be thermalized within a small gas target. Ions, on the other hand, have much lower initial kinetic energy. As a result the track image obtained using an ion-counting device will reflect the place where ionizations were formed whereas an image obtained using an electron based device will reflect the location of the electrons after they have thermalized. The former is, of course the more interesting as the damage is formed at the place of ionization. The use of an electron based device will therefore tend to shift the location of measured ionizations from the track core to the δ-electron track ends, resulting in a reduced efficiency to image the track core and an over-estimation of the ionization density at the δ-electron track ends.

The drawback of using ions is the great difficulty of their detection in a low-pressure gas environment. With the invention of modern vacuum-operated ion counters, a track ion counter similar in principle to the SEC was proposed [76] and implemented [77]; at that time, the vacuum system only permitted attaining small sensitive volume diameters, of 0.15 nm. Additionally, the ion counters available at that time provided single-ion detection efficiencies of only 40-50% [77]. This limited the applicability of the track ion counter in radio-biology investigations. We have revived this idea [78] in the form of **the ion counting nanodosimeter**, investigated in this work.

A conceptual scheme of the ion counting ND is shown in figure 2.9. The ND consists of a low-pressure gas volume, the ionization volume (IV) coupled by a small aperture to a vacuum detection volume. A strong electric field separates the radiation-induced electron-ion pairs, sweeping the electrons away from and the ions towards the *ion-extraction aperture*. Due to the relatively low ion-diffusion, only ions formed within a tunable, wall-less region of the IV, the ***sensitive volume*** **(SV)**, are extracted into vacuum where they are detected and counted by an ion counter (IC - a vacuum operated electron multiplier).

An important advantage of counting ions in vacuum is the relaxation of the limitations on the choice of gas. In the electron-based schemes, the gas target is required to support high

gain charge multiplication or to be scintillating. In the ion-based schemes there is no such demand and, in-principle, any gas (including, for example water vapor) can be used.

The resolution limit is set by the ion diffusion statistics [79]. An ion drifting through a length $L$ in gas will undergo a transverse diffusion of

$$\Delta x_{gas} = \sqrt{2L}\sqrt{\frac{D_i/K_i}{E/P}}\sqrt{\frac{1}{P}} \tag{2.5}$$

Where $D_i/K_i$ is the ratio of diffusion to mobility, $E$ is the electric field (assumed uniform) and $P$ is the pressure. In the simulated tissue frame this reduces to:

$$\Delta x_{tissue} = \sqrt{k}\sqrt{2l}\sqrt{\frac{D_i/K_i}{E/P}} \tag{2.6}$$

with $k$ being a correction to the gas-tissue scaling factor, discussed above (see eq. 2.4)

$$\Lambda_{tissue} = k\frac{\rho_{gas}}{\rho_{tissue}}\Lambda_{gas} \Rightarrow \quad \Delta x = k\frac{\rho_{gas}}{\rho_{tissue}}\Delta X; \quad l = k\frac{\rho_{gas}}{\rho_{tissue}}L \tag{2.7}$$

It should be noted that the resolution in the tissue-equivalent scale $\Delta x_{tissue}$ depends on the pressure only through the reduced electric field $E/p$. The selection of pressure is therefore dictated only by the attainable spatial resolution of the ion detector in the "lab frame" (In our case the size of the aperture coupling the gas and vacuum regions).

**For the ND design described in this work *L=1.5 cm*, E=60 V/cm, $D_i/K_i$=40 mV leading to a lab frame resolution of 0.5 mm. For 0.9 Torr of propane this corresponds to a tissue equivalent resolution of 1.2 nm.**

The ion counting nanodosimeter is described in detail in chapter 3 of this work.

An interesting variant of an ion counting ND is the jet counter [80-82] seen in figure 2.10. It consists of small (albeit walled) chamber (denoted IV), connected by a pulsed valve to a gas reservoir. As the valve opens, a gas jet expands into the volume, reaching a stable 1 Torr pressure for a few hundreds of μsec. During this time ions are formed by radiation within the chamber. They are then extracted, by an electric field towards the ion counter (IC). Although the sensitive volume of this device is defined by physical walls, it is claimed that, as the primary beam does not interact with the walls, they do not interfere with the measurement. The silicon detector is used for detection of the primary radiation beam as a trigger for the DAQ system. The calibration and operation of the jet counter is detailed elsewhere [80].

The jet counter has been successfully used to measure ionization cluster size distributions, induced by 4.6 MeV α-particles, in nanometer-equivalent volumes ($D$=0.15, 1 and 2 nm diameter at unit density, see figure 2.5d for exact geometry) of nitrogen gas [82]. The obtained data are shown in symbols in figure 2.11. MC simulations, using a similar code to ours (see appendix A) yielded good agreement with the data, assuming 50% ion detection efficiency for all ions formed within the SV. This value was verified by MC simulation [82] and was seen to vary with the gas pressure, indicating that it might be due to ion losses to molecular processes in the gas. From figure 2.11 it is also clear that for sensitive volumes larger than a fraction of a nanometer, the ionization cluster size differs significantly from a Poisson distribution. This is explained [82] by the contribution of δ-electron tracks. Ion clusters formed in such tracks cannot be described as being formed in a Poisson process (i.e. the ions are not independent of each other).

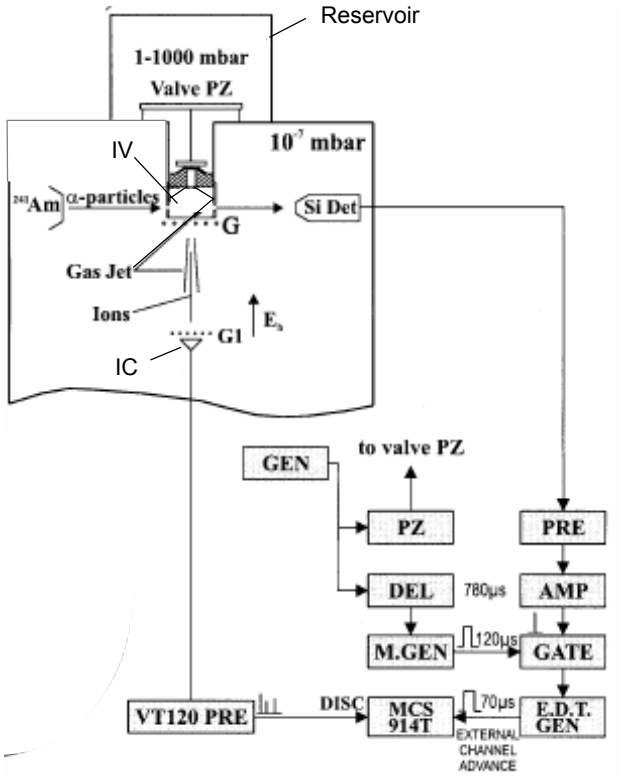


**Figure 2.10: Schematic view of the Jet Counter.** See text for details. Reproduced from [82] ©2002 Springer-Verlag.

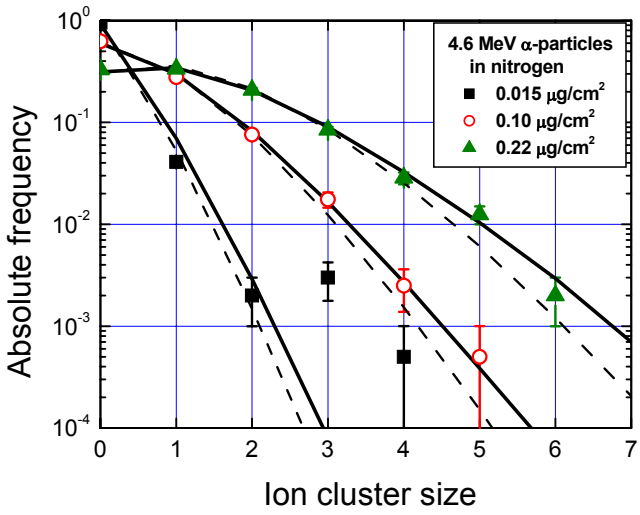


**Figure 2.11: Ion cluster size distribution** produced by 4.6 MeV α-particles in nitrogen upon diametrical penetration through right regular cylinders of 0.15 nm, 1 nm and 2.2 nm diameter and an aspect ratio of 1. The dashed curves denote a Poisson distribution having the same mean ion cluster size; The solid curve is a Montè-Carlo simulation assuming a uniform single ion detection efficiency of 50% within the volume. Reproduced from [82]. ©2002 Springer-Verlag.

# Chapter 3 :

# The ion-counting Nanodosimeter

Ion counting nanodosimetry is a novel technique developed in our group [59-61, 75, 78, 83-86] for the quantification of minute energy deposits in a millimetric gas volume modeling a short DNA segment.

The ion-counting nanodosimeter (ND) consists of a large (50 mm long x 150 mm diameter) gas-filled ionization volume (IV), traversed by a radiation field. Radiation-induced ions formed within a small subsection of this volume (about 2mm in diameter and 5-40 mm long - termed the ***sensitive volume*** **- SV**) are efficiently extracted into vacuum, detected and counted.

After extensive characterization with an internal alpha particle source, the ND was installed at the WIS Pelletron accelerator; it was irradiated with narrow pencil beams of protons and carbon nuclei, having a typical diameter of 1 mm and well-defined energy. Although this mode of operation has little biophysical meaning, it was crucial for diagnostics and characterization of the ND. The ionization distributions recorded in these conditions permitted validation of our MC codes simulating the basic physical interactions in the IV as well as the ND response. They permitted probing of the performance of the ND and optimizing its operating parameters.

## *3.1 ND structure*

A detailed scheme of the ion counting ND is shown in figure 3.1. A charged particle beam of a given type, energy and geometry traverses a gas-filled interaction volume (IV) and reaches a trigger detector. Ions induced within a wall-less region, denoted the "sensitive volume" (SV), within the IV, are extracted into the vacuum-operated detection volume (DV) and are detected by an ion counter (IC). The pressure difference between the IV and the DV is maintained by a differential pumping system (see §3.1.2 below).

### 3.1.1 The ionization volume

The IV is enclosed in a stainless steel vessel of 150 mm diameter, much larger than the few-mm diameter sensitive volume. The electric field, $E_1$, is shaped by an aluminum anode, placed 50 mm above the grounded cathode encompassing the ion-extraction aperture. Additional field shaping electrodes (biased at half the anode potential) ensure field uniformity in the IV region. A photograph of the IV region is shown in figure 3.2.

The IV contains a low-pressure gas (in this work, we used propane at 0.9 Torr, having a density of $2.1 \times 10^{-6}$ g/cm$^3$). Under these conditions, 1 mm in gas corresponds to 2.8 nm at unit density (see §2.2.3).

As noted above only ions created within a small subsection of the IV, denoted the sensitive volume (SV) can be extracted into vacuum and counted. The size and shape of the wall-less SV are determined by the transport of ions in the gas and the spatial distribution of their extraction efficiency through the aperture. The latter also depends on the field $E_2$, below the ion extraction aperture; this is further discussed in §3.4.

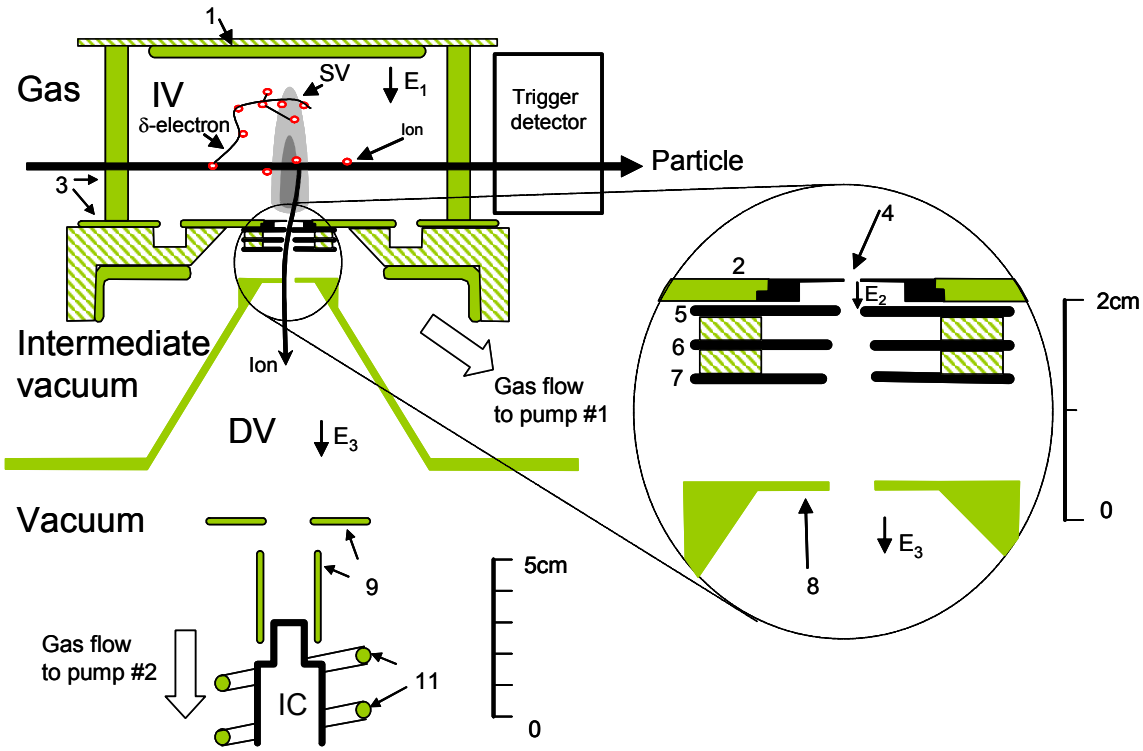


**Figure 3.1: A detailed diagram of the ion counting nanodosimeter.** In the ionization volume (IV), the anode (1), cathode (2) and field shaping electrodes (3) determine the ion extraction field $E_1$. A charged particle passes through the IV creating ions. Only ions created within the sensitive volume (SV), are extracted via a small aperture (4) into the intermediate vacuum region; these ions are focused via the electrodes $A_1$ - $A_4$ (5-8) into the detection volume (DV). They are then accelerated and focused, by the electrodes (9) onto the ion counter (IC) where pulses are generated. A helical coil (11) protects the ion counter from discharges. Note that the SV and δ-electron are schematic representations and not to scale.

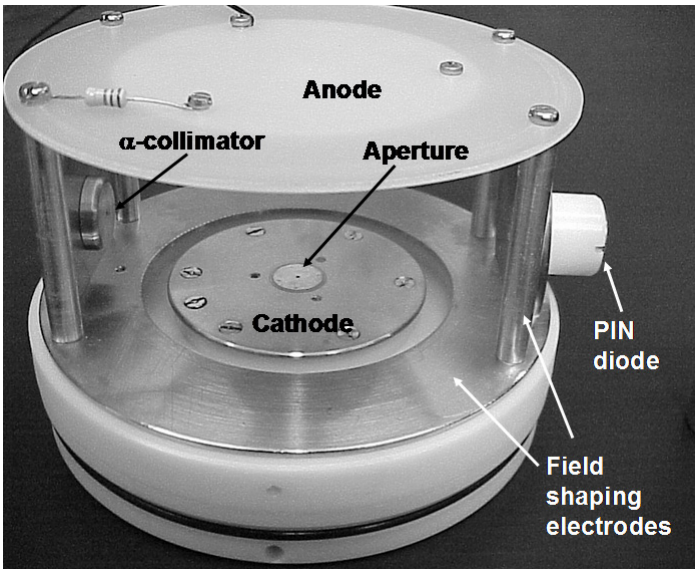


**Figure 3.2: A photo of the electrodes within the ionization volume.** The α-particle source is off to the left (its collimator is visible) and the PIN diode detector, used in measurements with it, is seen on the right. In accelerator experiments, the accelerator beam traverses the IV on an axis perpendicular to that of the α-particle beam. The anode is hidden below its support frame (at the top of the photo).

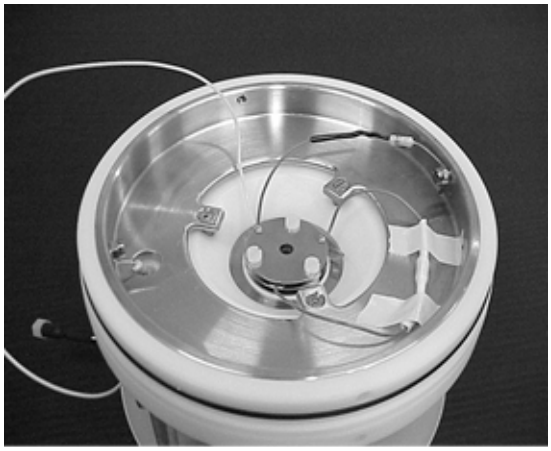

**Figure 3.3 : A photo of the focusing electrodes below the ion extraction aperture.**

### 3.1.2 The intermediate and detection volumes

The IV is coupled by a 1 mm-diameter, 0.1 mm thick aperture to the intermediate vacuum region and to the DV (figure 3.1). The operation of the IC necessitates a vacuum level close to $10^{-5}$ Torr. The five-orders-of-magnitude pressure difference within our instrument is reached by a double-differential pumping system. It consists of two turbomolecular pumps (Varian VT250 and VT550, denoted Pump #1 and #2, respectively, in figure 3.1), a set of three orifices placed below the aperture, and a conical screen, deflecting the gas flow from the aperture and orifices into one of the pumps. To compensate for the continuous gas flow from the IV to the DV, gas is continuously added to the ionization volume via a proportional regulating valve (MKS 248A). The pressure in the ionization volume is controlled by a temperature-stabilized Baratron pressure gauge (MKS 128) and pressure control system (MKS 250E), with an accuracy of better than 0.01 Torr.

The three orifices placed below the ion extraction aperture (figure 3.3) serve as ion-focusing electrodes, generating the focusing field $E_2$ near the aperture and focusing the extracted ions into the DV. The aperture and the focusing electrodes were gold-plated to avoid distortions of the electric fields by up charging of oxidized surfaces (as seen in the first experiments). Their dimensions were selected to allow for maximal ion transmission, while keeping an efficient differential pumping. The respective diameters of the aperture and of the electrodes $A_1$-$A_4$ are 1 mm, 3 mm, 5 mm, 5 mm and 4 mm; the distance between each two consecutive electrodes was 2.5 mm except for $A_3$ and $A_4$, which were separated by 10 mm. The potentials on these electrodes as well as that in the IV were optimized for maximal ion transfer efficiency (see below). A close- up of the electrode geometry and typical electric field map are shown in figure 3.4.

Within the vacuum-operated DV, ions are accelerated onto the ion counter (IC). This is a discrete-dynode electron multiplier (SGE model AF180HIG – see figure 3.5). Fast ions, impinging on the first dynode, induce secondary electron emission. The resulting electrons are multiplied in a 20-dynode chain, permitting efficient detection of individual ions and their counting [87] (see below). To avoid eventual discharges from the ion counter body to the vacuum chamber, the IC is surrounded by a helical copper shield, kept at the cathode potential.

The signals are read out of the last dynode of the IC, decoupled from the high voltage via a pulse transformer. The signals are processed by a fast preamplifier (Ortec model VT120A), followed by a timing filter amplifier, resulting in 20 nsec wide pulses, with amplitudes reaching up to 600 mV and with a noise level of 16 mV (see figure 3.6).

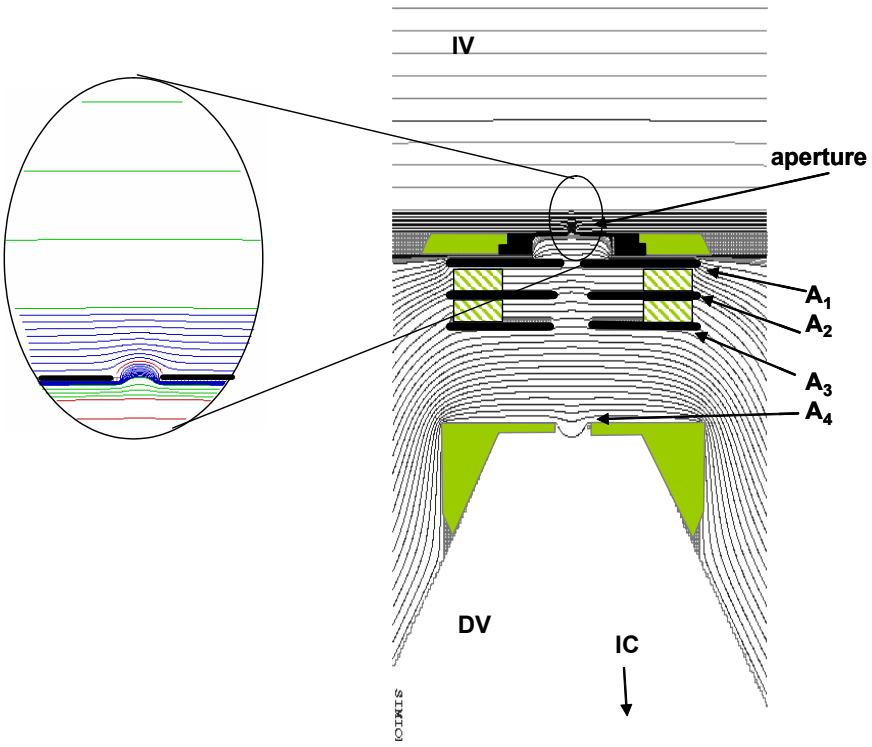


**Figure 3.4: Typical electric field map near the ion extraction aperture.** The field $E_1$ is above the aperture. The field $E_2$ is between the aperture and $A_1$. The inlay shows an expanded view of the region of the aperture, showing the penetration of the electric field, which results in a focusing of the ions. See §3.4. In both pictures the first 10 lines on either side of the aperture are 1 V increments. The next 10 (wider spaced) lines are 10 V increments and the rest of the lines are 100 V increments.

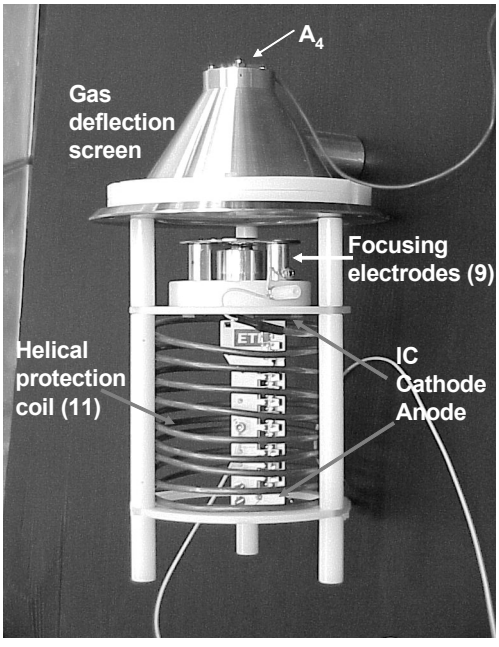


**Figure 3.5: Photo of the Ion counter (IC) and its holder.** Note the conical gas deflection screen and the helical protection coil.

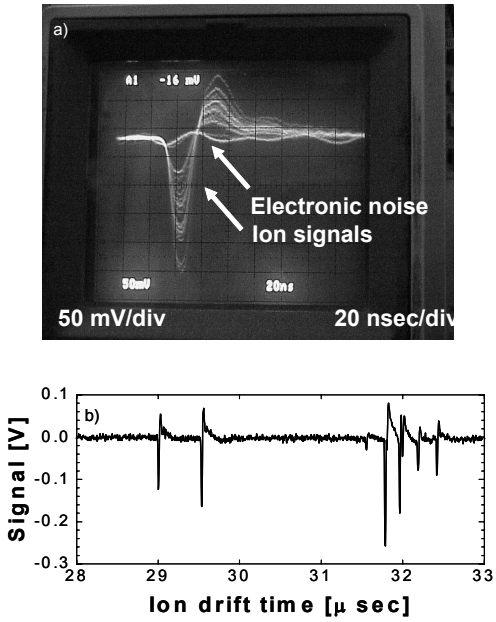


**Figure 3.6: Examples of single ion pulses recorded from the ion counter after a fast amplifier**: a) an oscilloscope photograph of single ion pulses. b) Ion pulse train of a single event induced by an alpha particle.

### 3.1.3 The internal calibration source

For detector calibration and monitoring of its long-term performance (under well defined operating conditions), we have incorporated an $^{241}$Am alpha source into the ND. We are using a gold-plated source, with an average energy of 4.25 MeV and a FWHM of 0.3 MeV; this corresponds to an average LET value of 107 keV/μm (in water) [88]. A 1 mm diameter alpha particle beam (of ~3 particles/second) is defined by a source collimator. The trigger is obtained by a PIN diode (Hamamatsu S1223-01, with the entrance window removed), located behind the SV. The beam crosses the sensitive volume orthogonal to its axis, at a distance of 15 mm above the ion extraction aperture. The alpha particle beam is in the same plane but perpendicular to the accelerator beam (see below) and can be turned off using a shutter.

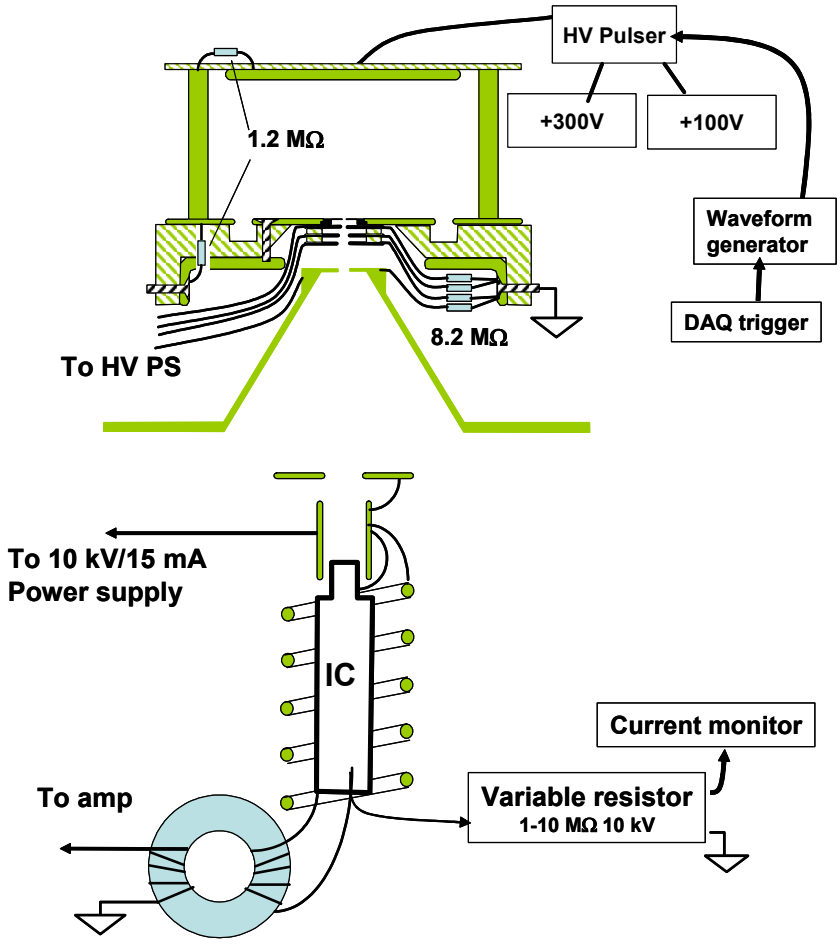


**Figure 3.7: The electronic Scheme of the ND.** See text for details

### 3.1.4 Biasing of the ND

Figure 3.7a depicts an electrical layout of the ND. All electrodes of the ND are connected via resistors to ground. This was done so that we could verify that the electrode is biased properly by monitoring the current drawn from the power supply.

In order to avoid creating excess ions (due to charge multiplication of particle-induced ionization electrons in the IV region, see §4.2.1) we have connected the IV anode and field shaping electrodes to a high voltage pulse generator (DEI model GRX driven by a standard waveform generator). During standby mode (when no ions are being collected) the anode is polarized at a 100 V "clearing" potential. After a projectile has passed through the ND, and

sufficient time (typically 5 μsec) has passed for all electrons to be swept away, the anode voltage is raised to 300 V for 100-200 μsec and then returned to 100 V.

We have connected the anode to the field shaping electrodes (through a 1.2 MΩ resistor); the field-shaping electrodes were connected to ground via an identical resistor. This ensures a constant potential ratio (1:2) between the field-shaping electrodes and the anode and minimal field distortions due to the grounded vacuum chamber.

The apertures $A_1$-$A_4$ were connected independently to four power supplies, to allow fine tuning of their voltages; they were connected to ground via 8.2 MΩ resistors. The applied voltages were, in most experiments: -284 V on $A_1$, -470 V on $A_2$, -800 V on $A_3$ and -2830 V on $A_4$.

The ion counter (IC - of 3.4 MΩ internal resistance) was connected on the cathode-side to a Glassman PS/LG10R15-220 bipolar power supply (set to -8.2 kV) and on the anode-side to ground via a variable resistor with a current monitor. This allows maintaining the IC at a potential difference (cathode to anode) of 2.5-3.5 kV, required for efficient operation, while maintaining the cathode at a potential of -8.2 kV. The ions, extracted from the ionization volume, are therefore accelerated to 8.2 keV, resulting in large signals, well above noise, and in high detection efficiencies [87].

The ion signals were read off the pickup electrode (an extra electrode following the IC anode) which was connected to the anode via an inductance coil. A second coil, wound on the same core was used to read out the ion signal relative to ground (rather than relative to about -5kV).

The electrodes (9) and the helical protection coil were connected directly to the IC cathode.

### 3.1.5 The DAQ system

The data acquisition (DAQ) system (designed in collaboration with Dr. V. Bashkirov of LLUMC) correlates between each projectile and its associated ions, registering the arrival time of each ion with respect to a trigger. Optionally, the DAQ records information regarding the projectile particle (energy, trajectory, etc'). In the offline analysis, the validity of each event is checked against strict triggering requirements. Relevant events are selected and appropriate histograms are generated.

The pulses are properly shaped and recorded by a custom-designed, PC-based DAQ system shown schematically in figure 3.8. The DAQ system is fed by negative fast analog pulses from the ion counter (figure 3.6), the trigger detector and, optionally, by a secondary trigger detector (flag). It is based on a National Instruments PCI6602 timer/counter card, essentially a PC-borne multi-channel 80 MHz time-to-digit converter. It is configured to digitize and record, in real-time, two data streams with a time resolution of about 25 ns (determined by the signal shaping hardware) at a rate up to 8 MB/s.

The signal from the trigger detector is injected into the "trigger" data stream of the PCI card. It is also used to generate an appropriate gate signal for enabling the ion-counter channel discriminator. When working in pulsed mode of the electric field $E_1$ (see §4.2.1 below), this signal is also used to activate, after a 5 μsec delay, the high voltage ion-extraction pulse. The "trigger" data stream is used by the DAQ as a time reference for measuring the ion arrival times and for offline pile-up rejection.

The "trigger" data stream can also be used to analyze the time structure of the primary beam, relevant in accelerators with pulsed beam structures, as is the case for experiments carried out at the Loma-Linda proton synchrotron [86].

The signals from the IC are injected, into the "ion" data stream of the PCI card. This provides information about the individual ion drift time and the number of ionizations per primary particle event.

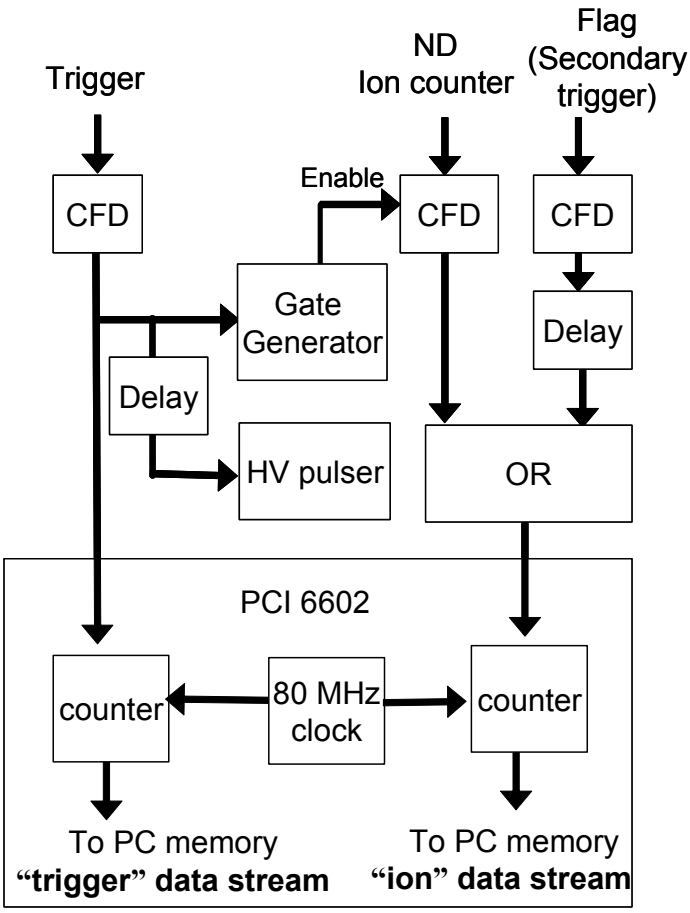


**Figure 3.8: A flow diagram of the DAQ system.** See text for details.

The (optional) signal from the secondary trigger is introduced as a logic flag for offline selection of events: it is delayed, and then incorporated into the "ion" data stream via an OR gate. The time delay is set such that this signal does not interfere with the ion pulses. In the "pencil beam" experiments, we used a well collimated scintillator signal (see §3.2) to select the projectiles passing through the core of the beam; in one experiment (see §4.3.3) we used a collimated solid-state detector to select the fraction of the beam having very precisely defined energy.

A data storage algorithm manages the data stream transfer to the PC computer hard disk. The full data analysis is carried out offline but a simplified on-line data analysis is provided for rapid data diagnostics and control of proper system functioning.

### 3.1.6 The analysis

The ion drift velocity in our experimental conditions is 0.4 mm/μsec (see §4.2.3) resulting in ion drift times of up to 125 μsec, depending on where the ion was created along the SV. This poses a limitation on the maximal possible beam rate; in order to avoid counting ions resulting from more than one projectile within the same cluster, we usually require a (conservative) minimal interval of 200 μsec between consecutive projectiles.

Therefore, in the offline analysis, we first performed a pile-up rejection, namely rejecting all events that are followed or preceded by another event within less than 200 μsec. When performing measurements with a secondary trigger (e.g. in the pencil beam studies), only those events containing a flag are selected **after** the pileup rejection. The significance of this order is discussed in §4.3.1.

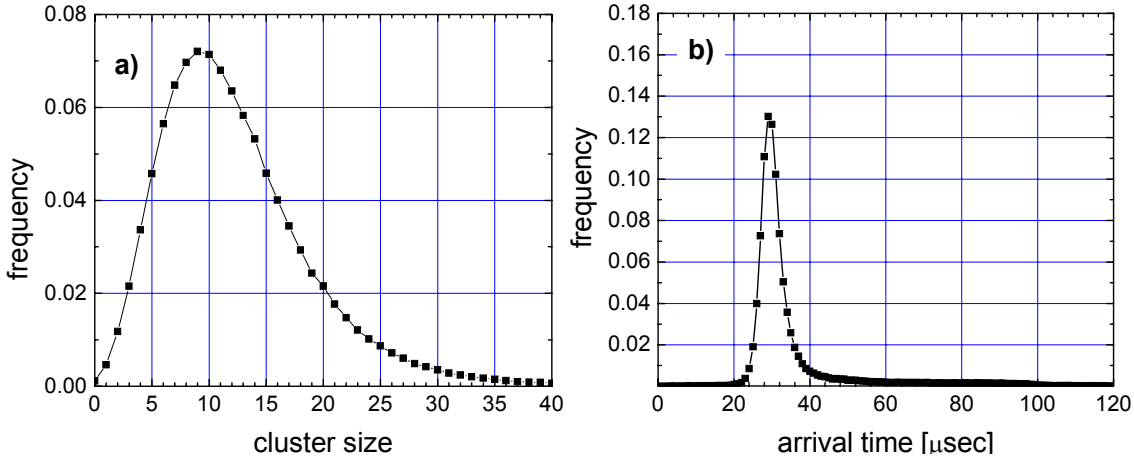


**Figure 3.9: Data obtained with the internal alpha source**: a) a sample of the ion cluster size distribution, using the sensitive volume of 3.16b. b) The ion arrival time distribution in the same conditions.

Each data set, of up to 2 $10^6$ non-overlapping events (e.g. figure 3.6b), was measured over a period of several hours, at a trigger rate of a few hundreds to a few thousands of particles/sec in accelerator experiments (data sets of a few times $10^4$ were typically recorded at 3/sec using the built in α-source). The analysis software then generates an ion cluster-size distribution (for example, figure 3.9a), providing the frequency at which clusters of a given number of ions are induced by a single ionizing particle, within the SV. Optionally, only those events having a coincident signal in the secondary trigger are selected. The analysis also provides the ion arrival time distribution (figure 3.9b); it is correlated with the initial ion deposition location along the SV axis, namely its distance from the extraction aperture. This information may be used to measure the ionization density profile across the particle's track. It can also be used to subdivide the data into selected time windows, equivalent to the division of the SV length into small segments, a few nanometers long (see §4.2.4 below). Due to the rather small ion diffusion in the gas (about 1 mm FWHM for 1 cm drift in our conditions), the information on the initial ion deposition distance is well preserved, with a resolution of a few equivalent nm. This feature may serve as a basis for *experimental track-nanodosimetry,* providing a way of mapping ionization clusters deposited by a single projectile at different distances from the track axis.

Furthermore, the number of ions arriving at very long times, when no ions are expected can serve as an indication of the efficiency of pileup rejections (see appendix B).

## 3.2 The accelerator setup

For measurement of ionization clusters induced by pencil beams of protons and carbon nuclei, the ND was mounted on the N2 beam line of the Weizmann Institute's UD14 Pelletron (figure 3.10). The beam-line setup is shown schematically in figure 3.11.

The accelerator beam is scattered by a thin scattering foil, covered by a 1 mm aperture. This foil also brings the ion beam, initially consisting of highly charged ions having a single charge state, to charge state equilibrium. After spreading out (over a distance of 1.74 m), it is collimated to 1 mm by a movable collimator. These two apertures precisely define the beam diameter and its direction. We have chosen the scattering foil such that the beam divergence is a few degrees. As a result we are rather insensitive to the precise angle and alignment of the beam, delivered by the accelerator.

The collimated beam enters the ND gas volume through a thin (2.5 μm Mylar) window, traversing the SV, 15 mm above the center of the ion extraction aperture (the movable collimator allows irradiation at different positions within the SV)

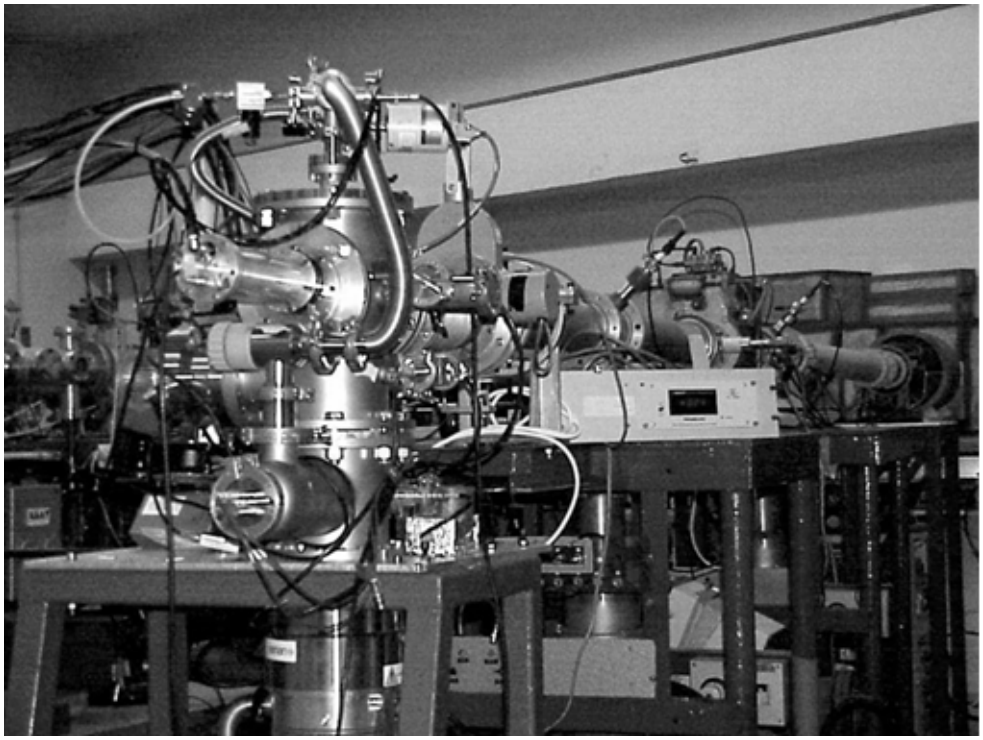

**Figure 3.10: Photo of the ion counting ND mounted at the WIS Pelletron.**

As a primary event trigger, we used a position-sensitive, 10 cm diameter multiwire proportional chamber (MWPC) shown in figure 3.12 (20 μm anode wires, 1 mm pitch, 3.2 mm anode-to-cathode gap), preceded by a 3.2 mm thick parallel-grid pre-amplification gap. The MWPC was separated from the ND volume by a thin Mylar foil (2.5 or 6 μm depending on the MWPC pressure). The MWPC was operated under a flow of 10-100 Torr of propane.

The MWPC anode provides the trigger signal to the ND DAQ system (figure 3.8). Although the MWPC anode pulse is clearly separated from the electronic noise (see figure **3.13**a), indicating high trigger efficiency, due to scattering of the projectiles on the first mesh of the preamplification gap, the effective trigger efficiency is about 80%. The implication of this, as discussed in appendix B, is a limitation on the maximum beam rate of a few kHz; at higher beam rates the measured cluster-size distributions will be distorted.

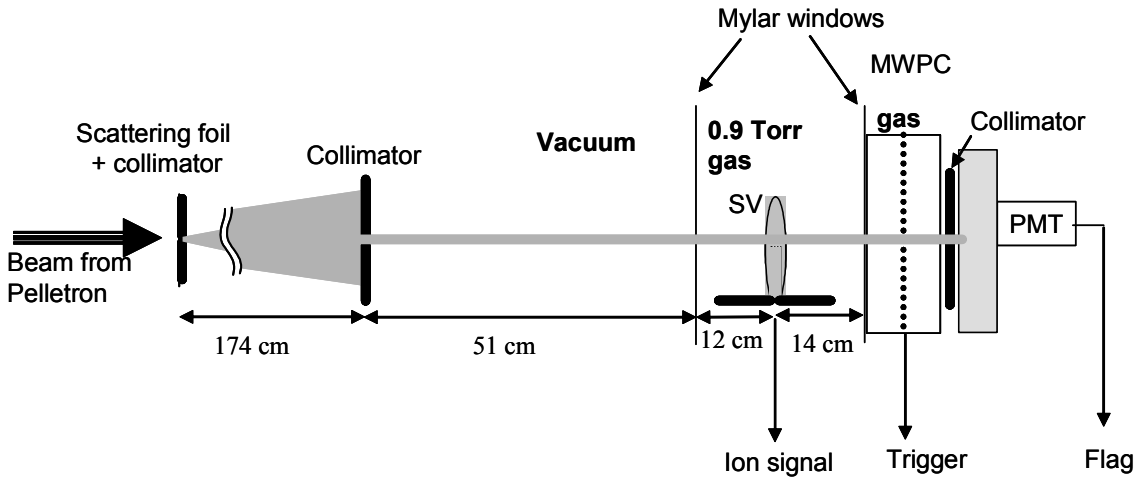


**Figure 3.11: A scheme of the accelerator beam line layout used for narrow beam measurements at the WIS Pelletron.** See text.

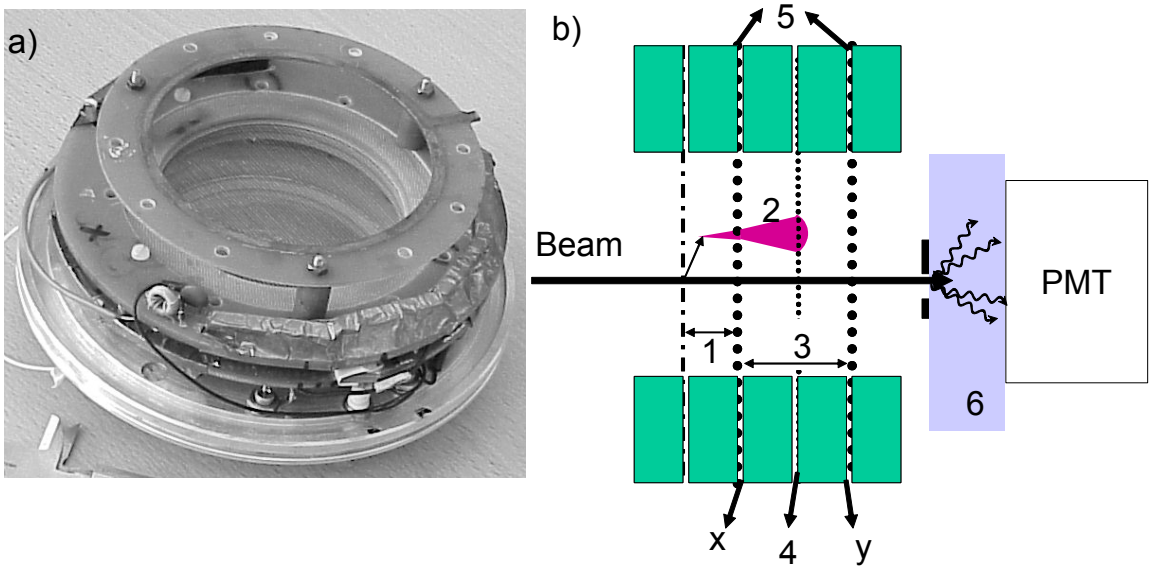


**Figure 3.12: MWPC photo (a) and scheme (b).** The projectile beam from the accelerator induces electrons which are multiplied in the preamplification gap (1). The electron avalanche (2-shown offset for clarity) further develops in the multiwire gap (3). Electrons are collected on the anode wires (4). The avalanche-induced ions induce signals on the cathode wires (5). Each cathode wire is connected to a delay line readout with the two cathode planes placed perpendicularly providing "*x*" and "*y*" localization of the avalanche. The projectile beam is stopped in a scintillator (6), creating photons which are detected in a PMT.

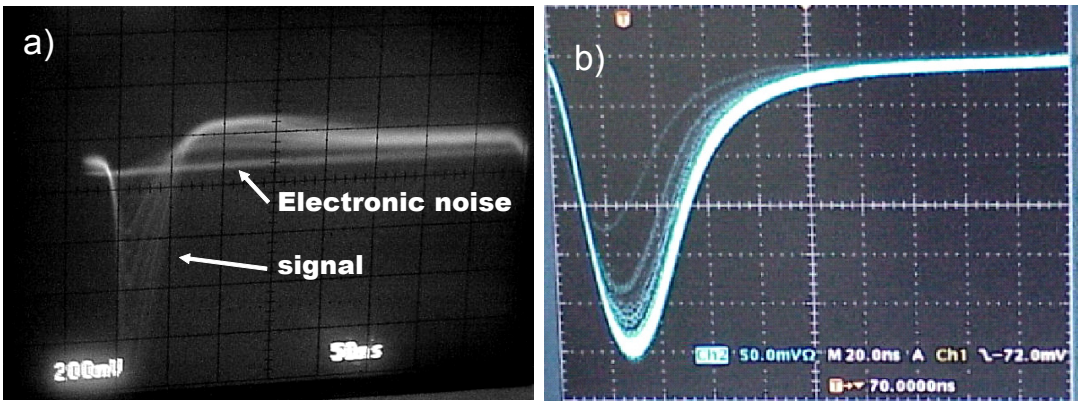


**Figure 3.13: a)MWPC anode pulses induced by 13.6 MeV protons** (200 mV/ 50 nsec per division). Note that the signal is well separated from the noise. b) Pulses from the PMT tube, PMT operated at 900 V (50 mV/ 20 nsec per division).

The cathodes' wires are connected to delay-line readout circuits, providing a rough means for 2D beam imaging. The cathode signals are processed by fast amplifiers, two time-to-amplitude converters and a PC-borne ADC card (Ack2D) [89], see figure 3.14. Although the MWPC permits visualizing the incident ion beam with sub-mm precision, it was only used for monitoring the beam shape and alignment.

The back of the MWPC is sealed with a thick plastic scintillator, coupled to a photomultiplier tube (PMT - serving as a secondary trigger); a 1 mm diameter collimator is placed in front of the scintillator. Due to scattering of particles in the degradation foil, the ND windows and in the MWPC itself (the scattering in the gas is negligible), 80-95% (depending on the beam type and energy) of the particles detected by the MWPC have been scattered outside of the 1 mm diameter beam, and do not induce a signal in the secondary trigger.

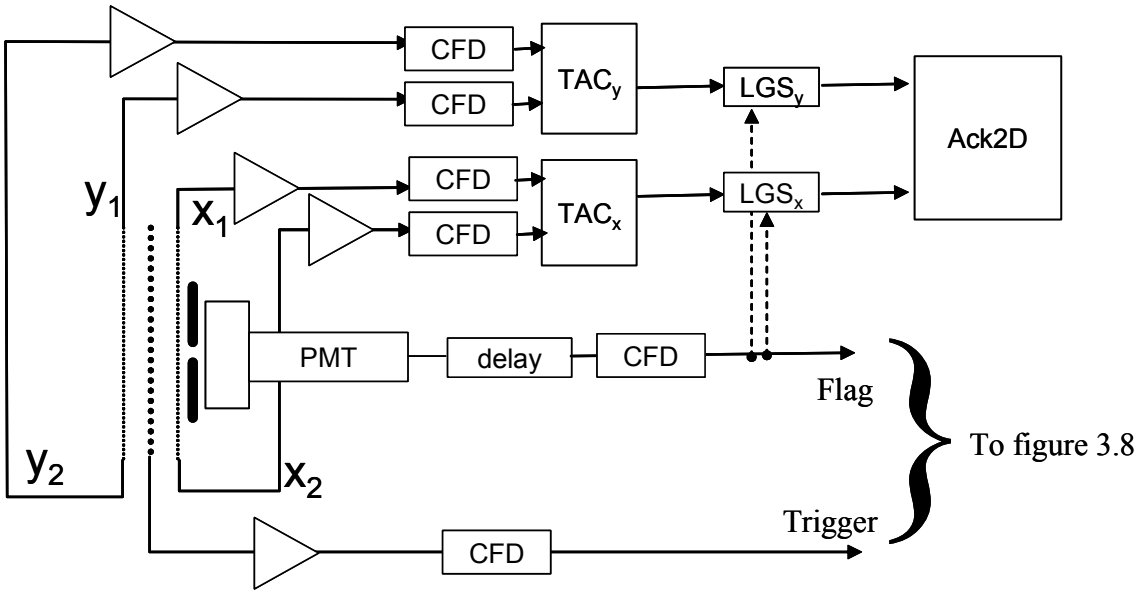


**Figure 3.14 : The trigger connection to the DAQ** ( see figure 3.8). The MWPC anode is connected via an amplifier and a discriminator (CFD) to the trigger data stream. The PMT signal (see figure 3.13b**)** does not require amplification and is connected to the flag stream. The cathode wires are connected to the taps of a 5 nsec/tap delay line. The first and last wires are connected (via an amplifier and a CFD) to a "time to analog" converter (TAC) which outputs an analog pulse whose amplitude is proportional to the delay and hence to the position. The timing of the two analog signals are adjusted (using a linear gate stretcher – LGS) to arrive simultaneously at the 2D imaging card (Ack2D). Optionally the signal from the PMT is used as a gate to the two LGS units to obtain a beam image in coincidence with the scintillator.

While the DAQ system records all triggered events, the selection of the collimated ones is done off line. This strategy is very important in order to ensure **full elimination** of pile-up ions from closely consecutive events (requiring **all** projectiles passing through the ND to be recorded), while rejecting all events due to projectiles scattered out of the primary beam.

## *3.3 Montè-Carlo simulations*

In order to better understand the physical processes occurring in the ND and to assist in the experiment planning we have extensively utilized the track-structure code developed by B. Grosswendt (PTB, Germany) and modified at our request, to model the irradiation geometry of the nanodosimeter. The code incorporates all relevant interactions and experimental ionization cross sections of light ions. It also contains electron interaction cross sections, with regard to elastic scattering, excitation and ionization in propane. The secondary and higher-order electrons induced by successive ionizing interactions are then followed through the gas until their energy reached a value below the ionization threshold (11 eV for propane).

After generating a "spatial map" of the ions formed by a single projectile, we must also take into account the response of the ND. In other works [63, 82] this is done by assuming a right regular (i.e. diameter = height) cylindrical sensitive volume and setting an absolute detection efficiency such that the measured and calculated cluster size distributions match. Within this work, we have performed extensive ion transport simulations (see details below) to obtain a spatial mapping of the efficiency to detect ions, formed anywhere within the IV. This ***efficiency map*** was incorporated into the track-structure code, resulting in a full simulation of the ND. It provided an excellent prediction of the measured cluster size

distributions, without any fitting parameters, as will be seen below. An in-depth description of the MC code and all relevant physical parameters are given in appendix A.

We have made extensive use of the MC code, both as a prediction of the measured data as well as for predicting the results of experiments which could not be practically done. It was used both for understanding the physical processes (e.g. δ-electron ranges) and the technical limitations (e.g. the importance of alignment in the narrow beam studies) of our ND.

## 3.4 The sensitive volume

Perhaps the most important feature of the ion counting nanodosimeter is its tunable wall-less sensitive volume (SV). In order to model radiation action on DNA dimensions, we must have a "DNA-sized" SV. Furthermore, due to the small amount of energy deposited within such a small volume, it is imperative to have, on the one hand excellent ion collection efficiency while on the other hand not to have any secondary effects (e.g. [49]) which may induce excess ions. Our ND was designed to contain no solids in the vicinity of the SV, apart for the anode and cathode; ions formed near these electrodes are rejected offline based on their arrival time. Subsequently, the SV is defined solely by electric fields. Apart from the entrance and exit windows, of thin Mylar, there are no solids along the beam path. The beam scattering in these windows was simulated using SRIM [90] and was seen to be negligible. As we did not detect any ions formed near the anode and cathode by a pencil beam irradiation, we conclude that there are indeed no wall effects in the ND.

As described above, the ionization volume of the ND is coupled to the detection volumes by a series of small apertures. Only ions deposited roughly above the first aperture are efficiently extracted from the ionization volume, transported to and detected by the ion counter. The SV diameter is therefore determined solely by the transport of ions in gas, under an electric field. The SV length is a-priori (almost) as long as the ionization volume, but we are able to segment it, by imposing off-line windows on the ion arrival time. The knowledge of the ion drift velocity permits the selection of an SV of arbitrary length, limited only by the diffusion of ions in a low-pressure gas. The SV diameter can be adjusted by varying both the pressure and the electric fields above and below the ion extraction aperture ($E_1$ and $E_2$ respectively in figure 3.1). While the value of $E_1$ largely defines the effective length of the SV, $E_2$ also has a strong effect on the SV shape.

### 3.4.1 Sensitive volume evaluation

#### 3.4.1.1 Montè-Carlo simulations

Under uniform electric field $E$, the efficiency of extracting an ion form any place in the gas volume can be calculated analytically: An ion cloud, formed a distance $L$ above the aperture, will drift along the field lines and diffuse to a Gaussian profile with (eq. 2.5):

$$\Delta x = \sqrt{2\frac{D_i/K_i}{E}} * \sqrt{L} \qquad (3.1)$$

where $D_i/K_i$ is the ratio of diffusion coefficient to mobility (which we have measured for propane in a previous work [75]- see figure 3.15). The extraction efficiency can then be calculated by integrating this Gaussian cloud over the area of the aperture. In the case of an arbitrary (non uniform) electric field, which is required for ion focusing, this calculation can be also (in principle) be carried out, assuming a piecewise constant $E$. However, as the calculation is extremely convoluted, we have decided to pursue another route. We have developed a MC calculation, based on measured ion transport parameters [75] in propane and on the electric field distribution within the ionization volume, as simulated using the SimIon [91] software package (see for example figure 3.4).

In the simulation we assume that:

1. The **only** ions, formed in the ND, are $C_3H_8^+$ ions (or that they are converted to $C_3H_8^+$ ions briefly after their formation).

2. These ions interact with the gas **only** via resonant charge-exchange: $\overrightarrow{C_3H_8^+} + C_3H_8 \rightarrow \overrightarrow{C_3H_8} + C_3H_8^+$ (where the arrow denotes the carrier of kinetic energy).

3. Based on 2) we assume that in each collision the ion is thermalized. From the data in figure 3.15 and based on the well known Einstein relation: $D_i/K_i=k_bT/e$, we have defined an electric-field dependant *effective temperature* ($T_{eff}$), used for calculating the ion velocity after the interaction (note that $T_{eff}$ is much higher than room temperature).

The first assumption is justified by our measurements of the ion mobility and diffusion coefficient of α-particle-induced ions in propane [75]. Figure 3.15 shows our measured value for $D_i/K_i$ (the ratio of the ion diffusion constant to the ion mobility) compared to the literature values for different ions and gases. It is clear that the ions formed in propane follow the same behavior as ions drifting in their parent gas.

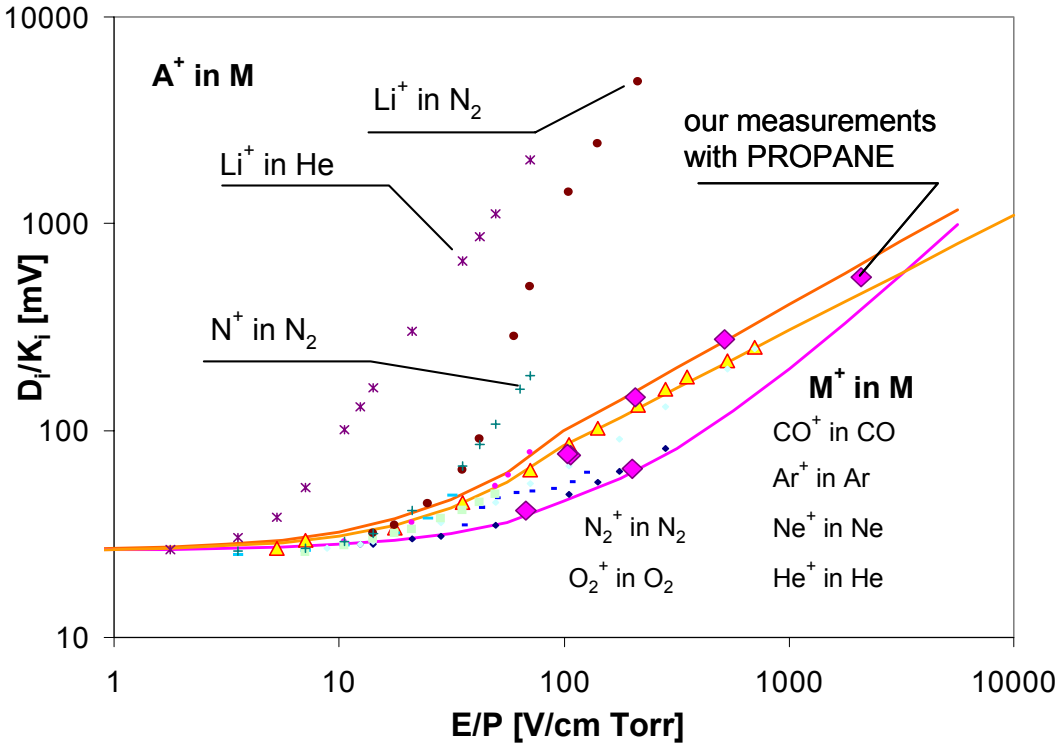


**Figure 3.15: Ion diffusion in gases.** A plot of the measured ratio of transverse diffusion to mobility for alpha-particle induced ions in propane (♦ [75]), compared to other literature values. It is clear that the ions formed in propane behave like ions drifting in a gas of identical molecules. Figure taken from [92].

Although assumption 2 neglects scattering processes (other than charge exchange) which will tend to transfer energy from the ions to the neutrals, we have seen that the effects of these processes are accounted for in the value of $T_{eff}$. Indeed our calculated $D_i/K_i$ value (for a simulated homogenous field) faithfully reproduces the measured one.

An ion extraction efficiency map is calculated by following many ions, originating from a grid of points in the ionization volume. Each ion, starting from a given point is given a velocity, based on the local temperature $T_{eff}$ in an arbitrary direction. The distance to the next

collision is calculated using a charge exchange cross section fitted so that the resulting ion drift velocity matches the measured one. The coordinate of the next collision is calculated based on the local electric field.

If the ion reaches the ion extraction aperture (of 1 mm diameter) it is considered "detected". Tracking many such ions, originating from one point, provides the ion extraction efficiency from that point. As a benchmark, we have calculated the expected (calculable) efficiency map for the case of a uniform electric field and found good agreement with the theoretical prediction. In this work we **define** the SV diameter as the width of the 50% ion extraction efficiency contour, at a distance of 15 mm from the aperture; the SV length is defined as that of the 50% contour along the aperture axis. These are, naturally, arbitrary definitions; the SV dimensions can only be truly defined in terms of the **entire** ion-extraction efficiency map.

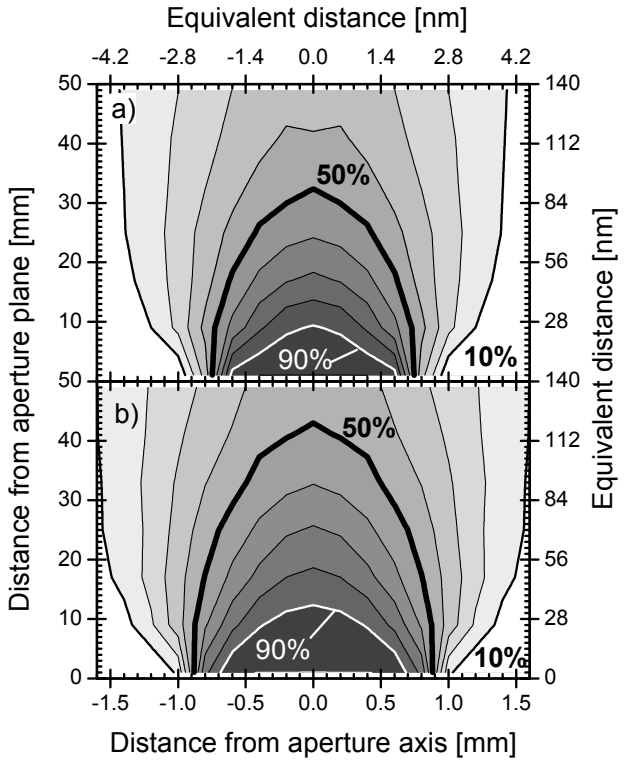


**Figure 3.16: Montè-Carlo-simulated maps of the ion extraction efficiency** from the ionization volume (through a 1 mm diameter aperture), defining the wall-less sensitive volume. Each contour line represents a change of 10% in the ion extraction efficiency. The bottom and left scales are real distances in gas, while the top and right scales provide the equivalent distances in tissue (calculated as explained in §2.2.3). Figure a) corresponds to an electric field configuration: anode = 300 V, $A_2$=184 V and b) corresponds to anode = 300 V, $A_2$=284 V. Note a factor of ~15 between vertical and horizontal scales.

Figure 3.16 shows two examples of MC-calculated ion extraction efficiency maps. In particular, the map shown in b) corresponds to the "standard" operating voltages of the ND (namely, 300 V on the IV anode, -284 V on $A_1$, -470 V on $A_2$, -800 V on $A_3$ and -2830 V on $A_4$). This results in a sensitive volume of 4.5 nm diameter and 120 nm length as defined above.

The SV diameter (1.3 and 1.6 mm in figure 3.16a and b respectively) was seen to be somewhat larger than the physical diameter of the aperture (1 mm). This is due to ion focusing into the aperture, caused by the electric field $E_2$. Indeed, the two maps shown in figure 3.16 differ only by the choice of $E_2$ values. The ion focusing effect can be clearly seen in figure 3.17, which depicts simulated single-ion trajectories in the case of "strong focusing" and "no focusing" conditions. While in the latter no ions may reach the aperture (due to the low diffusion), in the former about 20% of the ions, generated at the same spot (1.1 mm away from the aperture axis and 2 mm above it), may pass through the aperture.

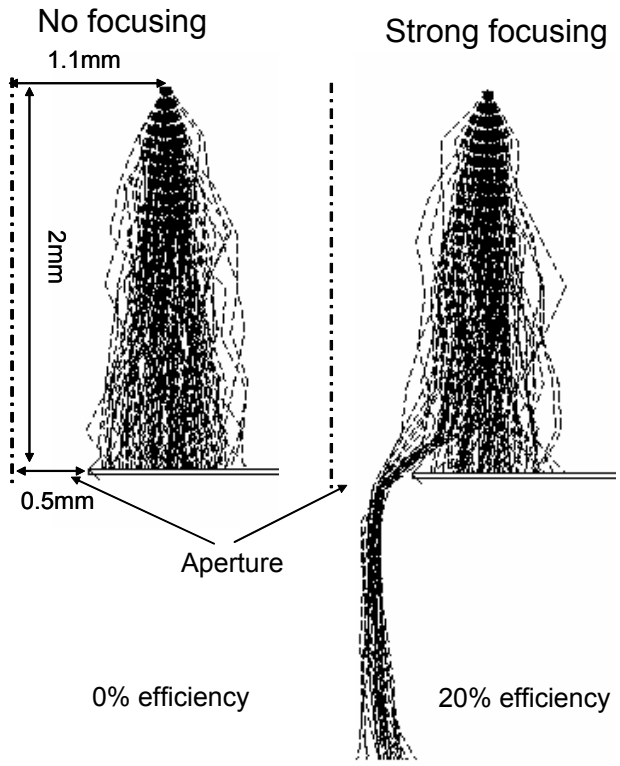


**Figure 3.17: Simulated single ion trajectories** with and without focusing for ions deposited two mm above the aperture and 1.1 mm (two aperture radii) aside from the aperture axis (denoted by the dash-dot line).

#### 3.4.1.2 Experimental evaluation of the efficiency map

To validate our simulated efficiency maps, we proceeded in a complex experimental evaluation. For that purpose, the nanodosimeter installed at the Loma Linda University Medical Center's proton synchrotron was modified to include 4 single-sided silicon micro-strip detectors [93]. This enables measuring the trajectory of each individual projectile, passing through the ND, with 60 μm resolution.

The ND was then illuminated with a uniform beam of 250 MeV protons. For each proton we have registered its trajectory and the number of counted ions.

Since 250 MeV protons have very low LET (8 $10^{-3}$ keV/cm in 1 Torr of propane, corresponding to about 1 ionization every 3 cm), clusters with 2 or more ions are exceedingly rare; therefore the fraction of events where one ion is detected is proportional to the track average ion extraction efficiency, namely:

$$\int_{track\ length} \varepsilon(x,y,z)dl = \frac{n}{\sigma^{ion}} f_1(x,y) \qquad (4.2)$$

where $x$ is the SV axis direction, $z$ is the beam direction, $n$ is the molecular density, $\sigma^{ion}$ is the ionization cross section, $\varepsilon(x, y, z)$ is the ion extraction efficiency map and $f_1(x, y)$ is the probability for a projectile, passing at $(x, y)$, to induce exactly one ion which is successfully extracted from the SV.

To solve numerically eq 4.2 and find $\varepsilon(x, y, z)$ given $f_1(x, y)$, we must also assume that the ion extraction efficiency map is cylindrically symmetric around the $x$ axis. The exact details of the numerical solution of these equations are given elsewhere [86]. A comparison of a measured map and one obtained from the MC simulation is given in figure 3.18; it shows a rather good agreement in the marked (dash-dot) region. This is the region which will be selected using time cuts (see below) to simulate a biological target. The simulated ion cluster size distributions in the two maps (figure 3.18b) differ by less than 4% (both in the average cluster size and in the cluster yields).

As this measurement is extremely difficult, requiring about 80 hours of beam time for the evaluation of a single map, we have preferred to use the MC simulation, which is validated by the good agreement with this experiment (see figure 3.18b).

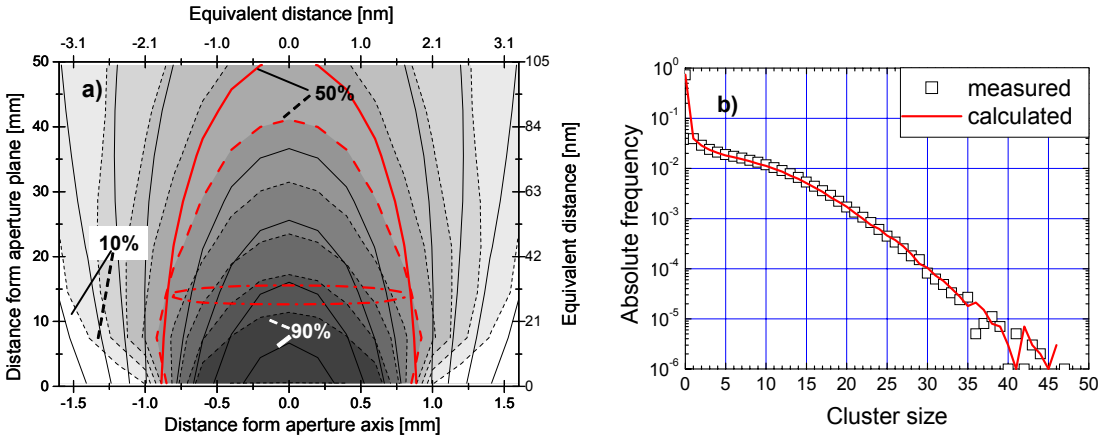


**Figure 3.18: a) comparison of scanned and simulated maps.** The shaded map (with dashed contours is the simulation. The solid lines are measurements (notation is as in figure **3.16**. The dash-dotted region is the one selected by the time cut (see below). b) Simulated ion cluster size distributions in the measured (squares) and calculated (line) SV. (5 MeV alpha particles 20 mm diameter beam)

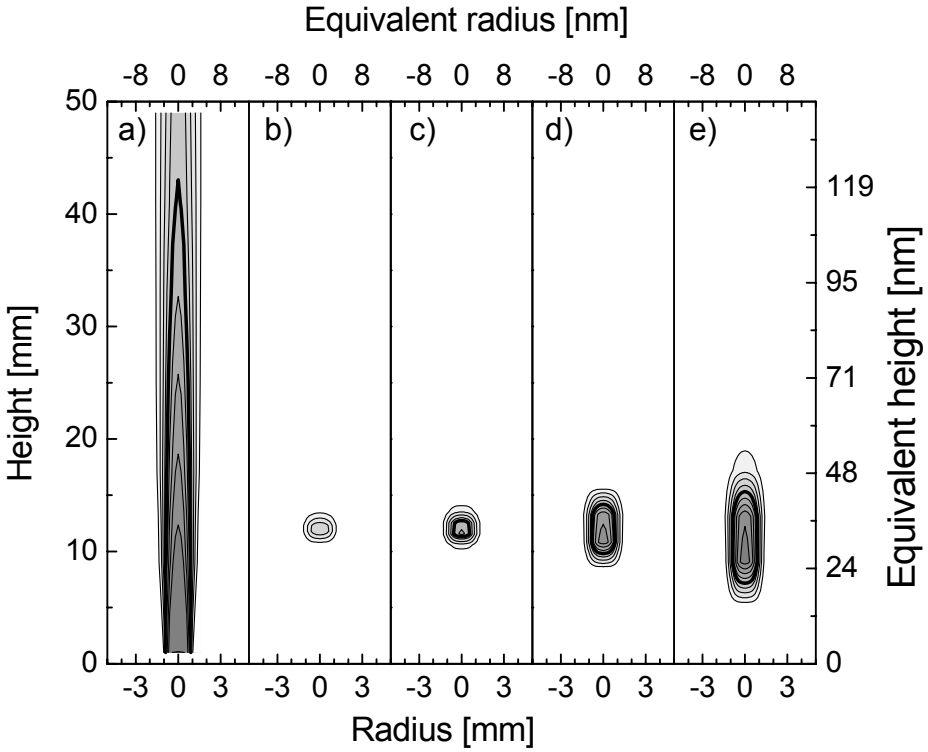


**Figure 3.19 : The time-cut SV maps corresponding** to a) The full SV map of figure 3.16b and b)-e) SVs of 2.5 nm, 5 nm, 12 nm and 24 nm lengths. The thin lines correspond to 10% increments of ion extraction efficiency; the thick line corresponds to 50% ion extraction efficiency.

### 3.4.2 Time cuts

As can be seen from figure 3.16, the sensitive volume is rather long (120 nm). In order to model shorter (10 bp) segments of DNA we need a sensitive volume of about 6 nm length

(see discussion below). Such a "short" sensitive volume can be obtained by segmenting the sensitive volume of figure 3.16. As we are recording the arrival time of each ion, it is possible to trace-back to its deposition distance within the gas volume. We can then select (offline) only ions arriving from a certain region of the SV, by performing a time-cut on the data. Sample time-cut sensitive volumes are depicted in figure 3.19. It should be stressed that the time cuts do not provide a sharp slicing of the SV. Rather, due to diffusion, the SV boundaries will always be smoothly varying over a few nm. Subsequently an attempt to create a SV shorter than this (see for example SV in figure 3.19b) will result in a SV of the same dimensions but with reduced maximal efficiency.

The time cut maps, in figure 3.19, are obtained from the full simulated maps by multiplying the ion detection efficiency at each point in the map by the probability of an ion generated at that coordinate to arrive within the selected time window:

$$\varepsilon_{TC}(x,y,z) = \varepsilon(x,y,z) \times \int_{\substack{\text{time cut} \\ \text{window}}} f(t,x)dt \tag{4.3}$$

where *f(t, x)* is the ion arrival time distribution of a needle beam passing at altitude *x* within the SV*:*

$$f(t,x) = \frac{1}{\Delta x\sqrt{2\pi}} e^{-\left(\frac{t-x/v}{2\Delta x(x)}\right)^2} \tag{4.4}$$

where *v* is the drift velocity and $\Delta x(x)$ is the (experimental) width of the distribution.

### 3.4.3 Choice of the sensitive volume

The main feature of the ion counting nanodosimeter, as a tool to study the biological effects of radiation, is that it can have a **DNA-sized** sensitive volume. As expected, and verified by experiments and MC simulations, the ion cluster size distributions, induced by pencil beams, are rather sensitive to the size of the SV. Although the choice of the SV is an important one, we have seen that the free parameter in the biophysical model, detailed in §7 below, can compensate for an incorrect selection of the SV size. This will be discussed in more detail in §7 and §8.3.

We have shown above that the SV is wall-less (i.e. distortion free) and tunable. We must now tune the sensitive volume to be DNA-sized. First we must define what is "DNA-sized":

The DNA is a very long and thin molecule (a diameter of 2 nm and a length of several microns to several meters), of which we are only interested in a short segment. It is inconceivable that two isolated damages, occurring on opposite edges of a DNA molecule would interact to form an irreparable damage cluster. On the other hand if the same two damages were formed on opposing bases, an irreparable double strand break would immediately follow. The length of our sensitive volume must be therefore equal to the "correlation length" of damages on the DNA. Studies of the repair of pairs of uracil residues located in predetermined locations in a short DNA segment, point to lesion interaction lengths of 7 [94] to 12 [95] bp. The data regarding other types of lesions are scarce. In our work we assumed that the interaction length of two general lesions is 10 bp

But it is not enough to know the size of the DNA segment. Except for a few academic studies [96, 97], the interaction of radiation with DNA is invariably in an aqueous environment. Depending on the actual chemistry of the solution, the majority of damage to the DNA is due to water radicals formed in the solution, these radicals diffuse and may attack the DNA. We should therefore expand the sensitive volume to include the range of radicals which may be of tens or even hundreds of nm depending on the scavenging capacity of the solution. In our radiobiological studies we have irradiated solutions of two scavenging

capacities, see table III (in §6); the significance of these two concentrations is discussed in §6.1.2.

On the other hand, due to the diffusive motion of radicals, they quickly lose correlation with each other and form a low-level homogenous background of isolated lesions. These do not interest us. Furthermore, radicals formed more than one or two DNA radii away, will have an extremely low probability to find the DNA molecule before they are scavenged. We have therefore selected our biologically relevant sensitive volume to be a cylinder of 4.5 nm diameter and 7 nm length corresponding to a 10 base pair segment of DNA with a 1.5 nm "shell" of water molecules (these numbers refer to the 50% ion extraction efficiency contour; neither the biological nor the ND sensitive volumes are sharp cylinders). This sensitive volume is reached by segmenting the sensitive volume of figure 3.16b as described above.

# Chapter 4 :

# ND studies with charged particle pencil beams

We have extensively studied the parameters affecting the ND performance and its operation, both using the internal alpha-particle source and in an accelerator environment, trying to identify and minimize the systematic errors.

We have investigated: the effect of the IC response, ion focusing and ion cluster-size on the ion counting efficiency; the effect of event repetition rate and trigger efficiency on pile-up rejection; the role of beam geometry (alignment and diameter); the effect of secondary charge multiplication in the sensitive volume and its elimination by pulsing techniques.

## *4.1 Ion counting efficiency*

The number of ions induced in our nanometric SV ranges typically from zero or one for low LET protons up to 100 for high LET carbon nuclei. *Ion losses* were seen due to inefficient transfer of the ions to the IC, inefficient ion detection by the IC and due to a deficiency in the DAQ system. We have also seen an *overcounting* of ions due to pile-up events and charge multiplication in the IV and possibly also in the intermediate vacuum region.

### 4.1.1 The Ion counter

As we are counting single ions, the efficiency of the IC (A discrete dynode electron multiplier, as noted above) to detect few-keV ions is of crucial importance. In [87] we reported on the absolute single-ion detection efficiency of an "out of the box" IC. It is seen to rise with the ion energy reaching an efficiency of about 90% for ions above 4 keV (see figure 4.1). Therefore, accelerating the ions in our setup to 8.2 keV ensures single ion detection efficiency values close to unity.

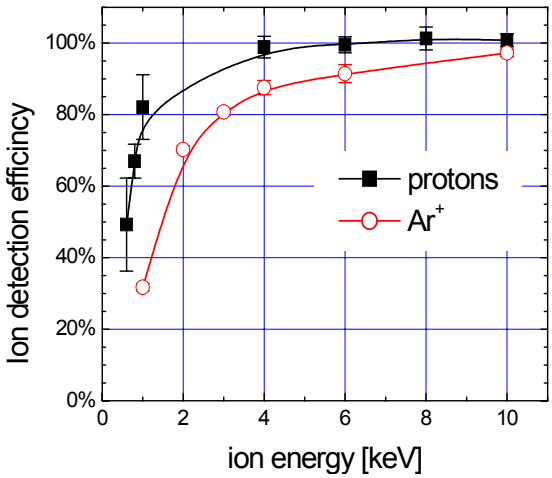


**Figure 4.1: The absolute efficiency for detection of single ions** in the IC, as a function of the ion energy.

A special concern is the long-term degradation of the IC under vacuum of $10^{-5}$ Torr of propane (in the detection volume), which is not specified by the producer. We have conducted

systematic aging studies, to assess the time evolution of the IC efficiency under continuous operation. These measurements were performed at pressures ranging from 3 $10^{-6}$ to 4 $10^{-5}$ Torr of argon, air, and propane, in conditions similar to those encountered during regular operation of the IC in our nanodosimeter.

It was found that the effect of the IC aging depends on the *accumulated output charge*, regardless of the operating IC voltage. After accumulating 0.004 Coulombs at its output (approximately $10^8$ counted ions), the gain and the output pulse-height of a new IC dropped by about a factor of 2, regardless of the gas type and pressure. For all multipliers units, investigated, we have found that the output signal stabilizes at a minimal plateau value. The dependence of the IC aging on the accumulated *output charge* indicates that the aging occurs at the surface of the last few (output) dynodes while the input dynodes, which are essential for providing high ion-counting efficiency, are apparently not affected. Therefore, the IC efficiency can be maintained at its original value by increasing the IC operating voltage (and hence its gain) to recover the average pulse height, keeping the electronic threshold unchanged. This was confirmed by direct measurements of the ion-counting efficiency of aged ICs. To make sure that all our measurements were performed under constant high efficiency, the pulse-height spectrum of the IC has been continuously monitored on an oscilloscope during experiments. The ion counting efficiency was frequently verified by recording α-particle induced ion cluster distributions. No visible decrease in pulse-height or in efficiency was seen during our experiments over a period of about two years.

In some cases, we have seen a marked instantaneous drop in the IC efficiency, following accidental exposure to an excessive ion flux (several nA at its input) or discharges. In most cases the ion-counting efficiency could be *fully restored* by adjusting the operating voltages.

Figure 4.2 demonstrates this long term stability of the ND. Shown are two α-particle-induced cluster size distributions, measured using two different IC units. In between the two measurements, the ND suffered a catastrophic vacuum failure, resulting in the destruction of the IC. The ND had to be completely dismantled, cleaned and a new IC was installed. Nevertheless the ion cluster size distributions are practically identical.

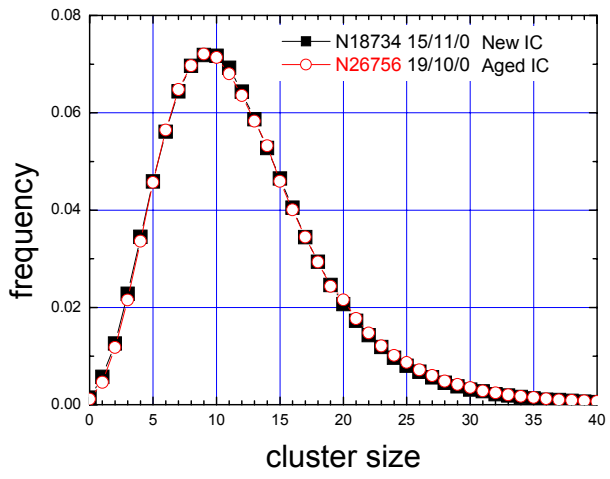


**Figure 4.2: A comparison between two alpha-particle induced cluster size distributions** recorded with a new and an aged IC. The two cluster size distributions are practically identical.

### 4.1.2 Loss of ions due to DAQ dead-time

The finite pulse duration (10 nsec at the IC output which is stretched to 25 nsec at the PC input) combined with the inefficient communication protocol of the DAQ system result in a dead-time of a few tens of nanoseconds following each ion. Therefore, if several ions, belonging to the same cluster, reach the IC within a few hundreds of nanoseconds, some of them could be missed. Moreover, it was found experimentally, that the counting deficiency, which affects the cluster size distribution, depends on the details of the ion arrival-time distribution, as well as on the DAQ properties.

To study this, a series of MC simulations of the DAQ system were performed, using a Gaussian arrival-time distribution with an RMS value, taken from the experiment (e.g. figure 3.9b). The distribution of time intervals (time between consecutive ions), for clusters of a given size, obtained from this simulation, with zero dead-time, was compared with the experimental one (figure 4.3). The latter shows a deficiency at short time intervals with practically no measured ions arriving at intervals below 40 nsec, corresponding to the width of the digital pulses entering the DAQ card. In fact, the deficiency extends to time intervals longer than the electronics' dead-time and was seen to depend on the cluster size. For example, for clusters of 40 ions (typical of high LET projectiles such as 40 MeV C nuclei), it extends to more than 200 nsec, as seen in figure 4.3. This effect is believed to arise from data corruption within the DAQ card or the PC data bus.

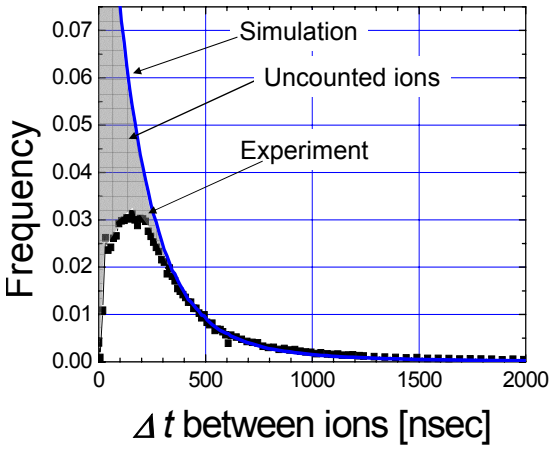


**Figure 4.3: Measured and simulated distributions of the time difference between consecutive ions in a 40-ion cluster.** The solid line is the expected (exponential) distribution. About 45% of the ions are missing from the experimental one.

To evaluate the consequence of this undercounting on the cluster size distributions we introduced into the DAQ Montè-Carlo simulation a cluster-size dependant *effective dead time*: namely a lower $\Delta t$ cutoff in the simulation curve of figure 4.3. $\Delta t$ was varied linearly as a function of the cluster size, so that the measured area under the simulated curve and the experimental one are the same, approximating the experimentally observed undercounting. Figure 4.4 shows the resulting cluster size as function of the size of the initial cluster deposited in the ND. The dashed line represents the case without dead time. We see that for small clusters up to about 5 ions, the undercounting amounts to <5%.It is about 10% for clusters of 10 ions and larger for larger clusters. The saturation and subsequent decline of the measured cluster size is due to overlapping single ion pulses which can no longer be separated.

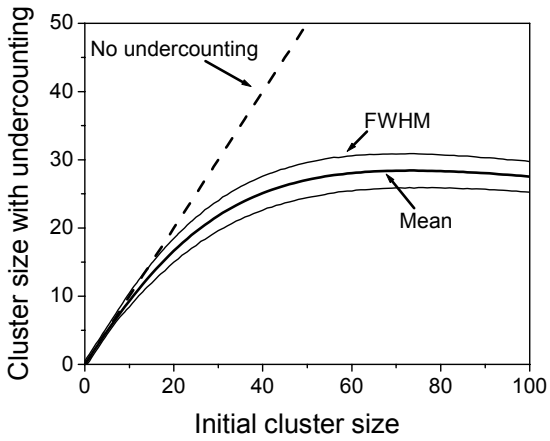


**Figure 4.4: The simulated effect of ion undercounting, due to cluster-size dependant dead-time.** Shown are the mean and FWHM values of the simulated cluster size distribution as function of the initially-created cluster size, taking into account the DAQ parameters. The dashed line represents the ideal case, without dead-time.

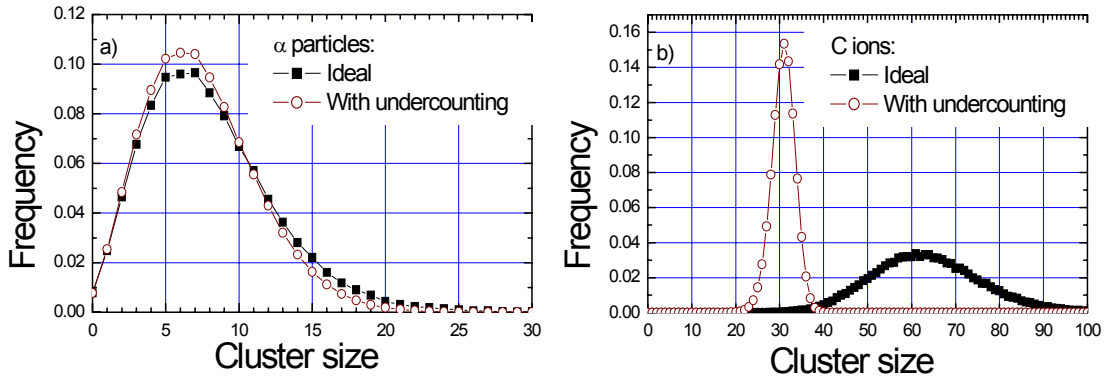


**Figure 4.5: The effect of undercounting on simulated cluster size distributions** induced by 4.25 MeV α-particles (a) and 24.8 MeV carbon nuclei (b). The full and open symbols represent simulated cluster size distributions without and with model-calculated undercounting, respectively. For the alpha particles (LET=107 keV/μm) the effect is mainly seen in the tail. For the carbon nuclei (LET= ~600 keV/μm) the effect is very pronounced.

This phenomenon limits the maximal cluster size that can be reliably measured with the current DAQ electronics. Figure 4.5 shows the effect of the undercounting on **simulated** ion cluster size distributions induced by alpha particles and carbon nuclei. For the lower LET alpha particles, there is a small shift in the distribution peak of about 10%, and the whole distribution is affected as the loss increases with cluster size. For the higher LET carbon nuclei, the situation is much worse; the average cluster size being more than 60 ions, half of them are lost due to the DAQ dead-time.

### 4.1.3 Ion transfer to the ion counter

The ion transfer efficiency to the IC depends on the electric fields below the extraction aperture, which should be carefully optimized. This was done by monitoring the alpha-induced average ion cluster size variation with the voltages applied on the four electrodes below the aperture (figure 3.4).

The first electrode ($A_1$) controls most of the focusing field ($E_2$) near the ion extraction aperture. The average cluster size increases linearly with the applied potential (see figure 4.6) due to the increasing focusing effect of $E_2$, leading to an increase in the sensitive volume diameter, this was also seen in our SV calculations. Only at very high fields the relationship becomes nonlinear due to secondary effects, possibly charge multiplication in the residual gas present in the intermediate vacuum region.

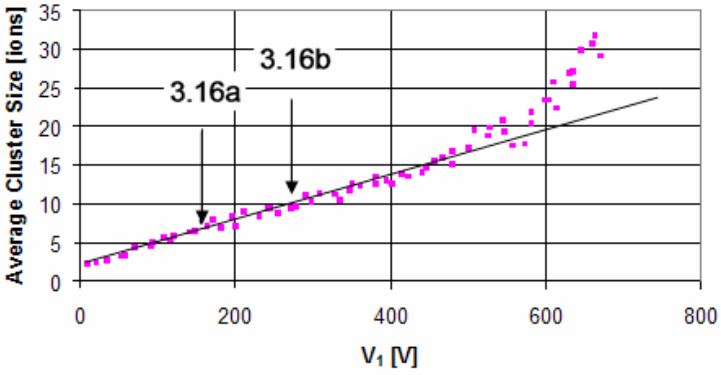


**Figure 4.6: Dependence of the average cluster size on the voltage on $A_1$.** The increase in average cluster size is due to increasing penetration of $E_2$ through the aperture and a subsequent increase in focusing. The deviation from a straight line is due to secondary effects (possibly charge multiplication) in the vicinity of the aperture and is accompanied by a significant broadening of the ion arrival time distribution. The arrow denotes the voltage required to obtain the maps of figure 3.16.

In addition, some electric field penetration from electrodes $A_2$-$A_4$ into the vicinity of the ion extraction aperture, may affect the focusing field by as much as 10%, resulting in a slight increase of the SV. This increase of $E_2$ was compensated by slightly decreasing the potential on $A_1$.

Significant losses of ions during their transport through the apertures $A_1$-$A_4$ were observed only in cases where the potential of a given electrode was more positive than that above it. The potential sequence on the electrodes $A_1$-$A_4$ was optimized according to this criterion. Except where implicitly noted, in all of our studies we used -284 V on $A_1$, -470 V on $A_2$, -800 V on $A_3$ and -2830 V on $A_4$. The SV map was then calculated, based on these voltages (see §3.4.1 above).

It should be noted however, that the conditions for optimal transfer of ions from the ion extraction aperture to the ion counter do not necessarily imply full transfer efficiency, although the agreement between measured and simulated cluster-size distributions support it.

### 4.1.4 Other secondary effects

We have also seen an excess of large ion clusters (with respect to simulations, see below) appearing at a frequency of $10^{-3}$. This effect was seen to some extent with all measured particle beams, including the internal alpha source. It was also seen in an experiment where triggering was performed using an energy-sensitive detector, selecting offline a "monochromatic" beam (see §4.3.3 below). Therefore, this distortion **cannot** be attributed to the beam quality, but rather is inherent to the ND.

Systematic studies revealed that this distortion probably arises from secondary processes, occurring below the ion extraction aperture (and probably very close to it). Such secondary effects could be attributed to the relatively high electric fields and the poor vacuum conditions (A residual gas pressure of between $10^{-3}$ to $10^{-1}$ Torr) in this region, which may join to induce excess ions.

We have found that this distortion, resulting in an excess of large ion clusters occurring in $10^{-3}$ of the events cannot be overcome by a simple adjustment of the electric fields in the ND without a significant loss of the ion detection efficiency. We have therefore decided to operate the ND at these conditions, keeping in mind that the distortion is orders of magnitude smaller than the expected accuracy of the gas model (about 12%, see §2.2.3).

## *4.2 Sensitive volume shaping*

### 4.2.1 Charge multiplication

The sensitive volume maps in figure 3.16 correspond to an electric field in the IV of $E_1$=60 V/cm. A lower electric field will lead to a shorter SV map and to reduced ion extraction efficiency. However, at such high electric fields, (specifically when $E_1$ > ~40 V/cm Torr), ionization *electrons* induced in the gas by the projectile particle, may induce further ionizations en route to the anode, generating additional ions. This is clearly seen in figure 4.7, which shows the gain curve of propane, measured at our conditions. At a field of 60 V/cm, the gain over a 35 mm distance (the typical electron path from the track to the anode) is 1.6. This excess is slightly corrected by the low ion extraction efficiency near the anode (see figure 3.16), where most excess ions are formed (due to the exponential development of the avalanche) but still results in an overestimation of the cluster size by about 20%.

In order to overcome this problem we have implemented a **pulsed field extraction** of the ions from the IV: At stand-by conditions, before a trigger, the electric field $E_1$ is kept at 20 V/cm Torr, below the gas multiplication threshold but sufficiently high to sweep away particle-induced electrons within one or two microseconds. Five microseconds after the beam

particle trigger, $E_1$ is raised to the desired value of 60 V/cm for sufficient time for collecting all ions form the IV (100-200 μsec).

The effect of pulsing $E_1$ is seen in figures 4.8 and 4.9, comparing the ND operation in pulsed- and DC-modes ($E_1$= 60 V/cm). Figure 4.8 compares the measured α-particle induced ion arrival time distributions. The excess of ions arriving after the main peak of the distribution in the DC mode is due to charge multiplication within the IV. The corresponding cluster size distributions are shown in figure 4.9, displaying a significant increase in the mean number of ions in DC compared to pulsed mode.

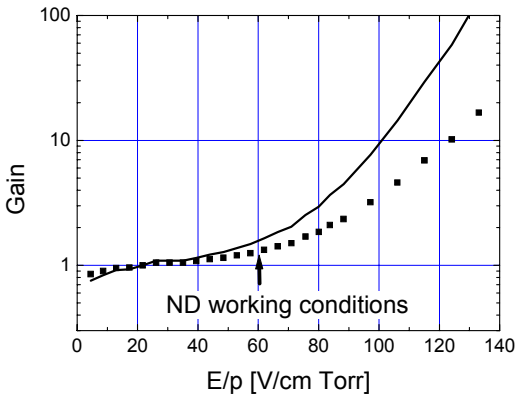


**Figure 4.7: Absolute gain in propane** measured at 1 Torr in a gap of 2 cm (symbols). As the gain is expected to be exponential in gap width, the expected gain in a 3.5 cm drift length (line) was calculated from the gain in a 2 cm gap as

(gain in 2 cm gap)$^{(3.5/2)}$.

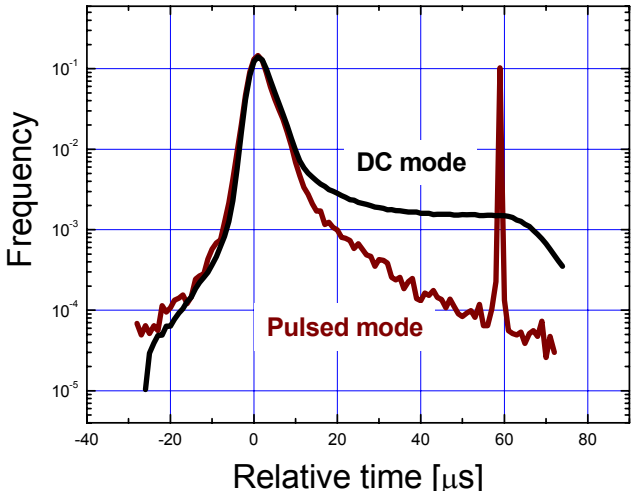


**Figure 4.8: Measured ion arrival time distributions** in pulsed- (60 V/cm pulse; 20 V/cm electron sweeping field) and DC-(60 V/cm) modes. Note the large tail in DC mode, originating from charge multiplication. The "spike" at about 60 μsec is due to electronic pickup (eliminated offline) from the HV pulse generator (Propane, 0.9 Torr).

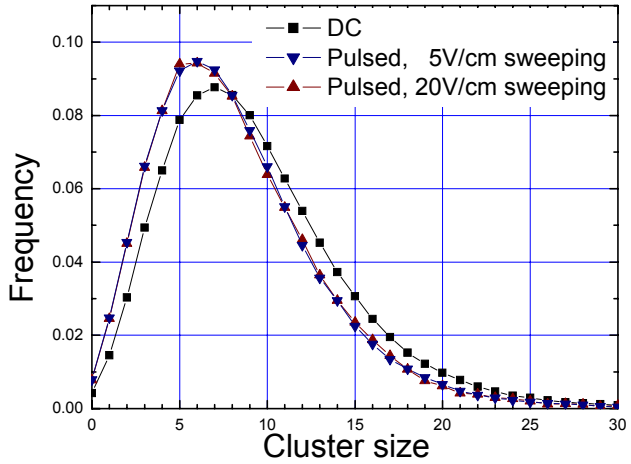


**Figure 4.9: Cluster size distributions induced by alpha particles in DC- and pulsed-modes** with low (5 V/cm) and high (20 V/cm) electron sweeping fields. The pulsed and DC fields are 60 V/cm. (Propane, 0.9 Torr)

### 4.2.2 Focusing field

As we have shown in the previous chapter, the sensitive volume shape can be tuned by an adjustment of the potential on the electrodes below the ion extraction aperture. By changing the focusing field, $E_2$, the sensitive volume diameter is varied. Figure 4.10 shows the **measured** ion cluster size distributions induced by 4.3 MeV alpha particles in the two sensitive volumes of figure 3.16. These two measurements differ only in the value of $E_2$. They demonstrate the flexibility of our ion counting nanodosimeter, which permits an easy adjustment of the SV dimensions

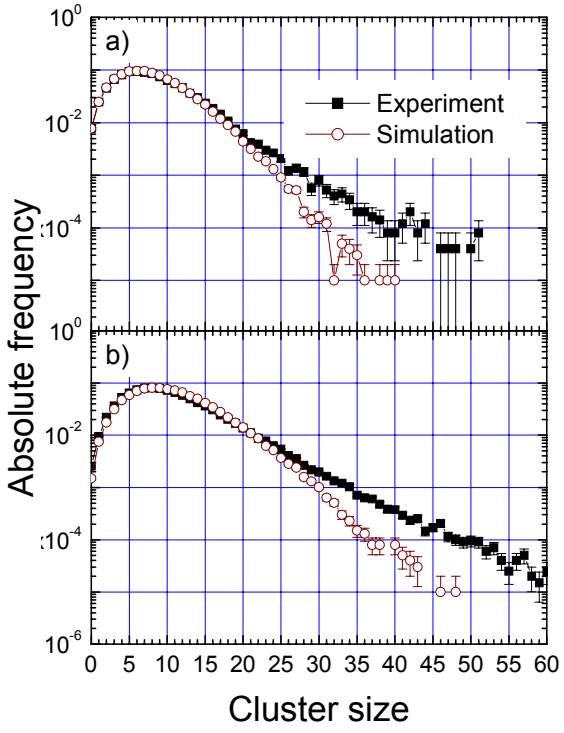


**Figure 4.10 : Experimental (full symbols) and model simulated (empty symbols) cluster size distributions** induced by 4.25 MeV alpha particles in the two respective (a, b) sensitive volumes depicted in figure **3.16** . (Propane, 0.9 Torr). The average cluster sizes are 8.3 (a) and 10.5 (b) ions.

### 4.2.3 Ion drift velocity

Using the movable collimator, on the Pelletron setup, it is rather simple to measure the ion drift velocity in our conditions. Figure 4.11 shows the measured ion arrival time, in pulsed and DC mode, when the beam was scanned along the SV. In both cases the ion drift velocity is 0.43±0.01 mm/μsec, which is equivalent to 1.2 nm/μsec in the tissue scale. This is in rather good agreement with the value in [98] (0.4 mm/μsec).

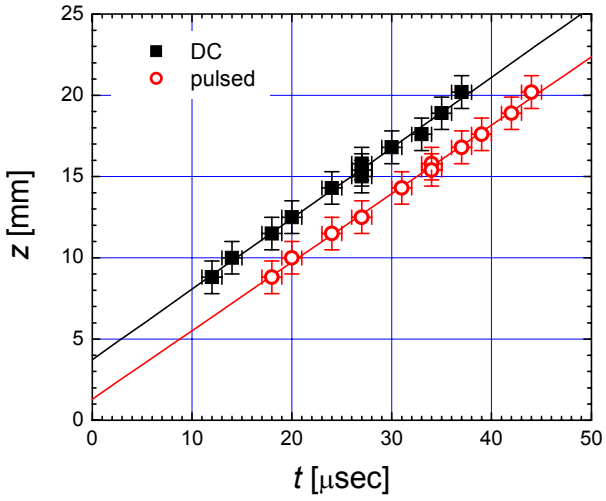


**Figure 4.11: The average ion arrival time t, as a function of the beam axis altitude *x*.** For both pulsed and DC mode, the obtained drift velocity is the slope of the linear fit: $v$=0.43±0.01 mm/μsec.

### 4.2.4 Time cuts along the sensitive volume

Applying time cuts along the SV permits correlating the frequency of ionization clusters of given size with the distance from the beam axis; thus providing information about beam ionization profile. Two examples are shown in figure 4.12.

Figure 4.12a shows the cluster size distribution within a 4.5 nm diameter and 5 nm long sensitive volume selected at different distances from the beam axis: centered on the beam axis and displaced towards the aperture plane by 6 nm and 12 nm, respectively. This type of analysis may be useful in investigating the track structure. The 1 mm diameter 13.6 MeV proton beam passes 15 mm (~ 42 nm) above the aperture.

Figure 4.12b provides the cluster size distributions in a series of slices, selected from the sensitive volume shown in figure 3.16b. The slices, of about 5 nm diameter extend 2.5, 5, 12 and 24 nm on both sides of the beam axis.

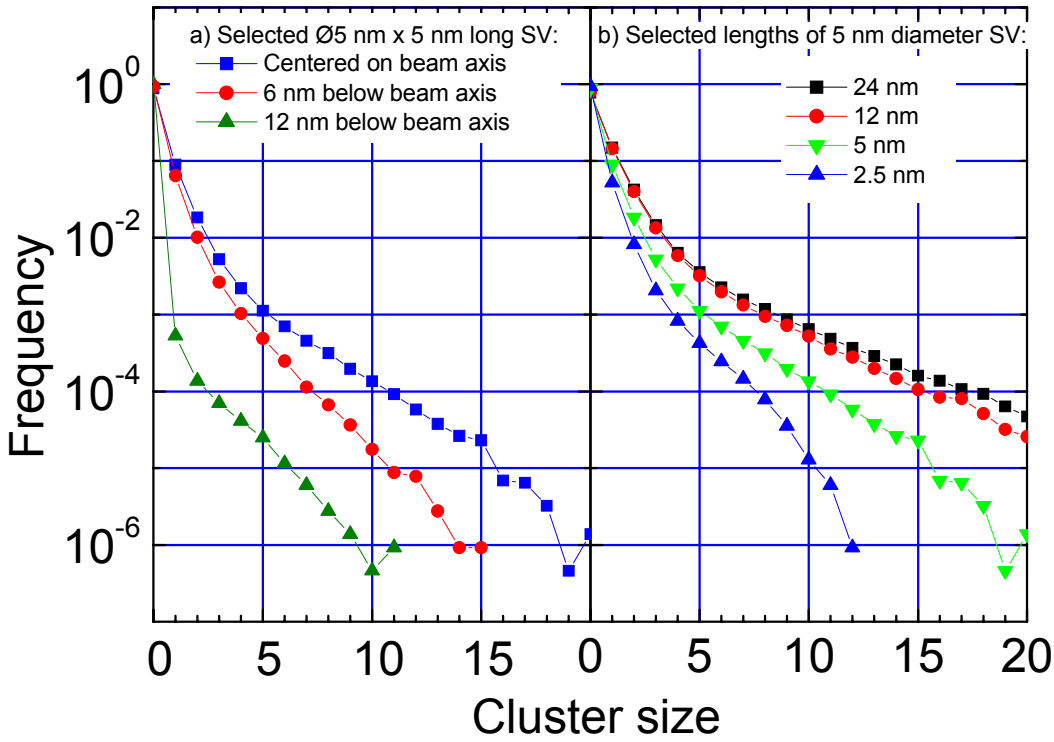


**Figure 4.12 : Experimental results of ionization cluster-size distributions,** induced in slices of the sensitive volume shown in figure **3.16**b, selecting various ion arrival-time windows. a) A 5 nm long SV, centered on the beam axis and displaced towards the aperture plane by 6 nm and 12 nm. b) Centered on the beam axis and extending by 2.5, 5, 12 and 24 nm on both sides (corresponding to the sensitive volumes in figure 3.19b-e.

## *4.3 Accelerator-related studies*

### 4.3.1 Beam flux

The main concern when operating the ND in an accelerator environment is the high flux of particles traversing the IV. Operating the ND at a high particle repetition rate (compared to the ND "dead time" of ~100 μsec - see §3.1.5) may result in an occasional overlap of ion clusters deposited by more than one projectile; this will be registered as a single cluster with a large number of ions (denoted cluster pileup – CPU). As a result we will have an artificial increase of the average cluster size (linear in beam flux),as shown in figure 4.13; the figure compares the measured average cluster sizes at different beam fluxes using "efficient" and

"inefficient" triggering (the latter resulting in inefficient CPU rejection). The CPU will also affect the ion arrival time distribution; it will result in a constant background of ions, originating from non-triggering projectiles (which are naturally not correlated with the trigger). This effect is clearly seen in figure B.4 (appendix B).

In order to quantify the effects of inefficient CPU rejection, we have performed MC simulations of the DAQ system, detailed in appendix B. The conclusion of these studies is that for an 80% efficient trigger, the current beam geometry and a beam flux of up to 1.5 kHz there is **no noticeable distortion** of the measured cluster size distribution, by CPU events. The beam flux in all experiments was set based on this criterion.

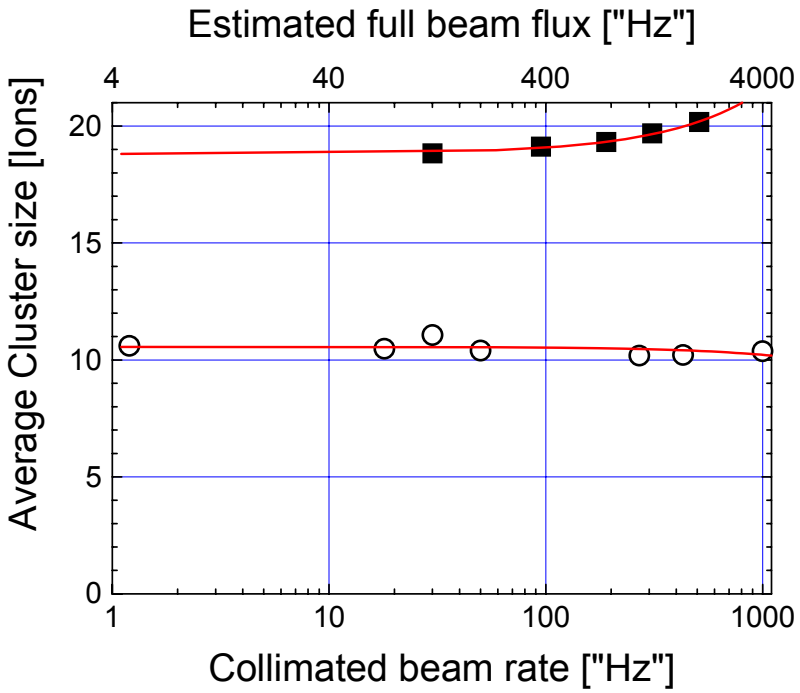


**Figure 4.13: Beam flux dependence of the measured average cluster size.** The solid symbols provide the flux dependence of the measured average cluster size of 24.8 MeV carbon nuclei, when the ND is triggered only on the collimated PMT (see figure 3.11). The open symbols provide the beam flux dependence of the average cluster size of 62.8 MeV carbon nuclei, when the ND is triggered on the MWPC and the collimated events are selected after pileup rejection (using the PMT signal as a flag – see §3.1.5. The lines are linear fits: In the first case there is an obvious linear increase of the measured cluster size with beam flux. In the second case the linear fit is almost flat (slope=-3 ±3 $10^{-4}$ $Hz^{-1}$).

### 4.3.2 Alignment

As the sensitive volume is rather small, of about 2 mm diameter in gas, and there is a strong variation in the ion collection efficiency across it, the beam alignment and shaping in a narrow-beam irradiation mode, is of crucial importance. Figure 4.14 illustrates this point, showing the effect of alignment on the **simulated** alpha-induced cluster size distributions. The mean cluster size drops by 40% when the beam shifts from the center of the SV by 0.6 mm. This type of behavior was also seen in early experiments, where the beam alignment was not well controlled.

In order to overcome this problem we have optically aligned all collimators and the ND sensitive volume axis to a precision of better than 0.2 mm. We have seen that once such an alignment was maintained, the measured cluster size distributions became reproducible, see for example figure 4.2.

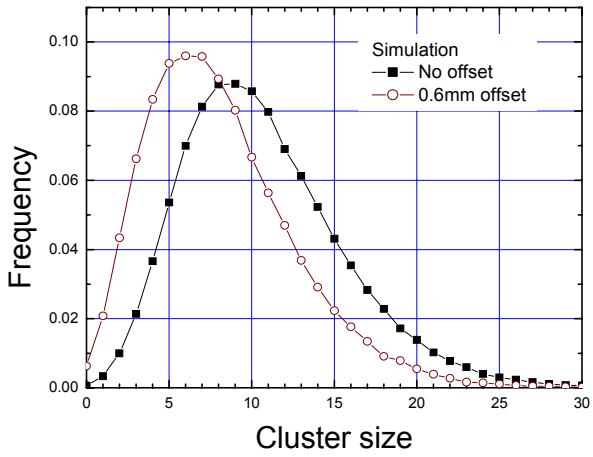


**Figure 4.14: Simulated alpha-particle induced cluster size distributions** with the beam either centred on the sensitive volume or displaced by 0.6 mm. (Propane 1 Torr)

### 4.3.3 Energy spread

During the alpha-particle measurements we have seen that the ND is sensitive to variations in the energy of the projectile particle: two $^{241}$Am sources, differing in energy by about 10% (probably due to a different thickness protective coating), yielded noticeably different cluster size distributions. It was therefore important to test if the cluster size distributions are sensitive to the **spread** in accelerator beam energy or to beam contaminations. To this end we modified the electronics scheme of figure 3.14. We removed the MWPC and replaced the collimated scintillation detector with a silicon surface barrier diode. The signal from the diode was split in to two signals, the first connected to the trigger data stream and the second, through a single channel analyzer (SCA) to the flag data stream. This enabled measuring the cluster size distribution due an energy-selected proton beam (This experiment was only performed with 7 MeV protons; the diode used was too thin for stopping higher energy protons). Figure 4.15 shows the full energy distribution of the beam as well as two examples of energy-selected beams, along with the obtained cluster size distributions. As can be clearly seen, the small amount of beam "contamination" (seen as a low energy tail in figure 4.15a) does not significantly affect the cluster size distribution. Furthermore, the cluster size distribution is not sensitive to the energy broadening in the beam. This is natural as the variation of specific ionization with energy is rather slow.

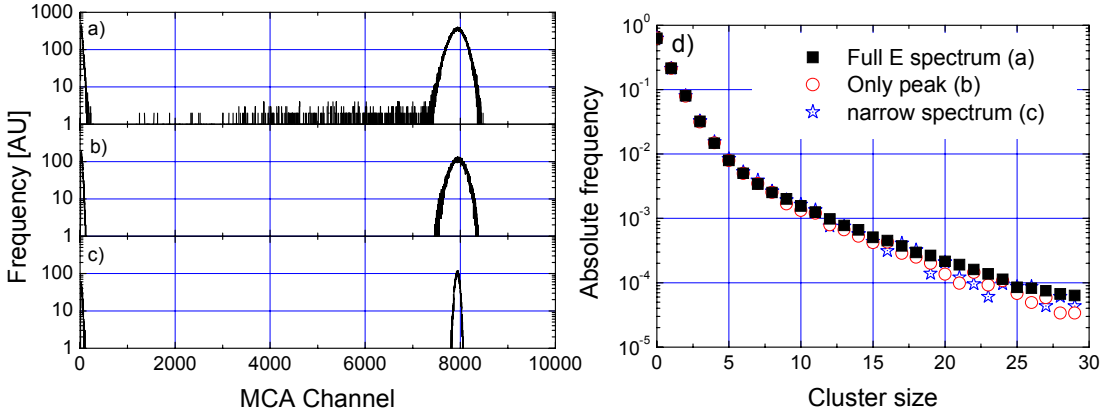


**Figure 4.15: The energy distribution of a 7.15 MeV protons beam**. a) The full beam having about 190 keV FWHM and a low energy tail , b) energy-selected beams without the tail, c) energy-selected beam with about 50 keV FWHM. d) The resulting cluster size distributions are practically identical.

## 4.4 Ion cluster distributions induced by pencil beams

The parameters of the various particle beams tested, spanning a large range of LET values, are shown in table I. Beam energies at the target as well as the straggling were calculated using the SRIM 2000 [90] software package, based on the known beamline geometry and the accelerator operating voltage. At all projectile energies, correspond to fully stripped ions, except for 24.8 MeV carbon ions which consists of 62% $C^{6+}$, 34% $C^{5+}$ and 2% $C^{4+}$ (an effective charge state of 5.7).

**Table I: Parameters and results of the narrow beam measurements. Average cluster sizes refer to the sensitive volume shown in figure** 3.17**b. (*SS=stainless steel)**

| Projectile Energy | | Scattering | LET in | Average cluster size | |
|---|---|---|---|---|---|
| Before foil [MeV] | After foil [MeV] | foil | water [keV/μm] | Measured [ions] | Simulated [ions] |
| 1. Protons | | | | | |
| 22 | 19.3±0.1 | 100 μm SS* | 2.3 | 0.29 | 0.26 |
| 17 | 13.6±0.1 | 50.8 μm SS* | 3.6 | 0.38 | 0.36 |
| 12 | 7.15±0.23 | 50.8 μm SS* | 6 | 0.63 | 0.62 |
| 2. Alpha aprticles | | | | | |
| | 4.25±0.27 | | 107 | 10.5 | 10.6 |
| 3. Carbon nuclei | | | | | |
| 72 | 62.8±0.1 | 25 μm mylar | 270 | 21.06 | 26.91 |
| 60 | 49.2±0.1 | 25 μm mylar | 320 | 23.99 | 33.69 |
| 40 | 24.8±0.2 | 25 μm mylar | 500 | 27.76 | 51.13 |

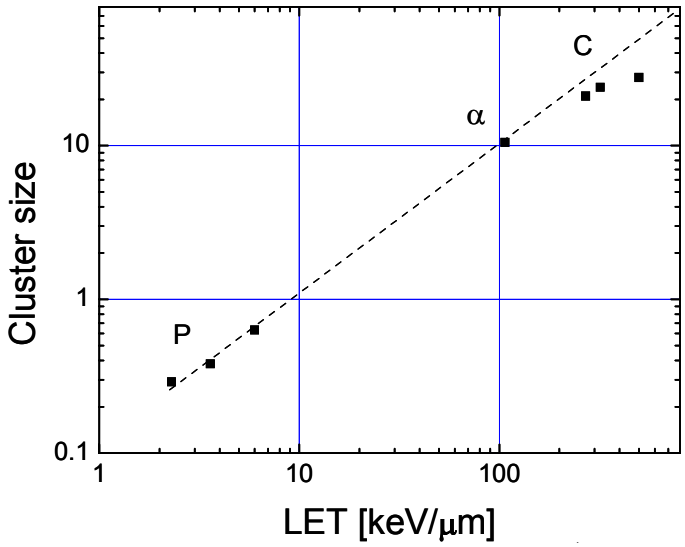


**Figure 4.16: Dependence of the measured average cluster size on the LET** (in water). Data is shown for different particles and energies in the sensitive volume in figure 3.16b. The dashed line is given to guide the eye. The deviation from linearity at large LET values is due to the DAQ dead-time as described in §4.1.2.

### 4.4.1 Proton results

Protons of 7-20 MeV have LET values in water between 2.7 and 6 keV/μm. At these relatively low LET values, large ion clusters are rare and 50-90% of the projectiles generate no ions within the sensitive volume (even though the projectile passes through its center). As

expected, the average cluster size rises linearly with LET (see figure 4.16), by approximately one ion for every 10.5 keV/μm (corresponding to a $w_i$ value of 24 eV, consistent with the ICRU recommended value of 26.2 eV [99]), up to LET values of ~100 keV/μm; then ion undercounting begins to distort the measurements. The **measured** and **MC-calculated** cluster-size distributions for protons of various energies are compared in figure **4.17**a-c. There is a very good correspondence between the measurements and simulations, down to frequencies of 1 $10^{-3}$ (~10 ions per cluster).

At lower frequencies, we have an excess of measured ions with respect to the simulation. This excess, resulting in an excess of $10^{-3}$-$10^{-4}$ in large cluster yields, is apparently due to secondary processes occurring in the volume immediately below the ion extraction aperture (as discussed in §4.1.4).

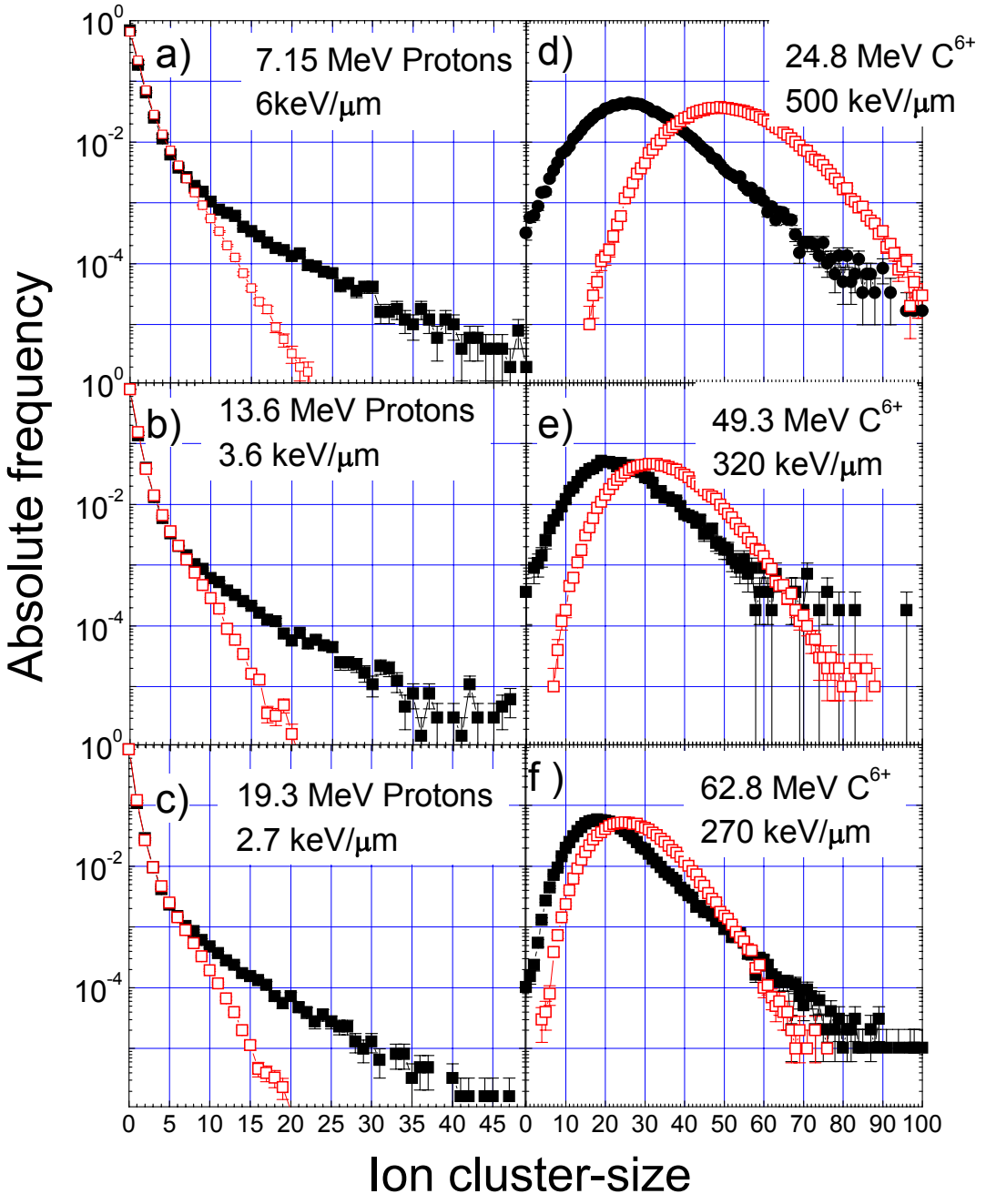


**Figure 4.17: Experimental (full symbols) and simulated (open symbols) ionization cluster-size distributions** for protons and carbon ions of different energies. Propane 0.9 Torr; the sensitive volume map is shown in figure 3.16b; in all cases the beam diameter is 1 mm.

### 4.4.2 High LET projectiles

Cluster size distributions induced by alpha particles and carbon nuclei were measured in the LET range of 100 to >500 keV/μm (in water) (see figures 4.10 and 4.17d-f). At this LET range, the measured average cluster size is between 10 and 30 ions and undercounting of ions (described in §4.1.2) becomes evident. Consequently, the correspondence between the measurements and the simulations deteriorates with rising LET. In the alpha-particle data (figures 4.5a and 4.10) the undercounting only leads to a small shift in the peak of the distribution of about 10%, whereas in the carbon data (figures 4.5b and 4.17d-f) it is clearly manifested as a large shift of the whole distribution.

As with the proton data, here too there is an excess of large clusters compared to that expected from the MC. This is clearly seen as an excess of clusters larger than ~20 ions in the alpha particle data (figure 4.10). In the carbon data (figure 4.17d-f), the excess is seen as a change in the falling slope of the cluster size distribution, as compared to that of the MC simulation.

## *4.5 Conclusions*

The presented data demonstrate the strength and the limitations of the ion-counting nanodosimeter. The nanodosimeter provides a **tunable, wall-less** sensitive volume, where SV tuning can be performed either by an adjustment of the applied voltages or by an off line analysis of the data collected in a larger sensitive volume. Ions, formed in the SV are efficiently extracted and counted; this is assured by the efficient ion transport to the ion counter and by the IC's excellent single-ion counting efficiency. The ND can reliably record ion cluster sizes up to about 20 ions/cluster. We have however seen that secondary effects in the ND limit it to detecting rare, large, ion clusters only at frequencies above $10^{-3}$.

Although the ND is rather sensitive to variations in its operating voltages, we have developed procedures for ensuring optimal operating conditions. The ion-counting nanodosimeter can therefore operate **reliably** and **reproducibly** at moderate particle repetition rates (up to 10 kHz – with a fully efficient trigger).

The good agreement between the measured ion cluster size distributions and the simulated ones indicates our full understanding of both the ND operation and the physics of ion deposition in gas. In the next chapter we describe precise measurements of ionization cluster size distributions in conditions relevant to the understanding of radiation damage to DNA.

# Chapter 5 :

# Measurements with biologically relevant beams

While the ND characterization was performed with well-defined pencil beams, nanodosimetric experiments, relevant to radiation biology, require use of broad, spatially uniform radiation fields. This is indeed the situation when irradiating tissue, where the relevant target size is a DNA segment of a few tens of $nm^3$, randomly located within a few-$\mu m^3$ nucleus. Naturally, there is no spatial correlation between the radiation track and the target. Therefore in order to correlate between biological and physical experiments, we have to use sufficiently broad beams.

## *5.1 The required beam dimensions*

The logical criterion for a "sufficiently" broad beam is the following:

*The beam should be broad enough so that any further increase in the beam diameter would not result in a difference in the ionization cluster spectra.*

To fulfill this criterion the beam diameter should be larger than that of the SV by the maximal range of δ-electrons, the track ends of which induce dense ionization clusters. From figure 2.1 this range is seen to be up to a few μm in water (which corresponds to many meters in gas in the lab frame. Due to the limited size of the vacuum chamber it is not feasible to use a beam larger than a few centimeters, centered on the SV, while avoiding beam impact on walls and electrodes and maintaining high ion extraction efficiency. Luckily, the delta electron's range distribution is steeply dropping and only a very small fraction of the δ-electrons actually attain the highest range.

In order to evaluate the effect of long-range delta electrons we have used our Montè-Carlo simulation code for recording the distance of ion formation from the projectile track (see example in figure 5.1). From these simulations we see that for 20 MeV protons and similarly 26 MeV helium nuclei (not shown), ~93% of the ions are formed within a 10 mm distance from the projectile's track. This implies that a beam of about 20 mm diameter could be adequately used as a broad beam. For 1 MeV protons, an even narrower beam would be sufficient as 97% of the ionizations are formed within 10 mm of the track axis.

The fact that the maximal kinematically allowed range of δ-electrons is much larger than this beam diameter does not change significantly our cluster size distribution, neither in simulations nor in measurements, due to the very low probability to attain this maximum. We have therefore selected to work with a **20 mm diameter** beam. In our experiments, described below, we have verified that this beam diameter is adequate; indeed, even narrower, 7 mm diameter, beams (roughly twice the SV diameter) yielded *"similar ionization cluster size distributions"* to those of the 20 mm diameter beams in both experiments and simulations (see §5.3.2 below and table II).

Some care has to be taken when defining "*similar ionization cluster size distributions"*. It is expected that, above a certain beam diameter, the relative yield of "zero-ion" clusters will increase linearly with the beam area (quadratically with the diameter). This is simply due to ions passing **far** from the SV and not depositing any ions in it. This type of "difference in effect" is not physically meaningful and should be ignored.

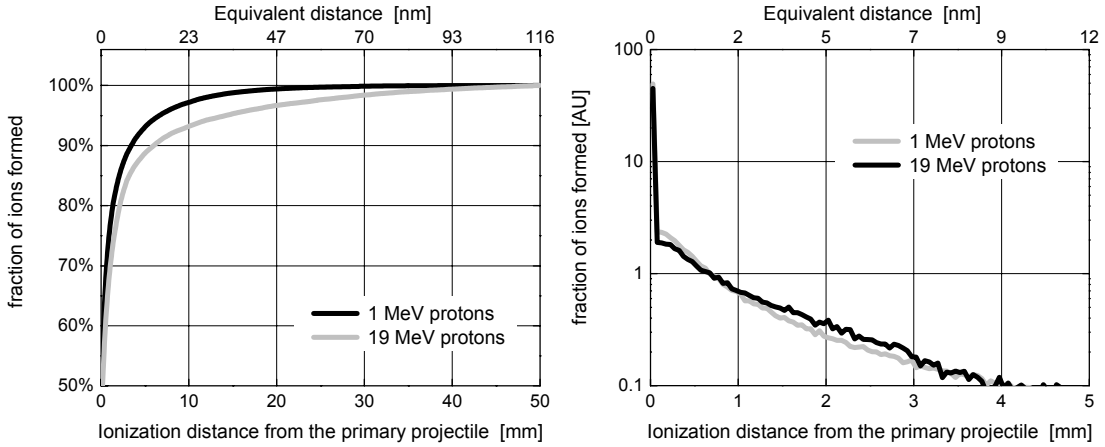


**Figure 5.1: Simulated beam profile** of 1 and 19 MeV protons (the data for 26 MeV helium nuclei nearly overlaps that of the 19 MeV protons and is not shown for clarity).
a) The cumulative fraction of the ions as a function of the distance from the proton track. b) The differential fraction of ions induced as a function of the distance from the track. Note that the low-energy protons have smaller δ-electron range compared to the high-energy ones.

In order to physically characterize a broad beam radiation field, independent of its diameter, we must look at the ionization cluster size distributions normalized **without the zero-ion clusters** (the so-called "*conditional distributions"* described in [63] – see §2.3). It should be stressed that the use of such distributions results in the loss of important information, related to primary particle passing through the SV without interaction. However, for the characterization of our nanodosimetric method and for comparison with other microdosimetric techniques and with biology (also not sensitive to "zero-dose" events) the use of a ***conditional cluster size distribution*** is sufficient.

It should be further stressed that the broad-beam geometry we are using is still different from that experienced by an irradiated DNA molecule: in biological matter, DNA has no preferred orientation, while in our experiments the beam is always perpendicular to the SV (±3°). This effect is only important when looking at primary ionizations, which comprise ~50% of the deposited ionizations; the δ-electrons have no preferred orientation in the plane perpendicular to the beam and therefore no preferred orientation with respect to the SV axis which lies in this plane . The energy deposited in the sensitive volume (due to primary ionizations in a single track) is proportional to the track length. The difference between an isotropic irradiation and the one in our ND is seen in figure 5.2. The magnitude of the resulting distortion in the ionization cluster size spectra can be estimated by comparing the average length of track segments within the SV irradiated isotropically and by a parallel infinite beam. The first case corresponds to calculating the average chord length of a cylinder, while the second corresponds to calculating the same average chord length but in only two dimensions.

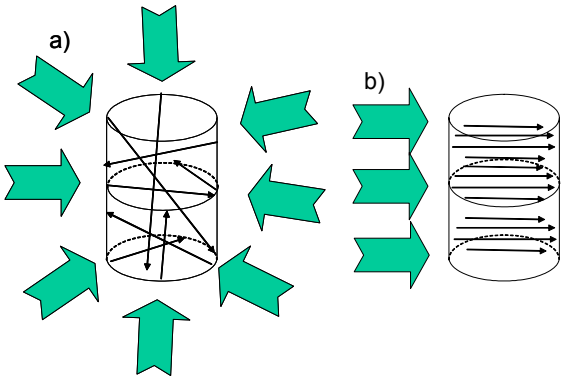


**Figure 5.2: A schematic comparison of possible ion tracks** in (a) an isotropic irradiation field and (b) the one in our ND: In the ND the beam is perpendicular to the SV axis. In both cases, the arrows denote possible radiation tracks traversing the SV.

Assuming that the SV is a right cylinder (of diameter *D* and height *2D*) we get, according to [100], an average chord length of $\tilde{L}_{SV}=0.8D$ for the SV irradiated isotropically and $\tilde{L}_{2D}=\pi/4D=0.785D$ for the SV irradiated by a parallel beam. Since the number of primary ionizations (induced by a single particle along a track segment) is Poisson distributed with an average proportional to the track segment length, the two irradiation modes (isotropic and parallel) should yield (at least on average) the same primary-ionization cluster size distribution.

## 5.2 Broad-beam setup

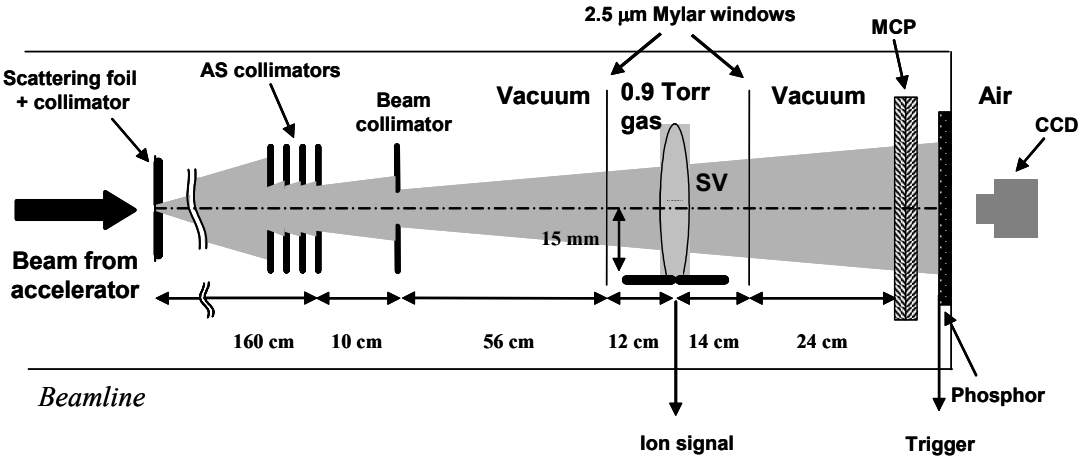


**Figure 5.3: The accelerator beam line setup used for broad beam measurements** at the WIS Pelletron accelerator. The distances between the scattering foil and the anti-scattering (AS) rings are somewhat different in the Van de Graaff setup.

The beam line setup used for broad-beam irradiation of the nanodosimeter, at the WIS Pelletron and Van de Graaff accelerators, is shown in figure 5.3. As for the pencil beam, the accelerator beam is spread by a scattering foil and then defined with a collimator. The beam collimator, however, has a larger diameter of 5 or 15 mm. As we no longer confine the beam to one mm diameter, we have added several 20 mm diameter anti-scattering (AS) apertures within the beam line to prevent unwanted scattering from the beam pipe walls. The, previously employed, MWPC trigger detector was replaced with a vacuum operated double MCP (multi channel plate; Elmul model E033VP43) detector coupled to a phosphor screen and a CCD camera. The projectile particles impinging on the MCP surface (or the channel walls) create secondary electrons which are then multiplied inside channels. The large ($10^6$) electron cloud emerging from the other side of the channel is accelerated onto a phosphor screen forming a light spot which is imaged onto a CCD camera (see figure 5.4). The electron signal is also used as a trigger for the ND. The MCP provides higher detection efficiency and better uniformity. Fast pulses from the phosphor were used to trigger the ND while the 2D image, integrated over many events, was used for monitoring the beam geometry and uniformity. Here the exact beam geometry is less crucial, so there is no need for a secondary trigger (flag).

Due to gain inhomogeneities in the MCP, we could not use it directly as a measure of beam uniformity. Rather: the CCD camera was operated with short integration time such that each frame contains a few tens of particle-induced light spots (of varying size and intensity); each frame was analyzed separately, replacing each light spot with a "standard" one [101] and the frames were then integrated.

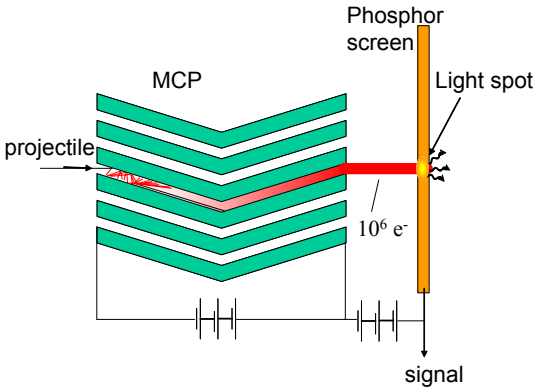


**Figure 5.4 : the operation of an MCP detector.**

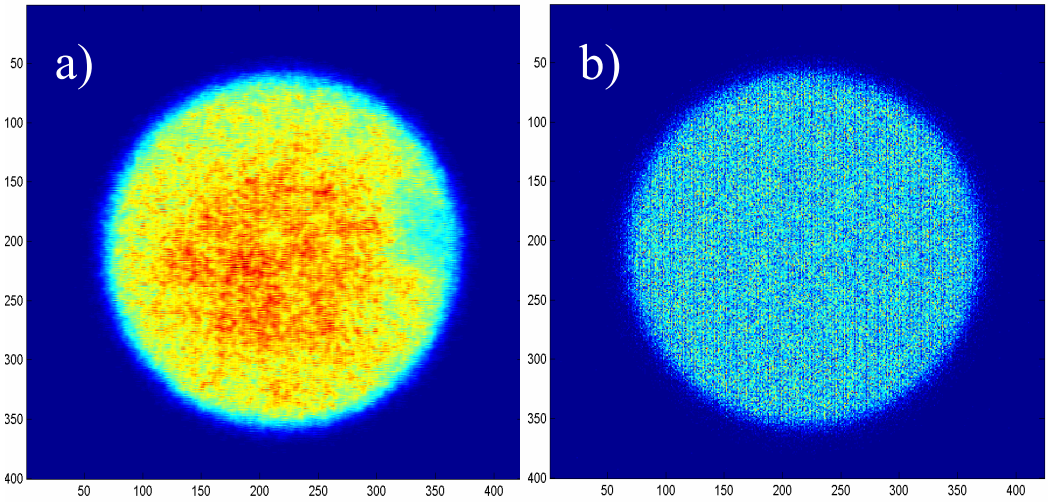


**Figure 5.5:a) Raw data from the phosphor screen**, integrated over $10^6$ projectiles (26 MeV helium nuclei). b) The same data set analyzed as described in the text, to eliminate the MCP inhomogeneity.

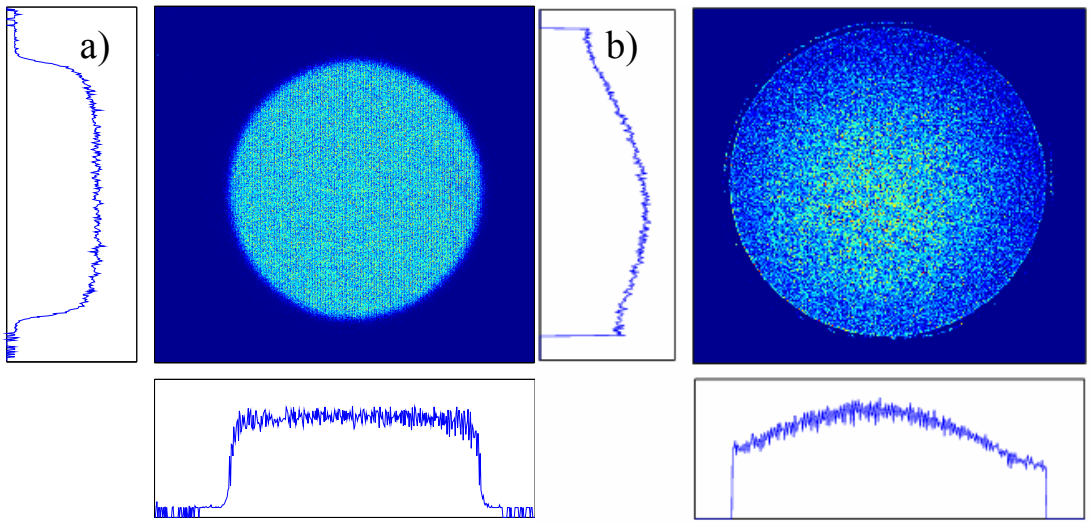


**Figure 5.6: The 2D images obtained from the MCP** detector for a (a)19.3 MeV proton beam and a (b) 1.03 MeV proton beam. Also shown are the beam profiles on both axes. For the 19.3 MeV protons there is <5% variation over the whole beam area (beam diameter 20 mm). For the 1.03 MeV protons the beam profile is a Gaussian with 24 mm FWHM.

The advantage of using such a technique is clear from figure 5.5. Figure 5.5a shows the integrated image (without the analysis) of a uniform helium nuclei beam (as verified using radiochromic film – Gafchromic, Nuclear Assoc., NY). Note the radially varying intensity, due to a nonuniform MCP gain and the region of lower intensity at the right hand side, due to a vacuum grease smudge on the outside of the vacuum window between the phosphor screen and the CCD camera. A more reliable measure of beam uniformity is seen in figure 5.5b, after the analysis.

The active diameter of the MCP (25 mm) was seen to be only slightly larger than the maximal diameter of the beam (23 mm at the MCP). Therefore, in order to maintain the trigger efficiency, care was taken to align the MCP to the beam axis, so that the entire beam is within its active area. The SV was optically aligned with respect to the beam axis as above (§4.3.2).

The Low LET data (250 MeV protons) were obtained at the proton synchrotron of the Loma Linda University Medical Center. A dataset was collected, with the nanodosimeter irradiated with a broad, non-uniform, beam of protons (5x1 cm). Using the tracking system, detailed elsewhere [86], precise beam geometry and beam energy could be selected on an event-by-event basis, offline.

## 5.3 Results and discussion

### 5.3.1 Beam quality

We have performed broad beam measurements using the beams detailed in table II, spanning an LET range of 0.4 to 25.5 keV/μm (in water). Measurements of 7-20 MeV protons and (fully stripped) helium nuclei, at the WIS Pelletron accelerator, as well as 250 MeV protons, at the LLU proton synchrotron, were done with sharply defined 7 mm diameter and 20 mm diameter beams.

For low-energy (1 MeV) proton measurements, performed at the WIS van de Graff accelerator, a considerable amount of scattering in the ND entrance window was observed; Figure 5.6 compares the beam spot on the MCP for 19.3 MeV and 1 MeV protons. As a result, the beam profile is Gaussian with FWHM values of 18 mm and 24 mm (at the SV). MC simulations (see 5.7) show that this beam inhomogeneity is manifested in the absolute cluster size distribution. However the conditional cluster size distributions are unaffected, implying that there is indeed no practical difference between an ideal beam and the one used.

On the other hand, for such a broadened beam there is a significant geometrical inefficiency of the MCP: As the MCP diameter is 25 mm, protons, which are scattered by the ND entrance and exit windows, may not be detected. Based on the beam geometry measurements, the fraction of non-triggering protons is 51% for the larger beam diameter. As we have measured at a low beam flux (~800 protons/sec), this is not expected to affect the results. Indeed, MC simulations of the DAQ system (figure B.5 in Appendix B), operated at low flux and low trigger efficiency, indicate that at this beam flux, there is no distortion in the cluster size distribution.

Initially we have assumed that as long as the beam diameter is “large enough”, the cluster size distribution should be independent of it. Based on simulations, we claimed that a 20 mm diameter beam is “large enough”. This hypothesis is tested in figure 5.8. In figure 5.8 a, we see a large discrepancy, comparing the cluster size distributions induced by a 20 mm diameter and by a 6.5 mm diameter beams. But the discrepancy is **only in the frequency of zero clusters**, namely it is only due to an excess of protons passing far from the sensitive volume; this alters the relative normalization of the two distributions as evidenced by the fact that they are parallel. If we normalize the cluster size distribution without the zeros (as suggested above, seen in figure 5.8 b) the cluster size distributions overlap perfectly. This is a clear

indication that our SV is irradiated with a uniform beam, which is broad enough to be considered "infinite". This was seen in **all** studied beams (protons of 1 to 250 MeV and 26 MeV helium nuclei – see figures 5.9 and 5.10), spanning 3 orders of magnitude in ionization density, and indicating that a beam diameter of 6.5 mm is also "sufficiently broad" for our studies.

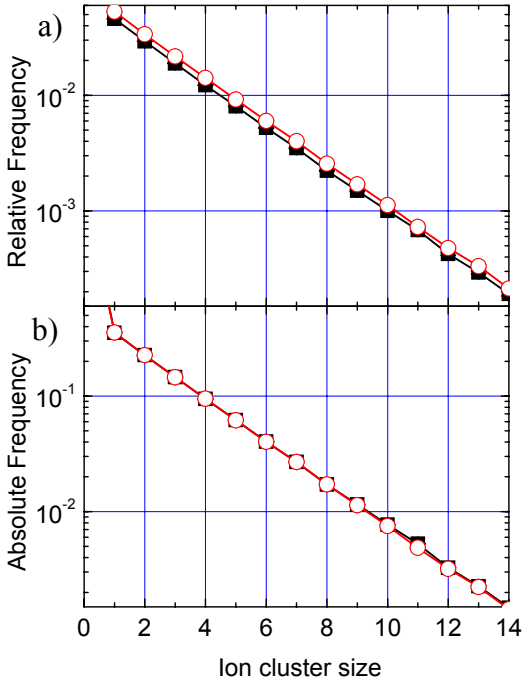


**Figure 5.7: Simulated ion cluster size distributions of 1 MeV protons** in the ideal case (20 mm diameter, monoenergetic and spatially uniform beam – open symbols) and the realistic one obtained in our experiments (full symbols). Both simulations were done using the sensitive volume of 3.17b. a) The absolute cluster size distribution and b) the conditional cluster size distribution (i.e. normalized without zero clusters). In b) the distributions are seen to coincide.

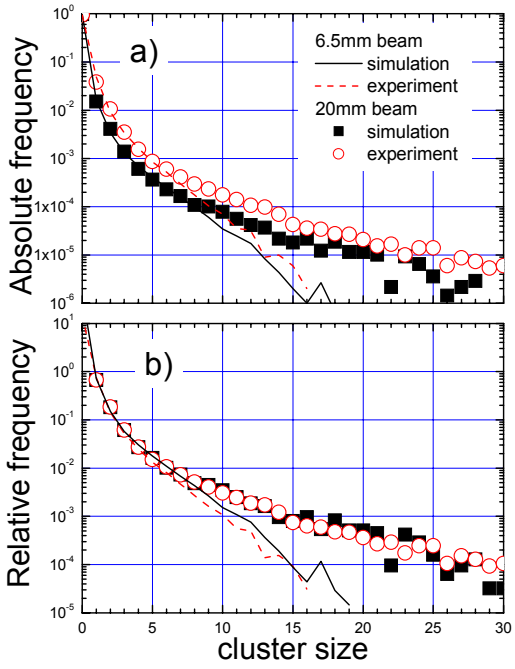


**Figure 5.8 : Cluster size distributions for 19.3 MeV protons** in the sensitive volume of figure 3.16b. A comparison of a 6.5 mm diameter beam and a 20 mm diameter beam with simulations (note the agreement between experiment and simulation).
a) Absolute cluster size distribution, b) conditional cluster size distribution

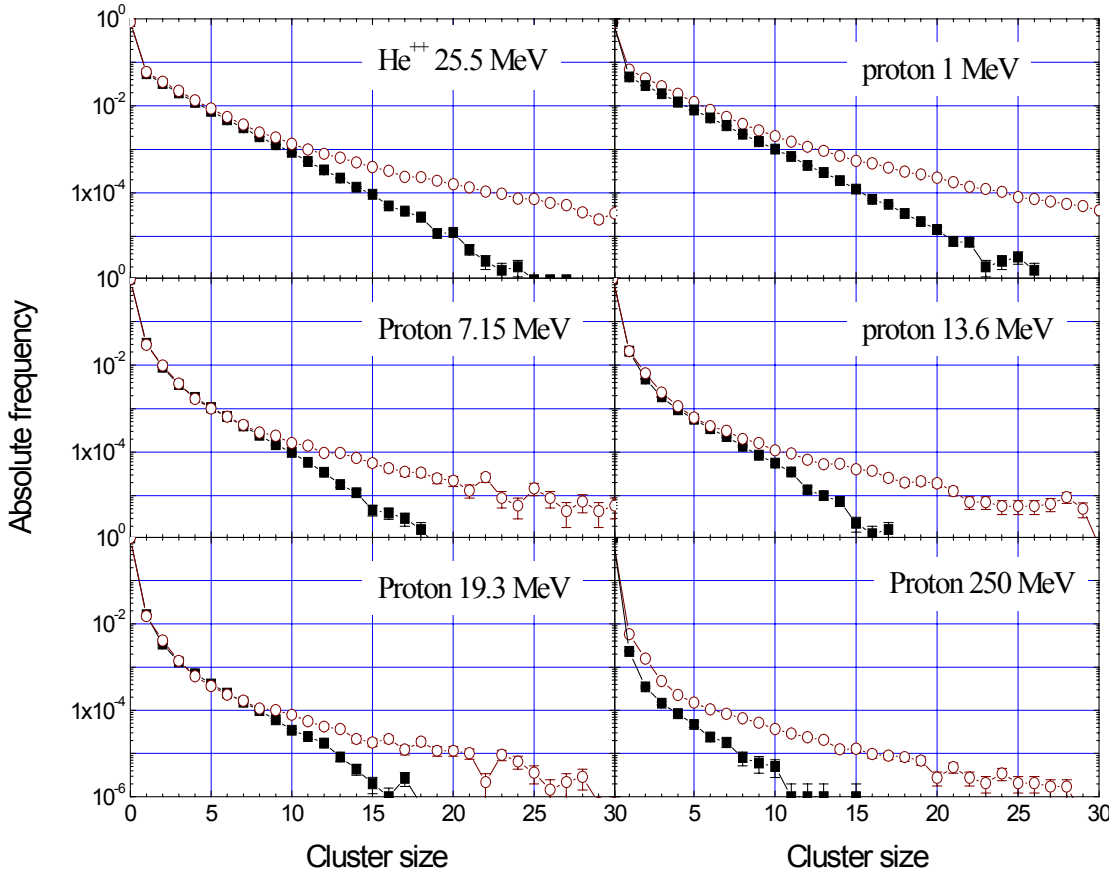


**Figure 5.9: Absolute cluster size distributions, taken under broad beam conditions,** ,induced by protons and helium nuclei of various energies in the sensitive volume of figure 3.17b. The frequency is relative to the number of projectiles (absolute cluster size distribution - see text). The open circles denote the measurements and the closed squares denote the MC simulations. In all cases the error bars are smaller than the symbols.

### 5.3.2 Cluster size distributions

In figure 5.9 we show the measured absolute cluster size distributions, in the sensitive volume of figure 3.17b, for all measured beams (see table II). As above, there is a rather good correspondence with the simulations for most data sets. The exceptions are the 1 MeV and 250 MeV protons where there is a large discrepancy between the measured and simulated cluster size distributions for all cluster sizes. For the first, the discrepancy probably arises from inappropriate description of the beam geometry, resulting in a small excess of zero clusters in the simulated dataset (and a change of the overall normalization, shifting the entire distribution upwards). For the 250 MeV protons, the discrepancy is probably due to inefficient triggering of the ND, resulting in an artificial formation of large clusters (see §4.3.1 and Appendix B).

When we compare the conditional cluster size distributions (figure 5.10), this discrepancy vanishes. However there remains in all data sets a consistent increase of 15% in the measured average cluster size with respect to the simulated one. This is due to the secondary effects in the low vacuum region of the ND (see §4.1.4). These rare large clusters are naturally more frequent in the conditional cluster size distributions, which contain only events with at least one ion.

| Projectile energy | | Average | | Average cluster size | | | | | |
|---|---|---|---|---|---|---|---|---|---|
| | | | | With zeros | | | Without zeros | | |
| Accelerator setting [MeV] | At SV [MeV] | LET (in water) [keV/µm] | Scattering foil | 7 mm | 20 mm | simulated | 7 mm | 20 mm | simulated |
| | | | | [ions] | | | | | |
| 1. Protons | | | | | | | | | |
| 250 | 248.5±0.5 | 0.4 | none | 0.0289 | 0.017 | 0.00449 | 1.8 | 1.96 | 1.495 |
| 22 | 19.3 ± 0.11 | 2.3 | 100µm SS* | 0.105 | 0.042 | 0.03692 | 1.84 | 1.85 | 1.621 |
| 17 | 13.6 ± 0.12 | 3.6 | 50.8µm SS | 0.148 | 0.066 | 0.04975 | 1.88 | 1.99 | 1.657 |
| 12 | 7.15 ± 0.23 | 6 | 50.8µm SS | 0.241 | 0.097 | 0.08548 | 1.99 | 2.02 | 1.756 |
| 1.2 | 1.03 ± 0.03 | 25.5 | 0.5 µm gold | 1.39 | 0.659 | 0.3722 | 3.42 | 3.3 | 2.869 |
| 2. Helium nuclei | | | | | | | | | |
| | 26 ± 0.1 | 25.5 | 50.8µm SS | 1.19 | 0.489 | 0.3693 | 3.13 | 3.07 | 2.641 |

**Table II: Broad beam parameters.** Average cluster size refers to the sensitive volume of 3.17b Simulated values correspond to a 20 mm diameter bream. The average cluster size "without zeros" was obtained from the *conditional distribution*. (*SS=stainless steel)

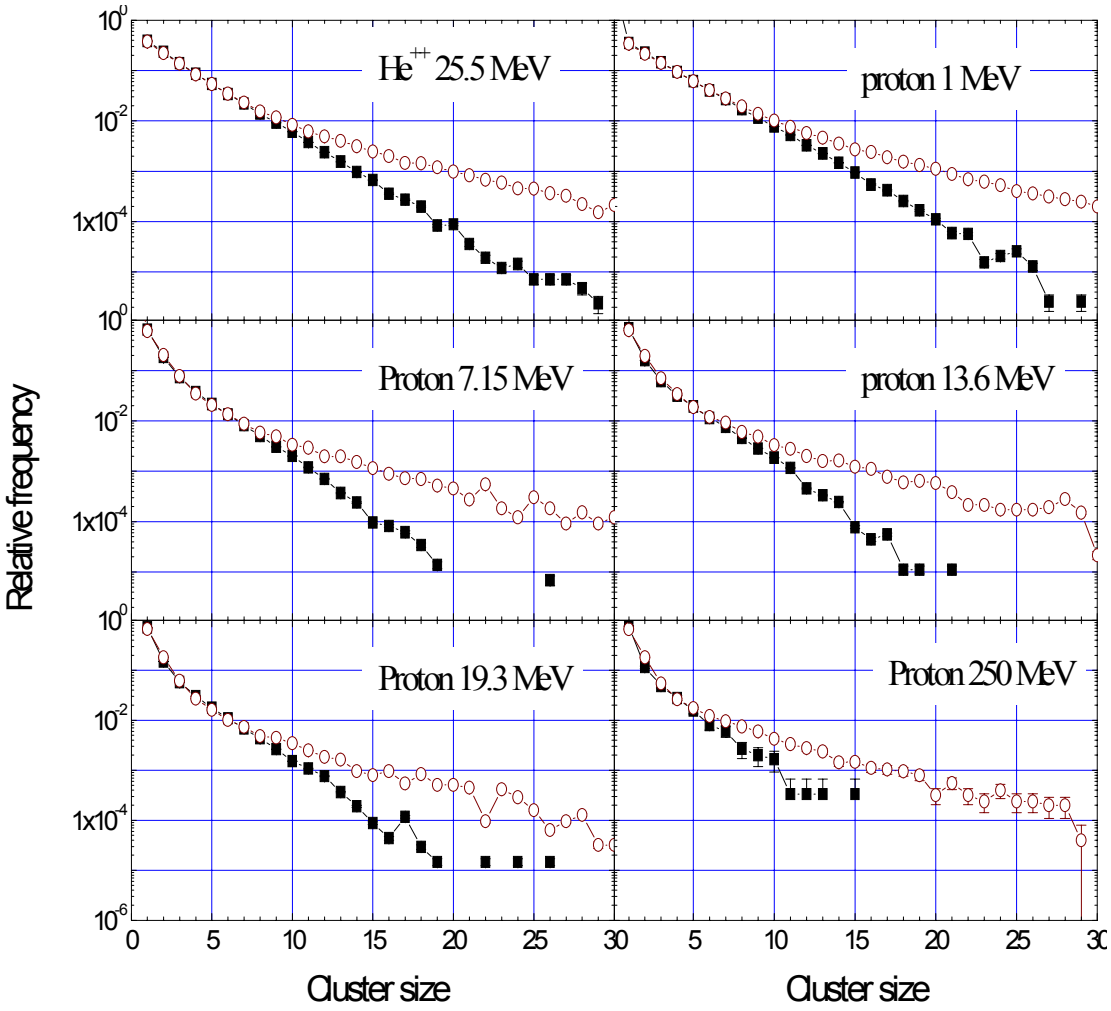


**Figure 5.10: Conditional cluster size distributions, taken under broad-beam conditions**, induced by protons and helium nuclei of various energies in the sensitive volume of figure 3.17b. The open circles denote the measurements and the closed squares denote the MC simulations. In all cases the error bars are smaller than the symbols.

### 5.3.3 Protons vs. helium nuclei

It is interesting to note the difference between the data for 1.03 MeV protons and 26 MeV helium nuclei (the two top panels in figure 5.10, overlaid in figure 5.11). These two radiation fields have the **same LET** (25.5 keV/μm), namely the same average energy deposition. However, we clearly see that the protons have higher probability to induce larger clusters, also in our simulations. We have found that this difference can be attributed to the smaller velocity of the protons, resulting in a shorter δ-electron range and therefore a more compact track structure (see also figures 2.1and 5.1).

Figure 5.11 demonstrates an important point studied within this thesis work: The ND focuses at measuring radiation effects on a nanometer scale. In the figure we see that two macroscopically-identical radiation fields (having the **same LET**) that differ in the δ-electron energy spectra, display **different** nanometric track structure. While this was known in the past, based on MC track structure codes, as well as on irradiation of various chemical and biological systems, this is the **first time** that this effect is measured **directly in a physical system**.

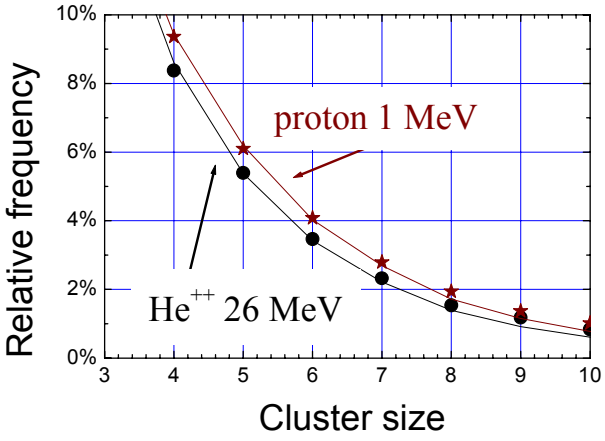


**Figure 5.11: Cluster size distributions induced by same LET protons and helium nuclei** in the sensitive volume depicted in 3.17b. The error bars (not shown) are smaller than the symbols. Note that the protons induce few-ion clusters with a higher probability than helium nuclei.

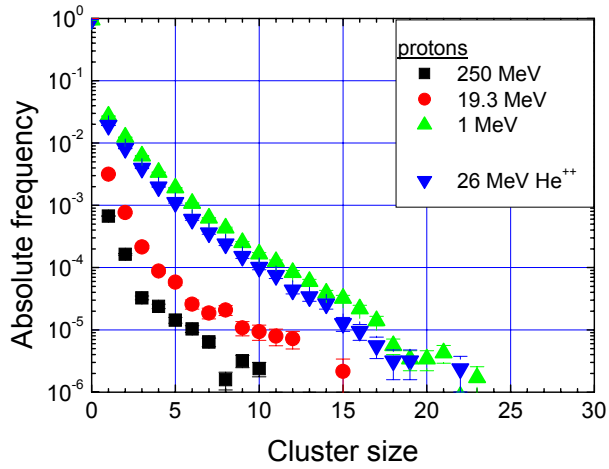


**Figure 5.12: Cluster size distributions in the SV of figure 3.19c,** based on a time cut analysis of the data of figure 5.9. For clarity, only the helium data and three proton energies are shown.

This effect is responsible, for example, for the results of [102-104]. In their work, Goodhead at al. exposed various types of cells to protons and helium nuclei having the same LET, and indeed observed that, in some cellular systems, the protons are twice as lethal. In §6 we will demonstrate the same trend in our irradiated DNA.

### 5.3.4 Measurements in a DNA-sized sensitive volume

As noted above, the SV with which we have measured the data of figure 5.10 is too large. The ideal SV for modeling DNA damage is a cylinder of 4.5 nm diameter and 8 nm length. Figure 5.12 shows the data of figure 5.9 reanalysed with a time cut corresponding to the sensitive volume of figure 3.19c. The significance of this sensitive volume is discussed in §3.4.3. These data will be used in the biophysical model of §7.

## *5.4 Conclusions*

After a thorough characterization of the ion-counting nanodosimeter, using well defined pencil beams, precise cluster size distributions could be measured in conditions relevant to radiation biology. We have exposed the ND to broad, homogenous particle beams (diameters of 6.5 and 20 mm). The ND sensitive volume in which the distributions were measured is larger than the ideal one (it is much longer). Using the ion time-of-flight we were able to select offline, a segment of this sensitive volume which **is** "DNA-sized".

These data are discussed in more detail in §8.1.2 and will be used in §7 as a comparison to radiobiological data presented in the next chapter.

# Chapter 6 :

# Radiobiological measurements

In parallel to the physical (nanodosimetric) measurements in a gas model of DNA, we have measured directly the radiation effects in a plasmid test system. These experiments are also described in [105].

## *6.1 The radiobiological test system*

The test system needs to be able to quantify the yield of clustered lesions in DNA in conditions mimicking the cellular environment.

Over the last three decades, simple experimental model systems of viral or plasmid DNA have been used to study the LET dependence of DNA lesions. These studies are typically performed at low scavenging concentrations to avoid the problem of large doses and long irradiation times needed at high scavenging conditions. However, these conditions are not necessarily representative for cellular ones. In our experiments we have performed DNA irradiations in both low and high scavenging conditions, the latter chosen as to be representative of the cellular environment.

In the irradiated DNA we have quantified the formation of strand breaks (by gel electrophoresis) and of clustered base lesions, by transforming them (within a bacterial host) to strand breaks.

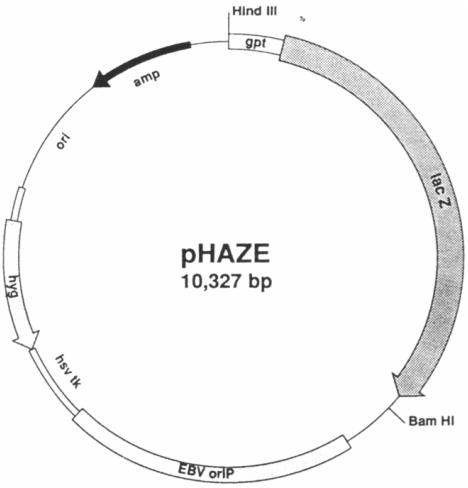


**Figure 6.1: The plasmid pHAZE**, contains a gene for antibiotics resistance (*amp*), and a bacterial origin of replication (*ori*). The other genes were not used in this work. Copied from [106]. © 1990 Elsevier.

### 6.1.1 The pHAZE plasmid

As a test system we used a thin film of the plasmid pHAZE [106] (10,327 base-pairs (bp), figure 6.1), containing a gene for antibiotics (*Ampicilin*) resistance, as well as several other genes required for its replication within *E. Coli* bacteria.

### 6.1.2 Irradiation conditions

As noted above (cf. §2.1.1), damage to DNA can occur through both direct ionization of the DNA molecule and through the mediation of $OH^{\bullet}$ radicals ("indirect effect"). In cells, the DNA is partially protected from radicals by scavenger molecules. It is, nevertheless, useful to study the damage yields under different scavenger concentrations. This may provide insight on the interplay between the direct and indirect effects in the cellular environment.

In our experiments, the plasmid was irradiated in a buffered (constant pH) aqueous solution, containing 2 mM or 200 mM of the radical scavenger glycerol, which modifies the radiation effect by scavenging the radicals formed by the radiation in water (see table III). We have chosen the radical scavenger glycerol because it does not form reactive species under irradiation [107].

| Glycerol concentration | Radical lifetime | Radical range | Contribution of radicals |
|---|---|---|---|
| [mM] | [nsec] | [nm] | |
| 2 | 260 | 77 | 99% |
| 200 | 2.6 | 7.7 | 65% |

**Table III: radical drift parameters.** The radical lifetimes were taken from [108]. The radical ranges were calculated using eq. 5 in [12]. The contribution of radicals corresponds to the ratio of SSBs induced by radicals to all SSBs formed, see text. The 200 mM glycerol concentration is equivalent to the scavenging capacity in a normal cell. The scavenging capacity of glycerol is $1.9\ 10^{9}\ M^{-1}\ sec^{-1}$.

In the high scavenging conditions (which mimic the cellular ones see §2.1.1), the contribution of the direct effect is about 35% of the total effect; in the low scavenging conditions it is approximately 1%. These value are obtained by comparing the SSB yield due to the direct effect ($2\ 10^{-10}\ Gy^{-1}\ Da^{-1}$ [109] with the values given for 2 or 200 mM glycerol see figure 5 of [110]). The concentration of 2 mM was chosen to provide a known, constant, amount of scavenger which would mask the random scavenging by contaminations in the irradiated buffer.

The use of a high scavenger concentration required irradiation of the plasmid samples to extremely high doses (At 200 mM glycerol, the typical dose required to form 1 DSB per plasmid is about 5000 Gy, roughly 100 particle traversals through the plasmid– see §6.4.2.3). In order to prevent oxygen depletion (J. Milligan private communication) from the sample (which will alter the yield of damages) we need to irradiate the sample at a very low dose rate (typically 10Gy/min) and to allow oxygen to enter the sample. On the other hand, due to the small sample size, great care has to be taken to prevent the sample from evaporating during the (several-hour long) irradiations. The sample holder described below (§6.2) was designed especially for this purpose.

At such high doses, there is a large probability for a single plasmid to be hit by many independent projectiles. In order to quantify the damage induced by a **single projectile**, we have compared the dose-dependence of the damage-yields (obtained by irradiating our samples at 10-20 different doses with the same radiation field) to a statistical model developed by R. Cowan [111], see appendix C.

### 6.1.3 Plasmid purification

In order to obtain meaningful data we must irradiate the plasmid in solution containing no proteins, no additional DNA or RNA and no scavenger molecules, other than the known concentration of glycerol. To this end we have purified the plasmid to a level beyond the

accepted standards of molecular biology. Any deviation from this DNA purification protocol was seen to result in irreproducibility of the measured data.

The plasmid was first amplified within *E. Coli* bacteria (for simplicity we used the same strain of bacteria as for the survival assay, see below), grown in 4 liters of medium containing 100 μg/ml of ampicilin (to eliminate foreign bacteria and bacteria which do not contain the plasmid from growing). Half way through the incubation, when the bacterial solution reached an $OD_{600}$ (optical density at 600 nm) value of 0.6, spectinomycin was added to stop the bacterial division. The plasmid however continues to be produced in the bacteria, resulting in a higher number of plasmids per bacterium. The plasmid was then purified from the bacteria using a plasmid purification kit (MegaPrep, Quiagen).

The resulting plasmid solution was run on an agarose gel, both in its natural state and after digestion with *Hind III* and *Bam HI* restriction enzymes. This serves as a consistency check. The full plasmid is 10,327 bp. After cleavage it should give bands of 3.8 and 6.5 kbp. The two bands can be easily identified on a gel, when compared to an appropriate DNA ladder.

The next purification step is a $CsCl_2$ density gradient. The DNA was added to a solution containing 100 g $CsCl_2$ in 100 ml TE (10 mM Tris-HCl, 1 mM EDTA, pH 8), containing also 10 ml from a 10 mg/ml ethidium bromide stock solution (a fluorescent marker for DNA). The solution is centrifuged for 72 Hours at 35 kRPM, in special test tubes. At the end of the centrifugation, two UV-fluorescent bands are seen in the tube. The lower band contains the plasmid DNA while the upper band contains the bacterial DNA. The lower band is recovered by piercing the side of the tube with a large bore syringe. The ethidium bromide is removed by adding the same volume of $CsCl_2$- or NaCl-saturated isopropanol (which is almost not soluble in water) shaking and removing of the upper, red, phase (isopropanol + ethidium bromide). This is repeated many times (until the solution is clear + twice more). In order to remove the isopropanol, the plasmid solution is dialyzed four times in excess of TE.

The final purification step is a gel filtration column using 750 ml *Sephacryl S-1000 Superfine* resin (Amersham-Pharmacia,) in TE/1 M NaCl buffer. The filtration column is 2.5 cm inner diameter, 1 m length. The fractions containing the plasmid DNA are identified by UV absorption (260 nm) and run on electrophoresis gel. The fractions containing at least 95% supercoiled DNA are pooled and stored at 4ºC.

To remove the excess NaCl, and replace the TE buffer with the phosphate buffer used in the irradiation, the plasmid was subjected to diafiltration with 10 mM phosphate buffer (pH 7) using a Centriplus-YM 100 ultrafiltration unit (Amicon, Millipore).

The typical amount of DNA recovered using this procedure is **1.5-2 mg per 4 liter of bacteria.** Each irradiated sample utilizes about 5μg of plasmid. In all of our experiments, we have used about 6 mg of plasmid DNA.

## 6.2 The irradiation setup

For plasmid irradiations using 1-20 MeV/AMU ions we have adopted the setup described in [112]. This setup was designed for irradiation of thin plasmid samples by light ions having well-defined energies. The use of thin samples is definitely required for the study of equal-LET protons and helium nuclei, but is less critical for the other measurements. The radiation fields (detailed in table IV in §6.4.2.1) were chosen as to span a large range of LET values (0.2 to 26 keV/μm). In comparing equal-LET protons and helium nuclei, we were limited by the maximum available acceleration voltage of the WIS Pelletron and Van de Graaff accelerators (12 MV and 2.5 MV respectively). Both accelerators were run close to their maximum stable voltage. The accelerator voltages were tuned (based on SRIM [90] simulations) to yield the same projectile energies (19.3 and 1.03 MeV for protons and 26 MeV for helium nuclei), at the center of the biological sample, as we had within the ND (see previous chapter and table IV in §6.4.2.1 below). Due to the rapid energy degradation of low-

energy ions (1 MeV protons in particular) in matter, it is important to irradiate very thin films of the DNA. This inevitably requires the beam to be broad and uniform.

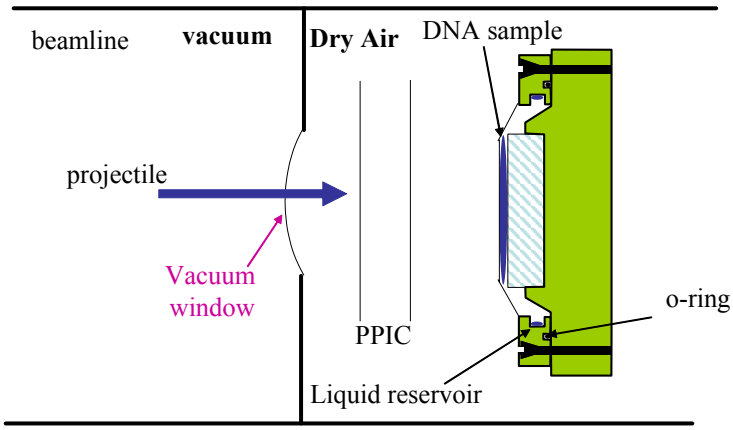


**Figure 6.2: DNA irradiation setup**. A particle beam exits the accelerator beamline via a thin Kapton window, passes through a parallel plate ionization counter (PPIC) and impinges on the DNA sample holder. See text for details.

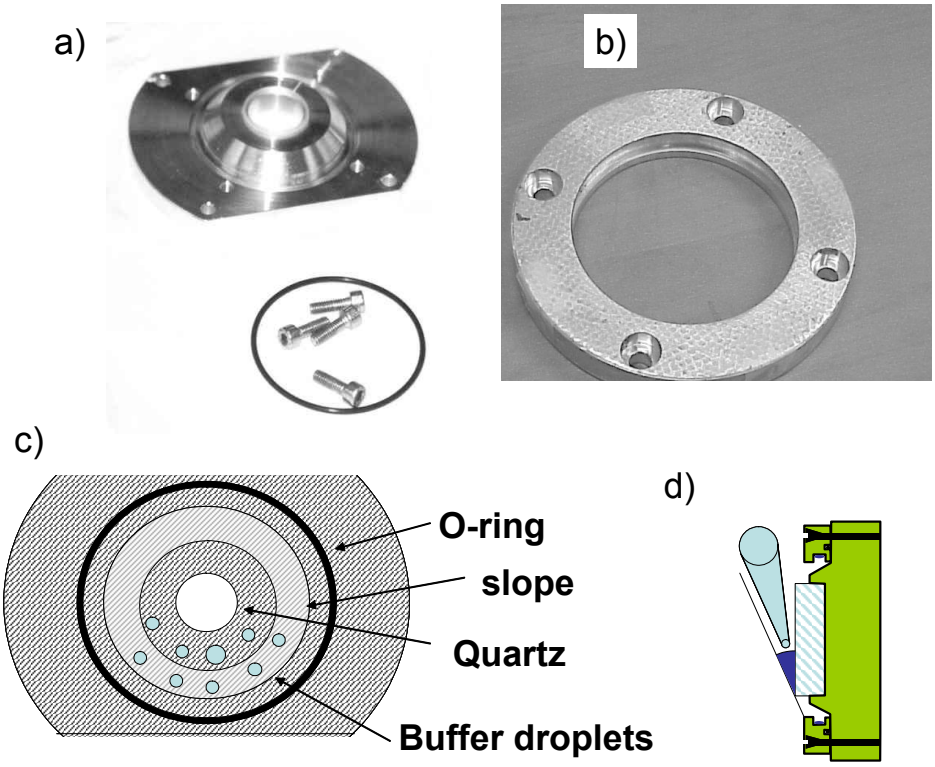


**Figure 6.3: a) A photo of the DNA sample holder.** b) The foil support ring. c) Front view of a) showing the buffer droplets (of varying size) added to prevent DNA drying. d) Side view of a) showing sample extraction after irradiation (The pipette tip and sample drop were exaggerated for clarity).

The irradiation setup is shown schematically in figure 6.2: The scattered beam exits the accelerator beam line into air via a thin 25 mm diameter window (Kapton 12.7 μm). It traverses a parallel plate ionization chamber (PPIC - used for dose-rate monitoring, see §5.4 of [113] and below) and hits the DNA sample.

The sample holder (on the right in figure 6.2, also shown in figure 6.3) consists of a 20 mm diameter quartz disk (smaller than the beam diameter) embedded in an aluminum frame. A 5 μl drop of DNA solution is placed on the disk and pressed down with a thin polymer foil (6μm Mylar or 12.7 μm Teflon). This results in the formation of a 16 μm thick, 20 mm diameter, film of the DNA solution. In our initial studies we have seen that the Mylar film is

permeable to water, resulting in a sample-drying time of a few hours. Several alternative films (Kapton, Saran and various thickness of Mylar) were tested before we found that a 12.7 μm thick Teflon foil is practically impermeable to water and enables >8 hour long irradiations. Further measures were taken to prevent sample evaporation: we have added about 80 μl of buffer to the "liquid reservoir" and onto the aluminum frame (around the quartz disk - see figure 6.3c), creating a humid atmosphere within the sample holder. The holder was also sealed with an o-ring and its edges were coated with Parafilm. After irradiation the film is cut along the edge of the holder (opposite from the droplet of irradiation buffer) and pealed off gently until it is just barely touching the edge of the quartz. The plasmid containing solution forms a droplet at the boundary between the quartz and the polymer film and can be collected.

For verification of the beam energy we have used a calibrated surface barrier detector, placed instead of the DNA sample, but covered by the same polymer foil. For verification of the beam uniformity we have used radiochromic film (Gafchromic™ MD-810, Nuclear Associates), see for example figure 6.4).

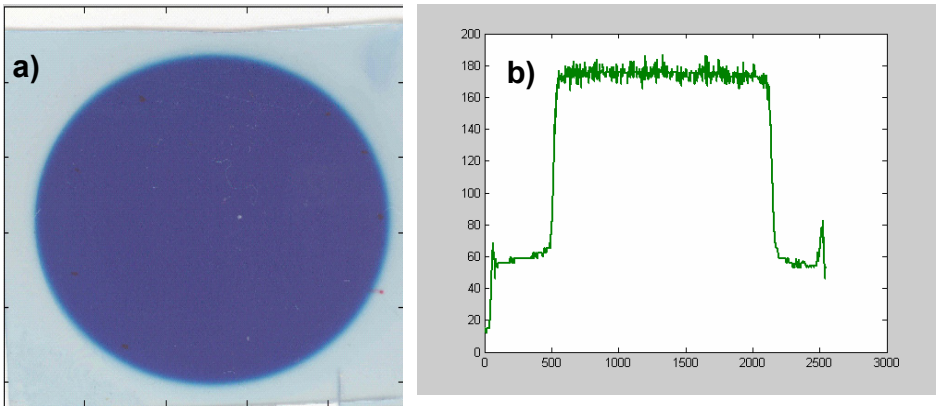


**Figure 6.4: a) A photo of a 19 MeV proton beam, taken using radiochromic film.** b) The digitized intensity along the vertical axis.

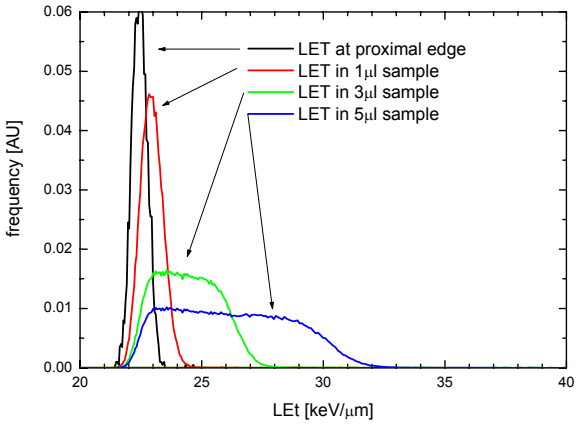


**Figure 6.5: Simulated LET distribution of (nominally) 1 MeV protons within samples of different thickness.** Note that the x-axis starts at 20 keV/μm. The energy at the proximal edge is the same in all cases.

In the low-energy proton irradiations we have seen that the energy degradation of the beam (within the 5μl – 16 μm thick sample) results in a large spread in LET (see figure 6.5). We have therefore used a 3μl sample (forming a 10 μm thick film) in these experiments. A smaller sample could not be handled accurately enough. In these conditions the LET variation across the sample is ~18% (FWHM). The LET variation in a 5 μl sample traversed by helium nuclei of the same LET (not shown) is <1%.

As a low LET reference, we have also performed plasmid DNA irradiations with γ-rays, using intense, calibrated, radioactive sources ($^{60}$Co, $^{137}$Cs). In this case, due to the long range of the γ-rays, we could irradiate a 5 μl drop of plasmid solution in a 0.5 ml Eppendorf tube. DNA irradiations using 250 MeV protons were also preformed in the same way (i.e. in tubes) at the Loma Linda proton synchrotron.

## 6.3 Analysis

### 6.3.1 Sample dosimetry

The dose in the biological sample was measured using the air gap ionization chamber (IC). This is a simple parallel plate ionization chamber (PPIC - 1 μm Aluminized Mylar electrodes, 1.6 mm gap) operated in collection mode (i.e. without gain). The ionization chamber operates under continuous flow of dry air, required for reduction of its leakage current. The PPIC current was seen to saturate at a voltage above 50 V, corresponding to full collection efficiency. We did not see any further variation in its current up to above 600 V (see figure 6.6). We have therefore operated it at a bias of 300 V.

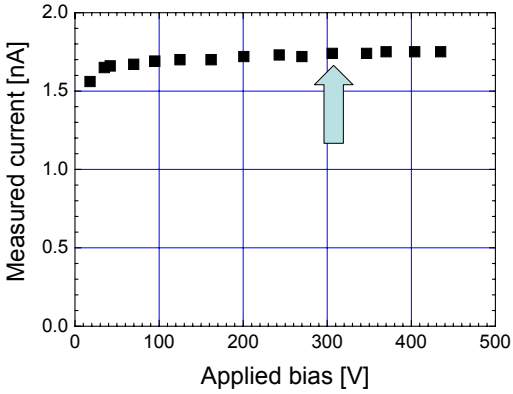


**Figure 6.6: Characteristic curve of the ionization chamber.** The arrow denotes the working voltage.

Given the (time dependant) current, $i_{PPIC}$, measured across the ionization chamber, the dose in the biological sample ($\tilde{D}$) is given by:

$$\tilde{D}_{DNA} = \int i_{PPIC}(t)dt \times \frac{w_i}{e} \times \frac{S_{DNA}}{S_{PPIC}} \times \frac{1}{\rho_{DNA}} \times \frac{V_{DNA}}{V_{PPIC}^{\ 2}} \qquad (6.1)$$

Where the DNA subscript denotes the DNA sample and the PPIC subscript denotes the PPIC. $S_x$ is the mass stopping power (in keV/μm [88]), $\rho_x$ the density, $w_i$ the differential specific ionization energy per ion pair (in dry air) [113], $V_x$ the irradiated volume and $e$ the electron charge. All particle irradiations were performed at an average dose rate of 10 Gy/min with occasional momentary fluctuations of up to 50% above or below this value.

Dosimetry of the γ experiments was performed using the Fricke solution (see pp. 111-113 of [6]).

The principal uncertainty in the accelerator dosimetry is due to an uncertainty in the thickness and pressure of the ionization chamber. The ionization chamber thickness was 1.6±0.1mm (6%). It was operated under a flow of dry air at atmospheric pressure, which could vary by up to 5%. Other factors included in the dose calculation (temperature, $w_i$ value, beam area, etc') are known to better than 1%. The uncertainty in the dose evaluation, determined by the uncertainty in IC thickness and the gas density, is estimated at 8%.

The uncertainty in the dosimetry of the gamma irradiations was quantified by comparing the slopes of the optical density of an irradiated Fricke solution as a function of the nominal dose. The standard deviation of 8 such slopes measured at different dates and using different Fricke solutions was 9%.

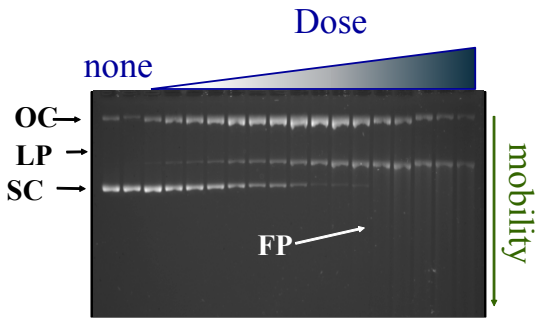


**Figure 6.7: a) Photo of an electrophoresis gel.** Each lane corresponds to a different dose of 1.03 MeV protons irradiated in 2mM Glycerol. The upper row corresponds to open circular DNA (OC) (having the lowest mobility), the middle row corresponds to linear DNA (LP) and the bottom row corresponds to supercoiled DNA (SC). A smear due to fragmented DNA (FP) is seen at high doses.

### 6.3.2 Gel electrophoresis - quantification of strand breaks

Plasmid DNA in general is well suited for the study of the induction of single- and double-strand breaks, as the plasmid is, initially, a closed *supercoiled* ring of DNA. The occurrence of **isolated** single-strand breaks (induced by radiation or some chemical agent) causes the plasmid to uncoil, forming a *relaxed* ring (open circle). Induction of a **single** double-strand break will cause it to *linearize*. At high doses, multiple double-strand breaks, which may be induced by several **independent** projectiles hitting the same plasmid, will cause its fragmentation. These four conformations have different mobility and can be easily separated by gel electrophoresis [114]:

100 ng of irradiated plasmid was diluted into 5 µl loading buffer (3x TBE, 60% glycerol, 0.6% sodium dodecyl sulfate, 0.06% bromophenol blue) and run on a 0.7% agarose gel in TBE buffer (89 mM Tris-borate, 2 mM EDTA pH 8) for 18-24 hours at 30 V/cm. Gels were stained in TBE buffer containing 0.5 µg/ml ethidium bromide for one hour and destained for one hour in TBE buffer. Gels were photographed with a fluor-S$^{TM}$ Multimager (Bio-Rad). Background was calculated as the average background above and below each DNA band. Amount of supercoiled DNA was corrected for a less efficient incorporation of ethidium bromide by a multiplication factor which we have measured to be 1.4. Figure 6.7 shows a typical photograph of an electrophoresis gel. Each lane (column) corresponds to a different dose (from 0 to 800 Gy). The bottom, top and middle rows correspond, respectively to the fractions of supercoiled (*SC*), relaxed *(OC*) and linear (*LP*) DNA (i.e. no strand breaks, one or more **isolated** SSBs and **at least one** DSB). A smear, due to fragmented DNA (*FP*) is also seen at high doses.

The quantities of supercoiled, open-circular and linear DNA (as a function of dose) are then compared to a statistical model ([111]), described in detail in Appendix C, unfolding the high-dose data to obtain the expected damage yields induced by a single projectile:

- $\mu$ - the average number of single strand breaks per unit dose (Gy) per unit mass (Da) of DNA (assuming that no two projectiles hit the same plasmid).
- $\phi$ - the average number of double strand breaks per Gy per Da of DNA (assuming that no two projectiles hit the same plasmid).

Figure 6.9 below shows the model fit to the data extracted from figure 6.7.

The experimental uncertainties inherent in the analysis of the gel data are due to the quantification of the band intensities and the varying binding efficiency of ethidium bromide to the various forms of DNA. The band intensity was calculated by subtracting the number of expected background counts within the band area from the number of counts in the band ($N_{band}$=$N_{tot}$-$N_{BG}$). The uncertainty in this number is $\Delta N_{band} = \sqrt{N_{tot} + N_{BG}}$ , which in our case is about 1%. The binding efficiency of ethidium bromide to supercoiled DNA is 1.3-1.5 times smaller than to the other forms. We have used an average value of 1.4; a change by ±0.1 affects the fitted values by less than 5%.

A free parameter in the Cowan model is the distance b between two SSBs required to form a DSB, which was set equal to 10 bp. Its variation by ±3 bp resulted in a variation of a few ‰ in the resulting fit parameters.

### 6.3.3 The bacterial survival assay

The irradiated plasmid can also be used to transform repair-deficient (i.e. *RecA*$^-$) *E. Coli* bacteria to antibiotics-resistance: When placed under stress (e.g. strong temperature variations), the bacteria will take up plasmid DNA, in its vicinity, and will produce any proteins coded in it.

XL2-Blue MRF' bacteria (Stratagene,) were prepared to be competent using the Calcium/MOPS method [115]. The bacteria were kept at 4 ºC and used up to 2 days after preparation.

Several hours (up to two days) after irradiation plasmid were transformed to the competent bacteria. For each dose, 50 ng plasmid (diluted to 10 µl) was added to a 15 ml plastic tube containing 150 µl buffer (75 mM $CaCl_2$) and 200 µl competent bacteria. The mix was incubated 45 min on ice and heat shocked at 42° C for 2 min. Bacteria were allowed to recover for one hour at 37° C after addition of LB.

For each radiation dose, two repeats of three dilutions were plated on LB plates containing 40 µg/ml ampicillin. The next day, colonies were counted (see figure 6.8). Plates containing between 25 and 400 colonies were used for analysis.

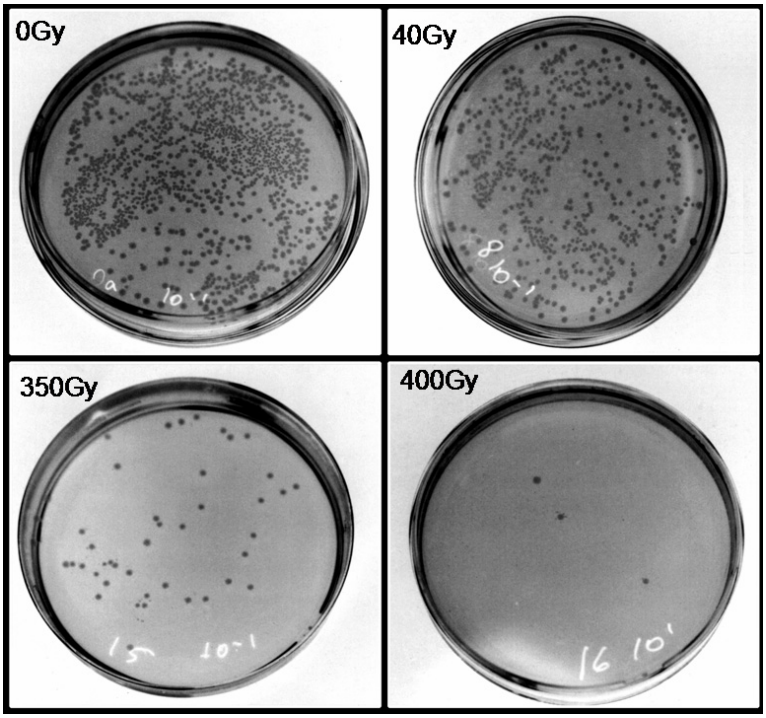


**Figure 6.8: Photographs** (negatives) **of bacterial colonies** irradiated by various doses of 1 MeV protons. Each spot is a bacterial colony arising from a single bacterium which has been successfully transformed by an undamaged plasmid. (A 10-fold dilution of transformed bacteria was plated in each case).

The strain of bacteria we used in this study is *recA*$^-$ (i.e. it does not contain the *recA* gene, crucial for recombination repair, see §2.1.1.1). This bacterium can repair isolated SSBs using the NER repair pathway. Isolated base damages are converted to SSBs by the BER pathway and can therefore also be repaired. The bacterium cannot repair clustered damages (DSBs or

clustered base lesions) which require the recombination repair pathway which is inactivated in this strain. When the bacteria are grown on an antibiotic medium, only bacteria, which have successfully incorporated an **undamaged** plasmid (or a plasmid containing reparable damage such as **isolated** base damages and isolated strand breaks), will survive.

The fraction of these plasmids can be evaluated by comparing the number of bacteria which are able to survive on antibiotic medium after incorporating irradiated plasmids irradiation to those incorporating unirradiated plasmids (see figure 6.8). Using essentially the same statistical model as in the previous section (see Appendix C) it is then possible to obtain:

- $\mu$'- the average number of isolated damages (SSBs or single base lesions that are not formed on opposite strands) per Gy per Da of DNA (assuming that no two projectiles hit the same plasmid).
- $\phi$'- the average number of damage clusters (containing multiple base damages and/or strand breaks on opposite strands) per Gy per Da of DNA (assuming that no two projectiles hit the same plasmid).

Sample model fits to survival data are shown in figure 6.10 below. The main difference between this assay and the previous one is that it is sensitive also to base damages and therefore we expect the values for $\mu$' and $\phi$' obtained from the model fit to be larger than $\mu$ and $\phi$. Based on the measurements of [116] as well as on simulations [117], we expect $\mu'/\mu = 3\text{-}4$, this excess of base damages compared to strand breaks is probably due to the volume ratio of the base region to the backbone, resulting in more frequent hits to bases.

The main uncertainty in this assay is the reproducibility of the amount of DNA recovered from the irradiation holder and used in the transformation. This amount was seen to be slightly different for each measured dose-point, resulting in a poorer quality model fit as compared to the gel data. The stochastic uncertainty in the number of colonies on each dish was taken into account by averaging the number of counts on several dishes (weighted by the quantity $1/\sqrt{n}$) of different dilutions. The error bars, shown in figure 6.10, represent the average of $1/\sqrt{n}$ of all dishes at the same dose-point.

## 6.4 Results

### 6.4.1 Dose dependence of the damage yields.

Figure 6.9 shows the, dose-dependant, yield of plasmid in the three conformational states (supercoiled, open circular and linear). At low doses, the quantity of undamaged DNA (SC) is seen to drop exponentially, as would be expected from Poisson statistics. The observed trend in the quantity of the open circle plasmid form (OC) is due to multiple hits on the same plasmid. At low dose, this is exceedingly rare as only a small fraction of the plasmids are damaged. As the dose increases, we expect plasmids containing a single SSB to acquire additional SSBs, which will not lead to a further increase of the OC fraction. On the other hand, when a DSB is formed in an open circular plasmid, the latter is converted to linear (LP) form. This explains the observed increase of LP forms accompanied by a decrease of OC forms. Further, if a second SSB is formed close enough to an existing SSB (and on the opposing strand), a DSB will result. As we are mainly interested in the yield of DSBs resulting from single-track events, these DSBs, which result from two or more independent particle tracks, should not be included in the yield determination. Fitting the relative amounts of different plasmid forms to the statistical model described in appendix C enabled us to take into account the effects of multiple SSBs on the same plasmid, observed at high doses, as well as separating the DSBs formed by single projectiles from those formed by the independent action of multiple projectiles. The SSB and DSB yields we obtained are, therefore, the *true single-track induced yields*.

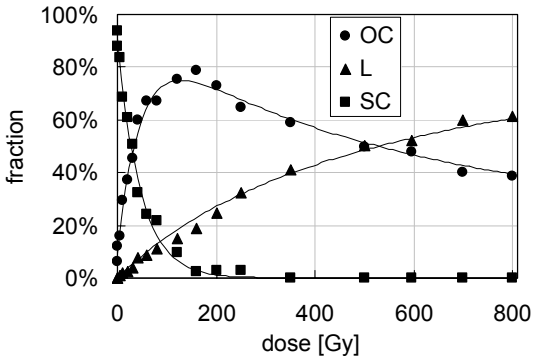


**Figure 6.9 : Model fit of the data of figure** 6.7**.** 100% corresponds to ***non-fragmented*** plasmids, see appendix C.

Correct application of the model requires the knowledge of the **interaction distance** between strand breaks. Since Dianov [95] and D'souza [94] showed that closely-spaced base lesions on opposite strands, at a distance of up to 7-13 base pairs, were transformed to DSBs by base excision repair enzymes, both *in-vivo* and *in-vitro*, we have used an interaction distance of 10 bp; generally resulting in a good model fit. It is, however, interesting to note that the model yielded similar results for an interaction distance of 20 bp; this indicates that the formation of DSBs by two independent lesions occurring within 10-20 bp (3-6 nm) is still a rare event over the dose range investigated.

The dose-dependence of the yield of clustered lesions per plasmid (*–ln(SF)* in figure 6.10) affords us some insight into the mechanism of clustered lesion formation. If clustered lesions are formed by a "one-hit" mechanism, i.e. they are induced by a single projectile, the yield will be linear in dose. If, however, the clusters are formed from the interaction of single lesions formed by several independent projectiles, the dose dependence of the yield would be quadratic or higher order. Indeed, we have seen that for low LET radiations, in general, the dose dependence of *-ln(SF)* was nonlinear whilst for higher LET radiations (25.5 keV/μm), where the lesions are more clustered in nature (see below), it was mostly linear.

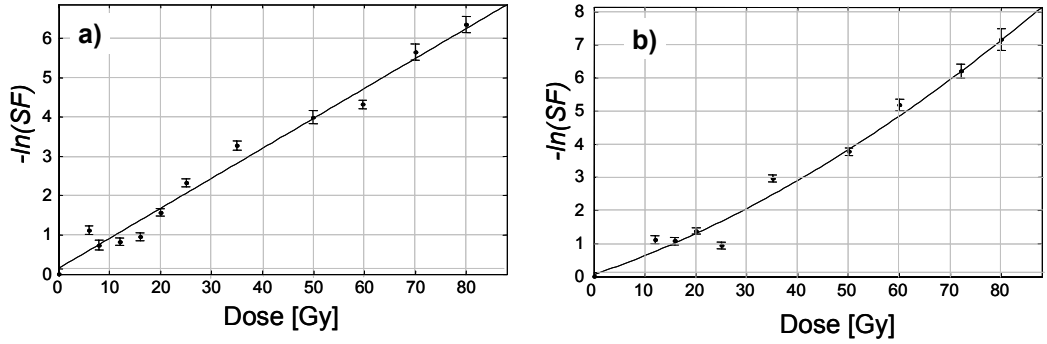


**Figure 6.10 : Model fit to the bacterial survival data.** Each dose point corresponds to the average of several plates (see figure 6.8). a) High LET (1.03 MeV protons -26 keV/μm). b) Low LET (19.3 MeV protons – 2.7 KeV/μm).

### 6.4.2 LET and track structure dependence of the damage yields.

We have irradiated the plasmid with various LET projectiles, as detailed in table IV, at glycerol concentrations of 2 mM or 200 mM. Irradiations with Cesium 137 and 250 MeV protons were performed by Dr. V. Bashkirov and Dr. J. Milligan at LLUMC whereas the other measurements were performed at WIS by Dr. C. Leloup, G. Garty and G. Assaf. The model fitting was performed independently by Dr. R. Schulte (LLUMC) and G. Garty (WIS), yielding good agreement.

The calculated yields of single strand breaks (SSB), isolated damages (ID), double strand breaks (DSB) and clustered lesions (CL) are shown respectively in figures 6.11 to 6.14.

In all figures, the *x*-axis error bars (barely visible for the 1 MeV proton data) correspond to the LET variations within the sample (see §6.2). The uncertainty in the fitted model parameters (i.e. the respective yields of SSBs DSBs and clustered lesions), resulting from the uncertainty in the experimental quantities is discussed in detail in §6.5 below.

These measurements are compared to others in the literature in the discussion (§8.2.4 below).

**2 mM Glycerol**

| Projectile | Energy [MeV] | LET [keV/μm] | $\mu$ [$10^{-9}$ SSB/Gy/Da] | $\phi$ [$10^{-9}$ DSB/Gy/Da] | $\mu'$ [$10^{-9}$ ID/Gy/Da ] | $\phi'$ [$10^{-9}$ CL/Gy/Da ] |
|---|---|---|---|---|---|---|
| γ $^{60}$Co | 1.33 | 0.267* | 8.5±01.3 | 0.16±0.04 | 71±12 | 1.8±0.9 |
| γ $^{137}$Cs | 0.662 | 0.395* | 18±2 | 0.31±0.05 | 73±16 | 2.1±0.5 |
| Protons | 250 | 0.39 | 29±6 | 0.52±0.06 | 100±17 | 2.3±0.4 |
| | 19.3 | 2.7± 0.1 | 8±3 | 0.16±0.04 | 20±3 | 0.58±0.25 |
| | 1.03 | 25.5 ± 2.3 | 2.6±0.4 | 0.25±0.03 | 5.8±4.7 | 0.8±0.2 |
| He nuclei | 26 | 25.5 ± 0.2 | 1.8±0.4 | 0.13±0.02 | 1.9±2.4 | 0.45±0.07 |

**200 mM Glycerol**

| | | | | | | |
|---|---|---|---|---|---|---|
| γ $^{60}$Co | 1.33 | 0.267* | 0.547±0.1 | 0.020±0.003 | 4.5±0.5 | 0.04±0.03 |
| γ $^{137}$Cs | 0.662 | 0.395* | 1.04±.14 | 0.02±0.002 | 6.5±1 | 0.07±0.05 |
| Protons | 250 | 0.39 | 1.43±0.3 | 0.045±0.009 | 1.7±1.8 | 0.27±0.04 |
| | 19.3 | 2.7± 0.1 | 0.61±0.14 | 0.017±0.006 | 2.8±0.4 | 0.057±0.03 |
| | 1.03 | 25.5 ± 2.3 | 0.59±0.09 | 0.028±0.003 | 0.44±0.5 | 0.13±0.03 |
| He nuclei | 26 | 25.5 ± 0.2 | 0.30±0.06 | 0.014±0.003 | 2.6±0.9 | 0.015±0.013 |

**Table IV: Biology measurements**. *The LET for gamma rays was estimated as the average LET of the generated Compton electrons. SSB- single strand break; DSB – double strand break; ID – strand break or base lesion; CL – clustered lesions.

#### 6.4.2.1 The yield of single strand breaks

The yield of SSBs (per unit absorbed dose) is shown in figure 6.11a. A decrease in the yield of SSBs with increasing proton LET was observed; it was more pronounced for 2 mM glycerol than for 200 mM. In fact, there was not much further decrease (at 200mM) of SSB yields between the proton LET values of 2.7 keV/μm (19.3 MeV) and 25.5 keV/μm (1.03 MeV). Despite similar or equal LET values, the SSB yields for helium nuclei as well as that for the gamma irradiation were smaller than those for protons of 1.03 MeV and 250 MeV, respectively.

The yield of SSBs per incident projectile (figure 6.11b) rises with LET as expected. This reflects the monotonous rise in ionization density with increasing LET. Note that in agreement with the data of figure 6.11a, the increase in the yield of SSBs for high scavenger concentration is stronger.

#### 6.4.2.2 The yield of isolated lesions

The yield of isolated lesions (i.e. SSBs or base damages which are not clustered) is shown in figure 6.12. The error bars here are somewhat larger than those of the previous measurement (in particular for the high LET radiations) but the same LET dependence is observed as in 6.11a.

Note that the damage yields are larger than those of 6.11a. In fact, based on measurements [116] and simulations [117], we expect that the yield of isolated damages will be 3-4 times higher than the yield of SSBs. Unfortunately the spread in the data is too large to conclusively show this (we see a ratio of 4±3 for the low scavenger and 5±4 for the high scavenger data).

Note that there is no difference, in the yield of isolated damages, between the γ-rays and the protons (at low scavenger only).

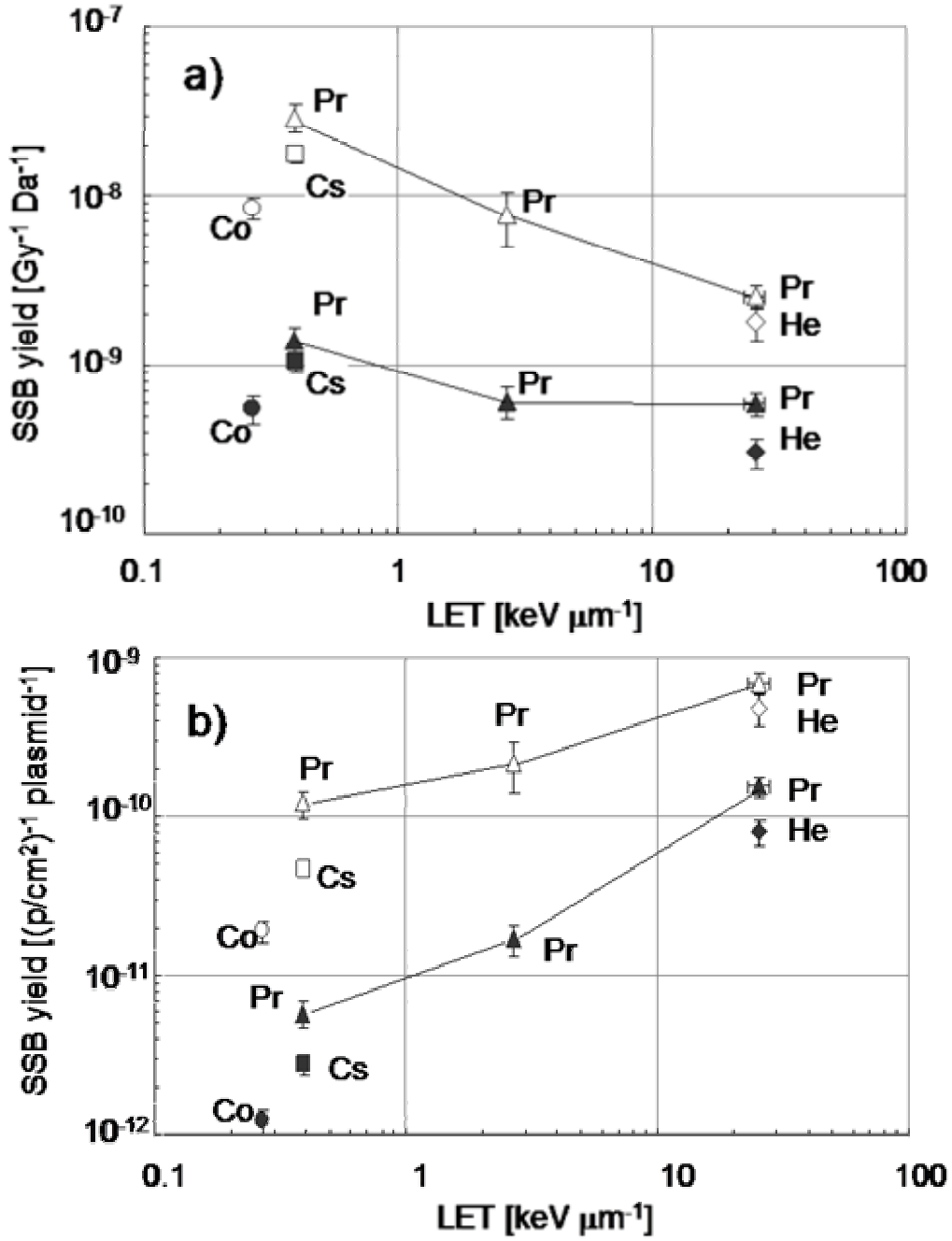


**Figure 6.11: The measured yield of SSBs for all radiation fields.** SSB yields as function of LET for proton (Pr - triangles), helium nuclei (He - diamonds), $^{60}$Co (Co - circles) and $^{137}$Cs (Cs - squares). Open symbols correspond to 2 mM glycerol and closed symbols to 200 mM. The protons data are joined by a line to guide the eye. Data are the mean of 2-3 experiments except for $^{137}$Cs with 200 mM glycerol (one experiment) a) Yields normalized per unit absorbed dose. b) Yields normalized per incident projectile. This renormalization was simply done by multiplying the yields of a) by the LET in units of [*J/(kg/cm²)*]) and by the plasmid mass in Da.

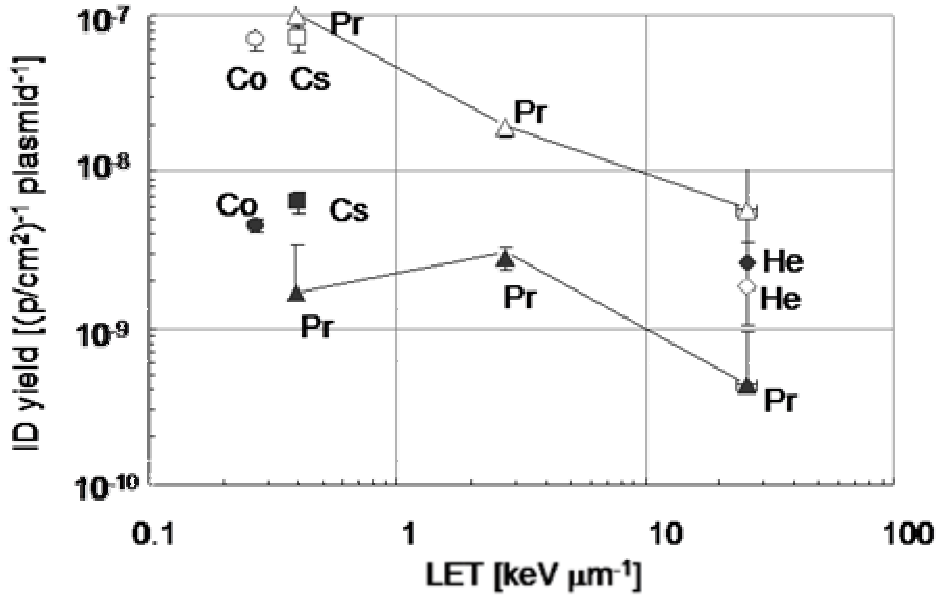


**Figure 6.12: The measured yield of isolated damages** (ID). Notations are the same as in figure 6.11.

#### 6.4.2.3 The yield of double strand breaks

In figure 6.13, we see the yield of double strand breaks (DSBs) at different LET values and for different particles. At both glycerol concentrations, there is first a decrease in the yield of DSB for protons between 0.4-2.7 KeV/μm, followed by a slight increase for 25.5 KeV/μm protons.

The yield of DSBs induced by helium nuclei are about twice lower than those induced by protons of the same LET. The yields induced by gamma rays are also lower than those induced by protons.

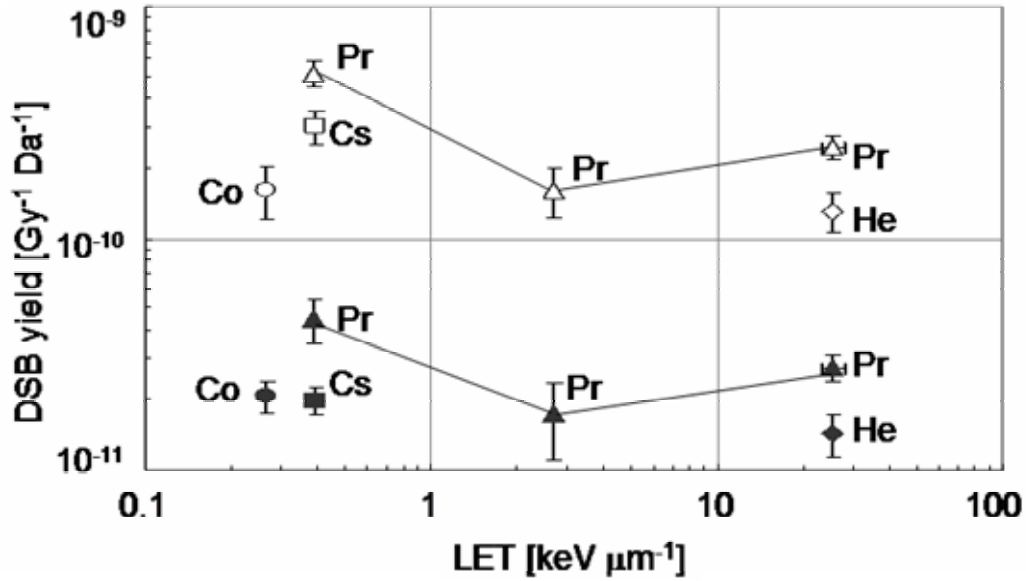


**Figure 6.13: The measured yield of double strand breaks.** Notations are the same as in figure 6.11.

#### 6.4.2.4 The total yield of clustered lesions

The yield of clustered lesions (containing also base damages) is shown in figure 6.14. The same trends described in the previous section are seen although the error bars are larger, due to the large fluctuations inherent to the bacterial survival assay. We see that this yield behaves as the yield of DSB, but is 2-8 times higher. In short, the yield reaches a minimum for the 2.7 KeV/μm protons and it is higher for protons than for helium nuclei of same LET. This difference is smaller at 200 mM glycerol than at 2mM.

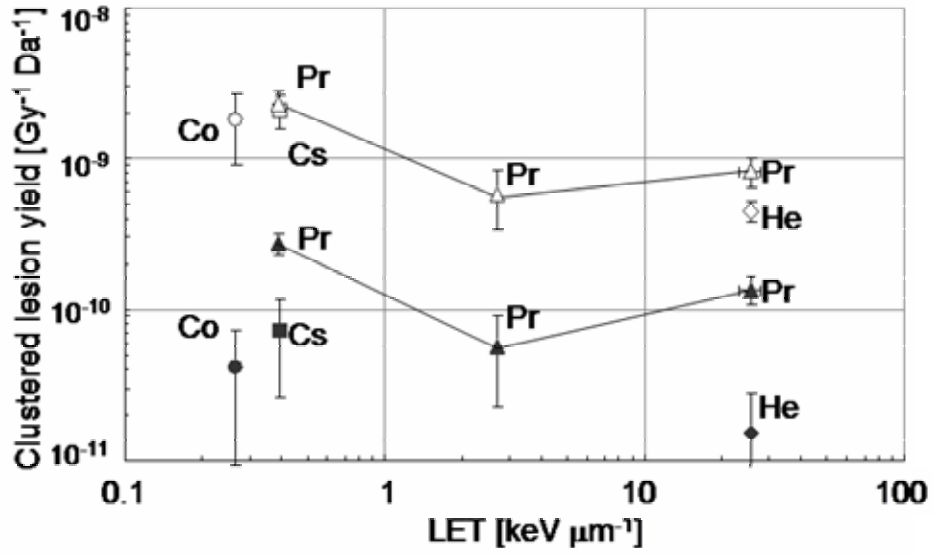


**Figure 6.14: The measured yield of clustered lesions**, which inactivate the plasmid. Notations are the same as in figure 6.11.

## 6.5 Experimental errors

In this work we have irradiated minute samples of DNA (3-5μl). The reliable handling of these samples was our biggest source of experimental error. The use of such small samples required extreme care to prevent their evaporation both during the long irradiations (up to 8 hours, in the dry environment required for reliable beam dosimetry [61]) as well as during the DNA recovery from the sample holder. In order to solve the former problem we have designed an elaborate sample holder, sealed to the dry atmosphere and containing a reservoir of irradiation buffer. Indeed we have seen that this sample holder, when properly closed, consistently kept the sample from evaporating even during 8-hour long exposures. This point is crucial as any evaporation of the sample will change the glycerol concentration and hence the scavenging capacity. We have also seen in some occasions a marked decrease in the fraction of recovered DNA from the irradiation setup. This was attributed to evaporation of the sample during the recovery process, as indeed it was somewhat correlated with the experience of the experimenter. As the evaporation occurs after the irradiation has ceased, the only effect of it is in introducing an uncertainty in the quantity of recovered DNA.

In the gel electrophoresis studies (quantification of SSBs and DSBs) the amount of recovered DNA is of no importance, as we normalize the measured *SC*, *OC* and *LP* fractions to the total DNA in each lane of the gel. Subsequently we were able to reliably quantify the strand break yields to within 10%.

Accurate amounts of DNA are, however, essential for the reliability of the survival assay. The uncertainty in the accuracy of DNA recovery led to a large spread in the survival curve and therefore to a less reliable fit. In this case the yield of isolated damages (base damaged + strand breaks) obtained form the model fit is particularly sensitive. In the low LET measurements, the *–ln(SF)* curve is non-linear. This was seen to result in a less reliable model

fit to the data. Occasionally, the model fit would yield clearly illogical results (i.e. 10 orders of magnitude smaller yields than expected). In all cases where this criterion was not met we could see that the model fit to the data was indeed poor. In our analysis we have rejected these values. After this rejection, we have seen that the remaining repetitions of the same experiment were in good agreement with each other (i.e. within 20-25%).

The total uncertainty in the fitted model parameters (i.e. the respective yields of SSBs DSBs and clustered lesions), resulting from the uncertainty in the experimental quantities, was obtained by a Montè-Carlo error propagation algorithm: For each irradiation experiment (consisting of one repetition of 10-20 dose points) 1000 data sets were generated by overlaying a Gaussian experimental error onto an actual data set. In the gel analysis we took the standard deviation of this distribution to be 5% of the measured yield of supercoiled, relaxed or linear DNA. In the analysis of the survival data we took the error as described in the previous paragraph.

The fitting procedure was then performed to obtain the various lesion yields (SSB, DSB or clustered lesion) for each of the 1000 data sets. The experimental value for each irradiation experiment was taken as the average of these (1000) lesion yields; the experimental uncertainty was taken as their standard deviation.

The value plotted in figures 6.11-6.14 is the average, over all repetitions (typically 2-3) of the same radiation field, of the experimental value calculated above. The error bars are obtained by adding (in quadrature) the uncertainty in dose (8%), the standard deviation of the three repetitions and the experimental uncertainty, described in the previous paragraph and averaged (also in quadrature) over all repetitions of the same radiation field.

Due to the rapid degradation of 1 MeV protons in the DNA sample, we have seen that the LET uncertainty within the sample is about 18% (FWHM). We have set the beam energy such that the average LET in the proton-irradiated sample is the same as in the helium-nuclei-irradiated sample. As the Let variation of the damage yields is rather slow, this LET-error cannot explain the factor-of-two difference between protons and helium nuclei.

## 6.6 Conclusions

The results of our experiments provide the following conclusions:

We have clearly seen the effect of the radical scavenger and of the radiation quality on the damage yields. As a function of LET the damage yields behave as expected: at very low LET they are dominated by radical formation and recombination far from the DNA; for higher LET values the track structure becomes more and more important and we see an increase in lesion clustering due to the increase of clustering in the track structure. Our data is also in good agreement with that found in the literature and complements it (see §8.2.4). Measurements of DNA damage yields in high scavenger concentration or using charged particles (other than from a radioactive source) are rather scarce. This is understandable from the complexity of such experiments. Although these measurements are interesting from a radiobiological point of view and demonstrate for the first time several important phenomena (see §8.2), our primary motivation in conducting them was to obtain clustered lesion yields which can be compared with nanodosimetric predictions. The next chapter presents a simplified biophysical model for predicting the measured clustered-lesion yields based on ionization cluster size distributions measured in the ND.

# Chapter 7 :

# Biophysical model

The trends observed in this work, of the ionization cluster-size distributions in the gaseous DNA model and the damage yields in *in-vitro* irradiated plasmid DNA, call for the development of a detailed correlation between the two sets of data. For that purpose we developed a biophysical model predicting the observed biological outcome, based on the measured cluster size distributions in gas. A general biophysical model should account for a complexity of physical, chemical and biological processes taking place in the modeled biological system. However, our biological model system was rather simple and therefore a simplified and straightforward model may be sufficient.

In this chapter we describe the biophysical model for prediction of clustered damages in DNA irradiated *in-vitro*. Its predictions indeed agree with the general trends seen in the radiobiological measurements but do not reproduce them exactly, mainly because we cannot model the radical-mediated indirect effect. Naturally, a much more complex model (far beyond the scope of this work) would be required for the prediction of damages induced in DNA, irradiated *in-vivo*.

## *7.1 Assumptions of the biophysical model*

### 7.1.1 The use of a gas model

We are using a gas model to simulate radiation damage in liquid medium (essentially water). This simulation rests on two assumptions:

1. There is a one-to-one relationship between ionizations in the gas model and those that would be formed in the DNA.
2. The ND's sensitive volume corresponds to the true biological one.

The validity of the first assumption rests on the discussion in §2.2.3. MC simulations in both propane and liquid water yield cluster size distributions differing by 12% (see figure 2.5c and [34]). We can therefore use the gas model for the study of radiation effects in liquid water and in DNA.

The second assumption is justified by our choice of the SV in the ND. We have chosen a SV of 6.4 nm length which corresponds to 10 bp (3.4 nm length) surrounded by a 1.5 nm water layer. Although the actual correlation length of lesions on DNA is not well known, some experiments [94, 95] point to an interaction length of about 10 bp.

### 7.1.2 The biological test system

The *in-vitro* plasmid model system, described in the previous chapter, allows us to perform several simplifications with respect to the *in-vivo* situation:

3. There is no repair of the damage.
4. The plasmid is composed of many independent targets.
5. The detected lesions are: a) a single strand break or combinations of strand breaks and b) a single general damage (which can be either a strand break

or a base damage) or combination of general damages (strand breaks and/or a base lesions).

The first assumption follows from our choice of the plasmid system. This is a simple system where some of the repair mechanisms are eliminated. In the strand break assay (§6.3.2) such mechanisms do not exist at all. In the bacterial survival assay (§6.3.3), we are intentionally using DSB-repair deficient bacteria, which can only repair single-stranded damages (which do not interest us).

The second assumption is justified by the short correlation lengths [94, 95] of damages on DNA. Damages created more than 7-13 base pairs apart cannot interact to form a clustered lesion. We can therefore assume that the plasmid is composed of many small independent targets of 10-20 bp length.

The third assumption arises from the facts that a) in the gel assay we are only sensitive to strand breaks and b) in the bacterial survival assay we cannot differentiate between a "genuine" strand break and one induced during the repair of a single base damage.

### 7.1.3 The radiation field

The assumptions on the radiation field are:

6. DNA lesions and ionization events in the sensitive gas volume are always caused by only one particle.
7. The radiation-induced ionizations create lesions independent of each other.

In the biological measurements we have exposed the DNA to a high dose of projectile particles: A typical dose of 5000 Gy, required to create 1 DSB in a plasmid (see table IV), corresponds to about $10^{13}$ projectiles through the sample; this corresponds to about 100 projectiles per plasmid and 0.1 projectiles per 10 bp segment. In such a case indeed all of the plasmids will include multiple damages from independent projectiles **but most individual segments will not** (In accordance with assumption 2 of the previous section). Under these conditions it is valid to use the statistical model of appendix C ([111]) to relate the damage yields in a DNA segment due to a **single projectile** particle, with the overall distribution measured with a high irradiation dose.

The nanodosimetric technique was developed to match the situation in the biological system. The nanodosimetric measurements were done in an event by event mode and great care was taken to reject all events having more than one projectile within the SV. We can therefore interpret the cluster size distributions as probabilities **per projectile**.

The second assumption is true only for direct ionization of the DNA and for relatively low LET values. For LET values above ~150 keV/μm the ionization density is such that there is a high probability for generating two (or more) ionizations within a single nucleotide of DNA. Obviously we can no longer regard the ionizations as independent. However even at lower LET values there is a problem. The radical-mediated *indirect effect* is responsible for about two thirds of the damage in irradiated DNA. In this case the damage is caused by radicals formed up to several tens of nm away from the DNA strands, diffusing to- and reacting with it. As we cannot model radical diffusion and recombination using our ND, we add a third assumption:

8. The probability for a single ionization to induce a single lesion does not depend on the number of ionizations in the same cluster.

The implications of this assumption and possible ways to avoid making it are detailed in the summary (§8.3).

Based on these assumptions we can state that each deposited ionization is converted, **individually**, with some probabilities $p_{SB}$ and $p_{BD}$, to a strand break or to a base damage; Furthermore, these probabilities **do not depend on the cluster size**.

Note that the ratio of $p_{SB}$ and $p_{BD}$ is roughly known: the yield of SSBs is smaller by a factor of about 2.5 than the yield of base damages (i.e. $p_{BD} = 2.5 \times p_{SB}$) (see §6.3.3).

## 7.2 The biophysical model

From the ND we obtain a measured **ion cluster-size distribution** within a SV of a given size, irradiated by a beam of diameter $D$. This distribution is denoted $f(n_{ion})$ gives the absolute probability, **per projectile,** to create $n_{ion}$ ions in the specified SV. We define the **cross section** for the production of a $n_{ion}$ ion cluster as:

$$\sigma(n_{ion}) := f(n_{ion}) \times beam\ area = f(n_{ion}) \times \tfrac{\pi}{4} D^2 . \qquad (7.1)$$

Note that $D$ is in units of tissue-equivalent *nm* so that $\sigma$ is obtained in $nm^2$. As explained in §5.1 above, $f(n_{ion})$, the absolute probability, per projectile, to generate a cluster of given size within the SV is inversely proportional to the beam area, due to the small chance of a projectile to hit the small SV in a broad beam. Consequently, $\sigma$ is **independent of the beam size,** as expected.

We assume that each ion has a probability of $p_{SB}$ to generate a strand break, independent of the cluster size. Similarly, we assume that it has a probability of $p_{BD}$ to generate a base damage, independent of the cluster size. Therefore, given a cluster of $n_{ion}$ ions, the probability to create $n_{SB}$ strand breaks **and** $n_{BD}$ base damages is given by the **trinomial distribution ( $\ddot{P}$ )**:

$$\ddot{P}(n_{SB}, n_{BD} | n_{ion}) = \binom{n_{ion}}{n_{SB}} \binom{n_{ion} - n_{SB}}{n_{BD}} (p_{SB})^{n_{SB}} (p_{BD})^{n_{BD}} (1 - p_{SB} - p_{BD})^{n_{ion} - n_{SB} - n_{BD}} \qquad (7.2)$$

with $\ddot{P}(n_{SB}, n_{BD} | n_{ion}) > 0$ only for $n_{ion} > n_{SB} + n_{BD}$. Using the probability distribution $\ddot{P}(n_{SB}, n_{BD} | n_{ion})$, we can obtain the cross section for the production of $n_{SB}$ strand breaks **and** $n_{BD}$ base damages

$$\sigma(n_{SB}, n_{BD}) = \sum_{n_{ion}} \sigma(n_{ion}) \ddot{P}(n_{SB}, n_{BD} | n_{ion}) \qquad (7.3)$$

The yield (per Gy per Da) is obtained by multiplying this expression by the beam fluence, required for 1 Gy, and dividing by the segment size in Daltons.

For a monoenergetic particle beam, the particle fluence required for 1 Gy is:

$$\Phi_{1Gy}[projectile / nm^2] = \frac{10^{-24}}{e} \times \frac{\rho[g / cm^3]}{LET[keV / \mu m]} = 6.24\, 10^{-6} \frac{\rho}{LET} \qquad (7.4)$$

where $\rho$ is the density (typically 1 g/cm$^3$) and $10^{-24}/e$ is a unit-conversion factor. As stated above the length of each segment is 10 bp, corresponding to 6.5 kDa.

The yield of events containing $n_{SB}$ strand breaks **and** $n_{BD}$ base damages is therefore:

$$
\begin{aligned}
G(n_{SB},n_{BD})[Gy^{-1}Da^{-1}] &= \frac{\Phi_{1Gy}}{6500}\times\sigma(n_{SB},n_{BD}) \\
&= \frac{\Phi_{1Gy}}{6500}\times\frac{\pi D^2}{4}\sum_{n_{ion}} f(n_{ion})\ddot{P}(n_{SB},n_{BD}|n_{ion}) \\
&= 7.55\ 10^{-10}\times\frac{D^2\rho}{LET}\sum_{n_{ion}} f(n_{ion})\ddot{P}(n_{SB},n_{BD}|n_{ion})
\end{aligned}
\tag{7.5}
$$

Formally this formula manifests a proportional dependence of the damage yields on the beam area ($D^2$); as noted above (§5.1) $f(n_{ion})$ is inversely proportional to the beam area. This formal (and unnecessary) dependence can be removed by using the *conditional cluster size distribution* ($\varphi(n_{ion})$).

It is trivial to show that the absolute and conditional cluster size distributions differ only by a multiplicative constant $\alpha$, which is given by:

$$
\varphi(n_{ion}) = \alpha\times f(n_{ion}) = \frac{1}{1-f(0)}\times f(n_{ion}) \tag{7.6}
$$

Comparing the average cluster size obtained in the two distributions we get:

$$
\begin{cases}
\langle n_{ion}\rangle_f = \sum_{n_{ion}} n_{ion} f(n_{ion}) \\
\langle n_{ion}\rangle_\varphi = \sum_{n_{ion}} n_{ion}\varphi(n_{ion}) = \sum_{n_{ion}} \alpha n_{ion} f(n_{ion})
\end{cases}
\Rightarrow \frac{\langle n_{ion}\rangle_\varphi}{\langle n_{ion}\rangle_f} = \alpha \tag{7.7}
$$

The average cluster size $\langle n_{ion}\rangle_f$ can be stated in terms of LET:

$$
\langle n_{ion}\rangle_f = \frac{V_{SV}LET}{\frac{\pi}{4}w_i D^2} \tag{7.8}
$$

where $V_{SV}$ is the volume of the SV in equivalent-nm$^3$. Eq. 7.8 merely states that the average cluster size is given by the amount of energy deposited in the SV ($LET/\frac{\pi}{4}D^2$ is the energy per unit volume) divided by the energy required to create an ion ($w_i$).

The term $\frac{V_{SV}LET}{D^2}$ is the same in the lab frame (dimensions in mm and LET in gas) and in the condensed matter which it models (dimensions in nm-equivalent and LET in water). For a deeper discussion of this equivalence see §2.2.3. Substituting (7.7) and (7.8) into (7.5) we obtain:

$$
G(n_{SB},n_{BD})[Gy^{-1}Da^{-1}] = 9.6\,10^{-10} * \frac{\rho V_{SV}}{w_i\langle n_{ion}\rangle_\varphi}\sum_{n_{ion}}\varphi(n_{ion}) * \ddot{P}(n_{SB},n_{BD}|n_{ion}) \tag{7.9}
$$

The formula for the damage yield in its transformed form (7.9) looks simpler and has some advantages. The SV volume $V_{SV}$ is a constant of the nanodosimeter, which does not depend on the radiation properties; the specific ionization $w_i$ is also practically a constant. Consequently, (7.9) contains only those characteristics of the radiation, which are measured in the nanodosimetric experiment.

This fact is an important one. It means that nanodosimetry is applicable for characterization of **unknown** radiation fields or at least radiation fields for which LET is not well defined (such as a "spread-out Bragg peak" beam used in proton therapy [118]).

### 7.2.1 Adaptation to our biological test system

In our experimental model of DNA/bacteria system, we cannot distinguish between single base-damage and strand break within a cluster. Therefore the trinomial distribution is replaced by two independent binomial distributions, giving the probability for $n_{SB}$ strand breaks and $n_{tot}$ general damages (strand breaks or base damages) (see appendix D.1).

$$\ddot{\ddot{P}}_{SB}\left(n_{SB},n_{BD}\middle|n_{ion}\right)\Rightarrow\begin{cases}\ddot{P}_{SB}\left(n_{SB}\middle|n_{ion}\right)=\binom{n_{ion}}{n_{SB}}\left(p_{SB}\right)^{n_{SB}}\left(1-p_{SB}\right)^{n_{ion}-n_{SB}}\\ \ddot{P}_{tot}\left(n_{tot}\middle|n_{ion}\right)=\binom{n_{ion}}{n_{tot}}\left(p_{tot}\right)^{n_{tot}}\left(1-p_{tot}\right)^{n_{ion}-n_{tot}}\end{cases}, \tag{7.10}$$

with $p_{tot}=p_{SB}+p_{BD}$ and $n_{tot}=n_{SB}+n_{BD}$.

The cross sections for $n_{SB}$ strand breaks and $n_{tot}$ total lesions are:

$$\begin{aligned}\sigma_{SB}\left(n_{SB}\right)&=\sum_{n_{ion}}\sigma\left(n_{ion}\right)\times\ddot{P}_{SB}\left(n_{SB}\middle|n_{ion}\right)\\ \sigma_{tot}\left(n_{tot}\right)&=\sum_{n_{ion}}\sigma\left(n_{ion}\right)\times\ddot{P}_{tot}\left(n_{tot}\middle|n_{ion}\right)\end{aligned} \tag{7.11}$$

The total cross section for creating a DSB is then given by:

$$\sigma_{DSB}=\sigma_{SB}\left(2\right)\times\tilde{p}(2)+\sigma_{SB}\left(3\right)\times\tilde{p}(3)+... \tag{7.12}$$

where $\tilde{p}\left(i\right)=1-\left(\frac{1}{2}\right)^{i-1}$ is the probability that, given $i$ strand breaks, at least two will be on opposite strands. The absolute yields of DSBs and clustered lesions are given by:

$$G_{DSB}[Gy^{-1}Da^{-1}]=9.6\,10^{-10}\times\frac{\rho V_{SV}}{w_i\left\langle n_{ion}\right\rangle_{\varphi}}\sum_{n_{ion}}f\left(n_{ion}\right)*\sum_{n_{SB}=2}^{\infty}\binom{n_{ion}}{n_{SB}}p_{SB}{}^{n_{SB}}\left(1-p_{SB}\right)^{n_{ion}-n_{sb}}\left(1-\tfrac{1}{2}^{n_{SB}-1}\right) \tag{7.13}$$

The sum over $n_{SB}$ can be calculated analytically (see appendix D.2) giving:

$$\sum_{n_{SB}=2}^{\infty}\binom{n_{ion}}{n_{SB}}p_{SB}^{n_{SB}}\left(1-p_{SB}\right)^{n_{ion}-n_{SB}}\left(1-\tfrac{1}{2}^{n_{SB}-1}\right)=1-2\left(1-\frac{p_{SB}}{2}\right)^{n_{ion}}+\left(1-p_{SB}\right)^{n_{ion}} \tag{7.14}$$

Leading to

$$G_{DSB}[Gy^{-1}Da^{-1}]=9.6\,10^{-10}\times\frac{\rho V_{SV}}{w_i\left\langle n_{ion}\right\rangle_{\varphi}}\sum_{n_{ion}}\left\{\varphi\left(n_{ion}\right)\left(1-2\left(1-\frac{p_{SB}}{2}\right)^{n_{ion}}+\left(1-p_{SB}\right)^{n_{ion}}\right)\right\} \tag{7.15}$$

With a similar expression for $G_{tot}$:

$$G_{tot}[Gy^{-1}Da^{-1}]=9.6\,10^{-10}\times\frac{\rho V_{SV}}{w_i\left\langle n_{ion}\right\rangle_{\varphi}}\sum_{n_{ion}}\left\{\varphi\left(n_{ion}\right)\left(1-2\left(1-\frac{p_{tot}}{2}\right)^{n_{ion}}+\left(1-p_{tot}\right)^{n_{ion}}\right)\right\} \tag{7.16}$$

## 7.3 Application of the biophysical model

In this work we compare biological clustered damages, which are assumed to occur in a 10 bp segment of plasmid DNA, with ionization clusters in a gaseous sensitive volume of about 6.4 nm long, 4.5 nm in diameter; the SV corresponds to 10 base pairs, including a 1.5 equivalent nm shell of water molecules. Figure 7.1a shows an absolute cluster size distribution, $f(n_{ion})$, obtained using 1 MeV protons, in the sensitive volume segment of

figure7.1b (obtained by an offline analysis of the data in figure 5.9). The cluster size distributions for all radiation fields studied by us, are shown in figure 5.12 above.

Also shown in 7.1a are the cross sections $\sigma_{SB}(n_{SB})$ and $\sigma_{tot}(n_{tot})$, calculated using eq. 7.11 with a $p_{SB}$ value of 10% and a $p_{tot}$ value of 35%. The former value was chosen to obtain the best possible fit of the model predicted and experimentally measured DSB yields. The value for $p_{tot}$ was fixed to 3.5×$p_{SB}$, in accordance with §6.3.3. Given these values of $p_{SB}$, $p_{BD}=p_{tot}-p_{SB}$ and using eq. 7.3 we can calculate the matrix $\sigma(n_{SB}, n_{tot})$ (shown in figure 7.2).

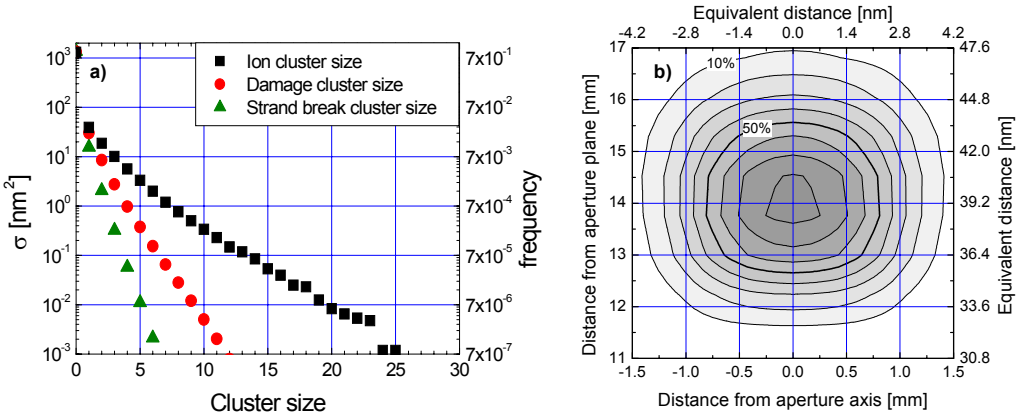


**Figure 7.1: a) The probabilities of a 1 MeV proton to induce an n ion cluster** (squares), to induce an n strand-break cluster (assuming $p_{SB}$=10% - circles) and to induce an n base-damage cluster (assuming $p_{BD}$=35% - triangles). The left hand axis gives the distributions as cross sections while the right hand axis gives probabilities per proton. b) The sensitive volume for this measurement (the notations are the same as in figure 3.16).

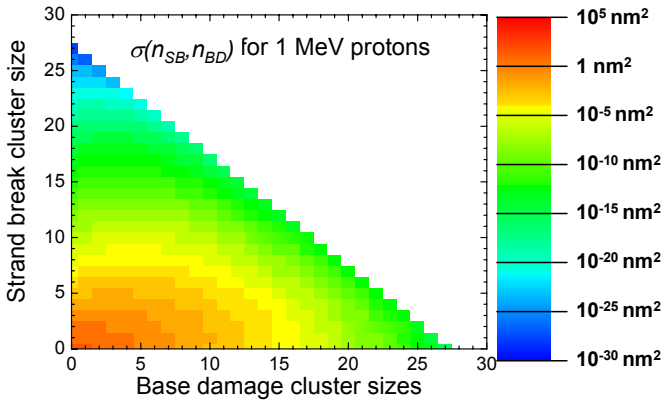


**Figure 7.2: The calculated double differential cross section** for production of a specific number of strand breaks and a specific number of base damages by 1 MeV protons. Based on the model parameters: $p_{SB}$=10% $P_{tot}$=35%.

### 7.3.1 DSB yield

Using formula 7.15 above, we have calculated the yield of DSBs. The calculated yields are shown in table V and graphically in figure 7.3. The rise in the yield of DSBs at low LET is predicted by the model but is not properly quantified, which seems to indicate that it is only partially due to actual clustering effect and partially due to radical recombination processes, not accounted for by the model.

It also appears that the difference in track structure between protons and helium nuclei, as quantified by the cluster size distribution cannot account for the observed difference in lesion-cluster yields. Indeed the model predicts a difference of 10% in the yield of clustered lesions (similar to the results in the ND) whereas a twofold difference was observed in irradiated DNA. These discrepancies are discussed in §8.3 below.

**Table V: A comparison between the measured and model predicted DSB and clustered lesion yields** for all measured radiation fields. This table is depicted graphically in figure 7.3. The model error bars correspond to the 12% predicted difference between the ion cluster size in gas and in liquid water (see figure 2.5c.

| Radiation field | | Yield of DSBs | | Yield of CLs | |
|---|---|---|---|---|---|
| Description | LET | Experiment | Model | Experiment | Model |
| | [keV/µm] | [$10^{-10}$ $Gy^{-1}$ $Da^{-1}$] | | | |
| Proton 250 MeV | 0.39 | 0.045±0.009 | 0.18±0.02 | 0.27±0.04 | 1.4±0.2 |
| Proton 19.3 MeV | 2.7 | 0.017±0.006 | 0.17±0.02 | 0.057±0.03 | 1.3±0.2 |
| Proton 1 MeV | 25.5 | 0.028±0.003 | 0.26±0.03 | 0.13±0.03 | 2.1±0.3 |
| $He^{++}$ 26 MeV | 25.5 | 0.14±0.03 | 0.25±0.03 | 0.015±0.013 | 2.0±0.2 |

### 7.3.2 Clustered lesion yields

Using eq. 7.16 we have evaluated the expected yield of clustered lesions (which may contain base damages and not only strand breaks). As can be seen from figure 7.3, the biophysical model overestimates the yield of clustered lesions (CL) by a factor of approximately two. As the DSB data is in rather good agreement with the model, we must assume that we have overestimated the efficiency of transforming clustered base lesions to DSBs in the bacteria. In the model we have assumed that if two base lesions are formed, on opposite strands, within a 10 bp DNA segment, they will always be converted to a DSB. It would be more reasonable to measure the probability of converting two base lesions to a DSB as a function of their spacing. Some work in this direction has been conducted by D'Souza et al. [94].

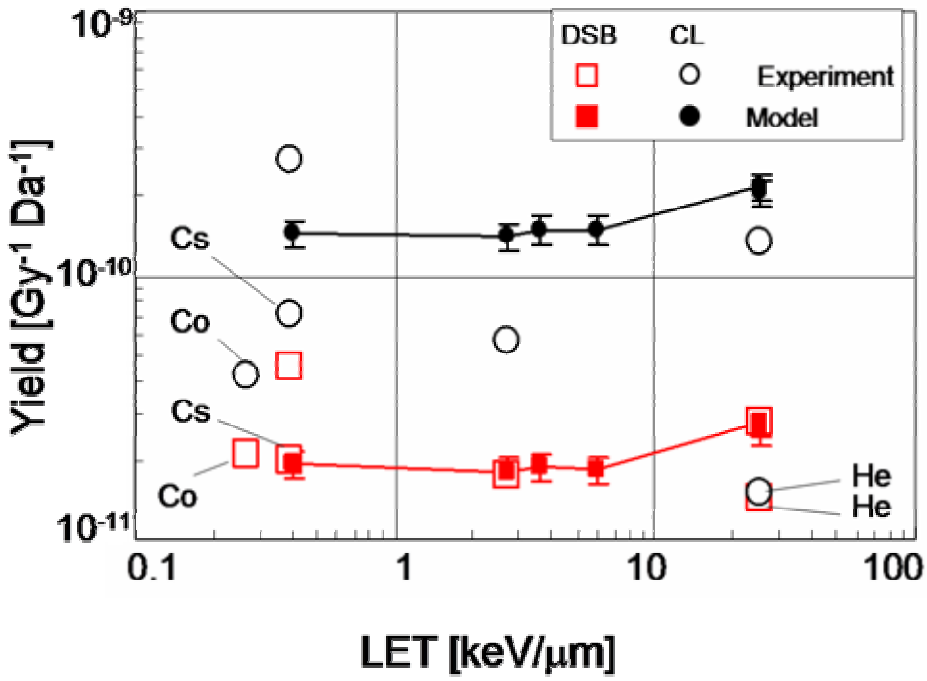


**Figure 7.3: The model calculated yield of DSBs (squares) and clustered lesions (circles).** The measured data (open symbols) are compared to the model prediction (closed symbols). Based on the model parameters: $p_{SB}$=10% $p_{tot}$=35%. The $^{60}$Co and $^{137}$Cs data are shown for reference. The experimental He values are noted, the model predicted ones are not discernible from the proton values of the same LET.

## 7.4 Conclusions

The nanodosimetric cluster-size distributions give a good description of the radiation effects in a gas model of condensed matter. This description is only valid for the first few psec after the particle track is formed. But following the initial ionization process, radicals are generated and diffuse to and form lesions in the DNA, on a nsec time scale. The DNA lesions are then repaired (or misrepaired) by the inter-cellular DNA repair mechanisms (within minutes to hours).

We have presented a simplified biophysical model for predicting the yields of clustered lesions in irradiated DNA based on ion cluster size distributions measured in the ND. The model rests on two main assumptions, (1) that the ND gives a good modeling of the radiation interaction with DNA and that (2) each ionization, formed in tissue, is converted to a lesion in DNA with fixed probability, regardless of any other ionization which may have occurred. The validity of these assumptions is discussed in detail in §8.3 below.

Applying the biophysical model presented here to the measure ion cluster size distributions, we have obtained a good prediction of the yield of DSBs, measured in §6.4.2.3. We could not reproduce the measured yield of SSBs or of clustered lesions, containing also base damages. The reasons for this, as well as possible modifications to the model are discussed below.

# Chapter 8 :

# Discussion

The methods and results of this work have been described in detail in chapters 3-7. Here we will present a concise discussion of our main results as well as of key points in the techniques we have employed.

We have set out to design and build an **ion-counting nanodosimeter (ND)**, in order to study the interaction of radiation with matter on a nanometer scale. In particular we are interested in investigating the basic physical phenomena (ionizations and their clustering) leading to the formation of irreparable damage in DNA. In order to interpret the **ionization cluster size distributions** obtained with the ND in different radiation fields, we have performed **systematic radiobiological studies**, irradiating plasmid DNA in similar radiation fields (see §6.1.2 for a discussion of the irradiation conditions). The measured cluster size distributions were converted into lesion-cluster yields, by a **basic biophysical model** developed within this work.

## *8.1 The ion-counting nanodosimeter*

The ion-counting nanodosimeter models a condensed matter target with a gas bubble of "similar" atomic composition, but considerably reduced density; in our case we modeled DNA (~ 1 g/cm$^3$) with 0.9 Torr propane (2.1 $10^{-6}$ g/cm$^3$). The validity of this gas model rests on the fact that the interaction mechanisms as well as their cross sections are independent on the density of the medium, as discussed in detail in [34, 119] and in §2.2.3.

### 8.1.1 The nanodosimeter's main properties and comparison with other techniques

The ND consists of a gas-filled ionization volume, coupled via a 1 mm aperture to a vacuum region containing an ion counter (IC). Ions, formed within a subsection of the gas volume (termed the sensitive volume - SV) are extracted with known efficiency from the SV, transported to and counted by the IC. We have written dedicated simulations for evaluation of the SV and the ion extraction efficiency, and for characterization of the DAQ response.

In order to perform reliable measurements of the small radiation-induced ionization clusters, inherent in nanometer size targets, we have designed the ion-counting nanodosimeter to be insusceptible to many systematic errors, appearing in other nanodosimetric devices (the single electron counter – SEC [63] and the Jet counter [80]), discussed in §2.3.

Our nanodosimeter's SV is defined by *electric fields*, rather than by *physical walls*. The adverse effects of placing solids within gas-based detectors have been discussed extensively in the literature [49, 120]. Our ND is totally wall-less: the gas is ionized between two electrodes and radiation-induced ions are extracted from a sensitive volume situated far from both; ions formed close to one of these electrodes are rejected in the offline analysis. The SV size may be adjusted by varying the gas pressure, aperture size, electric fields, or by an offline time selection of ions arriving to the ion counter from sub-sections of it. This is a significant improvement over the SEC and the Jet counter, where only the first two adjustments are available and the SV aspect ratio cannot be varied without disassembling the device. In this work we studied several sensitive volumes ranging in length from 3 to 120 tissue-equivalent

nm and diameters of 3-5 equivalent nm. All measurements could have been performed, in principle, on the same day (by varying the voltages on the ND between measurements); variations of the SV length could be performed by a different offline analysis of the same data set.

Other common techniques, based on the detection of radiation-induced electrons, cannot achieve such small sensitive volumes. This is due to the ten-fold higher diffusion coefficient of electrons with respect to ions, which prevent their efficient detection. Furthermore, the ionization- induced electrons are formed with a relatively high initial kinetic energy; subsequently they will be detected far away from the location of the actual ionizing impact. Electron-based detection techniques, used to probe radiation effects on scales comparable with the track structure, will therefore overestimate the size of ionization clusters (i.e. damage yields in the DNA) in the track's halo at the cost of that in the track's core. Nevertheless electron based techniques currently enable imaging of long track segments [70-72] as well as measurement of neutral particles (neutrons and γ-rays – e.g. [47, 48]) with sub-micron (equivalent to sub-cellular) resolution. These features are not yet available using ion based techniques.

The ion extraction from the SV as well as its transport to the ion counter (IC) and subsequent detection has been thoroughly optimized. MC simulations as well as precise scanning measurements with narrow beams have shown that an ion deposited on the axis of the SV at a distance of 15 mm (42 equivalent nm) from the ion-extraction aperture will have a chance of more than 80% of being detected in the IC of figure 3.16b (where no offline selection is made) and more than 70% for the center of the DNA-equivalent SV that we have used in our modeling (6.5 equivalent nm length - see figure 7.1b). Obtaining a SV of shorter length by applying time cuts would result in much lower efficiencies, due to ion-diffusion, however smaller sensitive volumes can be obtained by a further reduction of the gas density. These SV sizes and ion-detection efficiencies should be compared with an estimated 40-50% (figure 7 of [82]) for the Jet counter operated at SVs of 0.15-2 equivalent nm and height and less than 20% (figure 7 of [63]) for the SEC, operated with a SV of 20nm diameter. Ion-counting inefficiencies (which would lead to an underestimation of the predicted damage in DNA) were seen only for very large ion-clusters containing more than 20 ions, which could not be reliably counted using our present data acquisition (DAQ) system. The SV modeled by the ND as well as that of the SEC (and probably also that of the Jet counter although no measurements or simulations have been made so far) is not a sharply defined one; the ion-extraction efficiency is maximal on the SV axis and drops smoothly to zero. This is similar to the case in the irradiation of DNA where ionizations formed far from the DNA have a lower (but nonzero) probability of causing a lesion in it, mainly via the mechanism of $OH^{\bullet}$ radical formation and their diffusion. Although this type of SV should give a better modeling of DNA damage than one with a uniform efficiency and a sharp cutoff, we have seen that our predicted yields of damage yields in DNA do not depend on the SV shape and size.

Some secondary effects leading to the formation of excess ions were seen both in the SV and below the ion extraction aperture. The former was completely solved by pulsing the ion-extracting filed; the latter, though very small, could not be solved and resulted in an over estimation of the yield of rare large clusters, appearing at frequencies below $10^{-3}$.

Using MC simulations we have shown that the ND is capable of operating at high beam fluence (up to 10kHz, depending on the trigger detector efficiency). This is required for precise measurements of the ion cluster-size distributions of low LET radiations (e.g. 250 MeV protons), where large ionization clusters are exceedingly rare. Similar beam fluxes can possibly be used in the SEC but not in the Jet counter. The latter requires the projectile particle to pass through the ionization volume within a short time window (200 μsec) and long dead time (0.2 sec resulting in a 10% duty cycle).

As expected from the small SV diameter (approximately 2mm in gas) the ND is extremely sensitive to beam alignment, during pencil beam irradiations. This is not a limitation when the ND is irradiated by a broad, homogenous radiation field, as required for biological measurements.

### 8.1.2 Nanodosimetry results

Although many microdosimetric detectors (such as the OPAC [72]) are extensively used for accelerator-based studies of radiation damage in sub-cellular targets, our ion-counting nanodosimeter is the first device of its class, modeling DNA-sized targets to be operated in an accelerator environment. We have operated our ND at three different accelerators (the UD14 Pelletron and the 2.5 MV Van de Graaff at WIS as well as the 250 MeV proton synchrotron at LLUMC) and performed measurements in biologically meaningful sensitive volumes using radiation fields having LET values between 0.4 and 700 keV/μm.

Cluster size distributions were measured using pencil beams (1mm diameter) as well as broad uniform beams (diameters of 7 and 20 mm), much wider than the size of the SV. While the pencil beam irradiations were found to be extremely useful for characterization of the ND, it is rather complicated to use them for prediction of radiobiological effects in DNA, where there is no spatial correlation between the radiation track and the DNA target. We therefore exposed the ND to broad, uniform particle beams having diameters much greater than the SV. Although the radiation fields we have employed for these studies were indeed homogenous, they could not, for technical reasons, be made isotropic; we believe, however that this will only have a minor effect on the results (§5.1) and that our irradiation conditions corresponds to the true radiobiological situation where there is no spatial correlation between the particle track and the cellular DNA.

Throughout this work, extensive use has been done of model-based MC simulations: we have employed the track-structure code developed by B. Grosswendt (PTB, Germany). This is the same code (with slight modifications, to fit our experiment) that is employed for modeling both the Jet counter and the SEC. Using MC simulations we have predicted that a beam diameter of ~40 equivalent nm is sufficient for modeling a uniform radiation field. In reality we have seen that a smaller beam diameter (6.5 mm) is practically sufficient; this is due to the rarity of very energetic δ-electrons which in principle could cause damages far from the track's core.

An alternative, but time-consuming approach would be to expose the ND to many pencil beams at known distances from the SV and then to sum the cluster size distributions, "reconstructing" a broad beam. Using this technique it is easy to reconstruct beams of any given diameter or indeed any shape, by a different "reconstruction" using the same measured data. Systematic studies in this direction, using the SEC, are described in [65] and will also be performed using the ND at the LLUMC proton synchrotron, for the study of proton-therapeutic beams.

In general there is a rather good agreement between the measured ion cluster size distributions and the simulated ones in all conditions where the accelerator beam is well defined. In particular the pencil beam measurements and simulations agree with each other rather well. For the broad beam studies the agreement was rather good in most cases, except for the 1 MeV and 250 MeV proton data. In the case of the 1 MeV data this was found to be due to an inaccurate modeling of the proton beam geometry (which was not sufficiently uniform) in the simulations, resulting in an underestimation of the yield of zero-ion clusters. In the 250 MeV this may be due to a triggering problem. In both cases the conditional cluster size distributions, used in the prediction of the DNA-damage yields were in good agreement with the simulated ones. The good agreement between the measured results and the simulated ones provides an indirect way of comparing the reliability of our accelerator-based data with that of the SEC [63] and the Jet counter [82], both measured with radioactive alpha particle

sources. In all three cases the **same track-structure MC code** is in good agreement with the measured results.

We also attempted to compare our data with that of the Harwell cloud chamber [42].This is not straightforward as the SV size, alpha particle energy and operating gas are different, however a qualitative agreement can be seen between the data of figure 6 of [43] and our measurements. In our measurements we found an average cluster size of 10.5 ions in a 4.5 nm long track segment, while the Harwell group found an average cluster size of 25.1 ions in a 10 nm long track segment [42].

Comparing various radiation fields we have seen the expected rise in the yield of large ionization clusters with increasing LET. A particularly interesting measurement is the comparison of the ionization cluster size distributions induced by protons and helium nuclei of the same LET. It is expected that the proton-induced cluster size distribution will contain a higher frequency of few-ion clusters, due to the more compact track structure. This was indeed seen in this work.

## *8.2 Radiobiological studies*

In order to interpret the nanodosimetric cluster-size distributions in terms of radiobiological damage, we have developed a corresponding biological test-system and measured the radiobiological effect of the same radiation fields in "live" DNA irradiated under well-controlled conditions (for discussion of the irradiation conditions see §6.1.2).

The purpose of these measurements is to quantify the yield of single- and double-strand breaks (SSB, DSB) and clustered lesions (CL), induced by single particle tracks in DNA. These measurements were performed for protons of various energies (250, 19.3 and 1.03 MeV having respective LET values of 0.39, 2.7 and 25.5 keV/μm), helium nuclei (26 MeV – 25.5 keV/μm) and gamma rays (about 0.2-0.4 keV/μm). The latter were used as a low LET reference for comparison to the published data (see below). The proton energies were chosen so as to span the LET range relevant to proton therapy [118]. In these measurements we could study the LET dependence of the various damage yields as well as their variation between radiation fields having the same or similar LET values.

### 8.2.1 Radiobiological test system

Typical radiobiological test systems are based on the irradiation of live cells and a subsequent, complex, evaluation of the yield of DSBs and of bacterial survival. However, experimental results of the LET dependence of the DSB yield in cells have been controversial. It is now believed that current techniques of DSB measurement in cells underestimate the true yield of DSBs [121], which may at least partially explain this discrepancy. We have therefore chosen a plasmid solution as our test system, in which the evaluation of break yields is simple. The plasmid system is however experimentally more complicated than the cellular one: In cellular systems, the cells are simply grown on a polymer foil, naturally forming a thin layer and can be easily irradiated, washed off and later analyzed. In the plasmid system, the plasmid must first be purified to a high degree, care must be taken to maintain the appropriate scavenging capacity of the irradiation buffer and a thin liquid film must be formed and maintained for the period of irradiation.

Our radiobiological test system consists of an aqueous solution of plasmid DNA and a given amount of radical scavenger (chosen to mimic the inter-cellular radical scavenging capacity). Due to the rapid energy degradation of low-energy ions in matter (1 MeV protons in particular), we have irradiated the DNA as very thin films (10-16 μm) over a wide range of doses. The irradiated DNA was scored for SSBs and DSBs, using gel electrophoresis (§6.3.2). The DNA was also transformed into repair deficient (*RecA*$^-$) bacteria (§6.3.3) allowing us to

quantify the yield of clustered lesions. In both cases we have calculated the damage yields due to a single particle track by fitting a statistical model ([111] and appendix C) to the measured dose-dependant yields.

A great effort was put to verify that our irradiation protocol does not result in a significant yield of damages to the irradiated DNA, beyond those induced by the particle radiation field. In particular we have seen that (a) the weak proton-induced activation of the quartz substrate does not induce a noticeable quantity of additional SSBs or DSBs compared to a proton irradiation of the same duration; (b) the storage of the DNA as a thin film within the sample holder for up to eight hours (at room temperature) does not induce a significant quantity of SSBs or DSBs.

### 8.2.2 Choice of scavenging conditions

In order to try and study the relative contribution of the direct and indirect effects (§2.1.1) we have measured damage yields in conditions where the direct effect is insignificant (2 mM glycerol) as well as in conditions mimicking the cellular environment (200 mM glycerol). We observed that in general the damage yields are 5-20 times lower for irradiation in the presence of 200 mM glycerol compared to 2 mM due to the protective effect of the glycerol. At high LET, the magnitude of the indirect effect is somewhat reduced due to the higher concentration of radicals resulting in increased radical recombination. This effect was seen to slightly reduce the differences in yields between the two scavenger concentrations.

### 8.2.3 Results

The data presented here represent a year of intensive efforts, during which we made precise measurements of the absolute yield of single- and double-strand breaks as well as of clustered lesions in DNA irradiated *in vitro*. As described above, these measurements are extremely complicated, requiring precise control of the irradiation conditions and extremely pure DNA. Only through these strict requirements does it become possible to collect meaningful biophysical data which may be compared to the nanodosimetric results

#### 8.2.3.1 LET dependence of damage yields

As the yield of ionizations per unit dose (namely $1/w_i$) is practically independent of LET [39], we would expect to find **no dependence** of the yield of isolated damages (SSBs and base damages) on LET. The negative slopes seen in figures 6.9 and 6.10 are due to radical recombination. In general, the vast majority of SSBs will be caused by interaction with $OH^{\bullet}$ radicals. Higher LET favors recombination of radicals formed in closely spaced spurs explaining the relatively strong decline of SSB yields with increasing LET. At the high scavenger concentration the influence of the indirect effect on SSB yields is reduced, which explains the difference in slopes.

The yield of DSBs and clustered lesions (figures 6.11 and 6.12) shows a more complicated relationship with LET, starting with a relatively high yield for 250 MeV protons, going through a minimum around 19.3 MeV and then rising again to a higher value for 1 MeV protons. Despite the several-fold larger yield of all clustered lesions compared to the DSB yields, the general LET dependence is very similar in both cases. One should note here that we could not distinguish between DSBs and clustered lesions of different sizes (i.e. a different number of individual lesions per damage) and that the yield of clustered lesions of larger sizes may have a different LET dependence than the yield of all lesions.

The LET dependence of the yield of CLs as well as DSBs (a subset of all CLs) is determined by the following factors: (1) the number of closely spaced radicals escaping the recombination process, and (2) the overall level of clustering of radicals and direct ionizations

on the DNA. These factors are modulated by the amount of scavenger present in the irradiated solution.

In all radiation fields DSBs and other clustered lesions are mainly formed by local regions of higher ionization density, which historically have been termed “spurs” and “blobs” [122]. At low LET, these events are widely spaced. As the LET increases, spurs and blobs become more closely spaced and may overlap thereby increasing the size of ionization clusters, and also of $OH^{\bullet}$ radical clusters. While the first effect (closer spacing) favors $OH^{\bullet}$ radical recombination and thereby reduces the yield of DSBs, the second effect (larger size of ionization clusters) favors the production of DSBs and clustered lesions. The competition of these two phenomena is probably responsible for the observed concave LET dependence of the yield of clustered lesions seen for protons.

#### 8.2.3.2 Track structure dependence of damage yields

The LET is not a sufficient parameter to describe the effect of various radiation fields as supported by the track structure effect that was observed for protons and helium nuclei of same LET (25.5 KeV/μm) as well as for 250 MeV protons and γ-rays having similar LET values. At both glycerol concentrations, the DSB and clustered lesions yields, obtained for plasmids irradiated with protons was higher than for the plasmids irradiated with helium nuclei (figures 6.11 and 6.12). This can be explained by the (radially) denser track structure of protons [123] compared to helium nuclei leading to closer ionizations and more clustered damage (e.g. see figure 5.1).

At both glycerol concentrations, the yield of SSBs is twofold higher for protons than for helium nuclei (see figure 6.9). This result may seem surprising at first. One would expect that the denser ionization track structure of 1.03 MeV protons (leading to the observed higher yield of large ionization clusters – see figure 5.11) causes fewer isolated lesions such as SSBs. This may be explained by the existence of additional damaged bases, which cannot be detected on the gel. Thus, the gel analysis cannot distinguish between isolated SSBs and lesion clusters consisting of one SSB and one (or more) damaged bases. The yield of this kind of clusters is indeed expected to be higher in the proton irradiations, compared with helium nuclei of the same LET and may explain the higher SSB yield seen with protons. In this case we would expect that the number of isolated lesions (a single SSBs or a single base lesion) would be the same (or slightly lower for protons due to increased recombination in its track). We have not been able to reliably quantify the yield of isolated lesions from the Cowan model for this case.

At low LET, we have compared γ-rays from $^{137}Cs$ and $^{60}Co$ radioactive sources (about 0.2-0.4 keV/μm) with 250 MeV protons (0.39 keV/μm). Although $^{137}Cs$ and $^{60}Co$ are generally considered equivalent low LET radiations, the break yields seem to be slightly different for *in vitro* irradiated plasmids. There was a consistently higher SSB yield (approximately twice higher) for $^{137}Cs$ irradiation than for $^{60}Co$ at similar scavenger concentrations. The proton-induced yields were higher than both. For DSB, there was a similar difference for the low scavenger data only. One may explain the difference between $^{137}Cs$ and $^{60}Co$ based on the different energy spectrum of Compton electrons generated by γ-rays of different energies from these two sources (1.17, 1.33 MeV γ-rays for the $^{60}Co$ and a 660 keV γ-ray for the $^{137}Cs$). The $^{60}Co$ γ-rays will generally generate Compton electrons which are twice more energetic (590 keV compared to 250 keV for $^{137}Cs$), resulting in half the yield of electron track ends per unit dose. It is expected therefore that the damage induced by $^{137}Cs$ γ-rays will be more clustered. The difference between protons and $^{137}Cs$ γ-rays is similarly explained by comparing the (lower energy) δ-electron distribution of the protons to the Compton electron distribution of the γ-rays. This difference in yields results from the formation of small radical clusters as indicated by the fact that it is seen in the formation of SSBs and in the low scavenger formation of DSBs. It is virtually not seen in DSBs at high scavenger concentration and not seen at all in the formation of complex lesions. The yield of isolated lesions, as quantified from the bacterial survival assay was the same (figure 6.10).

As far as we know, this is the first time that such a radiobiological difference between these two γ-ray sources ($^{60}$Co and $^{137}$Cs) and low-LET protons has been quantified directly in DNA. Variations of similar magnitude in the reproductive survival of V79 and HeLa cells, were reported in [124], from data of several γ-ray sources and heavy-ion irradiations. This finding demonstrates that the common notion that all γ-rays have the same relative biological effectiveness (RBE) (and in particular the equivalence of $^{137}$Cs and $^{60}$Co γ-rays) is inaccurate and that one should be careful using γ-rays, (rather than x-rays [118]) as a low LET reference.

The track structure effects can also be seen from the dose dependence of the clustered-lesions yield (figure 6.10). As LET increases and track structure becomes more compact, one can expect that the fraction of clustered lesions arising from a single-hit mechanism will increase compared with that arising from multiple hits. This is supported by our observation that the log bacterial survival curves for protons and helium nuclei of higher LET (25.5 KeV/μm) has a linear or almost linear dose response, indicating the prevalence of the one-hit mechanism, while log survival curves for lower LET radiation fields displays a nonlinear dose response, indicating that the damage was caused mainly by a multi-hit mechanism.

### 8.2.4 Comparison with other works

In table V we present the strand breaks yields obtained by us together with those obtained by other groups for comparable irradiation conditions. As data for bare DNA irradiated in aqueous solutions is scarce, we could not find other results taken at our exact conditions; however, the correspondence between our data and that measured in similar conditions is reasonable. In some cases we have interpolated data from a log-log graph, to fit our conditions, obtaining indicative, rather than exact, values, especially for the DSB yields.

In general there is a good agreement between our data and those of [109,110, 125-129].

| DNA type | Scavenging capacity [$s^{-1}$] | Radiation field | SSB yield [$Gy^{-1}$ $Da^{-1}$] | DSB yield [$Gy^{-1}$ $Da^{-1}$] | Ref. |
|---|---|---|---|---|---|
| SV40 | $1.5\ 10^{6}$ | 60Co | $2.3\ 10^{-8}$ | $8.8\ 10^{-10}$ | 125 |
| **plasmid** | **$3.8\ 10^{6}$** | **60Co** | **$8.5\ 10^{-9}$** | **$1.6\ 10^{-10}$** | **Our data** |
| **plasmid** | **$3.8\ 10^{8}$** | **60Co** | **$5.5\ 10^{-10}$** | **$2.0\ 10^{-11}$** | **Our data** |
| plasmid | $6\ 10^{8}$ | 60Co | $4\ 10^{-10}$ | $1\ 10^{-11}$ | 126 |
| plasmids † | $3.6\ 10^{6}$ | 137Cs | $2\ 10^{-8}$ | | 109 |
| **plasmid** | **$3.8\ 10^{6}$** | **137Cs** | **$1.8\ 10^{-8}$** | **$3.1\ 10^{-10}$** | **Our data** |
| Plasmid | $7.1\ 10^{6}$ | 137Cs | $1.5\ 10^{-8}$ | $1\ 10^{-10}$ | 110 |
| Plasmid† | $3.6\ 10^{8}$ | 137Cs | $1\ 10^{-9}$ | | 109 |
| **plasmid** | **$3.8\ 10^{8}$** | **137Cs** | **$1.0\ 10^{-9}$** | **$2\ 10^{-11}$** | **Our data** |
| Plasmid | $7.1\ 10^{8}$ | 137Cs | $6\ 10^{-10}$ | $6\ 10^{-12}$ | 110 |
| SV40 | $1.5\ 10^{6}$ | 20 keV/μm He | $1.8\ 10^{-8}$ | $8.8\ 10^{-10}$ | 125 |
| **plasmid** | **$3.8\ 10^{6}$** | **25.5 keV/μm He** | **$1.8\ 10^{-9}$** | **$1.3\ 10^{-10}$** | **Our data** |
| SV40 | $3.1\ 10^{7}$ | 26 keV/μm He | $1.8\ 10^{-9}$ | $7\ 10^{-11}$ | 127 |
| **plasmid** | **$3.8\ 10^{8}$** | **25.5 keV/μm He** | **$3.0\ 10^{-10}$** | **$1.4\ 10^{-11}$** | **Our data** |

**Table V : Comparison of our data (boldface) with that of other groups.** † Similar results obtained with various plasmids and SV40 DNA.

Our data for $^{60}$Co irradiation agrees well with that of [125] and of [126]. We expect the yields of SSBs as well as those of DSBs to increase with decreasing scavenger concentration as is indeed seen. For the Cesium 137 irradiation, the yields of SSB are consistent with the data of [109]. The helium nuclei data, shown in table V, gives a consistent picture of our results within the framework of existing data; both our SSB and DSB yields fit well with those of [127] and [125], giving a consistent dependence on scavenger concentration.

We could not find data for plasmid irradiation with protons in conditions comparable to ours. To the best of our knowledge our work is the first time that such results are presented.

The twofold difference in the yields of DSBs and CLs, that we have observed between same-LET protons and helium nuclei, are in good agreement with the data of Goodhead et al. [102-104]. They compared the yields of bacterial inactivation of 1.2 MeV protons with 30.5 MeV helium nuclei (an LET value of 22 keV/μm and 23 keV/μm respectively) and those of 1.4 MeV protons with 35 MeV helium nuclei (LET values of 19.5 KeV/μm and 20.5 keV/μm). They have seen that the difference in cellular inactivation depends largely on the type of cell irradiated. Goodhead et al. have found that, in general, protons are more effective in cellular inactivation than helium nuclei. This is in good agreement with our findings that protons are more effective in the formation of clustered lesions. The large variance between cell types they have observed is probably due to the effectiveness of the cellular DNA repair mechanisms in repairing clustered lesions. In this sense, our measurement is a cleaner one. In principle it should be possible to predict the results of [102-104] using our data together with a comprehensive knowledge of the cellular damage processing mechanisms; such knowledge is not yet available.

## 8.3 The biophysical model

In order to predict the actual radiation damage in DNA we have developed a simplified biophysical model based on the ion cluster size distributions, measured in the ND. The model assumes that there is a one-to-one correspondence between the ionizations measured in the ND and the ionizations that would be induced in condensed matter by the same track (assumption #1 in §7.1.1). The model further assumes that each ionization is converted to a lesion in DNA with a fixed probability, which depends on the lesion type but not on the number of ionizations formed (assumption #8 in §7.1.3). The validity of the first assumption is discussed in detail in §2.2.3 above. The validity of the second is somewhat problematic.

*In vivo*, about two thirds of the radiation-induced damage is due to the radical-mediated indirect effect (see table III in §6.1.2). We have seen that the yield of lesions induced by the indirect effect is determined by a complicated interplay of the ionization density and the recombination of radicals. Hence we would expect the probability for a single ionization to create a lesion in DNA to decrease with increasing LET (due to increasing recombination). Incorporation of this effect into the biophysical model would require a full description of the track structure on a scale of tens if not hundreds of nm; such a description is unavailable with the current ND. However the knowledge of the track structure is not sufficient for obtaining reliable lesion yields; a full simulation of the radical diffusion and recombination (see for example [130]) including all possible chemical reactions, scavenging etc' would be required. We describe the ideal ND and model in §8.4 below. Keeping in mind that neither the ideal ND nor the ideal model can be realized within this work we have preferred to assume that, at the high radical scavenging, where radical diffusion distances are short, radical recombination does not play a significant role in the formation of lesion clusters. Indeed we have seen that our biophysical model provides a rather good prediction of the yield of DSBs but greatly underestimates that of SSBs.

Based on these two assumptions as well as on other technical assumptions pertaining to the radiation field and the biological endpoints under study (see §7.1 for discussion), we have developed a combinatorial relationship between the conditional ion cluster size distribution, $\varphi(n_{ion})$, and the yield of strand breaks and base lesions. This model has only one free parameter, $p_{SB}$ - the probability for a single ionization to be converted to a single strand break. A second parameter, $p_{tot}$ (the probability for a single ionization to be converted into a single lesion) is derived from it based on the known ratio of lesions to strand breaks (discussed in §6.3.3). The value for $p_{SB}$ was determined by requiring a best fit of the model to the experimental DSB yields; this gives a $p_{SB}$ value of 10%. This value can be seen as an average of the probability of a direct ionization in the DNA leading to a strand break and the

probability of a radical formed in the water surrounding the DNA to drift to the DNA and form a strand break. While the former is unknown, the latter can be compared to the estimated efficiency of SSB induction per $OH^{\bullet}$ radical interaction with DNA of 32%-44% [109] (we get our value of $p_{SB}$ by arbitrarily assuming that a radical formed near the DNA will drift towards it in 33% of the cases).

We have also assumed that the biologically relevant sensitive volume and the nanodosimeter sensitive volume are of *roughly* the same size. Small variations in the sensitive volume dimensions could be absorbed into the parameters $p_{SB}$ and $p_{tot}$. It is therefore clear that the values that our model attributes to these parameters are strictly valid only for interpretation of data measured with one particular gas sensitive volume. The use of another gas volume of similar but not identical dimensions would require a "calibration" step; the values of $p_{SB}$ and $p_{tot}$ will need to be set such that the model prediction fits the DSB yield at one LET value. In this work we compare biological clustered damages, which are assumed to occur in a 10 bp segment of plasmid DNA, with ionization clusters in a gaseous sensitive volume of about 6.4 nm long, 4.5 nm in diameter; the SV corresponds to 10 base pairs, including a 1.5 equivalent nm shell of water molecules. For a deeper discussion of this assumption, see §3.4.3.

### 8.3.1 Results

Although the biophysical model developed in this work is a simplified one, it is encouraging to see that it provides a rather good prediction of the yield of DSBs in irradiated DNA (figure 7.3).

When we try to use this model for predicting the yield of isolated lesions (such as SSBs) we find that it underestimates them by a factor of about three. It seems that this is due to the fact that, in the nanodosimeter, we do not measure ionizations (single or clustered) formed far away from the sensitive volume, and they are not taken into account whatsoever; but such ionizations in the biological model system induce radicals which do arrive to the DNA corresponding to the so-called *indirect effect*. Indeed in physiological conditions the indirect effect accounts for about two thirds of the yield of SSBs (see table III). It is in principle possible to measure this effect with the gas model, using a much larger sensitive volume (tens of nm in diameter) but this was not done within this work.

The model overestimates the yield of clustered lesions by a factor of about two. As the DSB data is in rather good agreement with the model, we must assume that we have overestimated the efficiency of transforming clustered base lesions to DSBs in the bacteria. In the model we have assumed that if two base lesions are formed, on opposite strands, within a 10 bp DNA segment, they will always be converted to a DSB. It would be more reasonable to measure the probability of converting two base lesions to a DSB as a function of their spacing; some work in this direction has been conducted by D'Souza et al. [94].

In order to obtain more accurate predictions it is necessary to take into account also the radical-mediated indirect effect. This can be done by performing nanodosimetrical measurements in larger sensitive volumes (10 nm diameter or more) and using a diffusion-kinetic model [130, 131] to calculate the transport and recombination of $OH^{\bullet}$ radicals.

It is also necessary to better model the response of a biological system to clusters of strand breaks and base lesions. This can be done using synthesized DNA oligonucleotides, containing base lesions at specific locations. Some progress has already been made in this direction [94, 95].

We contend that such a complex model could be built based on nanodosimetric data, but would require a more rigorous and comprehensive representation of the biochemical environment of the DNA. However, despite its simplicity, our model demonstrates the

feasibility of correlating ion cluster-size distributions measured in a DNA-equivalent gas volume (nanodosimetric data) to real irradiated DNA.

## 8.4 General discussion and future outlook

The data presented in this work depict a qualitatively (if not quantitatively) consistent picture of the mechanisms of radiation damage in DNA. We have seen that the ionization clustering increases linearly with LET, as it should. At the same LET we have also seen (in one case) that the ionization clustering increases with decreasing δ-electron energy. Our ion cluster size distributions are in good agreement with other, similar, distributions obtained both by electron counting in TE gas [65, 119] and by ion counting in nitrogen [81, 119] (both for 4-5 MeV alpha particles). Using MC simulations we have also seen that our measured distributions are about 12% different from those which would be measured in liquid water (see figure 2.5). Based on these facts we can confidently claim that **the nanodosimetric ion cluster size distributions can be interpreted as ionization cluster sizes in nanometric volumes of irradiated tissue.**

Using a simplified and biophysical model containing one free parameter, whose value is within reasonable agreement with the experimental values quoted in [109], we have predicted the measured DSB yields in irradiated DNA. We have seen that our biophysical model is too simplified for predicting the yield of other types of damage.

We have operated the nanodosimeter as a scientific research tool, for deeper studies of the mechanisms of the interaction of radiation with condensed matter on nanometer scales. We envision its future operation as a diagnostic tool for the characterization of unknown or mixed radiation fields. A ND is currently installed at the LLUMC proton synchrotron where measurements of ionization clusters in degraded proton beams (used for proton therapy of cancer) are being conducted.

By replacing the propane filling gas with "semiconductor-equivalent" gases (Silane for example) the ND can be adapted to studies of radiation damage to micro- and nano-electronic devices, for example in space. This cannot be easily done with proportional chambers which do not operate with such exotic gases.

The ND, developed within this work, requires a trigger on each projectile passing through it. This requires some knowledge of the radiation field being investigated and does not permit measuring neutral particles. This limitation can be lifted by designing a *hybrid nanodosimeter*, consisting of a standard ion-counting nanodosimeter equipped with an additional electron-counting device (such as a SEC described in §2.3.1) both detectors having concentric sensitive volumes. This is somewhat similar to the image shown in figure 2.6: a radiation track traversing a gas volume induces ions and electrons in it. The ions are extracted into vacuum (from a nanometric sensitive volume) and counted while the electrons are simultaneously extracted in the opposite direction, multiplied and imaged. The electron component can be used as a trigger for the ion detector.

As we have seen, when trying to predict lesion yields in DNA, it is also important to take into account the radical-mediated indirect effect which cannot be modeled with the current ND. Using the suggested hybrid nanodosimeter we would be able to measure the ionization density also at larger scales (using the electron-counting properties) and model the formation of radicals far away from the SV by the **same track**. This will enable formulating a **more accurate biophysical model**. As we did in the present work, such a model should be calibrated, using a set of systematic radiobiological measurements. Such measurements, providing a direct quantification of radiation-induced DNA damage, are rather labor-intensive and require high doses, precise dosimetry and well-controlled conditions. These requirements can only be obtained in a laboratory setting and prohibit the application of this type of experiment for radiation protection/monitoring. For example, when studying complex radiation fields (such as in a degraded therapeutic beam), precise dosimetry is almost

impossible (due to the different depth dose curves of the various radiation fields) and a systematic study becomes extremely difficult. The combination of a nanodosimeter and a reliable biophysical model in these conditions would yield a more precise prediction of -damage yields than is available today.

# Chapter 9 :

# Conclusions

In this work we have developed, studied and applied a novel nanodosimeter to the study of radiation damage in DNA. The ion-counting nanodosimeter represents a significant improvement over existing techniques for the study of radiation effects, enabling **for the first time**, the modeling of the interaction of radiation with condensed mater on a **nanometer scale**. Taking that the most critical targets for radiation action are short nanometric segments of DNA, the importance of understanding, measuring and modeling radiation action at this scale is obvious. Before this work the radiation-track structure on nanometer scales was only accessible via MC simulations (e.g. [117]).

The ion-counting nanodosimeter provides a **wall-less, nanometer scale** sensitive volume, simulating (in principle) any type of condensed matter target. As required in such small sensitive volumes, the nanodosimeter is sensitive to and can accurately measure the single ionizations induced stochastically by radiation within them. On the other hand the nanodosimeter provides the possibility of operating in high particle flux as in accelerator environment, providing the possibility of quantifying the yields of rare, large ionization clusters, believed to be the cause of irreparable radiation damage.

We have shown, in this work that the ion-counting nanodosimeter provides a reliable, precise method for characterization of the nanometric track structure of ionizing radiation. We have investigated the implementation of a nanodosimeter within an accelerator environment and found the optimal operating protocols such that the measured cluster size distributions represent **true physical quantities** rather than instrumental parameters. We have shown that the ion-counting nanodosimeter can operate **reliably** and **reproducibly** at moderate particle repetition rates (up to 10 kHz) and can reliably quantify the frequency of rare, large ionization clusters down to a frequency of $10^{-3}$.

Using our nanodosimeter, we have measured ionization cluster size distributions induced by various charged particle beams, spanning a large range of specific ionization values. The measurements were made in conditions corresponding to those encountered in the actual irradiation of biological specimens, as for example in radiation therapy.

In order to test the relevance of nanodosimetry to radiation biology, we have irradiated aqueous solutions of plasmid DNA using various radiation-fields (equivalent to those used in the nanodosimetric measurements) and quantified the clustering of damage in these *in-vitro* irradiated plasmid DNA. We have quantified all lesions, strand breaks as well as base damage, in a repair deficient environment. In order to compare the results of the two types of experiments we have developed a basic biophysical model predicting the yield of clustered lesions in DNA segments based on the ion cluster size distribution in equivalent gas volumes. Although this is a simple model, which neglects some important processes related to single-damage creation and repair, we have been able to predict the trends observed in the biological data, particularly those related to clustered damage – of relevance to the radiation biology field.

We have performed systematic radiobiological studies of DNA irradiated *in vitro*. The yields of SSBs, DSBs and total clustered lesions were assessed for a plasmid in solution irradiated with γ-rays, protons and helium nuclei. Clustering of lesions became apparent at various levels of analysis and was dependant on the LET (micron-scale ionization density) of the radiation fields as well as on the nanometer-scale track structure variations between different radiation fields of equal LET and between different γ-ray energies.

We have observed complex LET-dependant clustered-lesion yields, attributable to a competition between the increase in the clusters induced by direct ionization of DNA and the decrease in the clustering of lesions formed by radical mediated damages, due to recombination of radicals. The effect of the track structure at the same LET, is reflected by the fact that protons have roughly twice higher damage yields than helium nuclei of equal LET (25.5 keV/μm). This is visible for DSBs and complex lesions, but also for SSBs since some of the SSB are generated as a cluster containing base lesions (not detected by our SSB assay). Most surprisingly we also see a noticeable difference in yield between $^{60}$Co and $^{137}$Cs γ-rays. Since this difference is seen mainly for SSBs (and not for complex clusters), it concerns probably only small clusters (SSB and one or few base lesions).

Subsequently we have seen that our implementation of ion-counting nanodosimetry does not provide a full picture of radiation effects in tissue. The small sensitive volume which is the great achievement of nanodosimetry has also a certain drawback. Within irradiated tissue some 65% of the damage occurs by the radical-mediated *indirect effect*. Here radiation-induced ionizations, formed up to **tens of nanometers** away from the DNA result in chemical damage to it. In order to model this type of damage it is required to know the ionization track structure on a scale much larger than that provided by the ion-counting nanodosimeter. This knowledge, coupled with an appropriate diffusion-kinetic model for describing free radical transport, reactions and recombination can predict the damage yields formed by indirect effect.

We envision that the next generation of *hybrid nanodosimeters* which will overcome this limitation; such instruments would permit simultaneous measurement of nanometer-scale ionization clusters, vital for the understanding of **direct** radiation damage to DNA, in correlation with the ionization density on the larger scale required for quantification of indirect effects. Currently it is only possible to measure the former (using our ion-counting nanodosimeter or the Jet counter) or the latter (using mini-TEPCs, the SEC or the OPAC), but a true understanding of the processes of radiation damage to DNA would ultimately require both measurements correlated on a track-by-track basis.

We have seen that the nanometer scale track structure plays a significant role both in the radiation damage to DNA and in the ionization cluster size distributions measured with the nanodosimeter. This was clearly demonstrated by comparing the results from protons and helium nuclei, having the same LET but different nanometric track structures, inflicting different radiation-damage to the DNA. Previously such indication was only seen in some limited cellular systems and in the irradiation of liquid water. Our results clearly demonstrate the relevance of the nanodosimetric information to the radiation impact outcome in the DNA system, and point at the **superiority of nanodosimetry over current macroscopic approaches** (such as the use of LET)**.**

Nanodosimetry could be used to predict the damage caused to condensed matter (tissue, nanoelectronic devices or any other interesting target) by ionizing radiation, much better than with current techniques. This will be useful in high radiation environments, such as near nuclear reactors, particle accelerators or in space, where nanodosimetry will enable the development of more accurate radiation protection standards. Furthermore, application of Nanodosimetry to therapeutic beams will permit the development of more efficient and safe radiation therapy protocols.

# Appendix A :

# Simulation of light-ion track structures

Within this work we have extensively employed a MC simulation code developed by B. Grosswendt (PTB, Germany). The original code simulates charged particle interactions in an arbitrary mixture of carbon, nitrogen and oxygen. The principles and application to propane are described in detail below.

The model and code developed for simulating the formation of ionization clusters in the ND is based on the following assumptions, valid for ions at energies above 1 MeV/nucleon:

1. The initial particle energy is not significantly changed by inelastic interactions of the primary particles, while penetrating through the ionization volume of the ND.

2. The energy and the flight direction of the particles within the ND are also not markedly changed by elastic interactions.

3. Electron capture or electron stripping processes along the particles' path within the ND do not influence ionization-cluster formation.

The first of these assumptions is justified, for instance, by the electronic stopping power of the particles, which is equal to 316.3 eV $cm^2/\mu g$ and 1253 eV $cm^2/\mu g$ for 1 MeV protons and 4 MeV α-particles in propane, respectively [132]. These stopping powers lead to a relative energy loss of about 0.7%, assuming a penetration length of 10 cm through propane at 0.9 Torr and 25° C (density 2.1 $\mu g/cm^3$). The corresponding energy loss of 12 MeV carbon nuclei is about 2%. The validity of the second assumption is obvious both from the nuclear stopping power, which is much smaller than the electronic stopping power at higher particle energies, and from the particles' detour factor. For 1 MeV protons and 4 MeV α-particles, for instance, the detour factors in propane [132] are 0.9949 and 0.9959, respectively, thus demonstrating that the particles' projected ranges are almost equal to their continuous-slowing-down ranges. The third assumption can be justified based on the results of Baek and Grosswendt [133] with respect to the influence of charge exchange processes of protons on their $W_i$ value.

The main steps for simulating the ionization pattern of track segments of light ions in gas are, therefore:

1. Determination of the distance to the subsequent point of ionization impact interaction.

2. Determination of the energy and direction of secondary electrons ejected by ionization processes.

3. Simulation of the slowing-down of these electrons in the gas

4. Analysis of ionization-cluster formation taking into account the efficiency map, which defines the sensitive volume of the ND (see §3.4).

## *A.1 Ionization patterns induced by the ions*

According to the basic assumptions made in our MC model, the distance an ion has to travel between two subsequent interaction points is governed by an exponential probability density which is characterized by the particle's mean-free-path length with respect to

ionization. This mean-free-path length is equal to $[n\sigma^{ion}(K_v)]^{-1}$ where N is the number density of target molecules, and $\sigma^{ion}(K_v)$ the integral ionization cross section of particles of type $v$ at energy $K_v$. The integrated ionization cross section is, therefore, the key parameter for ion cluster formation.

*Protons:* In the present MC model, $\sigma^{ion}(K_v)$ for protons is calculated using the analytical functions and experimentally-based parameters of Rudd et al. [134]. Since the appropriate parameters for propane are missing, those for methane are applied after scaling by the ratio of the number of weakly-bound electrons of both molecules, as proposed by Wilson and Toburen [135]. To simulate the secondary electron distribution after proton impact ionization, we used the single-differential cross sections of the Hansen-Kocbach-Stolterfoht (HKS) model [136] with respect to the secondary-electron energy for specific sub-shell $i$ with binding energy $B_i$ and electron occupation number $\tilde{n}_i$. The values of $B_i$ and $\tilde{n}_i$ are taken from Hwang et al. [137] for 10 orbitals of outer or weakly-bound valence electrons of propane. The advantage of using the semi-empirical HKS model is that it has no adjustable parameters and it gives the single-differential as well as the double-differential cross sections with respect to the energy and the emission angle of the secondary electrons. The model is also applicable to particles other than protons.

After selecting the secondary electron energy, the polar angle $\theta$ of the electron's trajectory relative to that of the proton is sampled. For that we use the double-differential cross section of the HKS model at specific electron energy, normalized to its integral over $cos(\theta)$ within the limits $-1 \leq cos(\theta) \leq 1$. The azimuthal angle of the electron direction is assumed to be uniformly distributed between 0 and $2\pi$. These data are then used as input parameters to the Montè-Carlo model for electrons, which is shortly described in section A.2.

*Alpha particles and carbon ions:* As no experimental integral ionization cross sections of α-particles or carbon ions at specified energy $K_v$ are available in the energy range of our measurements, we use the experimentally-based cross sections for protons at energy $K_p = (m_p/m_v)K_v$, where $m_p$ represents the proton mass and $m_v$ the mass of α-particles or carbon nuclei. To take into account the dependence of the ionization cross section on the charge of the projectile, the proton cross sections are multiplied by a scaling factor, proportional to the square of the projectiles' atomic number $z_v$, according to first order Born approximation to the Bethe theory [138]. A deviation from the $z^2$-dependence is included, based on the ratio of the ionization cross section for α-particles or bare carbon nuclei in He to the cross section of protons in He at the same velocity, multiplied by $z_v^2$ (as given in figure 4.16 of [136]). This leads to a reduction of the ionization cross section, for instance, by 3.6% in the case of 4 MeV α-particles and by 18.4% for 12 MeV carbon nuclei. To take into account the charge state of the particles on their way through our ND, a charge state equilibrium is assumed and the ratio $z_{eff}^2/z_v^2$ is used as a further correction to the ionization cross section for particle ν. Based on the procedure of Ziegler and Manoyan [139] to determine $z_{eff}^2$, this correction leads to a further reduction of the ionization cross section by about 6% for 4 MeV α-particles and by 31.1% for 12 MeV carbon ions. Both types of corrections become smaller with increasing particle energy.

## A.2 Ionization patterns induced by secondary electrons

The histories of all particle-induced electrons produced in the gas are followed from one interaction point to the other, taking into account elastic electron scattering, different excitation interactions, and impact ionization. The main steps for simulating the propagation of electrons through the gas are, therefore:

1. Determination of the distance to the subsequent point of interaction.

2. Determination of the type of interaction the electron will undergo at this point.

3. Sampling of the energy loss and flight direction resulting from the interaction selected in step 2.

As external electromagnetic fields are not included, it is assumed that the electrons travel along straight lines connecting subsequent interaction points. To determine the traveling distance, we assume that the target molecules can be treated as independent points homogeneously distributed in space. In this case the traveling distance is governed by an exponential probability density, which is characterized by the mean-free–interaction-length of the electrons. This mean free interaction length is equal to $[n\sigma^{tot}(K)]^{-1}$, where $N$ is the number density of target molecules, and $\sigma^{tot}(K)$ the total scattering cross section at electron kinetic energy $K$:

$$\sigma^{tot}(K) = \sigma^{el}(K) + \sum_j \sigma_j^{exc}(K) + \sigma^{ion}(K) \qquad \text{(A.1)}$$

Here, $\sigma^{el}(K)$ is the elastic scattering cross section, $\sigma_j^{exc}(K)$ the cross section for the excitation of a propane molecule to a state $j$, and $\sigma^{ion}(K)$ is the total ionization cross section.

The type of interaction that the electron suffers at each interaction point is sampled from the set of discrete probabilities, $p_\nu(K)$. These interaction probabilities are equal to the ratio of the cross section of a given interaction process $\sigma^{\nu}(K)$ to that of the total electron scattering, $\sigma^{tot}(K)$ .

In the case of elastic interaction, the polar angle of the electron's flight direction after scattering, relative to its initial direction is determined on the basis of the differential elastic cross section. We assume that the azimuthal scattering angle is uniformly distributed between 0 and $2\pi$. If an excitation to a particular state $j$ has been selected, the initial electron energy is reduced by the excitation energy required for the process but the electron direction is assumed to remain unchanged. In the case of impact ionization (only single ionization is taken into account), a secondary electron is ejected, which may contribute to the ionization pattern and must, therefore, be followed in the same manner as the primary electron.

The complete history of any electron is simulated until it leaves the volume of interest or until its energy becomes smaller than 10 eV, below the lowest ionization threshold (11.08 eV in the case of propane).

### A.2.1 Electron Scattering Cross Sections in Propane

The cross sections used for the present simulation in propane are based mostly on experimental data; they are described by analytical functions, useful for extrapolation and interpolation purposes. The details of the evaluation of cross sections and of their validation, are given in [140].

### A.2.2 Elastic Electron Scattering

The treatment of elastic electron scattering was based on Rutherford's differential cross section $(d\sigma/d\Omega)^{el}$ with respect to the solid angle, modified to take into account atomic screening effects:

$$\left(\frac{d\sigma(K)}{d\Omega}\right)^{el} = \frac{Z(Z+1)e^4}{(1-\cos\vartheta+2\eta)^2(4\pi\varepsilon_0)^2}\left[\frac{K+m_ec^2}{K(K+2m_ec^2)}\right]^2 \qquad \text{(A.2)}$$

Here, $\vartheta$ is the polar angle of scattering relative to the initial electron direction, and $K$ the kinetic electron energy; $Z$ is the atomic number of the target atom, $e$ the electron charge, $\varepsilon_0$ the permittivity of vacuum, $m_ec^2$ the electron rest energy, and $\eta$ is the so-called screening parameter.

The integral elastic electron scattering cross section $\sigma^{el}(K)$ at kinetic energy $K$ is obtained by integration of eq. (A.2) with respect to the solid angle:

$$\sigma^{el}(K) = \frac{Z(Z+1)\pi e^4}{\eta(1+\eta)(4\pi\varepsilon_0)^2}\left[\frac{K+m_e c^2}{K(K+2m_e c^2)}\right]^2 \qquad \text{(A.3)}$$

The last equation was used to determine the screening parameter $\eta$ as function of electron energy $K$, on the basis of integral cross sections, $\sigma^{el}(K)$, derived from experiments, as proposed by Grosswendt and Waibel [141]. The polar angle of scattering is then sampled conventionally using the differential elastic cross section. This procedure is a satisfactory approximation of differential elastic scattering at energies greater than about 200 eV; at smaller energies, however, large angle scattering is strongly underestimated. Because of this, a correction factor is applied at lower electron energies.

### A.2.3 Impact ionization

The ionization part of our Montè-Carlo simulation of electron histories is based almost exclusively on the integral ionization cross section $\sigma^{ion}(K)$ used by Chouki [142] in his analysis of swarm data, somewhat modified to get a better agreement with direct cross section measurements near the ionization threshold. $\sigma^{ion}(K)$ can be described by the following analytical function, which is consistent with the Bethe theory:

$$\sigma^{ion}(K) = 4\pi a_0^2 \frac{c_1}{(K/Ry)}\ln\left(1+\frac{K-I}{Ry}\right)\left[e^{-\frac{c_2}{(K/Ry)}} + c_3 e^{-\frac{c_4}{(K/Ry)^2}} + c_5 e^{-\frac{c_6(K-I)}{Ry(K/Ry)^2}}\right] \qquad \text{(A.4)}$$

Here, $a_0$ is the Bohr radius, $Ry=13.61\ eV$ is the Rydberg constant, $I=11.08\ eV$ is the lowest ionization threshold of propane, and $c_1..c_6$ are dimensionless fitting parameters [140].

The energy distribution of secondary electrons emitted after electron impact ionization was determined from a single-differential cross section $d\sigma(K)/d\varepsilon$ (where $\varepsilon$ is the outgoing electron's kinetic energy) expressed by the Breit-Wigner formula, as proposed by Green and Sawada [143]. As the parameters describing $d\sigma(K)/d\varepsilon$ in propane are not included in the tables of Green and Sawada [143] we use the data for methane. The errors induced by this procedure, due to the wrong shape of the energy distribution, for slow electrons in particular, and the non-ideal behavior at high energies, are acceptable for most applications.

The energy $K'$ of the primary electron after impact ionization is calculated according to $K'=[K-\varepsilon-I(K)]$, where $I(K)$ is the ionization threshold energy applied at a specified electron energy $K$. This ionization threshold is assumed to depend on the electron energy $K$, to approximate the contribution of sub-shells with binding energies greater than the lowest ionization threshold of 11.08 eV, which can contribute to $\sigma_{ion}$ if the electron energy is high enough. $I(K)$ was set equal to the average binding energy of the weakly-bound valence electrons of propane, calculated on the basis of the partial electron ionization cross sections of Hwang et al. [137].

No appropriate experimental data exist for the flight directions of the electron after scattering and of the ejected secondary electron. Therefore, the flight directions were determined approximately, using the kinematic equations proposed by Berger [144], which are based on conservation of momentum and energy. The azimuthal angles of the electron after scattering and the secondary electron are assumed to differ by $\pi$ and one of the two angles is assumed uniformly distributed between 0 and $2\pi$. This procedure represents a satisfactory approximation of the measured data of Opal et al. [145], at energies above ~200 eV. At lower energies the following assumptions [141] are made, which are more consistent with the experimental data:

1. Secondary electrons at energies smaller than 50 eV are emitted isotropically;

2. In the energy range between 50 eV and 200 eV, 90% of the secondary electrons are emitted in the angular range between 45° and 90° whereas the rest are emitted isotropically;

3. The scattering angle of primary electrons, at energies above 100 eV after an ionization event, is given by Berger's equation. It is uniformly distributed between 0° and 45° at smaller energies.

### A.2.4 Impact excitation

The treatment of excitation processes in propane was also largely based on the data set of Chouki [142]. It contains one discrete excitation cross section with a threshold at 9.13 eV, a series of cross sections for vibrational excitation, one cross section for molecular dissociation and one for electron attachment.

The discrete excitation cross section was fitted to an empirical function similar to that used for impact ionization:

$$\sigma^{exc}(K) = 4\pi a_0^2 \frac{c_1}{(K/Ry)} \ln\left(1 + \frac{K - c_2}{Ry}\right)\left[e^{-\frac{c_3}{(K/Ry)}} + c_4 e^{-\frac{c_5(K-c_2)}{Ry(K/Ry)^2}}\right] \qquad \text{(A.5)}$$

Here, the different parameters have the same meaning as in eq. (A.4).

Chouki's cross-sections for electron attachment, vibrational excitation and molecular dissociation were fitted to a formula, recommended by Jackman et al. [146]:

$$\sigma_j^{exc}(K) = 4\pi a_0^2 Ry^2 \frac{f_j}{W_j^2}\left[1 - \zeta^{A_j}\right]^{B_j} \zeta^{\Omega_j} \qquad \text{(A.6)}$$

where $\zeta = W_j/K$ and $f_j$, $W_j$, $A_j$, $B_j$ *or* $\Omega_j$ are parameters that are characteristic of different excitation processes; the other quantities are those of Eq. (A.4). For the parameters, see [140].

### A.2.5 K-shell ionization

When the ionization process results in the ejection of an inner shell electron, a vacancy is formed, which is filled by the collapse of a second electron from the outer shell into the vacancy. The excess energy is released as a characteristic X-ray or as an Auger electron. Both channels will result in the formation of additional ionizations in the medium, as the electron is stopped (or the photon absorbed). In the specific case of carbon, this may result in up to 12 ionizations.

Due to the small uncertainties in the total ionization cross sections in propane, it is assumed that the K-shell ionization cross section is already included in the total cross section.

As propane consists of 3 carbon atoms, the K-shell ionization cross section of propane was taken as three times the cross section for K-shell ionization in carbon atoms. The carbon cross sections, $\sigma_c^K(K)$, were taken, where available, from the literature [147]. When not available (proton energies above 18 MeV), they were calculated based on the electron cross sections, using the formulas of [148] at $K \leq 1400$ *eV*, and by using the Bethe formula at higher energies.

a) $K \leq 1400$ *eV*

If we denote the ratio $K/I_K$ of the electron energy $K$ and the K-shell threshold energy $I_K$= 288 eV by $U$, $\sigma_c^K(K)$ is given by the following equation:

$$\sigma_c^K(K) = \frac{\tilde{n}_c}{I_K^2} a_0^2 Ry^2 \times \Psi \times \Phi \times \frac{\ln U}{U} \tag{A.7}$$

where $\tilde{n}_C = 2$ is the number of electrons in the K-shell of the carbon atom, $a_0 = 0.529 \times 10^{-8}$ cm is the Bohr radius, and $Ry$ is the Rydberg constant (as above).

$$\Psi = \left( \frac{I_K}{Ry} \right)^{d_k} \tag{A.8a}$$

$$d_K = -0.0318 + \frac{0.3160}{U} - \frac{0.1135}{U^2} \tag{A.8b}$$

$$\Phi = 10.57\, e^{-\frac{1.736}{U} + \frac{0.317}{U^2}} \tag{A.8c}$$

b) $K > 1400$ eV (Bethe formula)

If we use the same definitions as at smaller energies, $\sigma_c^K(K)$ is given by the following equation:

$$\sigma_c^K(K) = 4\pi a_0^2 Ry^2 \frac{\tilde{n}_c}{I_K^2} \times b_{nl} \times \frac{\ln(c_{nl} \times U)}{U} \tag{A.9}$$

with $b_{nl} = 0.9$ and $c_{nl} = 0.65$ as dimensionless parameters.

In addition, the relativistic correction of the energy dependence was applied at electron energies greater than 70 keV.

The ejected auger electron ($K = 276$ eV) was tracked as a δ-electron. It was also assumed that the propane molecule, being doubly charged, dissociates into two singly charged ions.

## A.3 Simulation of the ND response

In order to perform the MC simulations in a way as close as possible to the experimental conditions, the MC code takes into account the energy spread of the projectile's beam and, at least in principle, also the radial distribution of the beam intensity. For the latter, we assume a homogenous 1 mm-diameter cylindrical beam for protons and carbon ions produced in the accelerator, and a radial beam profile for α-particles from an $^{241}$Am source (evaluated using the calculations according to Johns and Cunningham [149]). The energy spectrum of the different accelerator beams due to energy degradation in the scattering foil was determined using SRIM [90], and that of the α-particles by direct measurements using a calibrated solid-state detector.

# Appendix B :

# Model studies of cluster pileup in the DAQ

## *B.1 The MC simulation*

As described in §3.1.5, The DAQ is triggered by a pulse from the "triggering detector" (either the MWPC anode or the MCP); following the trigger an (optional) high voltage pulse is applied to the ionization volume (IV) anode, collecting all ions in the SV to the IC. The trigger also resets a clock and only ions counted within 100-200 μsec (the "DAQ acceptance window") after the trigger are registered.

We have seen that when operating the ND at high beam repetition rates cluster-pileup (CPU) occurs. This refers to a case where two projectiles pass through the IV within the DAQ acceptance window, depositing ions in the SV; these ions will be registered as belonging to a single cluster. To overcome this, we have rejected, offline all events in which a second projectile particle arrives within the DAQ acceptance window, however this method relies on an efficient trigger detector. In our experiments we have seen that the trigger detector efficiency was about 80% (the MWPC detector) and in one case (MCP irradiated by 1 MeV protons) as low as 50%.

In order to better understand the influence of the beam rate and trigger efficiency on the measured cluster size distributions, we have developed a simple MC code of the ND DAQ system. The structure of the code is as follows:

1. Generate the $x$ coordinate (altitude in the SV) of the incident projectile.

2. Randomly assign the projectile to be triggering or not triggering, using the trigger efficiency, which may depend on $x$ (The MCP detector, for example had an active area smaller than the beam in the case of 1 MeV protons – see §5.3.1).

3. Generate the arrival time of the projectile, according to a uniform time distribution with given average rate, such that the rate of triggering projectiles matches that of the experiment.

4. Calculate the (time dependant) electric field, $E_1(t)$. In pulsing mode the field is low (typically 20 V/cm) except for a 100-200 μsec period of high field (typically 60 V/cm) following (almost) each triggering projectile. The only exception being a projectile which passes within the DAQ acceptance window and does not generate a HV pulse.

5. Generate the number of ions induced by each proton (according to an experimental or "idealized" cluster-size distribution – see below).

6. Calculate the ion arrival time, using the (time-dependant) electric field $E_1(t)$ calculated above. and the ion drift velocity measured in §4.2.3 ($v$ = 0.43 mm/μsec at 60V/cm). It is assumed that $v$ is proportional to $E_1$. The spread in ion arrival time is taken from the pencil beam experiments.

7. Save the arrival times of the triggering protons and of all ions to a file, in the same format as used by the DAQ software

8. Analyze the resulting file using the standard data analysis software.

The resulting cluster size and ion arrival time distributions were then compared to those used as the input.

## *B.2 Model results – pencil beam*

At first the model was applied to a pencil beam, where the ion arrival time distribution was fitted to measured results with a 1 mm beam diameter passing 15 mm above the ion extraction aperture. We have checked the dependence of the **measured** cluster size distribution on three parameters: the beam rate, the trigger efficiency and the ratio of the pulse field and the electron-sweeping field (DC corresponds to a value of 1; pulsed mode corresponds to 3 (see §4.2.1).

To estimate the fraction of CPU events (i.e. for how many events, contain ions from more than one projectile) we used, as input, an artificial cluster size distribution where all triggering projectiles had exactly 0 ions and the rest had a cluster size distribution taken from experimental data (e.g. figure 3.9).

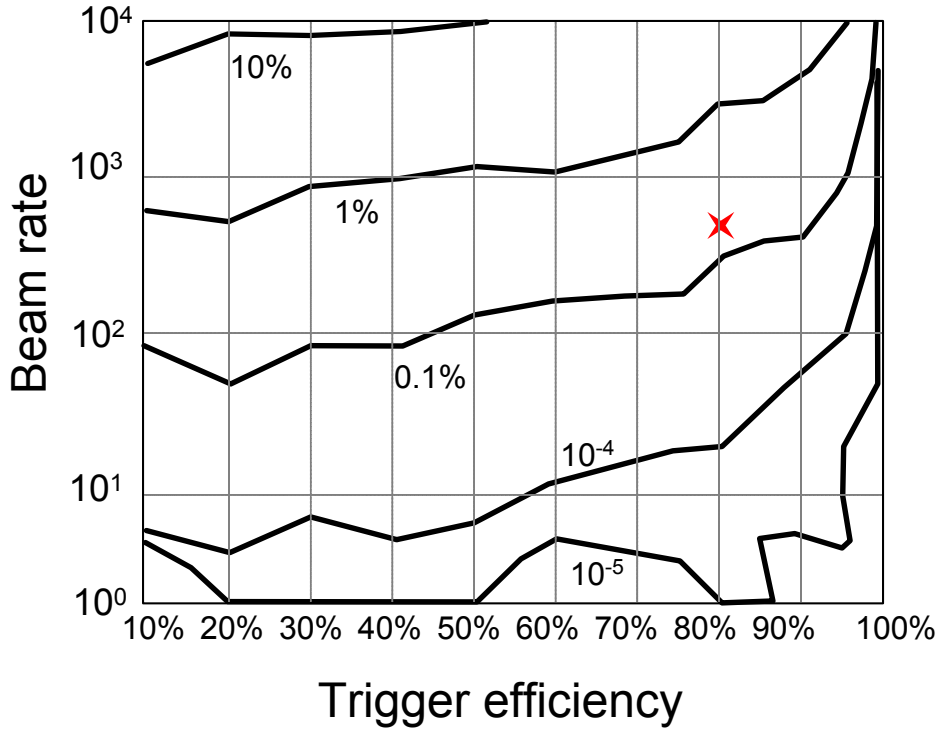


**Figure B.1: Fraction of CPU events** as a function of trigger efficiency and rate (for 13.6 MeV protons). In our conditions (rate~500 Hz Trigger efficiency ~80%, marked by the cross) there are about 0.2% of affected events. The values on the contours correspond to the fraction of CPU events.

In figure B.1 we see the resulting two-dimensional plot where the contours correspond to an equal fraction of CPU events. For example we see that at our experimental conditions (80% trigger efficiency and a rate of 500 Hz marked with an "x") there will be 0.2% CPU events. By looking at different cluster size distributions we have seen that this value increases with the average cluster size but saturates once most events are non-empty. In particular we have seen no difference between an artificial situation where all clusters contained 1 ion and a situation where all clusters contain 3 ions.

By comparing cluster size distributions at different trigger efficiencies and beam fluxes we saw that at a beam flux of 500 Hz, even a 10% efficient trigger (i.e. one in ten projectiles is a triggering one) results in a curve which is indistinguishable from the real distribution (not shown), containing <1% pileup events (see figure B.1).

At higher rates, on the other hand we do require an efficient trigger. For 10 kHz, for example, a trigger efficiency of 80% would result in about 4% CPU events, and a noticeably different cluster size distribution. Figure B.2 compares the simulated cluster size distributions at trigger efficiency of 80% and beam fluxes of 1 and 10kHz. At 1 kHz the difference between the cluster size distribution with and without pileup is smaller than the statistical error. For 10 kHz it is significantly larger.

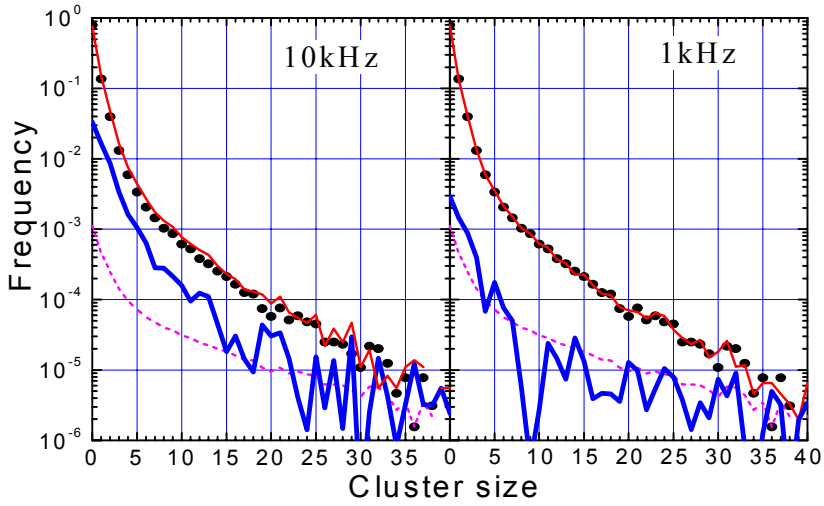


**Figure B.2: Simulated cluster size distributions( thin line) at a rate of 500 Hz and 10 kHz at 80% trigger efficiency.** The symbols denote the experimental cluster size distribution, used as input to the simulation; the dashed and (thick) solid lines at the bottom show respectively the statistical error and the absolute value of the difference

A second phenomenon, seen already in the experiment (figure **B.3**) is the apparent pedestal in the ion arrival time distribution. This is due to ions from non-triggering protons, arriving at random times. The area under the pedestal corresponds to the increase of the average cluster size; for 2 Hz there is no change, for 500 Hz ~1% and for 10 kHz ~10%. The level of this pedestal was used as a quick check of the CPU level during the measurements.

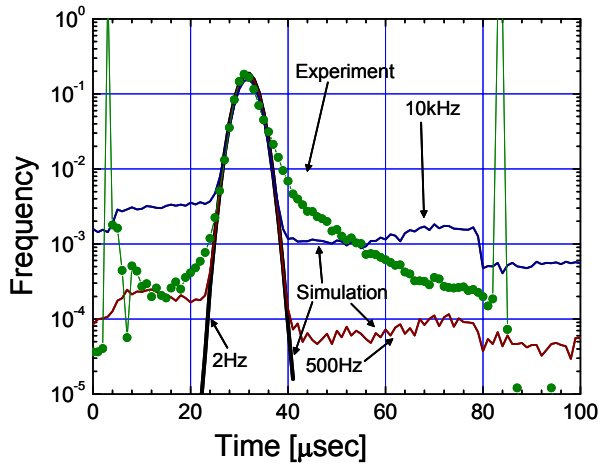


**Figure B.3: Simulated ion arrival time distributions.** The increase in the average cluster size, due to CPU, is proportional to the area under the pedestal.

### B.2.1 Significance of the electron-sweeping field

In our experiments, and all simulations reported above we have used a ratio of the pulsed field to the sweeping field of 3. This ratio was chosen such that the sweeping field is below that required for avalanche multiplication in propane (see §4.2.1). From these simulations we have seen that the magnitude of the electron-sweeping field is also an important factor in determining the fraction of CPU events. This is easy to see when considering a very low

sweeping field (a sweeping field of 5V/cm is sufficient to efficiently sweep the electrons). In such a case, the ions generated by a non-triggering projectile will remain in the SV for very long times and the ND will be much more sensitive to CPU events.

At a beam flux of 500 Hz, at a trigger efficiency of 80%, we have seen that field ratios of up to 10 (i.e. a sweeping field of 6 V/cm) can be used before noticeable distortions arise; nevertheless we have used a field of 20V/cm in all of our experiments. It should be noted that at high beam flux (10 kHz), at the same trigger efficiency there will be distortions no matter what this ratio is.

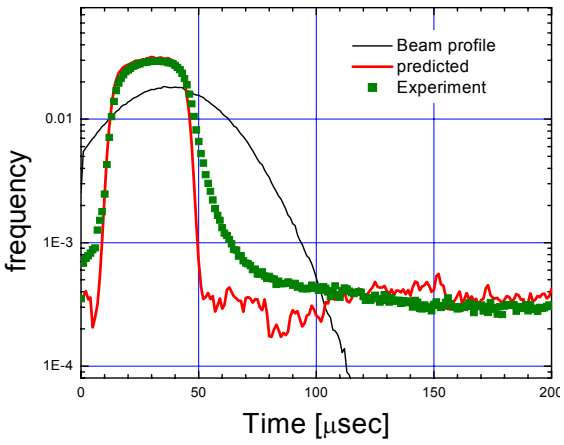


**Figure B.4: ion arrival time distributions**: the thin line is the measured beam profile (converted to time units using the measured ion drift velocity). The thick line is the simulated ion arrival time distribution. The squares are the measured ion arrival time distribution.

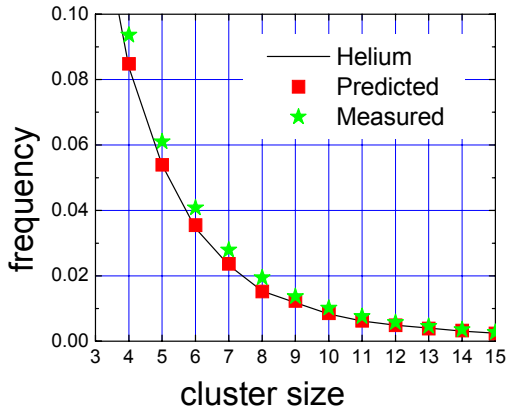


**Figure B.5: The effect of CPU on broad beam cluster size distributions.** The line represents the measured cluster size distribution induced by helium nuclei. The squares are the simulated cluster size distribution, based on the helium data and on the expected CPU. The diamonds are the measured proton data. It is obvious that the CPU cannot explain the difference in the cluster size distribution between protons and helium nuclei.

## *B.3 Model results – broad beam*

In the low energy proton measurements we had a beam, which was Gaussian in shape (RMS=10 cm), and much larger than the trigger detector's active area. We saw that in such a case only **51%** of the projectiles generate a trigger in the MCP detector, assuming that the MCP has no additional inefficiencies.

We want to prove that this deficiency **cannot** account for the observed difference between the 26 MeV $He^{++}$ data and the 1.03 MeV proton data (cf. §5.3.3). We therefore repeated the simulation above using the measured 1.03 MeV proton beam profile (see B.4). A good indication is that we indeed reproduce the ion arrival time distribution measured in the experiment (apart from the falling edge, which has a different slope, due to secondary effects in the ion channel; this is a known imperfection of our ND (discussed in §4.1.4) and appears in ALL measurements). Note the excellent agreement in the 0-50 μsec region corresponding to ions generated by triggering projectiles.

The pedestal observed at long times (150-200 μsec) is characteristic of CPU. At these times there is no chance to have "legitimate" ions. About 5% of all ions arrive in this tail region (note that when we perform a time cut this fraction will reduce to ~1%, same as we had in the narrow beam studies). What we see in this figure is that the MC simulation faithfully reproduces the effect of the CPU.

In order to prove that the difference between the helium- and proton-induced cluster size distributions is not due to pileup, we have used this code to predict the pile-up distorted, proton-induced, cluster size distribution, assuming that the "real" cluster size distribution is the one we measured with the helium nuclei. Figure B.8 compares the two measured distributions (from figure 5.11) with the CPU-distorted helium-induced cluster size distribution. It is clear that distortions due to CPU CANNOT account for the observed difference between the helium and proton data. It was also seen that if we impose an additional inefficiency on the trigger (down to a trigger efficiency of <20%), we could still not reproduce the difference between the protons and the helium nuclei.

# Appendix C :

# Modeling of plasmid damage yields

## *C.1 The model*

### C.1.1 Assumptions

The formation of single strand breaks (SSBs) and double strand breaks (DSBs) by chemical agents has been theoretically studied by Cowan [111]. We have adapted this model for the formation of strand breaks and bacterial inactivation by ionizing radiation. The main assumptions of the original model are:

1. Two independent agents exist: a nicking agent, which forms a single isolated SSB, and a cutting agent, which forms a single, isolated "direct" DSB.
2. SSBs are formed with equal probability on both strands.
3. Both SSBs and DSBs are formed at random locations along the plasmid.
4. Two close SSBs on opposing strands will always join to form an "indirect" DSB. The interaction distance is discussed in depth in §3.4.3 and in §6.3.3.

Based on these assumptions a theoretical model was developed to predict the measured fraction of plasmids, after action of given concentrations of both agents, in the 4 states:

- *SC*: supercoiled (no SSBs and no DSBs),
- *OC*: open circle (one or more **isolated** SSB and no DSBs),
- *LP*: linear (exactly one (direct or indirect) DSB and any number of **isolated** SSBs)
- *FP*: fragmented (more than one (direct or indirect) DSB and any number of SSBs).

The parameters of this model are:

- $\mu$ - The yield of isolated SSBs (per plasmid per nicking agent molecule).
- $\phi$ - The yield of isolated DSBs (per plasmid per cutting agent molecule).
- $b$ - The "interaction distance" between SSBs as a fraction of the plasmid length. Two independent SSBs formed (by different nicking molecules) on opposing strands at a distance of $b$ or less will be transformed to a DSB with unit efficiency. Within this work we have used $b=10^{-3}$ (i.e. 10 bp).

### C.1.2 The model equations

The modification of this model to ionizing radiation consists of a simple replacement of the parameters $\mu$ and $\phi$, by $\tilde{D}\mu$ and $\tilde{D}\phi$, where $\tilde{D}$ is the irradiation dose and the parameters $\mu$ and $\phi$ can be interpreted as the rate (per unit dose of irradiation) of formation of isolated SSBs and isolated DSBs per plasmid. Note that this assumes that both processes are linear in dose; the induction of indirect DSBs will then be quadratic in dose (in first approximation).

In terms of these parameters the final probability of an initially supercoiled plasmid to be in any of the states, after irradiation by dose $\tilde{D}$ is given by:

$$\begin{cases} SC\left(\mu,\phi,b,\widetilde{D}\right)=e^{-\phi\widetilde{D}}e^{-\mu\widetilde{D}} \\ OC\left(\mu,\phi,b,\widetilde{D}\right)=e^{-\phi\widetilde{D}}\left(2\,\mathrm{e}^{\mu\widetilde{D}/2}-2\,\mathrm{e}^{\mu\widetilde{D}}+\mu\widetilde{D}X_D\right) \\ LP\left(\mu,\phi,b,\widetilde{D}\right)\cong e^{-\phi\widetilde{D}}\left(\dfrac{\mu\widetilde{D}}{2-b\mu\widetilde{D}}\left(\mu\widetilde{D}X_D-Y_D+\mathrm{e}^{-\mu\widetilde{D}/2}-\mathrm{e}^{-\mu\widetilde{D}}\right)+\phi\widetilde{D}\left(e^{-\mu\widetilde{D}}+\left(2\,\mathrm{e}^{\mu\widetilde{D}/2}-2\,\mathrm{e}^{\mu\widetilde{D}}+\mu\widetilde{D}X_D\right)\right)\right) \\ FP\left(\mu,\phi,b,\widetilde{D}\right)=1-S\left(\mu,\phi,b,\widetilde{D}\right)-R\left(\mu,\phi,b,\widetilde{D}\right)-L\left(\mu,\phi,b,\widetilde{D}\right) \end{cases} \quad \text{(B.1)}$$

with

$$\begin{cases} X_D=\displaystyle\sum_{\mathrm{j}=1}^{\lfloor 1/b\rfloor}\mathrm{e}^{-\mu\widetilde{D}(1+jb)/2}\,\frac{[\frac{1}{2}\mu\widetilde{D}(1-jb)]^{2j-1}}{2\mathrm{j}!} \\ Y_D=\displaystyle\sum_{\mathrm{k}=1}^{\lfloor 1/b\rfloor}\mathrm{e}^{-\mu\widetilde{D}(1+jb)/2}\left(2j+\frac{1}{2}\mu\widetilde{D}(1-jb)\right)\frac{[\frac{1}{2}\mu\widetilde{D}(1-jb)]^{2j-1}}{2\mathrm{j}!} \end{cases} \quad \text{(B.2)}$$

However, using the gel electrophoresis measurement we can only measure the fraction of supercoiled, open circle and linear DNA. The fragmented fraction will consist of an extremely broad distribution of plasmid lengths and will not be detectable on a gel. In order to compare our measurements to the model we should look at $SC^M=SC/(SC+OC+LP)$, instead of $SC$, $OC^M=OC/(SC+OC+LP)$ instead of $OC$ and $LP^M=LP/(SC+OC+LP)$ instead of $LP$. This corresponds to renormalizing the three fractions, $SC$, $OC$ and $LP$, ignoring $FP$ (which we cannot quantify accurately).

### C.1.3 Zero dose values

Even a perfectly prepared plasmid sample will have some background level of Open circular and linear plasmids. In order to take into account this initial population, we can assume that it is generated by an a priori action of some nicking and cutting agent. Using this approach we need only to replace $\mu\widetilde{D}$ and $\phi\widetilde{D}$, in the above expressions by $\mu\widetilde{D}+\mu_0$ and $\phi\widetilde{D}+\phi_0$ respectively, and to treat $\mu_0$ and $\phi_0$ as independent model parameters to be fitted to the data.

In his paper, Cowan, also presents a simplified version of the equations for $SC^M$, $OC^M$ and $LP^M$, which is valid at relatively low doses, when indirect DSB formation due to nicking can be ignored:

$$\begin{cases} SC^M=\dfrac{e^{-\mu\widetilde{D}}}{1+\phi\widetilde{D}} \\ OC^M=\dfrac{1-e^{-\mu\widetilde{D}}}{1+\phi\widetilde{D}} \\ LP^M=\dfrac{\phi\widetilde{D}}{1+\phi\widetilde{D}} \end{cases} \quad \text{(B.3)}$$

In this case, one can extract the parameters $\mu_0$ and $\phi_0$ analytically. This gives:

$$\phi_0=\frac{LP_0^M}{1-LP_0^M} \quad ; \quad \mu_0=-\ln\left[\frac{SC_0^M}{1-LP_0^M}\right] \quad \text{(B4)}$$

One should note that, for real data, nicking is the dominant mechanism, in particular, at low scavenging concentration. In order to get accurate measurements of the linear fraction we have to use relatively high doses, for which DSB production due to nicking cannot be

ignored. Therefore, we should use the exact model rather than the approximate formulas. However, at the low dose range (which is relevant for calculating $\mu_0$ and $\phi_0$) these approximations are valid.

## C.2 Gel data fitting

In order to extract the parameter values ($\mu$, $\phi$, $\mu_0$ and $\phi_0$; $b$ was fixed as 10 bp) from the measured gel data, we have used the Levenberg-Marquardt [150] algorithm for minimizing the $\chi^2$ function:

$$\chi^2 = \frac{1}{n_{DOF}} \sum_{\substack{All \\ doses}} \left\{ \left(SC - SC^M\right)^2 + \left(OC - OC^M\right)^2 + \left(LP - LP^M\right)^2 \right\} \qquad \text{(B.5)}$$

(where $n_{DOF}$ is the number of degrees of freedom in the problem) as a function of the parameters $\mu$, $\phi$ and the zero dose values ($LP_0^M$ *and* $SC_0^M$). Both the direct fitting of $\mu_0$ and $\phi_0$ to the data and the recipe suggested by Cowen were tested. It was seen that the direct fitting yields a rather bad fit whereas if $PL_0^M$ and $SC_0^M$.are fitted (using the given relationship to calculate $\mu_0$ and $\phi_0$), the fit quality is much better. Probably this is due to the logarithmic dependence of $\mu_0$ on $LP_0^M$ and $SC_0^M$.

A sample plot of the measured fractions (SC, OC and LP) as a function of dose is shown in figure 6.9, along with the model fit.

## C.3 Survival data fitting

In the previous section we assumed that the radiation could only induce strand breaks in the plasmid. While this is appropriate for the analysis of the electrophoresis data, where only the strand breaks are detectable, in reality the radiation can also induce base oxidations (typically at a 2.5 times higher yield than that of the strand breaks). When the plasmid is inserted into a bacterium it is assumed that each base damage is converted with unit efficiency to a single strand break. We also assume that SSBs (both the initial SSB and the base damage induced SSB) will be fully repaired if they are isolated see §6.3.3 for the validity of these assumptions.

As the bacterium needs an intact plasmid to survive, the number of surviving bacteria will be proportional to the fraction of plasmids with no damage (*SC*) or with a single damage (*OC*), which may be either a strand break or a base oxidation.

The surviving fraction (*SF*) of cells in a transformation experiment involving a control experiment with unirradiated plasmids and an experiment with plasmids irradiated to a dose $D$ is thus given by:

$$SF(\widetilde{D}) = \frac{N_c(\widetilde{D})}{N_c(0)} = \frac{SC(\mu', \mu'_0\, \phi', \phi'_0, \widetilde{D}) + OC(\mu', \mu'_0\, \phi', \phi'_0, \widetilde{D})}{SC(\mu'_0, \phi'_0, 0) + OC(\mu'_0, \phi'_0, 0)} \qquad \text{(B.6)}$$

Where $\mu'_0$ and $\mu'$ correspond to the yield of total damages (SSB + base oxidations) pre irradiation and after unit dose. Similarly $\phi'_0$ and $\phi'$correspond to the yield of "clustered damages". The functional forms of *SC* and *OC* are given in the previous section.

Since the surviving fraction was seen to vary over several orders of magnitude (between 100% and 0.5%), the fitting procedure was seen to be more reliable, when fitting *–ln(SF)* rather than *SF* itself. This has the added advantage that the fitting results are independent of the zero dose values of *SC* and *OC*. Note also that if we assume that the inactivation events are statistically independent (i.e. Poisson distributed), *–ln(SF)* is equivalent to the average number of inactivation events per plasmid per unit dose.

In this case the minimized $\chi^2$ function is:

$$\chi^2 = \frac{1}{n_{DOF}} \sum_{\substack{All \\ doses}} \left\{ \ln(SF) - \ln\left(SC^M + OC^M\right) \right\} \qquad \text{(B.7)}$$

A sample plot of the measured –log survival as a function of dose is shown in figure 6.10, along with the model fit.

# Appendix D :

# Mathematical derivations

## *D.1 Reduction of the trinomial distribution to a binomial distribution*

### D.1.1 In the case of strand break formation

Eq. 7.9 gave the yield of an ionization cluster containing $n_{SB}$ strand breaks and $n_{BD}$ base lesions in terms of the trinomial distribution:

$$G(n_{SB},n_{BD})[Gy^{-1}Da^{-1}] = 9.6\,10^{-10} * \frac{\rho V_{SV}}{w_i \langle n_{ion} \rangle_{\varphi}} \sum_{n_{ion}} \varphi(n_{ion}) * \ddot{\ddot{P}}(n_{SB},n_{BD}|n_{ion}) \qquad \text{(D.1)}$$

In the gel electrophoresis measurement we are not sensitive at all to the base lesions therefore we can sum eq. D.1 over all values of $n_{BD}$.

$$\begin{aligned} G(n_{SB}) &= \sum_{n_{BD}=0}^{\infty} G(n_{SB},n_{BD}) \\ &= \sum_{n_{BD}=0}^{\infty} 9.6\,10^{-10} * \frac{\rho V_{SV}}{w_i \langle n_{ion} \rangle_{\varphi}} \sum_{n_{ion}} \varphi(n_{ion}) \times \ddot{\ddot{P}}(n_{SB},n_{BD}|n_{ion}) \\ &= 9.6\,10^{-10} * \frac{\rho V_{SV}}{w_i \langle n_{ion} \rangle_{\varphi}} \sum_{n_{ion}} \left\{ \varphi(n_{ion}) \times \sum_{n_{BD}=0}^{\infty} \ddot{\ddot{P}}(n_{SB},n_{BD}|n_{ion}) \right\} \end{aligned} \qquad \text{(D.2)}$$

The sum over $n_{BD}$ can be performed analytically. Substituting *i, j, n, p* and *q* for $n_{SB}$, $n_{BD}$, $n_{ion}$, $p_{SB}$ and $p_{BD}$ we get:

$$\begin{aligned} \sum_{j=0}^{\infty} \ddot{\ddot{P}}(i,j \mid n) &= \sum_{j=0}^{\infty} \binom{n}{i} \times \binom{n-i}{j} \times (p)^i \times (q)^j \times (1-p-q)^{n-i-j} \\ &= \binom{n}{i} \times (p)^n \times \sum_{j=0}^{\infty} \binom{i-n}{j} \times (q)^j \times (1-p-q)^{n-i-j} \\ &= \binom{n}{i} \times (p)^n \times \sum_{j=0}^{\infty} \binom{i'}{j} \times (q)^j \times (a-q)^{i'-j} \end{aligned} \qquad \text{(D.3)}$$

where $i'=i-k$ and $a=1-p$. the sum over $j$ is simply a binomial expansion

$$\begin{aligned} \sum_{j=0}^{\infty} \ddot{\ddot{P}}(i,j \mid n) &= \binom{n}{i} \times (p)^n \times (q-a-q)^{i'} \\ &= \binom{n}{i} \times (p)^n \times a^{i'} \\ &= \binom{k}{i} \times (p)^n \times (1-p)^{i-n} \\ &= \ddot{P}(i \mid n) \end{aligned} \qquad \text{(D.4)}$$

We have shown that in the case where $n_{SB}$ is not known the trinomial distribution of eq. 7.9 can be replaced by a binomial distribution.

### D.1.2 In the case of "general lesion" formation

In the bacterial survival measurement we are not sensitive to the partition of the lesions (base lesions and strand breaks are equivalent) therefore we can sum eq. D.1 over all values of $n_{BD,}$ replacing $n_{SB}=n_{tot}-n_{BD:}$

$$\begin{aligned} G(n_{SB}) &= \sum_{n_{BD}=0}^{\infty} G(n_{tot}-n_{BD}, n_{BD}) \\ &= \sum_{n_{BD}=0}^{\infty} 9.6\,10^{-10} * \frac{\rho V_{SV}}{w_i \langle n_{ion} \rangle_{\varphi}} \sum_{n_{ion}} \varphi(n_{ion}) \times \ddot{P}(n_{tot}-n_{BD}, n_{BD} | n_{ion}) \qquad \text{(D.5)} \\ &= 9.6\,10^{-10} * \frac{\rho V_{SV}}{w_i \langle n_{ion} \rangle_{\varphi}} \sum_{n_{ion}} \left\{ \varphi(n_{ion}) \times \sum_{n_{BD}=0}^{\infty} \ddot{P}(n_{tot}-n_{BD}, n_{BD} | n_{ion}) \right\} \end{aligned}$$

Substituting *i, j, n, p* and *q* for $n_{tot}$, $n_{BD}$, $n_{ion}$, $p_{SB}$ and $p_{BD}$ we get:

$$\begin{aligned} \sum_{j=0}^{\infty} \ddot{P}(i-j, j \mid n) &= \sum_{j=0}^{\infty} \binom{n}{i-j} \times \binom{n-i+j}{j} \times (p)^{i-j} \times (q)^{j} \times (1-p-q)^{n-j-i+j} \\ &= (1-p-q)^{n-i} \times \sum_{j=0}^{\infty} \binom{n}{i-j} \times \binom{n-i+j}{j} \times (p)^{i-j} \times (q)^{j} \\ &= (1-p-q)^{n-i} \times \sum_{j=0}^{\infty} \frac{n!}{(i-j)!\,(n-i+j)!} \times \frac{(n-i+j)!}{j!\,(n-i)!} \times (p)^{i-j} \times (q)^{j} \\ &= (1-p-q)^{n-i} \times \frac{n!}{(n-i)!} \sum_{j=0}^{\infty} \frac{1}{(i-j)!\,(j)!} (p)^{i-j} \times (q)^{j} \end{aligned} \qquad \text{(D.6)}$$

multiply and divide by (*i!)*

$$\begin{aligned} \sum_{j=0}^{\infty} \ddot{P}(i-j, j \mid n) &= (1-p-q)^{n-i} \times \frac{n!}{(n-i)!\,i!} \sum_{j=0}^{\infty} \frac{i!}{(i-j)!\,(j)!} (p)^{i-j} \times (q)^{j} \\ &= (1-p-q)^{n-i} \times \binom{n}{i} \sum_{j=0}^{\infty} \binom{i}{j} (p)^{i-j} \times (q)^{j} \\ &= \binom{n}{i} \times (1-p-q)^{n-i} \times (p+q)^{i} \\ &\ddot{P}(i \mid n) \end{aligned} \qquad \text{(D.7)}$$

We have obtained once again the binomial distribution with *p* replaced with *p+q*.

## *D.2 Resolving the sum in eq. 7.13*

Eq. 7.13, the yield of DSBs, contains a sum over the number of strand breaks in a cluster:

$$G_{DSB}[Gy^{-1}Da^{-1}] = \frac{10^{-24}}{6500} * \frac{\rho V_{SV}}{e \cdot w_i \langle n_{ion} \rangle_{\varphi}} \sum_{n_{ion}} f(n_{ion}) * \sum_{n_{SB}=2}^{\infty} \binom{n_{ion}}{n_{SB}} p_{SB}{}^{n_{SB}} (1-p_{SB})^{n_{ion}-n_{sb}} \left(1-\tfrac{1}{2}^{n_{SB}-1}\right) \qquad \text{(D.8)}$$

the second sum can be solved analytically. Replacing $n_{ion}$, $n_{SB}$ and $p_{SB}$ with $n$, $i$, and $p$ this sum is:

$$S = \sum_{i=2}^{n} \binom{n}{i} p^i (1-p)^{n-i} \left(1 - \tfrac{1}{2}^{i-1}\right) \tag{D.9}$$

completing the sum (i.e. adding and subtracting the terms corresponding to $i=0,1$:

$$\begin{aligned} S &= \sum_{i=0}^{n} \binom{n}{i} p^i (1-p)^{n-i} \left(1 - \tfrac{1}{2}^{i-1}\right) - \binom{n}{0} (1-p)^n \left(1 - \tfrac{1}{2}^{-1}\right) - \binom{n}{1} p(1-p)^{n-1} \left(1 - \tfrac{1}{2}^{0}\right) \\ &= \sum_{i=0}^{n} \binom{n}{i} p^i (1-p)^{n-i} \left(1 - \tfrac{1}{2}^{i-1}\right) + (1-p)^n - 0 \end{aligned} \tag{D.10}$$

Expanding the term $(1-½^{i-1})$

$$\begin{aligned} S &= \sum_{i=0}^{n} \binom{n}{i} p^i (1-p)^{n-i} - \sum_{i=0}^{n} \binom{n}{i} p^i (1-p)^{n-i} \left(\tfrac{1}{2}^{i-1}\right) + (1-p)^n \\ &= \sum_{i=0}^{n} \binom{n}{i} p^i (1-p)^{n-i} - \sum_{i=0}^{n} \binom{n}{i} p^i (1-p)^{n-i} \, \tfrac{1}{2}^{i-1} + (1-p)^n \\ &= \sum_{i=0}^{n} \binom{n}{i} p^i (1-p)^{n-i} - 2\sum_{i=0}^{n} \binom{n}{i} \left(\frac{p}{2}\right)^i (1-p)^{n-i} + (1-p)^n \end{aligned} \tag{D.11}$$

The first two terms are just binomial expansions:

$$\begin{aligned} S &= \sum_{i=0}^{n} \binom{n}{i} p^i (1-p)^{n-i} - 2\sum_{i=0}^{n} \binom{n}{i} \left(\frac{p}{2}\right)^i (1-p)^{n-i} + (1-p)^n \\ &= (p+1-p)^n - 2\left(1 - p + \frac{p}{2}\right)^n + (1-p)^n \\ &= 1 - 2\left(1 - \frac{p}{2}\right)^n + (1-p)^n \end{aligned} \tag{D.12}$$

Therefore:

$$\sum_{i=2}^{n} \binom{n}{i} p^i (1-p)^{n-i} \left(1 - \tfrac{1}{2}^{i-1}\right) = 1 - 2\left(1 - \frac{p}{2}\right)^n + (1-p)^n \tag{D.13}$$

# Bibliography

† - Written by Guy Garty


1 *For example:* Heineke H., *Experimentelle untersuchungen über die einwirkung de röntgenstrahlen auf innere organe (Experimental investigations on the influence of x-rays on inner organs).* Mitt. Grenzg. Med. Chir. **14** (1905) 21-94.

2 Ward J.F., *DNA damage produced by ionizing radiation in mammalian cells: identities, mechanisms of formation and reparability.* Progress in Nucleic Acid research and Molecular Biology, **35**(1988) 95-125.

3 Wilson C.T.R. *On an expansion apparatus for making visible the tracks of ionizing particles in gases and some results obtained by its use.* Proc. Roy. Soc. Lon. **87** (1912) pp. 277-292.

4 Ahlen S.P. *Theoretical and experimental aspects of the energy loss of relativistic heavily ionizing particles.* Rev. Mod. Phys. **52** (1980) pp. 121-173.

5 F.Sauli, *Principles of operation of multiwire proportional and drift chambers*. In: Experimental Techniques in High Energy Physics. Ferbel T. (Ed.), Addison-Wesley (1987), pp. 79-188.

6 Alpen E.L. *Radiation Biophysics* (2nd ed.) Academic Press 1990.

7 Crispin A. & Fowler G.N. *Density effect in the ionization energy loss of fast charged particles in matter.* Rev. Mod. Phys. **42** (1970) pp. 290-316.

8 Fernow R. *Introduction to experimental particle physics.* Cambridge university press, Cambridge, 1986.

9 Kobetich E.J. & Katz R., *Energy deposition of electron beam and $\delta$ rays.* Phys. Rev. **170** (1968) pp. 391-396.

10 Friedland W, Jacob P, Bernhardt P, Paretzke HG, Dingfelder M. *Simulation of DNA damage after proton irradiation*. Radiat Res. 159 (2003) pp. 401-10.

11 Platzman R. *Conference on basic mechanisms in radiation biology.* National research council publication 305, National academy of science, Washington D.C. (1953)

12 Roots R. and Okada S., *Estimation of lifetimes and diffusion distances of radicals involved in X-ray induced DNA strand breaks or killing of mammalian cells*. Rad. Res. **64** (1975) 306-320.

13 Livneh Z. DNA *Damage Control by Novel DNA Polymerases: Translesion Replication and Mutagenesis*. J. Biol. Chem. **276** (2001) 25639-25642.

14 Elkind M.M. and Redpath J.L. In: Cancer: A comprehensive treatise. Becker F.F. (Ed.) Plenum, NY., Vol.6, pp 51, 1977.

15 Wallace S.S. "DNA damages processed by base excision repair: biological consequences" *Int. J. Radiat. Biol.* **66** (1994) 579-589

16 Martin S.J., Green D.R. and Cotter T.G. *Dicing with death: dissecting the components of the apoptosis machinery*. Trends Biochem. Sci. **19**(1994) 26-30

17 Friedberg E.C., Walker G.C. & Wolfram S. "DNA repair and mutagenesis" ASM press (Washington DC) 1995.

18 Powell S. & McMillan T.J. "DNA damage and repair following treatment with ionizing radiation" *Radiother. Oncol.* **19** (1990) 95-108.

19 The ATLAS radiation-hard electronics webpage: http://atlas.web.cern.ch/Atlas/GROUPS/FRONTEND/radhard.htm

20 Stassinopoulos E.G. & Raymond J.P., *Th espace radiation environment for electronics.* Proc IEEE **76** (1988) pp. 1423-1441.

21 Holmes-Siedle A. & Adams L. *Handbook of radiation effects (2nd ed.)* Oxford univ. press (2002).

22 Srour J.R. & McGarrity J.M., *Radiation effects on microelectronics in space* Proc. IEEE **76** (1988) pp. 1443-1469.

23 Petersen E.L. & Marshall P.W. "Single event phenomena in the space and SDI arena" *J. Rad. Effects Res. Eng.* **6** (1988) pp. 1.

24 Odero D.O. *The densitometric response of the high sensitivity Gafchromic film exposed to X-rays*. J. Mech. Med. Biol. **2** (2002) pp. 29-36.

25 Rana M.A. & Qureshi I.E., *Studies of CR-39 etch rates.* Nucl. Instr. & Meth. **B198** (2002) pp. 129-134.

26 Barberini L., Cadeddu S. & Caria M. *A new material for imaging in the UV: CVD diamond.* Nucl. Instr. & Meth. **A460** (2001) pp. 127-137.

27 Buttar C.M., Conway J., Mayfarth R., Scarsbrook G., Sellin P.J. & Whitehead A. *CVD diamond detectors as dosimeters for radiothrrapy.*Nucl. Instr. & Meth. **A392** (1997) pp. 281-284.

28 Manfredotti C., Lo Guidice A., Ricciardi C., Paolini C., Massa E., Fizzotti F. & Vittone E. *CVD diamond microdosimeters.* Nucl. Instr. & Meth. **A458** (2001) pp. 360-364.

29 Whitehead A.J., Airy R., Buttar C.M., Conway J., Hill G., Ramkumar S., Scarsbrook G.A., Sussmann R.S. & Walker S. *CVD diamond for medical dosimetry applications.* Nucl. Instr. & Meth. **A460** (2001) pp. 20-26.

30 Nikjoo H, O'Neill P, Goodhead DT, Terrissol M "Computational modelling of low-energy electron-induced DNA damage by early physical and chemical events", *Int. J. Rad. Biol.* **71** (1997) pp. 467–483.

31 Rossi H.H. & Rosenzweig W., *A device for the measurement of dose as a function of specific ionization.* Radiobiology, **64** (1955) pp. 404-411.

32 Rossi H.H. & Failla G., *Tissue equivalent ionization chambers.* Nucleonics **14** (1956) pp. 32-37.

33 Srdoč D. *Experimental technique for measurement of microscopic energy distribution in irradiated matter using Rossi counters.* Rad. Res. **43** pp. 302-319.

34 Grosswendt B. *Recent advances of nanodosimetry.* Ninth symposium on neutron dosimetry, Sept 2003, Delft, the Netherlands. To be printed in Rad. Prot. Dos.

35 Pimblott SM, LaVerne JA, Mozumder A., "Montè Carlo simulation of range and energy deposition by electrons in gaseous and liquid water", *J. Phys. Chem.* **100** (1996) pp. 8595–8606.

36 Fano U. "Note on the Bragg-Gary cavity principle for measuring energy dissipation" *Radiat. Res.* **1** (1954) 237-240.

37 *Tissue substitutes in radiation dosimetry and measurement*, ICRU 44, International Commission on Radiation Units and Measurements, Bethesda, MD 20814, USA, 1977

38 Grosswendt B., *On the equivalence of propane-based tissue-equivalent gas and liquid water with respect to the ionization-yield formation by electrons and α-particles.* Rad. Prot. Dos. **99** (2002) 401-404.

39 Grosswendt B. *Formation of ionization clusters in nanometric structures of propane-based tissue-equivalent gas or liquid water by electrons and α-particles.* Radiat. Environ.

Biophys. **41** (2002) 103-112.

40 Inokuti M. "How is radiation energy absorption different between the condensed phase and the gas phase" *Radiat. Effects & Defects in Solids* **117**(1991)143-162.

41 IAEA TECDOC 799 "Atomic and molecular data for radiotherapy and radiation research" (1995).

42 Budd T., Marshall M. & Kwok C.S, *Advances in cloud-chamber techniques and measurements of W value in tissue-equivalent gas.* Rad. Res. **88** (1981) pp. 228-239.

43 Budd T., Kwock C.S., Marshall M. & Lythe S., *Microdosimetric properties of alpha-particle tracks measured in a low-pressure cloud chamber.* Rad. Res. **95** (1983) pp. 217-230

44 Smathers J.B., Otte V.A., Smith A.R., Almond P.R., Attix F.H., Spokas J.J., Quam W.M. & Goodman L.J., *Composition of A-150 tissue equivalent plastic.* Med. Phys. **4** (1977) pp. 74-77.

45 Taylor G.C., Bentley R.D., Conroy T.J., Hunter R., Jones J.B.L., Pond A. & Thomas D.J., *The evaluation and use of a portable TEPC system for measuring in-flight exposure to cosmic radiation.* Rad. Prot. Dos. **99** (2002) pp. 435-438.

46 Badhwar G.D, *Radiation measurement on the international space station.* Phys. Med. **XVII** (2001) pp. 287-291

47 Marino S.A. &Johnson G.W. *A microdosimetry chamber for low energy X-rays.* Rad. Prot. Dos. 99 (2002) pp. 377-378.

48 Cesari V., Colautti P., Margin G., De Nardo L., Baek W.Y., Grosswenddt B., Alkaa a., Khamphan C., Ségur P. & Tornielli G., *Nanodosimetric measurements with an avalanche confinement TEPC.* Rad. Prot. Dos. **99** (2002) pp. 337-342.

49 Gersey B.B., Borak T.B., Guetersloh S.B., Zeitlin C., Miller J., Heilbronn L., Murakami T. and Iwata I., *The Response of a Spherical Tissue-Equivalent Proportional Counter to Iron Particles from 200–1000 MeV/nucleon*, Rad. Res. **157** (2002) 350-360.

50 Kliauga P., *Measurements of single event energy deposition spectra at 5nm to 250 nm simulated site size.* Rad. Prot. Dosim. **30** (1990) 119-123.

51 Alkhazov G.D., *Statistics of electron avalanches and ultimate resolution of proportional counters.* Nucl. Instr. & Meth. **89** (1970) pp. 155-165.

52 Waker A.J., *Principles of experimental microdosimetery*. Rad. Prot. Dos. **61** (1995) 297-308

53 Breskin A., Chechik R., Malamud G. and Sauvage D., *Primary ionization cluster counting with low-pressure multistep detectors.* IEEE Trans. Nucl. Sci. **36** (1989) 316-321.

54 Malamud G., Breskin A. & Chechik R., *A study of relativistic charged particle identification by primary cluster counting in low-pressure gaseous detectors.* Nucl. Instr. & Meth. **A372** (1996) pp. 19-30.

55 Pansky A, Breskin A. and Chechik R. *A new technique for studying the fano factor and the mean energy per ion pair in counting gases.* J. App. Phys. **79** (1996) 8892-8898.

56 Pansky A, Breskin A. and Chechik R. *The fano factor and the mean energy per ion pair in counting gases, at low X-ray energies.* J. App. Phys. **82** (1997) 871-877.

57 Pansky A, Breskin A. and Chechik R. *Sub-keV X-ray spectroscopy using a low-pressure electron counting detector.* X-ray Spect. **26** (1997) 159-164.

58 Pansky A, Breskin A., Chechik R., Garty G. & Klein E. *Application of the electron counting method to low-Z elemental analysis.* Nucl. Instr. & Meth **A392** (1997) 465-470.

59† Garty G., Shchemelinin S., Breskin A., Chechik R., Orion I., Guedes G.P., Schulte R.,

Bashkirov V. and Grosswendt B., *Wall-less ion-counting nanodosimetry applied to protons*, Rad. Prot. Dos. **99** (2002) 325-330.

60† Garty G., Shchemelinin S., Breskin A., Chechik R., Assaf G., Orion I., Bashkirov V., Schulte R. and Grosswendt B., *The performance of a novel ion-counting nanodosimeter*, Nucl. Instr. & Meth **A492** (2002) 212-235.

61† Garty G., Assaf G., Leloup C., milligan J., Bashkirov V., Shchemelinin S., Grosswendt B., Schulte R., Breskin A. and Chechik R., *Experimental system for correlating nanodosimetric measurements and biological effects of ionizing radiation*. **In preparation.**

62 Breskin A., Chechik R., Colautti P., Conte V., Pansky A., Schchemelinin S., Talpo G. and Tornielli G., *A single-electron counter for nanodosimetry*. Radiat. Prot. Dosim. **61** (1995) 199-204.

63 De Nardo L., Alkaa A., Khamphan C., Conte V. Colautti P., Dona G., Segur P. and Torinieli G., *A detector for track nanodosimetry.* Nucl. Instr. & Meth. **A484** (2002) 312-326.

64 De Nardo L., Alkaa A., Khamphan C., Conte V. Colautti P., Dona G., Segur P. and Torinieli G., *A single-electron counter for track nanodosimetry.* LNL-INFN reprot 147 (2001)

65 De Nardo L., Colautti P. Baek W.Y., Grosswendt B., Alkaa A., Segur P. and Tornielli G., *Track nanodosimetry of an alpha particle*. Rad. Prot. Dos. **99** (2002) 355-358.

66 De Nardo L., Collauti P., Conte V., Baek W., Grosswendt B. & Tornielli G., *Ionization-cluster distributions of α-particles in nanometric volumes of propan: measurement and calculation.* Rad. Envir. Bioph. **41** (2002) pp. 235-256.

67† Garty G. *Study of fast gaseous electron multipliers for electron counting applications.* M.Sc. thesis (1997).

68 Turner J.E., Hunter S.R., Hamm R.N., Wright H.A., Hurst G.S. and Gibson W.A., Development of an optical digital ionization chamber. Rad. Prot. Dosim. **29** (1989) 9-14.

69 Hunter S.R., Gibson W.A., Hurst G.S., Turner J.E., Hamm R.N. and Wright H.A., *Optical imaging of charged particle tracks in a gas.* Rad. Prot. Dosim. **52** (1994) 323-328.

70 Titt U., Breskin A., Chechik R., Dangendorf V., Schmidt-Böcking H., and Schumacher H., *A time projection chamber with optical readout for charged particle track structure imaging.* Nucl. Instrum. & Meth. **A416** (1998) 85-99.

71 Dangendorf V. Schuhmacher H., Titt U. and Tittelmeier K. *Imaging of microscopic features of charged particle tracks in low-pressure gas.*Rad. Prot. Dosim. **99** (2002) 353-354.

72 Laczko G., Dangendorf V., Krämer M., Schardt D. & Tittelmeier K., *High resolution heavy track structure imaging.* Submitted to Rad. Prot. Dos.

73 Breskin A. *New developments in optical imaging detectors.* Nucl. Phys. **A498** (1989) pp. 457c-468c.

74 Jean-Marie B., Lepeltier V. & L'Hote D., *Systematic measurement of electron drift velocity and study of some properties of four gas mixtures: A-$CH_4$, A-$C_2H_4$, A-$C_2H_6$, A-$C_3H_8$.* Nucl. Instr. & Meth. **159** (1979) pp. 213-219.

75 Shchemelinin S., Breskin A., Chechik R., Colautti P., and Schulte R.W. *First ionization cluster measurements on the DNA scale in a wall-less sensitive volume.* Radiat. Prot. Dosim, **82** (1999) 43-50.

76 Chmelewski D., Parmentier N. and Le Grand J. *Dispositif experimental en vue d'etudes dosimetriques au niveau du nanometre* Proceedings of the fourth symposium on microdosimetry, EUR 5122 d-e-f, CEC, Luxemburg, 1973, p.869-885.

77 Pszona S.*, A track ion counter*. Proceedings of Fifth Symposium on Microdosimetry EUR

5452 d-e-f, pp 1107-1122, Published by the Commission of the European Communities, Luxembourg, (1976)

78 Shchemelinin S., Breskin A., Chechik R., Pansky A., Colauti P., Conte V., De Nardo L., and Tornielli G. *Ionization measurements in small gas samples by single ion counting*. Nucl. Instr. & Meth. **A368** (1996) 859-861.

79 Mason E.A. & McDaniel E.W., *Transport properties of ions in gases*. Wiley International (1987).

80 Pszona S., Kula J. and Marjanska S., *A new method for measuring ion clusters produced by charged particles in nanometre track sections of DNA size.* Nucl. Instrum. & Meth. **A447** (2000) 601-607.

81 Pszona S. Kula J., *Ionization clusters at DNA level: Experimental modeling.* Rad. Prot. Dosim. **99** (2002) 387-390

82 Grosswendt B. and Pszona S. *The formation of ionization clusters by $\alpha$ particles in 'nanometric' volumes of nitrogen: Experiment and calculation.* Rad. Prot. Dosim. **99** (2002) 331-335.

83 Schulte R., Bashkirov V., Shchemelinin S., Garty G., Chechik R., Breskin A., *Modeling of radiation action based on nanodosimetric event spectra*. Physica Medica, Vol. **XVII**, Suppl. 1 (2001) 177-180.

84 Shchemelinin S., Breskin A., Chechik R., Pansky A., and Colautti P. *A nanodosimeter based on single ion counting*. In: Microdosimetry - An interdisciplinary approach. Goodhead D., O'Neill P. & Menzel H. (Eds.), The Royal Society of Chemistry (Cambridge), pp 375-378, 1997.

85 Shchemelinin S., Garty G., Breskin A., Chechik R. and Schulte R.W., *Ion-counting nanodosimetry: a new method for assessing radiation damage to DNA*. Nucl. Instr. & Meth. **A477** (2002) 527-530

86 Bashkirov V., Coutrakon G., Koss P., Schulte R., Garty G., Shchemelinin S., Breskin A., Chechik R., Assaf G., Orion I., Keeney B., Johnson R.P., Kroeger W., Sadrozinski H.F.W., Seiden A., Spradlin P. and Grosswendt B., *An Ion-Counting Nanodosimeter with Particle Tracking Capabilities*. **In preparation**

87† Shchemelinin S., Pszona S., Garty G., Breskin A., and Chechik R. *The absolute detection efficiency of vacuum electron multipliers to keV protons and $Ar^+$ ions*. Nucl. Instr. & Meth. **A438** (1999) 447-451.

88 Berger M.J., *ESTAR, PSTAR and ASTAR: Computer programs for calculating stopping powers and ranges for electrons, protons and helium ions,* In: IAEA TECDOC 799: Atomic and molecular data for radiotherapy and radiation research. International Atomic Energy Agency, Vienna, (1995) 723-740

89 Barbosa A.F., Guedes G.P. and Lima H.P. Jr., *Recent results on a simple scheme for 2D localization of particles in a wire chamber.* Nucl. Instr. & Meth. **A477** (2002) 41-47

90 Ziegler J.F., Biersack J.P. and Littmark U. *The stopping and range of ions in solids* Pergamon Press, New York, 1985.

91 Dahl D.A. *SimIon 3D version 7.0* Idaho Nat. Eng. & Env. Lab. Idaho falls, ID 83415, USA.

92 Shchmelinin S., *Ion-counting nanodosimetry: limitations coming from ion diffusion.* Internal report, Radiation detection physics group, Weizmann Institute of Science Oct. 2003.

93 Keeney B., Bashkirov V., Johnson R.P., Kroeger W., Ohyama H., Sadozinski H.F.W., Schulte R.W.M., Seiden A. & Spradlin P., *A silicon telescope for applications in nanodosimetry*. IEEE Trans. Nucl. Sci. 49 (2002) pp. 1724-1727.

94 D'Souza D.I. & Harrison L., *Repair of clustered uracil DNA damage in Escherichia Coli.* Nucleic Acid Res. **31** (2003) pp. 4573-4581.

95 Dianov G.L., Timchenko T.V., Sinitsina O.I., Kuzminov A.V., Medvedev O.A. & Salaganik R.I., *Repair of uracil residues closely spaced on the opposite strand of plasmid DNA results in double strand break and deletion formation.* Mol. Gen. Genet. **225** (1991) pp. 448-452.

96 Zhao Y., Tan Z., Du Y. & Qui G., *Electrophoresis examination of strand breaks in plasmid DNA induced bylow-energy nitrogen ion irradiation.* Nucl. Instr. & Meth. **B211** (2003) pp. 211-218.

97 Folkard M., Prise K.M., Vojnovic B., Davies S., Roper M.J. & Michael B.D. *Measurement of DNA damage by electrons with energies between 25 and 4000 eV*. Int. J. Rad. Biol. **64** (1993) pp651-658.

98 Yamashita T., Kurashige H., Morii M.M., Nakamura T.T., Nomura T., Sasao N., Shibata K., Fukushima Y. Ikegami Y. Kobayashi H. and Taniguchi T., *Measurements of electron drift velocities and positive ion mobilities for gases containing $CF_4$ II.* Nucl. Instr. & Meth. **A317** (1992) 213-220.

99 *Average energy required to produce an ion pair*, ICRU 31, International Commission on Radiation Units and Measurements, Bethesda, MD 20814, USA, 1971

100 De Kruijf W.J.M. and Kloosterman J.L., *On the average chord length in reactor physics.* Ann. Nuc. Ener. **30** (2002) 549-553.

101 Assaf G. *Comparison of the biophysical effects on DNA of protons and α-particles of equal mean ionization.* M.Sc. Thesis

102 Goodhead D.T., Belli M, Mill A.J., Bance D.A., Allen L.A., Hall S.C., Ianzani F., Simone G., Stevens D.L., Stretch A., Tabocchini M.A. and Wilkinson R.E., *Direct comparison between protons and alpha particles of the same LET: I. Irradiaton methods and inactivation of asynchronos V79, HeLa and C3H 10T½ cells.* Int. J. Radiat. Biol. **61** (1992) 611-624.

103 Belli M, Goodhead D.T., Ianzani F., Simone G and Tabocchini M.A., *Direct comparison between protons and alpha particles of the same LET: II. Mutation induction at the HPRT locus in V79 cells.* Int. J. Radiat. Biol. **61** (1992) 625-629.

104 Jenner T.J., Belli M, Goodhead D.T., Ianzani F., Simone G. and Tabocchini M.A., *Direct comparison between protons and alpha particles of the same LET: III.Initial yield of DNA double strand breaks in V79 cells.* Int. J. Radiat. Biol. **61** (1992) 630-637.

105 Leloup C., Garty G., Milligan J., Schulte R., Paz-Elitzur T., Assaf G., Livneh Z., Breskin A. and Chechik R., *Evaluation of lesion clustering in proton-irradiated DNA.* Submitted to Int. J. Rad. Biol.

106 Lutze L.H., Winegar R.A., *pHAZE: a shuttle vector system for the detection and analysis of ionizing radiation-induced mutations*, Mutat. Res. **245** (1990) 305-310.

107 Milligan J.R., Ng J.Y-Y., Wu C.C.L., Aguilega J.A., Ward J.F., Kow Y.W., Wallace S.S. & Cunningham R.P., *Methylperoxyl radicals as intermediates in the damage to DNA irradiated in aqueous dimethyl sulfoxide with gamma rays.* Rad. Res. **146** (1996) pp. 436-443.

108 Klimczak U., Ludwig D.C., Mark F. Rettberg P., & Schulte-Frohlinde D. *Irradiation of plasmid and phage DNA in water-alcohol mixtures: strand breaks and lethal damage as a function of scavenger concentration.* Int. J. Radiat. Biol. **64** (1993) 497-510.

109 Milligan J.R., Aguilera J.A. & Ward J.F. *Variation of single-strand break yield with scavenger concentration for plasmid DNA irradiated in aqueous solution.* Rad. Res. **133**

(1993) pp. 151-157.

110 Milligan J.R., Aguilera J.A., Wu C.C.L., Ng J.Y-Y. & Ward J.F. *The difference that linear energy transfer makes to precursors of DNA strand breaks.* Rad. Res. **146** (1996) pp.436-443.

111 Cowan R., Collis C.M. and Grigg G.W., *Breakage of double-stranded DNA due to single-stranded nicking*, J. Theor. Biol. **127** (1987) 229-245

112 Bashkirov V., Schulte R.W. *Dosimetry system for the irradiation of thin biological samples with therapeutic proton beams.* Phys. Med. Biol. **47** (2002) pp. 409-420.

113 ICRU *Clinical proton dosimetry part I: Beam production, beam delivery and measurement of absorbed dose*; ICRU 59, International Commission on Radiation Units and Measurements, Bethesda, MD 20814, USA, 1998.

114 CRC handbook of electrophoresis. (CRC Press) Bocca Raton, FL 1980.

115 Strike P., Humphreys G.O. & Roberts R.J., *Nature of transforming dioxiribonucleic-acid in Calcium-treated Escherichia-Coli.* J. Bact. 138 (1979) pp. 1033-1035

116 Gulston M., Fulford J., Jenner T., deLara T. & O'Niell P. *Clustered DNA damage induced by γ radiation in human fibroblasts (HF19), Hamster (V79-4) cells and plasmid DNA is revealed as Fpg and Nth sensitive sites.* Nucl. Acids. Res. **30** (2002) 3464-3472.

117 Nikjoo H., O'Nield P., Terrisol M. and Goodhead D.T., *Quantitative modeling of DNA damage using Montè Carlo track structure method.* Radiat. Environ. Biophys. **38** (1999) 31-38.

118 Kraft G. *Tumor therapy with heavy charged particles.* Prog. Par. Nuc. Phys. **45** (2000) pp. S473-S544.

119 Grosswendt B., De Nardo L., Collautti P., Pszona S., Conte V. & Tornielli G., *Experimental equivalent cluster-size distributions in nanometric volumes of liquid water.* Ninth symposium on neutron dosimetry, Sept 2003, Delft, the Netherlands. To be printed in Rad. Prot. Dos.

120 Kellerer A.M. *An assessment of wall effects in microdosimetric measurements* Rad. Res. **47**(1971) pp. 377-386.

121 Prise K.M., Pinto M., Newman H.C. & Michael B.D. *A review of studies of ionizing radiation-induced double-strand break clustering.* Rad. Res. 156 (2001) pp. 572-576.

122 Mozumder A. & Magee J.L. *Theory of radiation chemistry 7: structure and reactions in low LET tracks.*J. Chem. Phys. **45** (1966) pp. 3332-3341.

123 Paretzke H.G. *Radiation track structure theory*. In: The Dosimetry of Ionizing Radiation. Vol. II. Kase, K.R., Bjarngaard, B.E., Attix, F.H.(Eds.). Academic Press (1987), Orlando, pp. 89-170.

124 Chen C.Z. & Watt D.E., *Biophysical mechanism of radiation damage to mammalian cells by X- and gamma-rays*. Int. J. Rad. Biol. **49** (1986) pp. 131-42.

125 Roots R., Holley W., Chatterjee A., Irizarry M. & Kraft G. *The formation of strand breaks in DNA after high-LET irradiation: a comparison of data from in-vitro and cellular systems.* Int. J. Rad. Biol. **58** (1990) pp. 55-69.

126 O'Neill P., Cunniffe S.M.T., Stevens D.L., Botchway S.W. & Nikjoo H. *Strand break induction in DNA by Aluminium K ultrasoft X-rays: Comparison of experimental data and track structure analysis.* In: Microdosimetry - An interdisciplinary approach. Goodhead D., O'Neill P. & Menzel H. (Eds.), The Royal Society of Chemistry (Cambridge), pp 81-84, 1997.

127 Taucher-Scholz G. & Kraft G., *Influence of radiation quality on the yield of DNA strand*

*breaks in SV40 DNA irradiated in solution.* Rad. Res. **151** (1999) pp. 595-604.

128 Taucher-Scholz G., Stanton J.A., Schneider M. & Kraft G., *Induction of DNA breaks in SV40 by heavy ions.* Adv. Space Res. **12** (1992) pp. (2)73-(2)80

129 Christensen R.C., Tobias C.A & Taylor W.D., *Heavy-ion-induced single- and double-strand breaks in phiX-174 replicative form DNA.* Int. J. Rad. Biol. Relat. Stud. Phys. Chem. Med. **22**(1972) pp. 457-477.

130 Pimblott S.M. & La Verne J.A., *Effects of track structure on the ion radiolysis of the Fricke dosimeter.* J. Phys. Chem. A **106** (2002) pp. 9420-9427.

131 LaVerne J.A. & Pimblott S.M. *Yields of hydroxyl radical and hydrated electron scavenging reactions in aqueous solutions of biological interest.* Rad. Res. **135** (1993) pp. 16-23.

132 *Stopping powers and ranges for protons and alpha particles.* ICRU 49, International Commission on Radiation Units and Measurements, Bethesda, MD 20814, USA, 1993

133 Baek W. Y., Grosswendt B., *Energy dependence of W values for protons in gases.* Radiat. Prot. Dosim. **52** (1994) 97-104.

134 Rudd M.E., Kim Y.K., Madison D.H., Gallagher J.W., *Electron production in proton collisions: total cross sections*, Rev. Mod. Phys. **57** (1985) 965-994

135 Wilson W.E., Toburen L.H., *Electron emission from proton-hydrocarbon-molecule collisions at 0.3-2.0 MeV*. Phys. Rev. **A11** (1975) 1303-1308.

136 *Secondary electron spectra from charged particle interactions*; ICRU 55, International Commission on Radiation Units and Measurements, Bethesda, MD 20814, USA, 1996.

137 Hwang W., Kim Y. K., Rudd M. E., *New model for electron-impact ionization cross-sections of molecules.* J. Chem. Phys. **104** (1996) 2956-2966.

138 Bethe H.A. *Zur theorie des durchgangs schneller korpuskularstrahlen durch materie.* Ann. D. Physik **5** (1930) 325.

139 Ziegler J. F., Manoyan J. M., *The stopping of ions in compounds*, Nucl. Instrum. & Meth. **B35** (1988) 215-228

140 De Nardo L., Conte V., Baek W. Y., Grosswendt B., Colautti P., Tornielli G., *Measurements and calculations of ionization cluster distributions in 20 nm size site*, (Report 175/2001) Istituto Nazionale di Fisica Nucleare - Laboratori Nazionali di Legnaro; Legnaro, Padova, Italy;(2001

141 Grosswendt B. & Waibel E., *Transport of low energy electrons in nitrogen and air.* Nucl. Instrum. & Meth. **155** (1978) 145-156.

142 Chouki A., *Détermination des sections efficaces de Collision électron-molécule dans l'Ethane, le Propane et l'Isobutane*; Doctoral thesis, University Paul Sabatier, Toulouse, 1994.

143 Green A.E.S., Sawada T., *Ionization cross sections and secondary electron distributions.* J. Atmosph. & Terr. Phys. **34** (1972) 1719-1728.

144 Berger M. J., *Spectrum of Energy Deposited by Electrons in Spherical Regions*. in: Ebert H. G. (Ed.), Proc. Second Symposium on Microdosimetry, Report EUR 4452, Commission of the European Communities, Brussels, 1969, p. 541-558.

145 Opal C. B., Beaty E. C., Peterson W. K., *Secondary-electron- production cross sections.* Atomic Data **4** (1972) 209-253.

146 Jackman C.H., Garvey R.H., Green A.E.S., *Electron impact on atmospheric gases I. updated cross sections*. J. Geophys. Res. **82** (1977) 5081-5090.

147 D. Burch*, K-Shell ionization of carbon by 1- to 18-MeV protons,* Phys. Rev. A*,* **12** (1975)

pp. 2225-2226.

148 Casnati E., Tartari A. and Baraldi C., *An empirical approach to K-shell ionization cross-section by electrons.* J. Phys **B15** (1982) 155-167.

149 Johns H.E. and Cunningham J.R., *The physics of radiology*, Fourth Edition, Charles C. Thomas publisher 1983.

150 Marquardt, D., "An Algorithm for Least Squares Estimation of Nonlinear Parameters" *SIAM J. App. Math.* **11** (1963) pp. 431-441.

# תקציר


מטרת המחקר הנה פיתוח שיטות חדשניות לאפיון מדויק של תבנית היינון הנוצרת ע״י חלקיקים טעונים הנעים בתווך גזי. הַנַנוֹדוֹסִימֶטֶר שפותח למטרה זו מבוסס על ספירה של יונים בודדים, המושרים בנפח זעיר של גז דליל המדמה תווך מוצק או נוזלי שמימדיו קטנים פי מיליון. שיטה זו, של מדידת יינון בגז, משמשת בהצלחה כ50 שנה לאפיון נזקי קרינה לחומר ביולוגי בסקאלת התא (קוטר של מספר מיקרונים). הננודוסימטר מאפשר **לראשונה** הדמיה מוחשית ומידול של פעולת הקרינה המיננת על נפח קטן בתוך רקמה, בקנה מידה **ננומטרי**. מידול זה חיוני, למשל, להבנה של נזקי קרינה הנגרמים לדנ״א.

הננודוסימטר שפותח על ידנו מאפשר יצירת נפח רגיש, דמוי דנ״א, שקוטרו בין 2 ל 10 ננומטר ואורכו בין 5 ל 100 ננומטר. הנפח הרגיש מוגדר ע״י דיפוזיה של יונים בגז, תחת שדה חשמלי ולא ע״י קירות פיזיים העשויים לעוות את תוצאות המדידה. היונים הנוצרים בתוך הנפח הרגיש נספרים ביעילות גבוהה בהרבה מזו של מערכות אחרות [63, 80] שפותחו למטרה זו.

שני הננודוסימטרים, שפותחו ונבנו במשך עבודה זו, הותקנו במאיצי הפלטרון וה ואן-דה-גראף במכון ויצמן ובסינכרוטרון הפרוטונים הרפואי באוניברסיטת לומה-לינדה שבארה״ב. לאחר אפיון מקיף של אופן הפעולה של הננודוסימטר ביצענו מדידות מדויקות של תבנית היינון המושרית ע״י קרני יונים צרות, שצפיפות היינון הממוצעת (LET) שלהן משתרעת על פני ארבעה סדרי גודל (בין 0.4 keV/μm ל keV/μm 700). עבור צפיפויות יינון נמוכות מ 100 keV/μm תוצאות מדידות אלו מתאימות התאמה טובה לתוצאות סימולציות שבצענו , המבוססות על האינטראקציות הראשוניות והמשניות בגז, הובלת היונים וספירתם. הדבר מעיד על מהימנות השיטה הניסיונית לננודוסימטריה שפיתחנו. בעקבות מדידות אלה ביצענו מדידות של התפלגות צבירי היינון הנוצרים בתנאים המדמים הקרנה של דנ״א במבחנה עבור שדות קרינה הומוגניים בעלי צפיפות יינון של בין 0.4 keV/μm ל 26 keV/μm .

להשלמת מדידות אלה ביצענו גם מדידות מדויקות של הנזקים הנגרמים לדנ״א המוקרן בתמיסה. דנ״א טהור הוקרן בסביבה מימית המכילה כמות מבוקרת של לוכדי רדיקלים. בעקבות ההקרנה, כימתנו את הנזקים הנגרמים לדנ״א (שברים חד- ודו-גדיליים וכן צבירי נזקים הכוללים גם נזק לבסיסים). מתוך התלות של כמות הנזקים במינון הקרינה הסקנו את הנזק הנגרם ע״י מנת קרינה סטנדרטית. ניסיונות אלו הראו בבירור תלות בין כמות הנזקים לבין צפיפות היינון.

ברמה המקרוסקופית (LET) ראינו תלות מסובכת של כמות צבירי הנזקים בצפיפות היינון; התופעה נובעת מתגובות כימיות בין הרדיקלים הנוצרים ע״י הקרינה, דבר שגורם לירידה בכמות הנזק כאשר מגדילים את צפיפות היינון. ברמה הננומטרית, לעומת זאת, ראינו הבדל ברור בין כמות צבירי הנזקים הנגרמים ע״י שדות קרינה בעלי אותה צפיפות יינון ממוצעת אך המשרים צפיפות יינון ננומטרית שונה (פרוטונים וגרעיני הליום).

בעוד ששתי מדידות אלו (הביולוגית והפיסיקלית) חשובות בפני עצמן, רק דרך חיבורן ניתן להביט לעומק לתהליך שבו קרינה מיננת מובילה ליצירת מוטציות ולמות התא. בעבודה זו אנו מציגים מודל בסיסי המנבא את כמות הנזקים הנוצרים בעקבות הקרנת DNA, על בסיס התפלגות צבירי היינון הנוצרים במודל גזי. לפי מיטב ידיעתנו השוואה כזו לא הייתה אפשרית בטרם עבודה זו. השוואה זו מנבאת בהצלחה את התלות של כמות הנזקים בצפיפות היינון אך מנבאת הבדל קטן מדי עבור סוגי קרינה שונים בעלי אותה צפיפות יינון מקרוסקופית. ההבדלים שנצפו בין שתי המדידות נובעים בבירור מכך שבשיטה הננודוסימטרית אנו מתעלמים מיינונים הנוצרים רחוק מן הדנ״א. במציאות יינונים אלה גורמים ליצירת רדיקלים חופשיים האחראים לכשני שלישים מהנזק.

למרות זאת עבודה זו מדגימה בבירור את השימושיות של מדידות ננודוסימטריות ומדגימה כיצד ניתן לשפר אותן; ע״י ביצוע מדידות ננודוסימטריות במקביל למדידות מיקרו-דוסימטריות (בנפח רגיש של עשרות עד מאות ננומטר) ותוך מידול מדויק של התנועות והתגובות הכימיות של הרדיקלים החופשיים ניתן יהיה בעתיד לנבא במדויק את הנזק הנגרם לדנ״א ע״י קרינה.

# מכון ויצמן למדע

# Weizmann Institute of Science

Thesis for the degree
**Doctor of Philosophy**

**חבור לשם קבלת התואר**
**דוקטור לפילוסופיה**


by:
**Guy Y. Garty**

supervisor
Prof. A. Breskin

**מאת**
**גיא י. גרטי**
**מנחה**
**פרופ. ע. ברסקין**


# פתוח שיטה ננודוסימטרית המבוססת על ספירת יונים וחקר יישומיה ברדיוביולוגיה

# Development of ion-counting nanodosimetry and evaluation of its relevance to radiation biology

January 2004

**טבת תשס"ד**

Submitted to the Scientific Council of the
Weizmann Institute of Science
Rehovot, Israel

**מוגש למועצה המדעית של**
**מכון ויצמן למדע**
**רחובות, ישראל**